The elastic and dielectric properties of structural ceramics

Liu, Huijin

Award date:
1999

Awarding institution:
University of Bath

THE ELASTIC AND DIELECTRIC PROPERTIES OF STRUCTURAL CERAMICS

submitted by
HUIJIN LIU
for the degree of PhD
1999

Liu Huijin
刘慧津

ProQuest LLC
789 East Eisenhower Parkway
P.O. Box 1346
Ann Arbor, MI 48106-1346

ACKNOWLEDGEMENTS

I would like to express my sincere gratitude to my supervisor, Professor G A Saunders for his supervision, support, help and encouragement during the whole period of my time at University of Bath.

I must acknowledge the Defence Research Agency and the School of Physics, University of Bath for the financial support of this work.

Particular thanks go to Dr. B.J. James for his advice on my work and for his kindness in providing access to valuable research literature. Thanks to Ian Pickup for his advice on my work and for sample preparation.

I would like to thank Mr. E.F. Lambson for his professional assistance in the operation of ultrasonic equipment and pressure system, Mrs W.A. Lambson for sample preparation and Luo Jie in material science department for scanning electron microscopy sample preparation.

I would also like to thank Mr. B. Chapman for his kindness in making X-ray diffraction spectra of the alumina ceramics. In addition he gave me detailed instructions about how to use the X-ray diffraction spectrum analysis software.

Finally I would like to thank Mr. R.C.J. Draper and all my colleagues in the ultrasonics group for their help during this work.

Abstract

Six ceramic aluminas and two ceramic silicon carbides made by different manufacturing processes have been characterised using a variety of experimental techniques.

X-ray diffraction spectra show that aluminas D975, H880 and SINTOX FA are textured to some degree and have cylindrical symmetry. The c-axis of α-Al_2O_3 grains are preferentially aligned along a uniaxial axes in each sample (called the Z direction). No observable texture has been found in the aluminas D999 and AL23 or silicon carbide SiC PAD b. Crystalline secondary phases have been found.

Scanning electron microscopy results show that both the aluminas D999 and AL23 have equi-axed grains and that their microstructures are isotropic. A proportion of the grains of aluminas D975, H880 and SINC53 are platelet-like with their basal planes preferentially oriented perpendicular to the Z direction.

The propagation and polarisation directional dependence of longitudinal and shear mode ultrasonic wave velocities in the alumina samples have been examined at room temperature. Velocity data have been analysed using ultrasonic birefringence theory. Samples D999 and AL23 are isotropic, while the others show some anisotropy.

The hydrostatic pressure dependences of the ultrasonic wave velocities and attenuation have been measured at room temperature up to 0.3~0.35 GPa. The Poisson ratio, elastic moduli and their pressure derivatives, volume

compression and the long wavelength acoustic Grüneisen parameters have been determined.

Impedance spectra of ceramic aluminas have been measured over a frequency range from 5Hz to 10MHz between 20K and 600°C~704°C. The microstructure has been analysed using the "brick model". Dielectric relaxation processes and Maxwell-Wagner effects have been found.

The quasi-static stress damage effects on the hydrostatic pressure dependence of elastic properties and ultrasonic wave attenuation of ceramic alumina and silicon carbides have been studied in comparison with the pre-stressed samples. The size of the cracks introduced by quasi-static loading has been estimated.

CONTENTS

Chapter 1 Introduction

In its pure form alumina (Al_2O_3) ceramic is a structural material and a very good insulator. Its main applications are in electronics and mechanical engineering. Alumina ceramics can be used in particular to serve as structural parts subject to mechanical loads, when required at high temperatures. Applications in laboratory equipment, armour applications and medical applications are of growing importance. Alumina ceramics have been successfully employed for a long time. The scientific investigations on alumina date back to the last century while an early commercial use goes back to 1907 (Dörre 1984). Commercial production and application on a large scale started in the late 1920s and the early 1930s (Dörre 1984).

Like many other ceramics, alumina is not only fabricated and used in its pure form but also there exists a wide series of material compositions which start from Al_2O_3 as the base material and also contain one or more other phases. An alumina ceramic which contains at least 95% Al_2O_3 is called a high alumina ceramic. With increasing content of alumina, ceramics containing at least 99% alumina are called high-purity alumina ceramics, having additives in the range of some tenths of a percent in order to control the sintering process.

Silicon carbide is one of the most commonly used structural ceramics and semiconductors. Attractive properties of silicon carbide include extreme hardness, good specific strength and Young's modulus as a function of temperature, relatively low weight, corrosion and erosion resistance, very high thermal stability and semiconducting behaviour. Its main applications

are in abrasives, structural ceramic components, refractory materials and electronics.

The elastic moduli, which are related to interatomic forces, are fundamental for understanding and predicting material behaviour. Elastic moduli control the strain energy release rate and the stress wave propagation properties associated with shock, impact, fracture, etc. The pressure derivatives of the elastic moduli can be related to the anharmonicity of a crystal lattice. The determination of elastic properties of a ceramic material is an important step in studying mechanical behaviour: the utility of a ceramic material in an engineering application is critically determined by its mechanical behaviour. This applies not only to structural applications. The mechanical behaviour is also of importance in such uses as where the material is employed mainly because of its optical, electrical, or magnetic properties. Previous work on elastic properties of single crystal and ceramic alumina has been reviewed by Dörre (1984). The second order elastic constants of single crystal alumina were determined experimentally by Wachtman at al. (1961). The elastic moduli and their pressure derivatives of high purity, high density ceramic aluminas were measured by Chung and Simmons (1968) and Schreiber and Anderson (1966). Chung and Simmons (1968) interpreted the experimental data with respect to the ceramic alumina data calculated from the corresponding single-crystal data. The results of these earlier studies enable us to determinate the contribution of the additions and the resident impurity to the elastic properties of ceramic alumina which is very important in manufacture and applications of ceramic material.

Ultrasonic materials characterisation may be divided into two major categories. The first pertains to properties that are related to mechanical

properties such as elastic moduli and their pressure derivatives as introduced above. The second category refers to material conditions such as microstructure and morphology that govern mechanical properties and dynamic response. Ultrasonic birefringence, which was discovered by Bergmann and Shabbender (1958) and by Benson and Raelson (1959), has proved to be a very suitable approach to the non-destructive testing of the microstructure and morphology of ceramic materials. Ultrasonic birefringence can be used to determine the principal directions of elastic anisotropy caused by (residual) stress or texture and hence to characterise the state of stress or the degree of texture. Using the ultrasonic birefringence and attenuation theory together with scanning electron microscopy and the X-ray theory enables us to find the source of elastic anisotropy, which is caused mainly by the texture of the grains of the ceramic.

Since electronics and mechanical engineering are the main areas of application of alumina ceramics, not only elastic but also dielectric properties are important for their development and evaluation. Dielectric properties of polycrystalline ceramics are affected not only by the composition and crystal structure of the phases present but also by their microstructure. For a polycrystalline ceramic the microstructure is mainly composed of crystalline grains of the phases present, grain boundaries, microcracks and pores; moreover, it varies with the relative amounts, composition and arrangement of each phase, including that of grain-boundaries, and with geometrical characteristics of each phase such as size, shape and orientation. Analysing complex profiles of the impedance spectra can assist in development of an understanding of the nature of the microstructure.

This thesis details the basic theories, the techniques and the results and discussion of the ultrasonic properties and AC impedance measured on alumina ceramics. The techniques of X-ray diffraction spectra and scanning electron microscopy are used to analyse the texture and microstructure of ceramic aluminas. Furthermore stress damage effects on the elastic properties and the ultrasonic wave attenuation of ceramic alumina and silicon carbides have been measured and are discussed. Chapter 2 and Chapter 3 introduce the theoretical background, while Chapter 4 and Chapter 5 describe the experimental techniques. In Chapter 6 a general description of single crystal and ceramic aluminas is given. In Chapter 7 the effects of microstructure on the elastic anisotropy of the ceramic aluminas are analysed using a combination of the ultrasonic, X-ray diffraction and scanning electron microscopy. In Chapter 8 the ultrasonic wave velocities, elastic moduli, Poisson's ratio, pressure derivatives of natural velocities, pressure derivatives of the elastic moduli and the long wavelength acoustic mode Grüneisen parameters of the ceramic aluminas are determined. In Chapter 9 a detailed analysis of impedance spectra of ceramic aluminas is given; results are related to aspects of the microstructure and the relaxation processes. In Chapter 10 a general description of silicon carbide is given. Chapter 11 is a discussion of the quasi-static stress damage effect on the elastic properties and the ultrasonic wave attenuation of ceramic alumina and silicon carbides. Finally a summary of the wide range of findings is presented in chapter 12.

Chapter 2 Fundamental Theory of Elasticity and Lattice Vibrational Anharmonicity

2.1 Introduction

In a solid the constituent atoms are held together by a balancing of attractive and repulsive forces, which result in an atomic equilibrium separation distance such that the sum of the forces is zero, corresponding to the minimum potential energy. When external forces are applied to a solid body, the general motion of the body involves linear translation, rotation, and deformation. In elasticity only deformation is considered. The propagation of ultrasonic waves in a medium, which we shall regard as continuous, is accompanied by a periodic displacement of particles of the medium from their equilibrium positions under the action of periodic elastic force. Here, "particle" refers to an infinitesimal volume element, which itself may contain a very large number of molecules, so that the medium within it can be considered to be continuous.

2. 2 The strain tensor

Consider a point P within the body whose position coordinates are x_i (i=1, 2, 3) with respect to a set of Cartesian axes. Because of the deformation of the body, the P point is displaced to a new point P′ with coordinates x'_i. The component u_i of a displacement vector **u** is defined by

$$u_i = x'_i - x_i \qquad i = 1, 2, 3 \qquad (2.1)$$

Consider a second point Q adjacent to P with coordinates x_i+dx_i. If the body is deformed, then the line element PQ becomes P′Q′. While P moves to P′, Q moves to Q′ where the coordinates of Q′ are $x_i'+dx_i'$. A general expression for the components of strain tensor can be derived by the change in the square of distance dL between two nearby points, P and

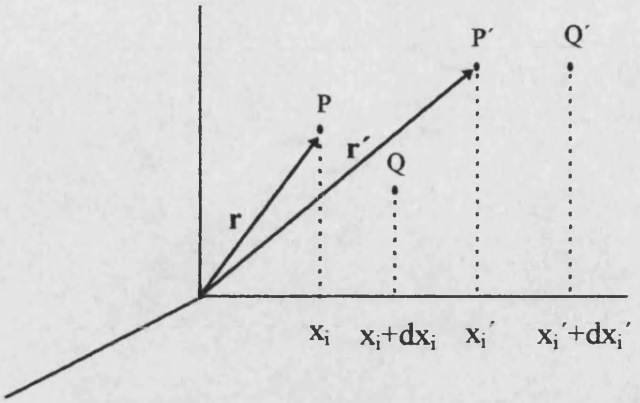

Fig 2.1 An element PQ of an elastic body becomes the element P′Q′ after deformation (Pollard, 1977).

Q, as a result of its deformation without making any approximations. The square of the distance between P and Q equals $(dL)^2 = dx_i dx_i$ before deformation and $(dL')^2 = dx'_i dx'_i = (dx_i+du_i)(dx_i+du_i)$ after deformation. The change in square of distance between two nearby points can be written in the form

$$(dL')^2 - (dL)^2 = (dx_i+du_i)(dx_i+du_i) - dx_i dx_i.$$

Since $du_i = \left(\frac{\partial u_i}{\partial x_j}\right) dx_j$ and $du_i = \left(\frac{\partial u_i}{\partial x_k}\right) dx_k$, we have

$$(dL')^2 - (dL)^2 = 2\, du_i\, dx_i + du_i\, du_i$$

$$= 2\frac{\partial u_i}{\partial x_k} dx_i dx_k + \frac{\partial u_i}{\partial x_k}\frac{\partial u_i}{\partial x_j} dx_k dx_j$$

$$= 2\eta_{ik} dx_i dx_k$$

where

$$\eta_{ik} = \frac{1}{2}\left(\frac{\partial u_i}{\partial x_k} + \frac{\partial u_k}{\partial x_i} + \frac{\partial u_j}{\partial x_i}\frac{\partial u_j}{\partial x_k}\right) \qquad i, j, k = 1, 2, 3 \qquad (2.2)$$

Equation (2.2) represents the exact expression for the components of a second rank strain tensor, which comprise the material or Lagrangian strain tensor and can be written in the form

$$\eta_{ik} = \begin{bmatrix} \eta_{11} & \eta_{12} & \eta_{13} \\ \eta_{21} & \eta_{22} & \eta_{23} \\ \eta_{31} & \eta_{32} & \eta_{33} \end{bmatrix} \tag{2.3}$$

For sufficiently small deformations, when the last term of Equation (2.2) can be neglected as a second order infinitesimal, Equation (2.2) transforms into the following linearized expression

$$\varepsilon_{ik} = \frac{1}{2}\left(\frac{\partial u_i}{\partial x_k} + \frac{\partial u_k}{\partial x_i}\right) \qquad i, k = 1, 2, 3 \tag{2.4}$$

From Equations (2.2) and (2.4), it can be seen that

$$\varepsilon_{ik} = \varepsilon_{ki} \tag{2.5}$$

Hence the strain tensor (2.3) is a symmetric tensor; thus only six components of strain tensor (2.3) are independent.

2.3 The stress tensor

In general, there are two types of mechanical force which may act on a body: (1) body force for which the force is proportional to the volume of the body, (2) surface force for which the force is proportional to the area of the surface. Stress is defined as the force divided by the area on which the force acts.

To describe completely the stress in the vicinity of a given point, nine quantities σ_{jk} are used. The σ_{jk} is the Cartesian component of the stress and equals the j-component of the force per unit area acting across a surface with a normal in the k-direction (Fig. 2.2). These nine quantities form a second rank tensor, called the stress tensor, which can be written in the form

$$\sigma_{ik} = \begin{bmatrix} \sigma_{11} & \sigma_{12} & \sigma_{13} \\ \sigma_{21} & \sigma_{22} & \sigma_{23} \\ \sigma_{31} & \sigma_{32} & \sigma_{33} \end{bmatrix} \tag{2.3}$$

Under the condition that all the parts of the body are in static equilibrium, the stress tensor σ_{jk} is a symmetric tensor expressed by the equation (Nye 1985)

$$\sigma_{jk} = \sigma_{kj} \tag{2.4}$$

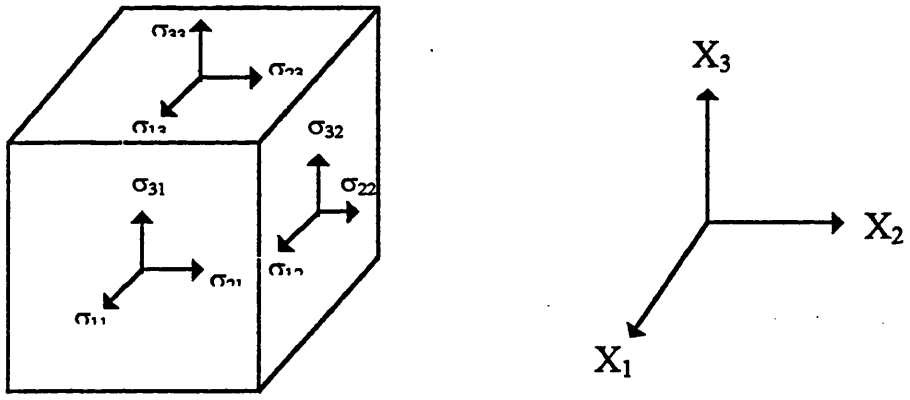

Fig 2.2 The stress components acting on each face of an elementary parallelepiped when a uniform force acts on the body.

2.4 The linear or harmonic theory of elasticity

For small displacements from the equilibrium position, the potential energy of the atoms can be considered to be a symmetrical function of displacement, so that to a first approximation the expression for the interatomic potential energy can be truncated at the quadratic term. This approximation gives rise to the linear or harmonic theory of elasticity, which is the basis of Hooke's law. Knowledge of the values of the second order elastic stiffness constants enables calculation of the bulk modulus,

Young's modulus and Poisson's ratio, which describe the elastic behaviour of a material in this linear region.

2.4.1 The generalised Hooke's law

Hooke's law may be generalised to state that, for a perfectly elastic body each component of stress at a given point of the body is linearly related to each component of strain, i.e. ,

$$\sigma_{ik} = c_{iklj}\,\varepsilon_{lj} \qquad (i, k, l, j = 1, 2, 3) \qquad (2.5)$$

In a real solid, Hooke's law is valid only for an infinitesimally small stress. The tensor c_{iklj} is fourth rank and is called the second order elastic tensor or stiffness tensor; it has 81 components in the most general case. Since σ_{ik} and ε_{lj} are symmetrical, there are only six independent components of stress and six independent components of strain. These reduce the number of independent components of c_{iklj} to 36. This makes it possible to abbreviate the double subscript notation to a single subscript running from 1 to 6 using Voigt's notation:

$11 \rightarrow 1$; $22 \rightarrow 2$; $33 \rightarrow 3$; 23 and $32 \rightarrow 4$; 13 and $31 \rightarrow 5$; 12 and $21 \rightarrow 6$.

By using Voigt's notation, the tensor form of the second order elastic constant can be transformed into the matrix form. The generalised Hooke's Law can therefore be written as:

$$\sigma_n = C_{nm}\varepsilon_m \qquad (n,m = 1, 2, 3, 4, 5, 6) \qquad (2.6)$$

where $C_{nm} = c_{iklj}$, $\sigma_{ik} = \sigma_n$, $\varepsilon_m = \varepsilon_{lj}$ ($l = j$, $m = 1, 2, 3$) and $\varepsilon_m = 2\varepsilon_{lj}$ ($i \neq j$, $m = 4, 5, 6$) (Nye 1985). These 36 quantities C_{nm} form a matrix which can been written in the form

$$C_{nm} = \begin{bmatrix} C_{11} & C_{12} & C_{13} & C_{14} & C_{15} & C_{16} \\ C_{21} & C_{22} & C_{23} & C_{24} & C_{25} & C_{26} \\ C_{31} & C_{32} & C_{33} & C_{34} & C_{35} & C_{36} \\ C_{41} & C_{42} & C_{43} & C_{44} & C_{45} & C_{46} \\ C_{51} & C_{52} & C_{53} & C_{54} & C_{55} & C_{56} \\ C_{61} & C_{62} & C_{63} & C_{64} & C_{65} & C_{66} \end{bmatrix} \tag{2.7}$$

The law of conservation of energy gives an additional restriction on the possible values for the components of C_{nm}. From this restriction, it can be shown that C_{nm} matrix is symmetric, i.e., $C_{nm} = C_{mn}$ (Nye 1985), so that the number of independent components of C_{nm} is further reduced from 36 to 21. The presence of symmetry in the crystal reduces still further the number of independent C_{nm}. A detailed derivation of the number of independent elastic constants for the different crystal systems is given by Nye (1985).

For an isotropic body the physical properties do not depend on the orientation of the body. In an isotropic medium there are only two independent second order elastic constants. The second order elastic matrix for an isotropic body can be written in the form (Nye 1985)

$$C_{nm} = \begin{bmatrix} C_{11} & C_{12} & C_{12} & 0 & 0 & 0 \\ C_{12} & C_{11} & C_{12} & 0 & 0 & 0 \\ C_{12} & C_{12} & C_{11} & 0 & 0 & 0 \\ 0 & 0 & 0 & C_{44} & 0 & 0 \\ 0 & 0 & 0 & 0 & C_{44} & 0 \\ 0 & 0 & 0 & 0 & 0 & C_{44} \end{bmatrix} \tag{2.8}$$

where $C_{44} = \frac{1}{2}(C_{11} - C_{12})$.

2.4.2 Relationships between ultrasonic wave velocities and the elastic properties of an isotropic solid

The velocities of longitudinal and shear ultrasonic waves propagated through a medium can be used to calculate the adiabatic second order elastic moduli. Assuming that the adiabatic conditions are satisfied, from Newton's Second Law and the Generalised Hooke's Law, relationships between ultrasonic wave velocities and the elastic constants of an isotropic solid can be derived as follows:

$$C_{11}^S = \rho V_L^2 \tag{2.9}$$

$$C_{44}^S = C_{44}^S = \rho V_S^2 \tag{2.10}$$

where ρ is the density of the unstrained medium, V_L and V_S are the longitudinal and shear wave velocities respectively, the subscript S denotes adiabatic conditions and subscript T denotes isothermal conditions. Using these moduli the adiabatic bulk modulus B^S, Young's modulus E^S and Poisson's ration σ^S, can be calculated:

$$B^S = (1/3)(3C_{11}^S - 4C_{44}) \tag{2.11}$$

$$E^S = C_{44}(3C_{11}^S - 4C_{44})/(C_{11}^S - C_{44}) \tag{2.12}$$

$$\sigma^S = (C_{11}^S - 2C_{44})/2(C_{11}^S - C_{44}) \tag{2.13}$$

2.5 Non-linear elasticity and lattice vibrational anharmonicity

2.5.1 The general aspects of lattice vibrational anharmonicity and limitation of harmonic approximation

On the base of the adiabatic approximation, whose central feature is that the ions move much more slowly than the electrons which "see" the ions as being fixed in their instantaneous positions (Born and Oppenheimer, 1927), the lattice potential energy Φ can be written as a function of the

displacement of all atoms. If the displacements of the ions from their equilibrium positions are small, the potential Φ can be expanded about its equilibrium value using the three-dimensional form of Taylor's theorem:

$$\begin{aligned}\Phi = \Phi_0 &+ \sum_{lk\alpha} \Phi_\alpha \begin{pmatrix} l \\ k \end{pmatrix} U_\alpha \begin{pmatrix} l \\ k \end{pmatrix} \\ &+ \frac{1}{2!} \sum_{lk\alpha} \sum_{l'k'\beta'} \Phi_{\alpha\beta} \begin{pmatrix} l & l' \\ k & k' \end{pmatrix} U_\alpha \begin{pmatrix} l \\ k \end{pmatrix} U_\beta \begin{pmatrix} l' \\ k' \end{pmatrix} \\ &+ \frac{1}{3!} \sum_{lk\alpha} \sum_{l'k'\beta} \sum_{l''k''\gamma} \Phi_{\alpha\beta\gamma} \begin{pmatrix} l & l' & l'' \\ k & k' & k'' \end{pmatrix} U_\alpha \begin{pmatrix} l \\ k \end{pmatrix} U_\beta \begin{pmatrix} l' \\ k' \end{pmatrix} U_\gamma \begin{pmatrix} l'' \\ k'' \end{pmatrix} \\ &+ \cdots \end{aligned} \tag{2.14}$$

where $U_\alpha \begin{pmatrix} l \\ k \end{pmatrix}$ is the displacement of the kth atom in the l^{th} unit cell in the direction α (α= x, y, z), and so on $U_\beta \begin{pmatrix} l \\ k \end{pmatrix}$ and $U_\gamma \begin{pmatrix} l \\ k \end{pmatrix}$. The coefficients Φ_α and $\Phi_{\alpha\beta}$ are defined as

$$\Phi_\alpha \begin{pmatrix} l \\ k \end{pmatrix} = \left. \frac{\partial \Phi}{\partial U_\alpha \begin{pmatrix} l \\ k \end{pmatrix}} \right|_0 \tag{2.15}$$

$$\Phi_{\alpha\beta} \begin{pmatrix} l & l' \\ k & k' \end{pmatrix} = \left. \frac{\partial^2 \Phi}{\partial U_\alpha \begin{pmatrix} l \\ k \end{pmatrix} \partial U_\beta \begin{pmatrix} l' \\ k' \end{pmatrix}} \right|_0 \tag{2.16}$$

and so forth. The subscript zero in Eqs. (2.15-16) means that the derivatives are evaluated at equilibrium values.

In the harmonic approximation, all cubic and higher-order terms in Eq. (2.14) are neglected. This equation reduces to

$$\begin{aligned}\Phi = \Phi_0 &+ \sum_{lk\alpha} \Phi_\alpha \begin{pmatrix} l \\ k \end{pmatrix} U_\alpha \begin{pmatrix} l \\ k \end{pmatrix} \\ &+ \frac{1}{2!} \sum_{lk\alpha} \sum_{l'k'\beta'} \Phi_{\alpha\beta} \begin{pmatrix} l & l' \\ k & k' \end{pmatrix} U_\alpha \begin{pmatrix} l \\ k \end{pmatrix} U_\beta \begin{pmatrix} l' \\ k' \end{pmatrix} \end{aligned} \tag{2.17}$$

As discussed by Brüesch (1982), from Eq. (2. 17) it can be shown that in the harmonic approximation the force on an atom is strictly proportional to its displacement relative to its neighbours, which is nothing other than Hooke's law.

In the harmonic approximation, the stress and strain are uniquely related through constant coefficients. As a result of this assumption the propagating wave is harmonic. A characteristic property of such waves is that they may be expressed as linear combinations of separate "monochromatic" waves. Each monochromatic wave may be propagated independently, and such waves do not interact with one another.

The harmonic approximation gives a simple picture of lattice vibrations. It is the starting point for all theories of lattice dynamics and can often provide reasonable results. Further corrections to Φ, especially cubic and quartic terms, are called anharmonic terms. They are often treated as a perturbation. These corrections are introduced not just for more accuracy. The anharmonic terms are responsible for many phenomena which cannot be explained by using harmonic approximation. Brüesch (1982) has listed some of the most important consequences of the harmonic approximation. The one related directly to our work is that the elastic constants would be independent of temperature and pressure. In real crystals none of the consequence of the harmonic approximation is satisfied. The elastic constants are temperature and pressure dependent. The lattice vibrations of real crystals are anharmonic.

2. 5. 2 The hydrostatic pressure derivatives of the second order elastic moduli

The change of the second order elastic moduli with the external pressure is an important anharmonic effect; this allows information to be found about the influence of interatomic binding of the solid. In general the normal behaviour of the second order elastic moduli is to increase linearly with increasing pressure, which leads to a positive value of the pressure derivative of an elastic modulus.

Assuming the isotropic propagation of small-amplitude waves in a continuous medium, Thurston (1965) derived a general formula for calculation of the pressure derivative of elastic constants (ie ρv^2) at zero pressure from natural velocity (Thurston and Brugger, 1964) and the pressure derivative of natural velocity. For an isotropic material under hydrostatic pressure, the formulae can be simplified as follows:

$$(\frac{\partial C_{11}}{\partial P})_{T,P=0} = C_{11}^0[\frac{2(\partial W_L / \partial P)}{W_L} + \frac{1}{3B^T}]_{T,P=0} \qquad (2.18)$$

$$(\frac{\partial C_{44}}{\partial P})_{T,P=0} = C_{44}^0[\frac{2(\partial W_S / \partial P)}{W_S} + \frac{1}{3B^T}]_{T,P=0} \qquad (2.19)$$

Here W_S and W_L are the shear and longitudinal mode natural velocities, which are defined as $W=2l_0/t$. Here l_0 is the unstressed length of the sample and t is the experimentally measured transit time of the ultrasonic waves across the sample. C_{11}^0 and C_{44}^0 are the second order elastic moduli under ambient conditions. B^T is the isothermal bulk modulus, which is related to the adiabatic bulk modulus B^S by

$$B^T = B^S(1 + T\beta\gamma_G)^{-1} \qquad (2.20)$$

Here β is the coefficient of volume thermal expansion and γ_G is the thermal Grüneisen parameter (see the next section). T is temperature in Kelvin. For the ceramics studied in this work, β and γ_G are not yet available. However, for most solids, the differences between the isothermal and adiabatic moduli are very small, especially for the solids with small expansion coefficient. For example, the values of B^s and B^T reported by Chung and Simmons (1968) for a high-purity, high-density, hot-pressed alumina sample at 298 K are 25.192 and 25.033. Hence $B^T \approx B^s$ is a good approximation.

The pressure derivative of the adiabatic bulk modulus B^S can be obtained using

$$\left(\frac{\partial B^S}{\partial P}\right)_{T,P=0} = \left(\frac{\partial C_{11}}{\partial P}\right)_{T,P=0} - \frac{4}{3}\left(\frac{\partial C_{44}}{\partial P}\right)_{T,P=0} \qquad (2.21)$$

2.5.3 Quasiharmonic approximation and Grüneisen parameter

In the quantum mechanical theory normal modes of lattice vibration in solids are particle-like and quantized as phonons. The energy of the lattice vibration can be changed only by integral units of the energy of a phonon which is given by the product of Planck's constant $\hbar$ and the angular frequency ω of the phonon. The mean energy of the vibration mode is given as

$$E(\vec{k},s) = \hbar\omega(\vec{k},s)\left[\frac{1}{2} + n(\vec{k},s)\right] \qquad (2.22)$$

where $n(\vec{k},s)$ is the number of phonons in the s branch with wave vector $\vec{k}$, and is called the phonon number or the occupation number.

In the quasiharmonic approximation (Leibfried and Ludwig, 1961), the effects of the higher order terms in Eq.(2.14) neglected by the harmonic approximation are, to a first approximation, taken into account by evaluating the second derivatives $\Phi_{\alpha\beta}$ in Eq.(2.16) at the mean positions which the atoms actually occupy at temperature T. The force constants, and thereby the phonon frequencies, are dependent only on temperature through the lattice dimensions, i.e. they are volume dependent.

A parameter, the mode Grüneisen parameter, is introduced in the quasiharmonic approximation to account for the contribution of each phonon mode to the thermal expansion of the solid:

$$\gamma_i = -\frac{d(\ln \nu_i)}{d(\ln V)} \tag{2.23}$$

where ν_i is the phonon frequency of the mode. For the normal behaviour of phonons, γ_i have positive values. The negative sign in equation 2.23 indicates that in the normal circumstances the phonon frequencies decrease as the lattice expands. The thermal Grüneisen parameter γ^{th} is expressed as the weighted average of the mode Grüneisen parameters (Slater 1939):

$$\gamma^{th} = \frac{\sum_i \gamma_i c_i}{\sum_i c_i} \tag{2.24}$$

where c_i is the Einstein specific heat of i^{th} mode, a temperature dependent weighting factor to reflect the contribution of the ith mode to the heat capacity C_V. The thermal Grüneisen parameter can be related to the measurable quantities as (Slater 1939):

$$\gamma^{th} = \frac{\alpha V B^T}{C_V} = \frac{\alpha V B^S}{C_P} \tag{2.25}$$

where α is the volume thermal expansion coefficient, B^T and B^S are the isothermal and adiabatic bulk moduli, and C_V and C_P are the heat capacity at constant volume and under constant pressure respectively. α used here should not be confused with the same symbols used for attenuation in section 2.7 of this chapter and for polarisability in Chapter 3.

The generalised Grüneisen parameters (Brugger 1965) are defined as

$$\gamma_{jk} = -\left\{ \frac{1}{\omega(s,\vec{k})} \left[\frac{\partial \omega(s,\vec{k})}{\partial \eta_{jk}} \right]_T \right\}_{\eta=0} \tag{2.26}$$

where ω is the angular frequency of the phonons.

Since in the quasiharmonic approximation phonon frequencies change with temperature through the lattice dimension, they are strain-dependent. This allows us to calculate the generalised Grüneisen parameter from the ultrasonically measured elastic constants. For an isotropic solid there are two contributions from the long wavelength acoustic mode to the Grüneisen parameter. They are γ_L for the longitudinal mode and γ_S for the shear mode, which can be obtained from the acoustic measurements (Brugger and Fritz 1967):

$$\gamma_L = -\frac{1}{6}\left[1 - \frac{3B^T}{C_{11}}\left(\frac{\partial C_{11}}{\partial P}\right)_{P=0}\right] \tag{2.27}$$

and

$$\gamma_S = -\frac{1}{6}\left[1 - \frac{3B^T}{C_{44}}\left(\frac{\partial C_{44}}{\partial P}\right)_{P=0}\right] . \tag{2.28}$$

At temperatures close to the Debye temperature the mean acoustic-mode Grüneisen parameter γ^{el}, which accounts for the contribution of the overall long wavelength acoustic modes to thermal expansion, can be obtained as (Brugger and Fritz 1967):

$$\gamma^{el} = \frac{1}{3}(\gamma_L + 2\gamma_S) \tag{2.29}$$

2. 5. 4 Estimation of compression of a solid at high pressure

Knowledge of the volume compression $V(P)/V_0$, the ratio of the volume V(P) at pressure P to that V_0 at atmospheric pressure, is useful in theoretical studies of the physical properties of materials under pressure. The dependence of ultrasonic wave velocity upon pressure can be measured with high precision; however, the pressure range is limited. The compression at pressures up to one, or even two orders of magnitude, higher than those available in ultrasonic experiments can be estimated from the elastic moduli and their hydrostatic pressure derivatives by using an equation-of-state such as that proposed by Murnaghan (1944). This extrapolation works well up to a very high pressure for many solids (Anderson 1966).

The physical basis for the equation-of-state rests upon the assumption that the isothermal bulk modulus B^T is linearly dependent upon pressure

$$B^T(P) = -V(\frac{\partial P}{\partial V})_T = B_0^T + P(\frac{\partial B^T}{\partial P})_{P=0,T} \tag{2.30}$$

By integrating Eq. (2.30), Murnaghan (1944) obtained the equation-of-state

$$P = \frac{B_0^T}{B_0^{T'}}\{[\frac{V_0}{V(P)}]^{B_0^{T'}} - 1\} \tag{2.31}$$

where $B_0^{T'} = (\partial B^T / \partial P)_{P=0,T}$. The equation is normally used in the logarithmic form

$$\ln[\frac{V_0}{V(P)}] = \frac{1}{B_0^{T'}}\ln[B_0^{T'}(\frac{P}{B_0^T}) + 1] \tag{2.32}$$

The pressure dependence of ultrasonic wave velocities can be used to determine the isothermal pressure derivative $B_0^{S'}$ $(= (\partial B^S / \partial P)_{P=0,T})$ of the adiabatic bulk modulus. The equation-of-state (Eq. (2.32) involves the

isothermal pressure derivative $B_0^T{}'$ of the isothermal bulk modulus. In order to transfer $B_0^S{}'$ into $B_0^T{}'$, it is necessary to obtain not only the volume thermal expansion β and the Grüneisen parameter γ_G but also their temperature derivatives, which are not available for the materials under study here. However, as for B^T, the difference between $B_0^S{}'$ and $B_0^T{}'$ is small for most solids. For hot-pressed polycrystalline alumina the difference between $B_0^S{}'$ and $B_0^T{}'$ is only 0.95% (Chung and Simmons 1968). Therefore, B^S and $B_0^S{}'$ can be used in place of B^T and $B_0^T{}'$ in the equation-of-state (Eq. (2.32)) in our works without causing significant deviations.

2. 6 Ultrasonic birefringence effect and its application for material characterisation

2. 6. 1 The phenomenon of ultrasonic birefringence

If the manufacturing process of a material includes rolling, uniaxial pressing or drawing, etc., such processes will induce anisotropy into the structure of a material in some degree. This anisotropy can result from residual stress, texture, preferred orientation of grains, etc.. In the most general case, a three-dimensional anisotropy can be induced into the solid. This anisotropy can be described using three mutually orthogonal principal axes as a reference frame. When a pulse of an ultrasonic shear wave is propagated along one of the axes with polarisation direction along another axis, the polarisation direction of the wave remains unchanged. After the reflection at the opposite surface of the solid, a backwall echo can be detected. Multiple back-and-forth reflections yield a backwall sequence as shown in Fig. 2.3(a). The amplitude decreases with time or transit length due to attenuation. Turning the polarisation direction of the incident shear ultrasonic waves with respect to the principal direction yields elliptical vibrations in the solid. This is caused by the velocity difference of the two

wave components polarised parallel to each of the two principal axes respectively. This phenomenon is called acoustic birefringence by analogy with optical birefringence. A special situation arises if the angle between principal axes and polarisation direction is 45°; the two wave components have not only the same frequency but also the same amplitude. The difference in the velocities of the two components propagating in the solid causes a phase shift between the components which increases with the path length. If this phase shift reaches ½λ , λ is the wave length, the vibration in the solid is linearly polarised. The plane of vibration is perpendicular to the vibration direction of the incident wave. In this case, destructive interference occurs, producing an echo train of the type shown in the Fig. 2.3 (b).

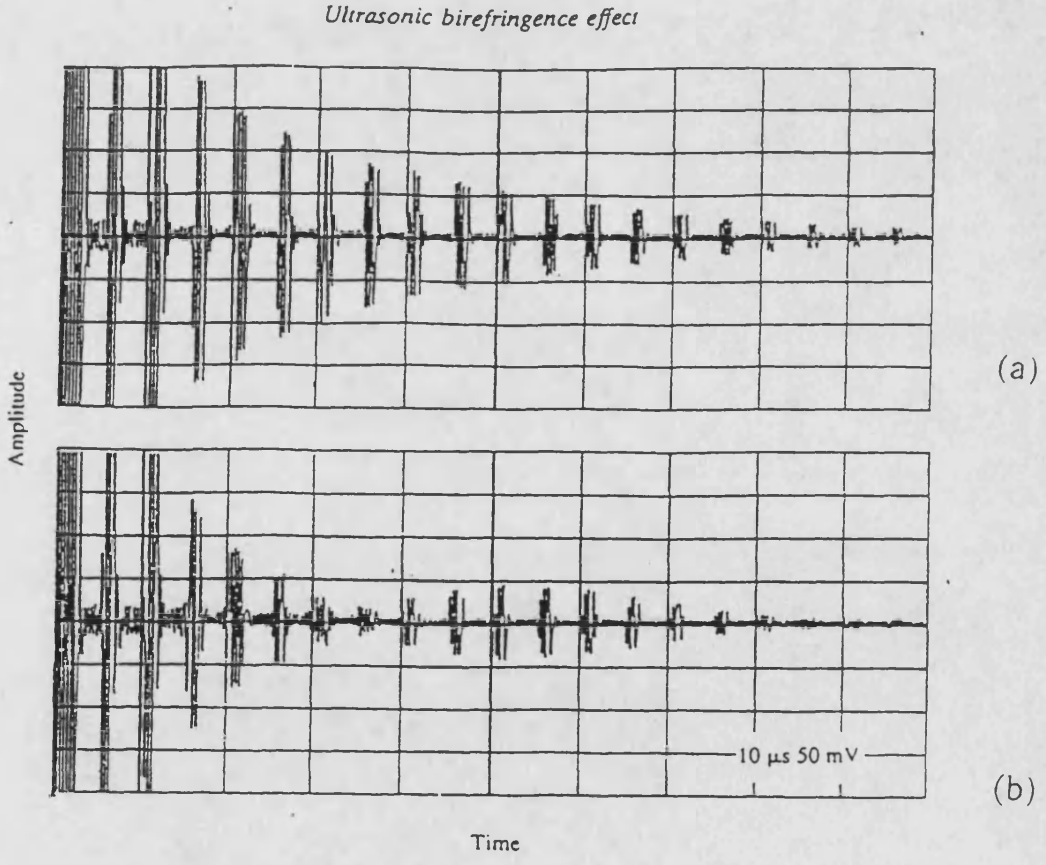

Fig. 2.3 The backwall echo sequence of shear ultrasonic waves: (a) polarised in the direction parallel to a principal axis, (b) polarised in the direction 45° to principal axes (Schneider, 1995).

2. 6. 2 Determination of the principal axes and the difference between the principal velocities.

By turning the transducer, the polarisation direction of which is known, a special polarisation direction can be found for which the destructive interference occurs. The principal axes are then at ±45° to that polarisation direction. By adjusting the vibration direction of the incident wave parallel to the principal axes just determined, extreme values of ultrasonic wave velocity and exponential echo-train are obtained, which confirm the determination of principal axes.

It is evident, that the difference between the two principal shear wave velocities (v_{S2} - v_{S1}) can be evaluated from the number of backwall echoes between the destructive interferences in the echo-train. For practical applications, the vibration of the incident wave can be adjusted to be parallel to each of the principal axes, respectively. This yields the individual values of the principal velocities.

2. 7 Attenuation of ultrasonic waves

The interactions of ultrasonic waves and pulses with microstructure are twofold: elastic and anelastic. The elastic interaction holds the character of mechanical vibrations and is given by the wave velocity v, by reflection, diffraction and scattering. The anelastic interaction arises from those interactions, by which energy is withdrawn from the ultrasonic pulse during propagation and transformed, via different mechanisms, transfers into heat or different ultrasound. The attenuation coefficient α of a wave is the sum of absorption (α_A) and scattering (α_S) contributions.

For a sequence of backwall echoes from a homogeneous, parallel-side material, the amplitude A(x) is an exponential function of the sound path length x:

$$A(x) = A_0(\exp(-\alpha x)) \qquad (2.33)$$

A_0 is the sound amplitude excited in the surface region (x=0). α used here should not be confused with the same symbol used for the volume thermal expansion coefficient in the section 2.5.3 of this chapter and for polarisability in section 3.2 in Chapter 3.

Chapter 3 Fundamental Theory of AC Impedance Spectroscopy

3.1 Introduction

Dielectric measurements provide a sensitive tool for the characterisation of defects and mobility mechanisms in materials. The a.c. impedance can be measured as a function of frequency at different temperatures or pressures. For ceramics such measurements can characterise the effects of impurity and specimen microstructure on dielectric properties. The technique is known as Complex Plane Analysis (C.P.A.). It is also termed Impedance Spectroscopy. The experimental data of the electrical impedance or admittance which are measured over a range of frequencies can be plotted in the complex plane. From the shape of the plot obtained, an equivalent circuit can be established to model the response of the material to the electric signal. A direct connection can be made between the behaviour of the real system and that of a simple idealised model circuit consisting of discrete electrical components.

3.2 Dielectric polarisation in static electric fields

The molecules comprising dielectrics can be broadly classified as polar or non-polar. A polar molecule has a permanent electric dipole moment which is dominated by the strong intermolecular interactions and is not seriously affected by external electric fields. In the absence of an electric field, the permanent dipole moments of polar molecules are distributed randomly in all directions and change direction constantly because of the thermal motion of the molecules. The vector summation of dipole moments of all molecules is zero. When an external electric field is applied, there is a tendency for the permanent dipoles to align themselves parallel to it, although exact alignment is not possible due to the thermal agitation. This alignment leads

to a non-zero vector summation of the dipole moments of all molecules which is called orientational polarisation.

A non-polar molecule has no significant charge separation which occurs as a result of intermolecular interactions. In an external electric field the non-polar molecules can be polarised. The induced dipole moment of a non-polar molecule is proportional to the external electric field according to the relation

$$\mu = \alpha E \tag{3.1}$$

where α is the polarisability of the molecule. α used here should not be confused with the same symbol used for attenuation and the volume thermal expansion coefficient in Chapter 2. The induced dipole moment of a non-polar molecule arises from two effects: (i) the electric field causes a displacement of the electrons relative to the nucleus in each atom (electron polarisation) and (ii) a displacement of the positive and negative ions relative one another in the molecule (atomic polarisation).

Interfacial or space charge polarisation usually arises from a localised accumulation of charges which are trapped by lattice defects, impurity centres, voids, strains, grain boundaries or electrode surfaces.

In considering a dielectric material from the macroscopic point of view, polarisation is defined as dipole moment per unit volume, which is the vector summation of the individual dipole moments per unit volume. In a static electric field, for linear dielectric response of an isotropic material, the general relation between the polarisation **P** and the field **E** can be written as

$$\mathbf{P} = \varepsilon_0 \chi \mathbf{E} \tag{3.2}$$

where ε_0 is the permittivity of free space and χ is the susceptibility. To a first approximation χ is the summation of contributions of all polarisation mechanisms.

The temperature-dependence of permanent dipole contributions to the susceptibility χ is different from that due to induced dipoles. For induced dipoles the polarisation is relatively independent of temperature since the forces opposing the displacements are not strongly temperature dependent. In polar materials the orientational polarisation falls off rapidly with rising temperature, because the increasing thermal motion at higher temperature opposes the alignment of the dipoles by the external electric field. For non-interacting freely floating dipoles (Debye 1945) in the case of a weak static field in the limit of weak orientation we have (Jonscher 1983)

$$\chi = \frac{N_d \mu^2}{3\varepsilon_0 kT} + N_m \alpha \tag{3.3}$$

where T is temperature, μ is the dipole moment of each dipole, k is Boltzmann's constant, N_d and N_m are, respectively, the number densities of permanent dipoles and of polarizable molecules. The first term arises from the contributions of permanent dipoles and the second item from the contributions of induced dipoles.

The polarisation vector **P** always appears together with the electric field **E**. It is convenient to introduce a vector **D** called electric flux density or the electric displacement density such that

$$\begin{aligned} \mathbf{D} &= \varepsilon_0 \mathbf{E} + \mathbf{P} \\ &= \varepsilon_0 (1+\chi)\mathbf{E} \\ &= \varepsilon_0 \varepsilon_r \mathbf{E} \\ &= \varepsilon \mathbf{E} \end{aligned} \tag{3.4}$$

where

$$\varepsilon_r = (1+\chi) \tag{3.5}$$

is known as the relative permittivity or the dielectric constant

while

$$\varepsilon = \varepsilon_0 \varepsilon_r \tag{3.6}$$

is known as the permittivity.

3.3 The dielectric response in alternating fields

The static response of a dielectric system to a static electric field represents one facet of the complete problem. An important feature of dielectric properties of materials is the dielectric response to alternating electric fields. Most engineering applications of dielectrics involve response to an alternating electric field; modern measuring techniques enable us to make measurements using frequency as a parameter with very high accuracy.

3.3.1 The dielectric response in the time domain

For the time dependence of the dielectric response, the time dependent polarisation P(t) is not the same function as the time-dependent driving field E(t) because of the "inertia" of all physical processes. When an electric field E is applied to a dielectric, the polarisation will take time to reach its equilibrium value. The response time constant of polarisation is mechanism dependent. The electron polarisation, which is due to the displacement of the electrons with respect to the nuclei, has an almost instantaneous response to the electric field. The time constant of electron polarisation is about 10^{-16}s (Macdonald 1987). The time constant of atomic polarisation is about 10^{-14} to 10^{-12}s (Smyth 1955) due to relatively heavy positive and negative ions. The time constant of permanent dipole polarisation is about 10^{-11} to 10^{-6} s (Smyth 1955) and depends on the frictional resistance of the dielectric to the change of dipole orientation. The interfacial or space

charge polarisation has a time constant which is usually longer than 1s (Harrop 1972).

If an electric field step is applied to the dielectric at a time t = 0, and then the field is held constant, the resulting polarisation **P** may be divided into two parts. Electrons follow the field almost instantaneously; the electron polarisation will be established very quickly. Atomic polarisation also changes almost instantaneously (compared with the permanent dipole polarisation). Thus if the time interval involved in the experiment are of the order of the time constant for permanent dipole polarisation, the electron polarisation and the atomic polarisation can be treated as instantaneous polarisation, which we represent by $\mathbf{P}_\infty$, and can be expressed as

$$\mathbf{P}_\infty = \mathbf{P}_e + \mathbf{P}_a = \varepsilon_0(\varepsilon_{r,\infty} - 1)\mathbf{E} \qquad (3.7)$$

where $\varepsilon_{r,\infty}$ is the contribution of electron polarisation and the atomic polarisation to the relative permittivity and also, as described in the next section, is the relative permittivity at frequencies that are too high for the permanent dipoles to follow. By contrast the permanent dipole part of the polarisation takes time to reach its equilibrium value. For an infinitely long time, the resulting total polarisation is represented by $\mathbf{P}_S$, which defines the static relative permittivity ε_S:

$$\mathbf{P}_S = \varepsilon_0(\varepsilon_S - 1)\mathbf{E} \qquad (3.8)$$

If we assume that the time-dependent polarisation, $\mathbf{P}'(t)$, due to the orientation of the permanent dipole increases at a rate proportional to its departure from its equilibrium value, we have:

$$\mathbf{P}'(t) = \mathbf{P}(t) - \mathbf{P}_\infty$$

$$\tau \frac{d\mathbf{P}'(t)}{dt} = \mathbf{P}_s - \mathbf{P}_\infty - \mathbf{P}'(t) \qquad (3.9)$$

τ is called the relaxation time of the dielectric medium. Solution of equation (3. 9) gives

$$\mathbf{P}(t) = \mathbf{P}_\infty + \mathbf{P}'(t)$$

$$= \mathbf{P}_\infty + (\mathbf{P}_S - \mathbf{P}_\infty)(1 - e^{-\frac{t}{\tau}}) \qquad (3.10)$$

Fig 3.1. describes the behaviour of **P**(t) after a step electric field is applied abruptly to the dielectric at t = 0. The vertical section of the curve represents the instantaneous electron and atomic polarisation.

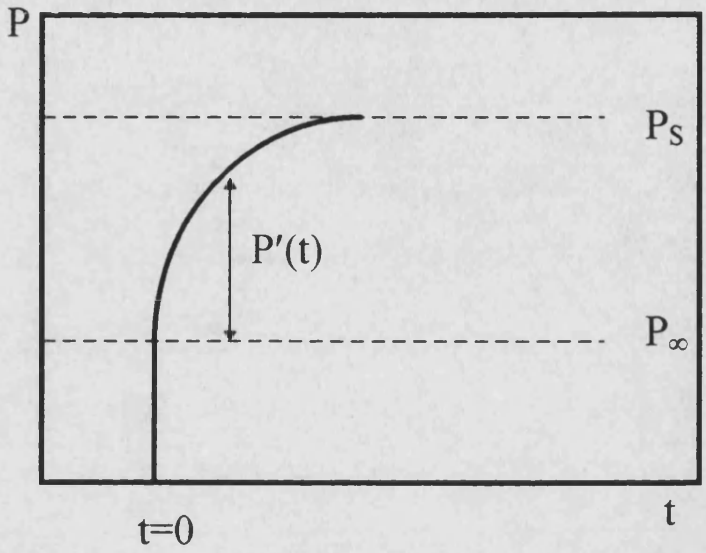

Fig. 3.1 Time dependence of the polarisation P after the application of an electric field step to a dielectric at t=0 (Macdonald 1987).

3.3.2 The dielectric response in the frequency domain

When a dielectric material is subjected to a sinusoidal electric field, as long as the frequency remains low enough, each kind of polarisation follows the alternations of the field and thus contributes fully to the total polarisation of the dielectric. The interfacial polarisation cannot usually follow the field variation at a frequency higher than about 1 Hz (Harrop 1972) and for the frequency higher than that the contribution of interfacial polarisation to the polarisation, and hence to the permittivity, is negligible. When the frequency increases to a certain value which usually lies in the radio and microwave frequency range (10^6-10^{11} Hz) (Smyth 1955), the dipoles cannot

follow the field variation without a measurable lag because of internal retarding or "friction" forces. When the frequency reaches the infrared region and beyond ($\geq 10^{12}$ Hz), the variations in the field are too rapid for the dipoles to follow, so that their contribution to the polarisation, and hence to the permittivity, is negligible. For the frequencies below the infrared the contributions of the atomic and electron polarisation to permittivity are independent of the frequency. At still higher frequencies, usually in the infrared (10^{12}-10^{14} Hz)(Smyth 1955), the positive and negative ions cannot follow the field variations so that the contribution to the permittivity from the atomic polarisation ceases and only the electron polarisation remains.

Hence the permittivity depends markedly on the measurement frequency; furthermore, the polarisation is not in phase with the driving electric field. Hence we write equations 3.2, 3.4, 3.5, and 3.6 in the complex form:

$$\hat{\mathbf{P}}(\omega) = \varepsilon_0 \hat{\chi}(\omega)\hat{\mathbf{E}}(\omega) \tag{3.11}$$

$$\begin{aligned}\hat{\mathbf{D}}(\omega) &= \varepsilon_0 \hat{\mathbf{E}}(\omega) + \hat{\mathbf{P}}(\omega) \\ &= \varepsilon_0 (1 + \hat{\chi}(\omega))\hat{\mathbf{E}}(\omega) \\ &= \varepsilon_0 \hat{\varepsilon}_r(\omega)\hat{\mathbf{E}}(\omega) \\ &= \hat{\varepsilon}(\omega)\hat{\mathbf{E}}(\omega)\end{aligned} \tag{3.12}$$

where

$$\hat{\varepsilon}(\omega) = \varepsilon'(\omega) - j\varepsilon''(\omega) \tag{3.13}$$

The complex permittivity or dielectric constant $\hat{\varepsilon}(\omega)$ is a function of the frequency. It gives information not only about the amplitude but also about the phase angle of the electric displacement density. The real component of permittivity $\varepsilon'(\omega)$ represents the ordinary dielectric constant, the in-phase component of the dielectric displacement, while the imaginary component of permittivity $\varepsilon''(\omega)$ represents the dielectric loss component, the out-of-

phase component of the dielectric displacement. The dielectric loss $\varepsilon''(\omega)$ is an important parameter for any critical discussion and interpretation of dielectric data: it is an essential requirement in theoretical models.

The loss tangent (tanδ) represents the ratio of the energy dissipated per radian in the dielectric to the energy stored at the peak of the polarisation, which is given by

$$\tan\delta(\omega) = \frac{\varepsilon''(\omega)}{\varepsilon'(\omega)} \quad . \tag{3.14}$$

3.3.3 The dielectric relaxation

Dispersion arising during the transition from full orientational polarisation at zero or low frequencies to negligible orientational polarisation at high radio frequencies is referred to as dielectric relaxation. Relaxation phenomena are associated with the frequency dependence of the orientation polarisation and hence with polar dielectric materials.

In the case of dipole relaxation with a single relaxation time τ (Debye model) (Debye 1929), the real ($\varepsilon'(\omega)$) and the imaginary ($\varepsilon''(\omega)$) parts of the dielectric constant $\hat{\varepsilon}(\omega)$ are frequency dependent according to the dispersion relation

$$\hat{\varepsilon}(\omega) = \varepsilon_\infty + \frac{\varepsilon_s - \varepsilon_\infty}{1 + j\omega\tau} = \varepsilon_\infty + \frac{\varepsilon_s - \varepsilon_\infty}{1 + \omega^2\tau^2} - j\omega\tau\frac{\varepsilon_s - \varepsilon_\infty}{1 + \omega^2\tau^2} \tag{3.15}$$

where ε_s and ε_∞ are the low- and high-frequency limits of the dielectric constant, and ω is the angular frequency. The real and imaginary parts of the complex permittivity (dielectric constant and loss), appropriate to the Debye model, as a function of the normalised angular frequency are shown

in Fig. 3.2. For the idealised Debye model the dielectric loss $\varepsilon''(\omega)$ has a peak, the Debye peak, at a characteristic frequency. The dielectric loss $\varepsilon''(\omega)$ goes through zero at zero frequency and approaches zero at frequencies well above the characteristic frequency. The Debye model is rarely applicable to real solids, for which it is often found that the loss peak is considerably broadened.

The response of most dielectrics cannot be described by assuming a single relaxation time. There is a distribution of relaxation times around the average value τ. The real measured relaxation peak is wider than the ideal Debye peak.

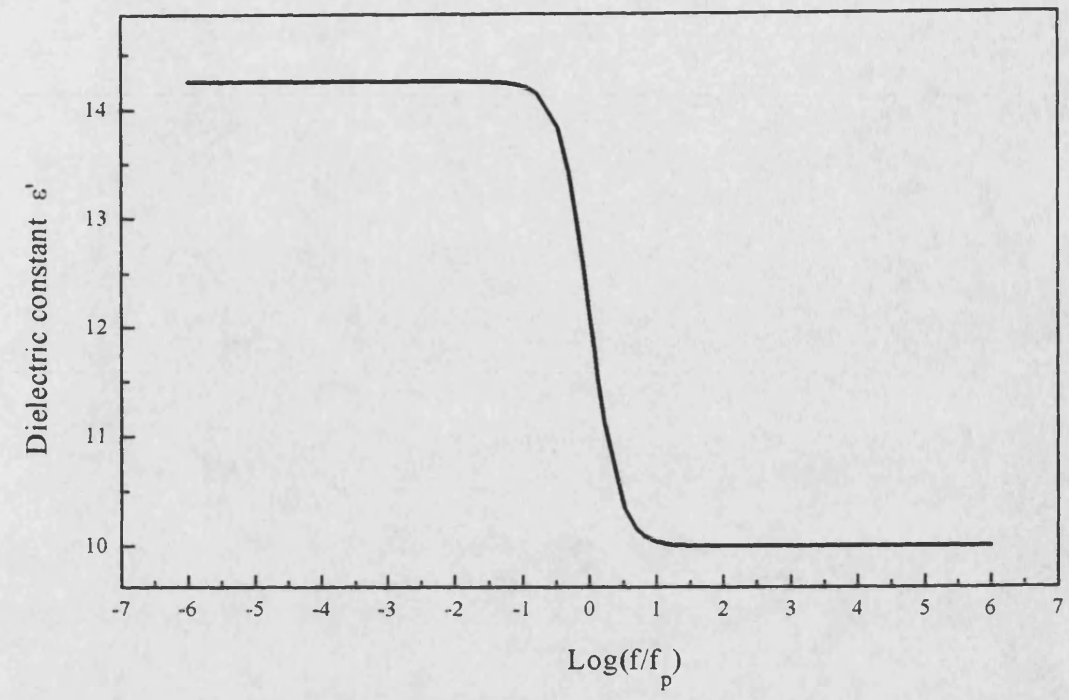

(a)

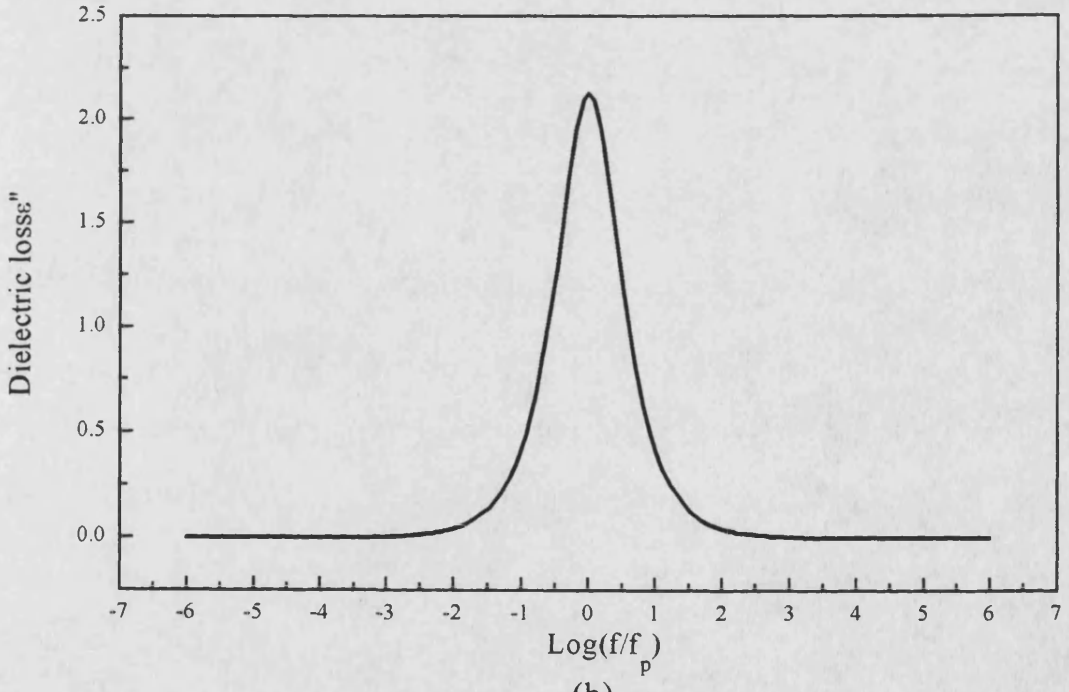

(b)

Fig.3.2 The frequency dependence of (a) dielectric constant and (b) dielectric loss of a Debye system corresponding to equation 3.15 with ε_s=14.25 and ε_∞=10.

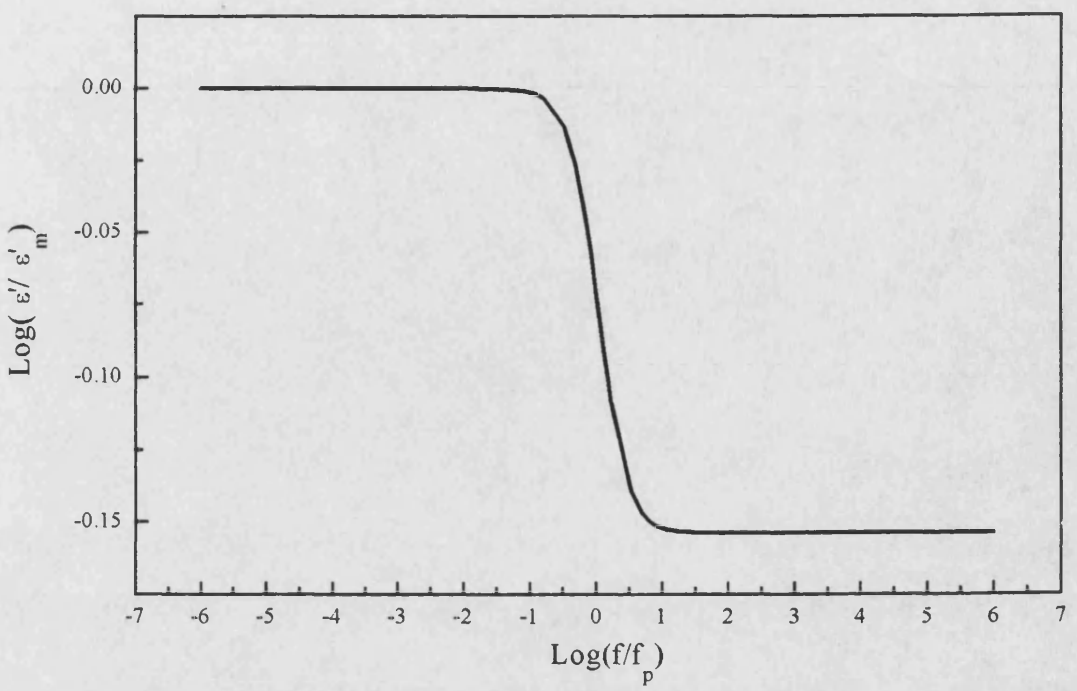

(c)

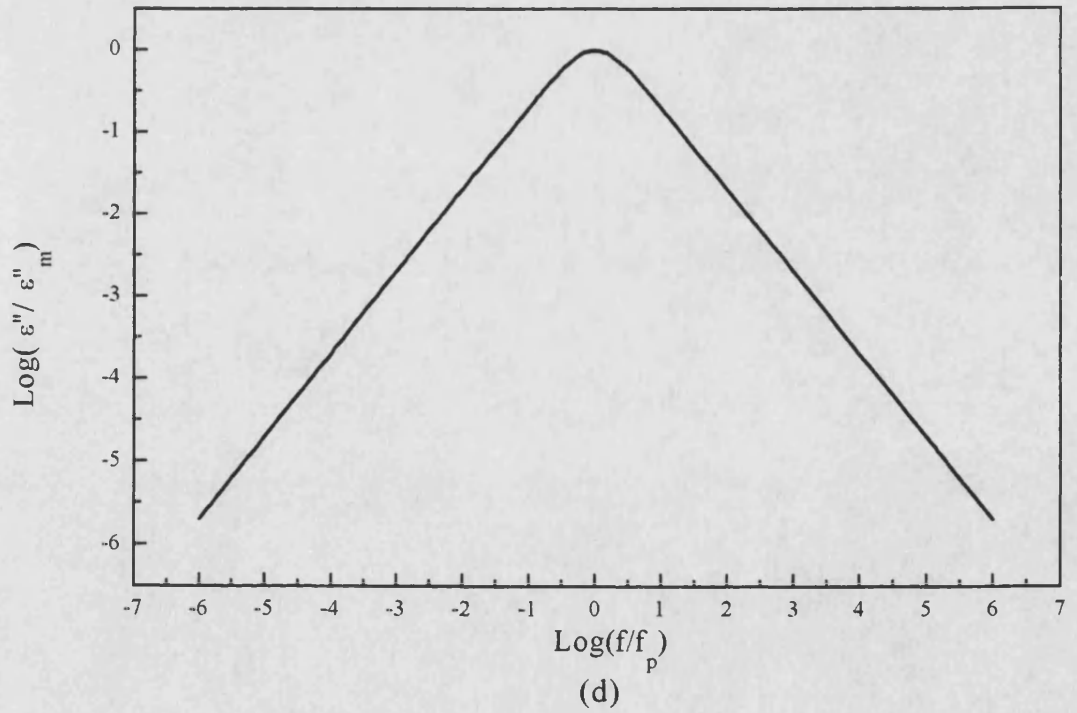

(d)

Fig.3.2 The frequency dependence of (c) dielectric constant and (d) dielectric loss of a Debye system corresponding to equation 3.15 with ε_s=14.25 and ε_∞=10 in logarithmic scale.

3.3.4 Interfacial or space charge polarisation and the Maxwell-Wagner effect

Interfacial or space charge polarisation may be of little fundamental interest, but it is of considerable practical interest because commercial insulating materials are usually heterogeneous. It is particularly important in ceramic materials in which the grain boundaries can be treated as a second phase. Due to the differences in the electrical conductivity of the grains and grain boundaries, charges can build up on the surfaces which separate the grains and grain boundaries. The conducting phase becomes polarised. This manifests itself as a high dielectric constant and causes a peak in the dielectric loss. This kind of inhomogeneous medium effect is known under the general name of the Maxwell-Wagner effect (Maxwell 1954, Wagner 1913).

The simplest model for calculation of interfacial or space charge polarisation is the Maxwell-Wagner two-layer condenser. If we have two plane electrodes of equal area A with two parallel layers of dielectric materials having different conductivities and different relative permittivities inserted between them, the equivalent circuit for the Maxwell-Wagner two-layer condenser is of the form show in Fig. 3.3.

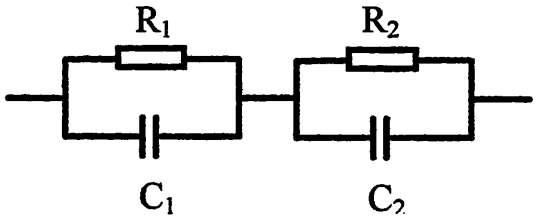

Fig.3.3 Equivalent circuit for the Maxwell-Wagner two-layer condenser.

On the basis of Gauss' law, Ohm's law and the continuity of the current, using the equivalent circuit in Fig.3.3, the frequency dependencies of dielectric constant and dielectric loss were calculated (Anderson 1964) as:

$$\varepsilon' = \varepsilon_\infty + \frac{\varepsilon_s - \varepsilon_\infty}{1+\omega^2\tau^2} \tag{3.16}$$

$$\varepsilon'' = \frac{1}{\omega C_0(R_1+R_2)} + \frac{(\varepsilon_s - \varepsilon_\infty)\omega\tau}{1+\omega^2\tau^2} \tag{3.17}$$

where $\tau = CR = (C_1 + C_2)\frac{R_1R_2}{R_1+R_2}$ and is the time constant of the complete circuit; $C_0 = \frac{A}{d_1+d_2}$, d_1 and d_2 being the thicknesses of two parallel layers of dielectric materials, ε_s and ε_∞ are the low- and high-frequency limits of the dielectric constant, and ω is the angular frequency. Comparing equation 3.16 with the real part of equation 3.15, it can be seen that the frequency dependence of ε' is precisely the same as that of the case of Debye relaxation (see equation 3.15), and τ may be identified with the relaxation time. Comparing equation 3.17 with the imaginary part of equation 3.15, it can been shown that the second term of equation 3.17 is exactly the dielectric loss ε'' of the Debye relaxation (see equation 3.15). There is an additional term which is inversely proportional to frequency. This means that the dielectric loss ε'' of interfacial polarisation tends to infinity as ω tends to zero. In the Debye relaxation case ε'' drops towards zero as frequency is lowered. Therefore, interfacial polarisation may be distinguished from the Debye relaxation by observing the variation of ε'' below the relaxation frequency.

3.3.5 The temperature dependence of loss peak frequency

In general, both the average relaxation time and the distribution width are a function of temperature. A useful approximation for a relaxation mechanism is often that the process is thermally activated. In that case the average relaxation time, τ, is given by

$$\tau(T) = \tau_0 \exp(W / kT) \tag{3.17}$$

or $\omega_p(T)$ $(=1/\tau)$ is given by

$$\omega_p(T) = \nu \exp(-W / kT) \tag{3.18}$$

where τ_0 is a characteristic time for the relaxation mechanism, W is the activation energy, k is the Boltzmann constant, T is the temperature and $\omega_p(T)$ is the temperature-dependent loss peak frequency. By plotting the logarithm of the peak frequency against reciprocal temperature it is possible to obtain the activation energy.

3. 4 Simple RC circuits

The current response of circuit elements to a sinusoidally varying voltage $\hat{V}(\omega)$ will be $\hat{I}(\omega)$ where ω is the angular frequency. The ratio of the voltage to the current is known as the impedance

$$\begin{aligned}\hat{Z}(\omega) &= \frac{\hat{V}(\omega)}{\hat{I}(\omega)} \\ &= Z'(\omega) + jZ''(\omega) \\ &= R(\omega) + jX(\omega)\end{aligned}$$

and this is, in general, a complex quantity which indicates a phase shift between $\hat{V}(\omega)$ and $\hat{I}(\omega)$. The real component $R(\omega)$ is termed resistive and the imaginary component $X(\omega)$ termed reactive. It is also necessary to define the other three related complex quantities those are:

$$\hat{Y}(\omega) = \frac{1}{\hat{Z}(\omega)} = Y'(\omega) + jY''(\omega) \qquad \text{ADMITTANCE}$$

$$\hat{C}(\omega) = \frac{1}{j\omega\hat{Z}(\omega)} = C' + jC'' \qquad \text{COMPLEX CAPACITANCE}$$

$$\hat{M}(\omega) = j\omega\hat{Z}(\omega) = M' + jM'' \qquad \text{COMPLEX}$$

MODULUS

The circuit impedance of an ideal resistor R and an ideal capacitor C which are connected in series is given by

$$\hat{Z}(\omega) = R + \frac{1}{j\omega C} = R - j\frac{1}{\omega C}$$

The Nyquist plot (i.e. imaginary component Z" versus real component Z') of this circuit is a vertical straight line whose length is inversely proportional to frequency and which intersects the real axis at R (Fig. 3.4). In the admittance plane the profile is a semicircle with diameter 1/R (Fig. 3.4).

Schematic plots for a simple parallel circuit are shown in Fig. 3.5. The Nyquist plot of a simple parallel circuit is a semicircle with a diameter R. In the admittance plane the profile is a straight line which intersects the real axis at 1/R. This response is often found in impedance spectra results for solids and liquids. The resistance R approximates the time delay of the response, as well as conductivity of the sample, while C approximates polarisation.

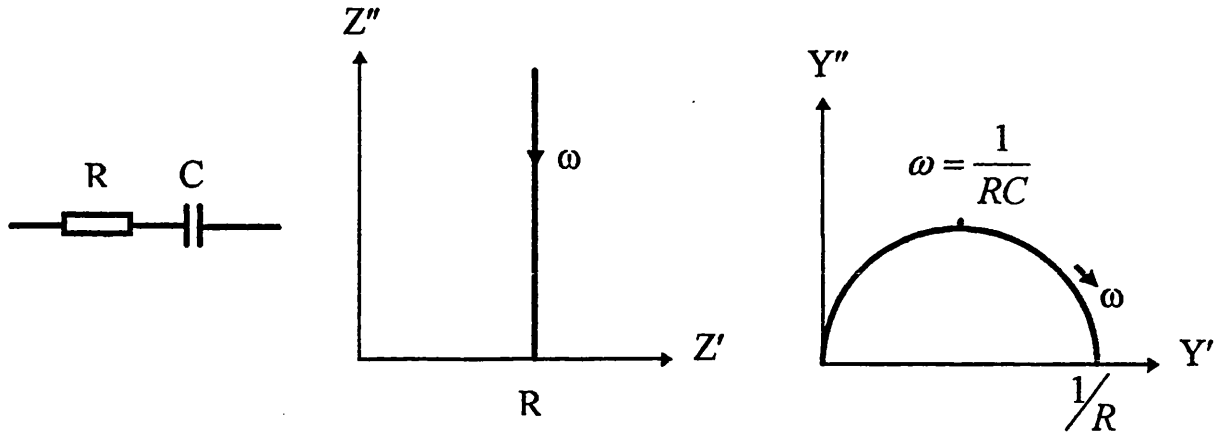

Fig. 3.4 The complex impedance and admittance representations for simple series circuits.

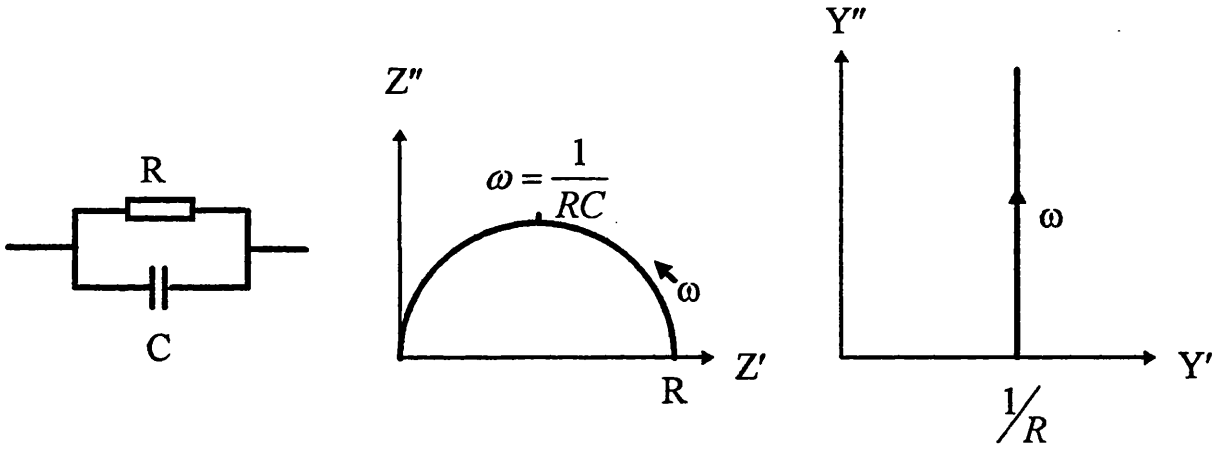

Fig. 3.5 The complex impedance and admittance representations for a simple parallel RC circuit.

The two simple circuits discussed so far provide the building blocks for more complicated networks. We can now look at an important example comprising two parallel configurations connected in series. This is a generalisation of the circuit to cover the possible existence of two different regions in samples which have different dielectric constants and resistivity, each region approximated by a parallel circuit. The corresponding impedance profile of this circuit with two parallel configurations connected in series takes the form of two adjoining semicircles (Fig. 3.6). The diameters of these two semicircles are determined by the magnitude of the resistances R_1 and R_2. These two semicircles may be completely or partially overlapped. In the limits of $C_1 << C_2$ and $R_1 << R_2$ the two semicircles are well separated (Jonscher 1983). The admittance representation is a semicircle with a spur at higher frequencies (Fig. 3.6).

Experimental impedance data can be modelled by the impedance of an equivalent circuit made up of ideal resistors, capacitors and possibly various distributed circuit elements. An appropriate equivalent circuit can be established according to the physical processes which take place in the material. The experimental impedance data can be plotted in the complex plane. From Figures 3.4-3.6 it can been seen how resistance and capacitance values of an equivalent circuit can be derived from complex admittance or impedance plots of the experiment impedance data. The resistance and capacitance values of an RC circuit can also be derived from the complex modulus or capacitance plots.

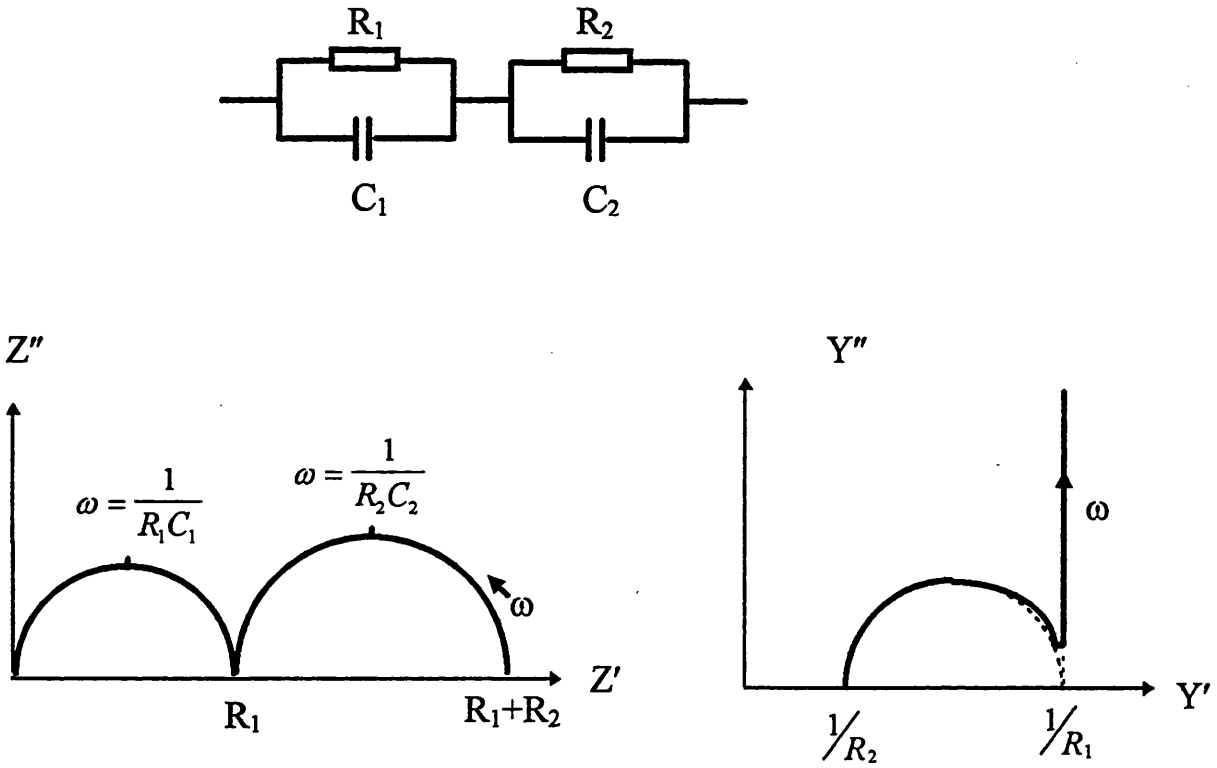

Fig. 3.6 The complex impedance and admittance plots for a circuit made of two parallel RC configurations connected in series.

3.5 Effect of microstructure on the dielectric properties of ceramics

3.5.1 Introduction

In polycrystalline solids, transport properties are strongly affected by microstructure, and impedance spectra usually contain features that can be directly related to the microstructure. Grain boundaries, which are always present in ceramics, can be treated as the second phases. The effects of two phase structures upon complex plane profiles are usually analysed in terms of either layer model or effective medium theorems. Both of these approaches have been reviewed by Macdonald (1987). The layer model used in this project is easier to relate physically to equivalent circuits

3.5.2 Brick layer model

The most commonly used and simplest layer model for a ceramic is the "brick-layer" model, which has been reviewed by Macdonald (1987). It is shown schematically in Fig. 3.7.(a): cubic grains of side D are surrounded by grain boundary of thickness d ($d \ll D$), which is treated as a second phase. The current flow is approximated as one-dimensional and the curvature of the current paths at the grain corners is neglected. There are two paths for one-dimensional current flow (Fig. 3.7.(b)): (i) through the grain and then across the grain boundary, (ii) along the grain boundary only. The relative magnitudes of the currents through those two paths are dependent on the relative magnitudes of the bulk (grain) and grain boundary conductivity, σ_b and σ_{gb}. There are two extreme cases:

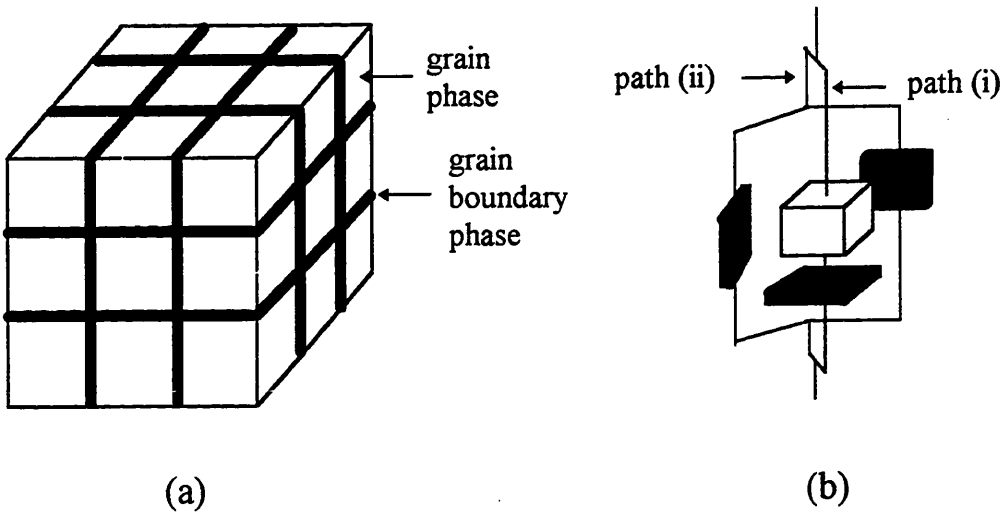

Fig. 3.7. Brick layer model for a two-phase ceramic: (a) Over view, showing array of cubic grains, separated by grain boundaries. (b) Exploded view of a single cell, showing parallel electric paths: (i) through grains and grain boundaries and (ii) along grain boundaries (Macdonald 1987).

Case (1) : $\sigma_b >> \sigma_{gb}$ Conduction along the grain boundaries is negligible, and conduction through the grains and across grain boundaries dominates. In this case, the brick model can be simplified to a series layer model. Its equivalent circuit is shown in Fig. 3.8.(a). The resistance R_b and the capacitance C_b are attributed to the bulk (grains) of the material and R_{gb} and C_{gb} to the grain boundaries. To include the electrical response of the electrodes, a resistance R_e and a capacitance C_e are added to the equivalent circuit, which is one of the most commonly used equivalent circuits for ceramics. The idealised impedance response for the circuit in Fig. 3.8.(a) is shown in Fig. 3.8.(b). With this model, from the measured electrical responses, it is possible to obtain crude estimates of the fraction of the total volume occupied by boundary phase (or grain boundary volume fraction X_{gb}) from

$$X_{gb} = \frac{3d}{D} = 3\frac{C_b}{C_{gb}}\frac{\varepsilon_{gb}}{\varepsilon_b} \tag{3.19}$$

or the ratio of grain boundary thickness (d) to grain size (D):

$$\frac{d}{D} = \frac{C_b}{C_{gb}} \frac{\varepsilon_{gb}}{\varepsilon_b} \tag{3.20}$$

In the Equations 3.19-20 , C_b and C_{gb} are the grain and grain boundary capacitances, ε_b and ε_{gb} are the grain and grain boundary static dielectric constants. Data for C_{gb} and C_b can be directly obtained from the complex plan plots of impedance experiment data. Normal practice is to assume that the two dielectric constants (ε_b and ε_{gb}) are equal (Macdonald 1987).

Case (2): $\sigma_{gb} >> \sigma_b$ conduction along the grain boundaries is dominant. The brick layer model is equivalent to the parallel layer model. A ceramic sample will then show only one arc in the impedance or modulus spectrum and little can be learned about the microstructure.

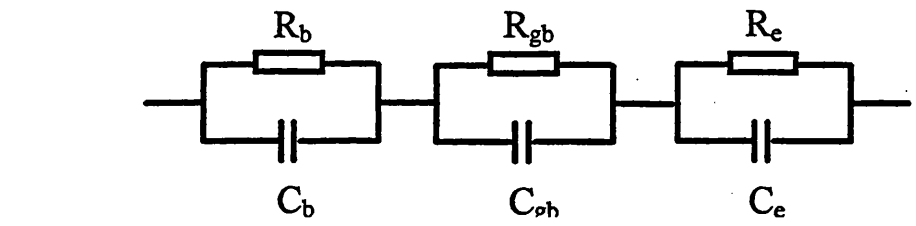

(a)

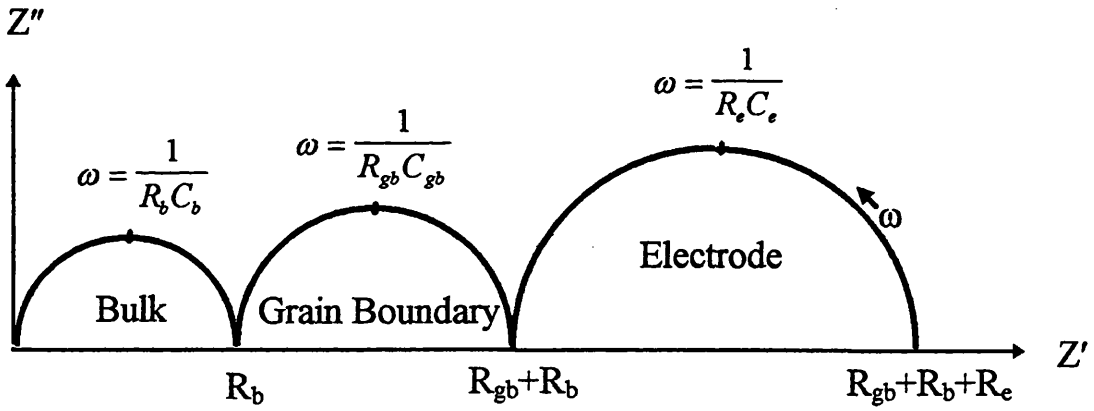

(b)

Fig. 3.8 (a) Equivalent circuit for the analysis of the impedance data of a ceramic. (b) Idealised impedance response for (a).

Chapter 4 Ultrasonic Experimental Techniques and Equipment

4.1 The pulse echo overlap measurement system and the basic principles for measurement of ultrasonic wave velocities and attenuation

The pulse echo overlap system can be used to measure both the transit time of a pulse round-trip and the attenuation of an ultrasonic wave in a sample which has two parallel flat faces normal to the propagation direction of the ultrasonic wave. The block diagram of the measurement system used is shown in Fig. 4.1. The system has a sensitivity which allows the change of wave velocity to be measured to better than 1 part in 10^4 (Yogurtcu 1980). A computer is included to enable the data to be collected semi-automatically. The apparatus used includes:

(1) MATEC high resolution frequency source (0.5Hz-50MHz, Model 110);

(2) MATEC pulse modulator and receiver (Model 6600);

(3) MATEC rf plug-in (10-90MHz, Model 760V);

(4) HITACHI oscilloscope V-1050F (100MHz);

(5) HEWLETT-PACKARD Model 5382A 225MHz frequency counter;

(6) Decade divider and strobe generator;

(7) A home-made pulse peak detector;

(8) Racal 5004 digital voltmeter;

(9) PC computer;

(10) HITACHI oscilloscope V-1060 (100MHz).

A high resolution frequency source generates a synchroniser square wave in the kHz range. The frequency of this synchroniser square wave is divided by a factor of 10, 100 or 1000 using the decade divider. This

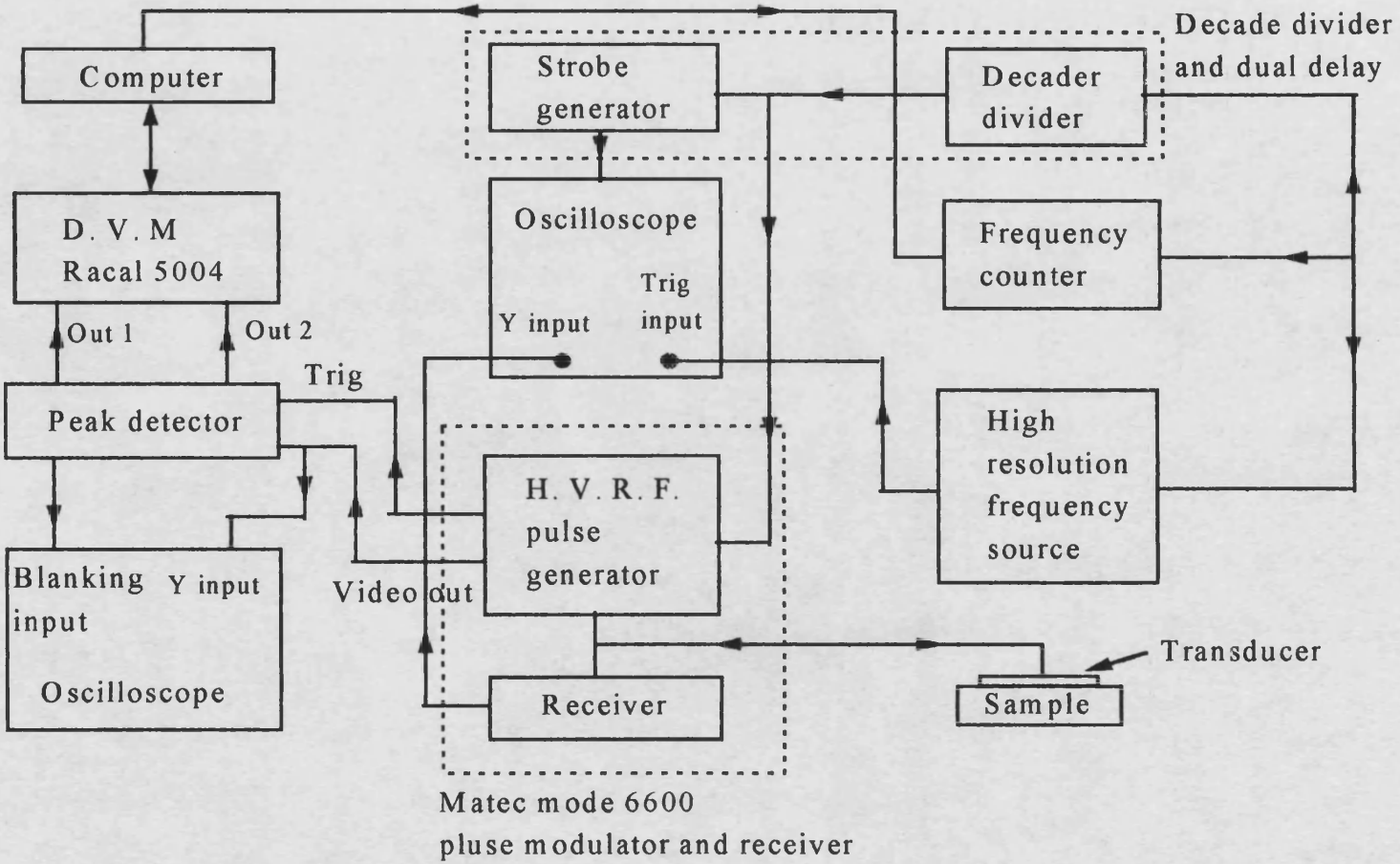

Fig.4.1 Block diagram of pulse echo overlap and peak detector system.

divided low frequency signal (Fig. 4.2(a)) is used to trigger an rf pulse generator which is contained in the MATEC pulse modulator and receiver (Model 6600). A short duration rf pulse (Fig. 4.2(b)) with a one to three microsecond time width and a maximum amplitude of 630 volts peak-to-peak is produced by the rf pulse generator. The carrier frequency of the rf pulse is set to the resonant frequency, or at one of the odd harmonics, of a transducer. The rf pulse is applied to a transducer, which is mounted on a sample and used as both a transmitter and a receiver. The rf pulse electrical signal is converted into a mechanical vibration by the transducer. The mechanical vibration passes through the sample and is reflected back and forth between the two parallel faces of the sample. The resulting pulse-echo pattern is shown in Fig. 4.2 (c). To enable observation of a complete set of echoes, the triggering frequency for the rf pulse generator has to be set low enough to ensure that all the echoes from one rf pulse have died away before the next rf pulse is applied. The decade divider is used to achieve low enough triggering frequency for the rf pulse generator. The returning ultrasonic waves are picked up by the same transducer and converted into electrical signals, which are fed to the amplifier in the receiver.

The output from the amplifier is displayed on the oscilloscope as seen in Fig. 4.3. For the measurement of the transit time of a round-trip, two echoes in one pulse-echo pattern are selected. To highlight these two selected echoes, a pair of square wave pulses (Fig. 4.2 (d)) is fed to the Z-mode of the oscilloscope. This pair of square wave pulses is produced by a strobe generator, which is triggered by the output signal from the decade divider.

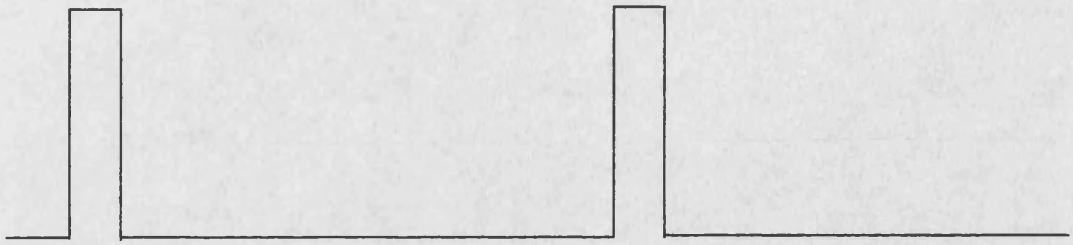

(a) The low frequency synchroniser square wave used to trigger the rf pulse generator.

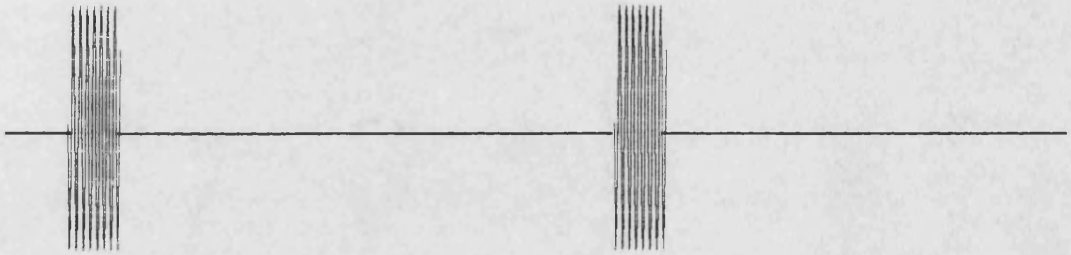

(b) The short duration rf pulse signal sent to the transducer.

(c) The echoes in the sample produced by the transducer using short duration rf pulses as shown in (b).

(d) Pairs of square wave pulses produced by the strobe used for highlighting two selected echoes on the oscilloscope.

Fig. 4.2 Signals in the pulse echo overlap system.

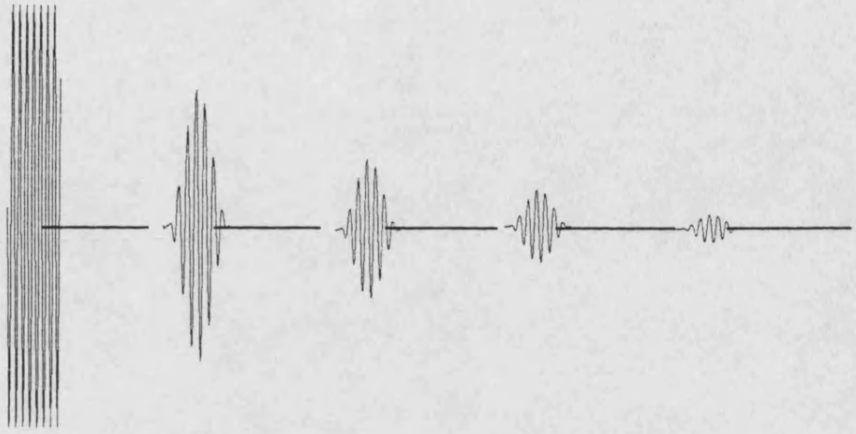

Fig. 4.3 The pulse-echo pattern displayed on the oscilloscope screen.

The unselected echoes are obscured by reducing the brightness of the oscilloscope. The output signal from the high resolution source is used to drive the X-axis of the oscilloscope. The selected echoes can be overlapped with each other on the screen of the oscilloscope as in Fig. 4.4 by driving the X-axis of the oscilloscope at a frequency equal or at an integer multiple to the reciprocal of the round-trip travel time of the echoes in the sample. The adjustment of the frequency of the high resolution source brings the rf cycles within the two echo envelopes to overlap cycle-by-cycle. The reading of the frequency counter indicates the overlap frequency, which can be used to calculate the ultrasonic wave velocity. Special criteria proposed by McSkimin and Andreatch (1962) can be used to decide which cycle is the correct one for matching in each echo.

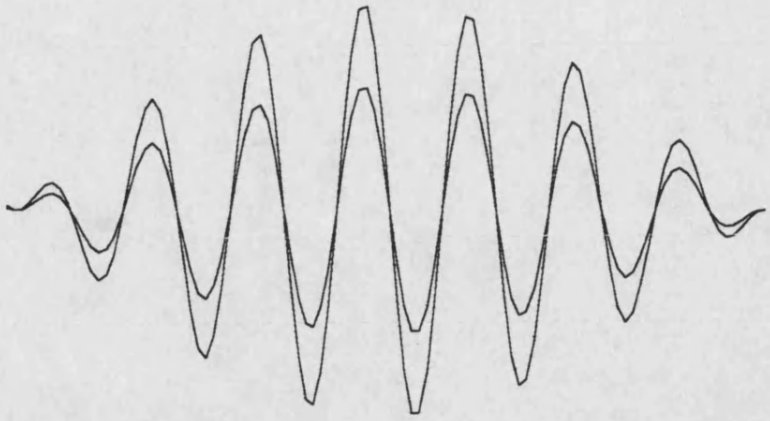

Fig. 4.4 Two overlapped ultrasonic echoes.

The attenuation data are taken at the same time as that of the overlap frequency. A pulse peak detector has been used, in conjunction with the VIDEO and SYNC OUT outputs from the MATEC pulse echo overlap system, to produce two DC output voltages, which are equal to the peak amplitude of two selected echoes in the pulse train. The two DC voltages are measured using a Racal 5004 digital voltmeter which has two inputs, one at the front and one at the rear, and the data are collected and processed by a computer.

4. 2 The transducers and bonding agents

In the measurements made here following X- and Y-cut quartz transducers are employed to generate longitudinal and shear waves respectively. As shown in Fig.4.5(a), the transducer cut with its length along the Y-crystallographic axis and its thickness normal to the X-axis is called an X-cut transducer. The Y-cut transducer is cut with its length along the X-axis and its thickness normal to the Y-axis (Fig.4.5(a)). Quartz transducers are

the most commonly used piezoelectric transducers due to the absence of dissipation in quartz transducers and the ease of generating the appropriate type of wave. As a consequence of the piezoelectric effect, a piezoelectric transducer can produce a mechanical displacement proportional to an applied electric field or vice versa. A single transducer can be used as both the source of the initial pulse and the receiver of all the successive echoes. One side of a transducer is coated coaxially with gold to form two electrodes with an insulating ring between them (Fig. 4.5 (b)). The central electrode is used to make a high voltage connection and the outer electrode is connected to the other side which is fully coated and provides an earth connection. Fig. 4.5(c) shows a transducer with two electrodes which is bonded on to a sample.

The working frequencies of a transducer are governed by its thickness L. The relationship between the thickness L of a transducer and the wavelength λ of the generated sound wave in the transducer at the fundamental resonance frequency f_0 is

$$L = \lambda/2 \tag{4.1}$$

Transducers can be driven at odd harmonics of their fundamental frequency. The working frequencies f_n of a transducer are:

$$f_n = (2n-1)f_0 \qquad (n=1,2,3,...) \tag{4.2}$$

Combining Eq. (4.1) and (4.2) gives the following relationship between the working frequencies f_n of a transducer and its thickness L:

$$f_n = \left(n - \frac{1}{2}\right)\frac{v_0}{L} \qquad (n=1,2,3,...) \tag{4.3}$$

where v_0 is the velocity and the fundamental frequency is f_1.

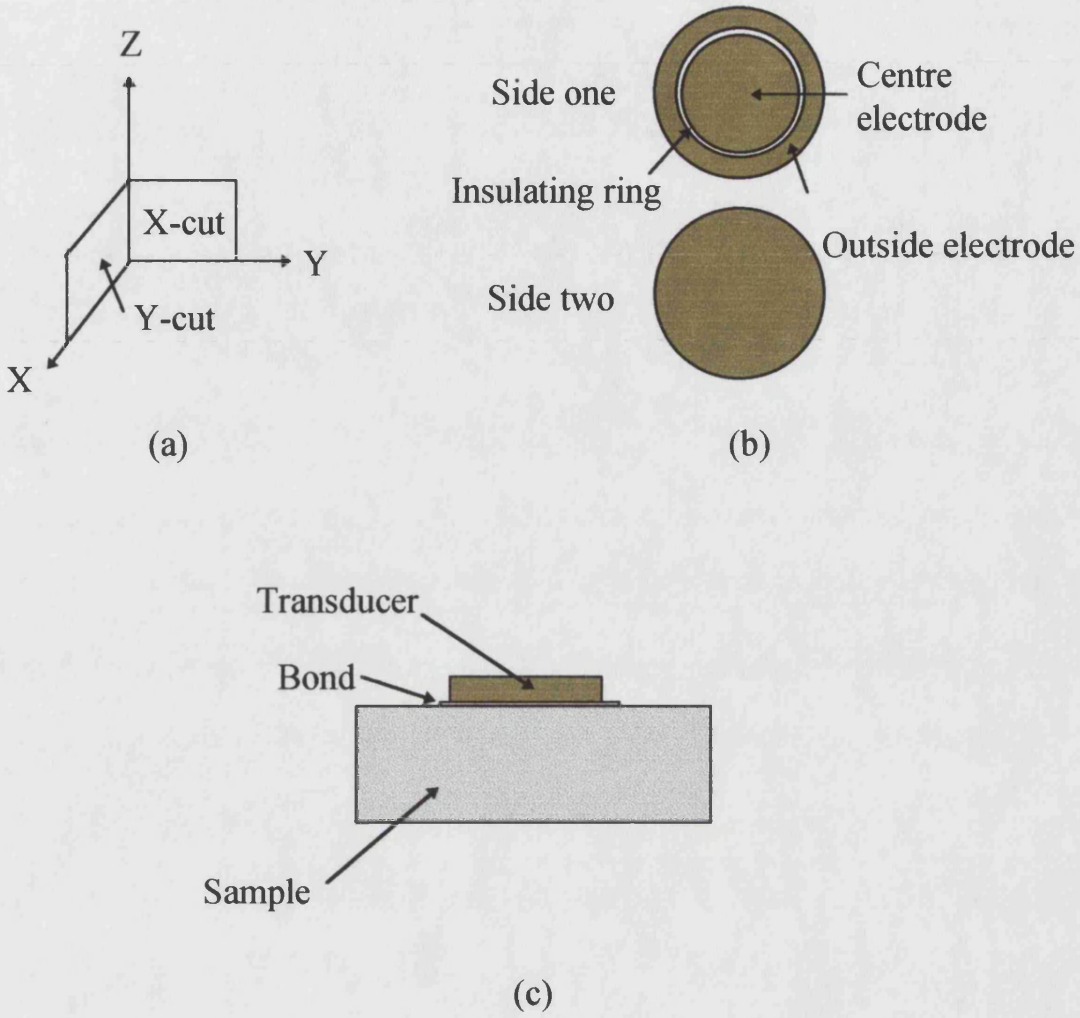

Fig. 4.5 (a) The transducer cuts. (b) The transducer. (c) The bonded transducer.

In order to prevent the sound energy from diverging, the diameter of transducers should be large enough. The sound wave generated by a circular transducer in the sample can be treated as a plane wave which has a width equal to the diameter of the transducer up to the distance given by

$$d = a^2/\lambda \tag{4.4}$$

where d is the axial distance which the plane wave travels and a is the radius of the transducer. This region is called the Fresnel region (Mason 1958).

To bond the transducer on to a sample, an intermediary bonding material must be used. There are a variety of bonding materials that can be used depending on the sample and the circumstance of use. Silicone oils, greases, glycerine, and epoxy resins are among the many bonding agents that have been used extensively over a wide range of temperatures (see Farley (1973) for details). Nonaq, DC 200 silicones, alcohol and various forms of pentene have been used at low temperatures (Bateman 1966). The following points have to be considered when choosing a bonding material. The acoustic characteristic impedance Z_b of the bonding material should result in a low reflection coefficient. It is desirable to obtain the thinnest possible, parallel and uniform bond over the largest temperature range. The bonding material should be easy to handle, not corrosive and not toxic. The bonded transducer should be removable after use. The bonding material used in this work is Dow Resin 276-V9 (Dow-Corning Corp., U.S.A.). It is easy to use and gives a good acoustic energy coupling from room temperature up to 340K.

4. 3 The hydrostatic pressure apparatus

As shown in Fig. 4.6, the hydrostatic pressure apparatus consists of a cylinder and two pistons made from EN26 nickel alloy carbon steel. The sample holder is fixed onto the top piston, which has four pins to connect the manganin pressure gauge, two pins to a NiCr/NiAl thermocouple and one pin to an electrode which is connected to a high voltage output of the pulse generator of the pulse echo overlap system. The body of the sample

holder provides an earth connection to the pulse generator of the pulse echo overlap system. The manganin pressure gauge has been calibrated up to 10 kbar in the temperature range 77-300K in another pressure apparatus, which was designed for resistance measurement. The resistance of the manganin pressure gauge has a linear relationship with the pressure. The pressure coefficient of the manganin pressure gauge is 2.42×10^{-6} bar^{-1} at 290K. The temperature coefficient of pressure coefficient is $1.3 \times 10^{-3} K^{-1}$ at 290K. A model 1999 system DMM scanner, with a sensitivity of 1mΩ, is used to measure the electric resistance of the manganin pressure gauge. The pressure data are calculated from the resistance using:

$$P = \frac{1}{2.4 \times 10^{-3}} \left(\frac{R}{R_0} - 1 \right) \quad \text{(kbar)} \tag{4.5}$$

where R and R_0 are the resistance of the manganin pressure gauge under arbitrary pressure P and initial pressure P_0 respectively. The NiCr/NiAl thermocouple is mounted adjacent to the sample to allow the accurate temperature measurement. The temperature is read with a "Digitron" digital thermometer (Digitron Instrumentation Ltd.). A safety alarm device is used on the top piston to prevent crushing of the sample if the piston position changes due to leaking of the transmitting medium. For the room temperature and above, a temperature controller (type 810, Eurotherm Ltd.) controlled electrical jacket is used to control the temperature of the sample and the pressure cell. Pressure is created by pressing the top piston downward to squeeze the oil using a hydraulic pressure pump. The theoretical work pressure is up to 10 kbar at room temperature considering only the pressure cell. The working temperature and pressure range of the hydrostatic pressure apparatus depends also on the pressure transmitting medium and the seals used. The pressure transmitting medium used in this work is "Dow Corning" 200/1000cs silicone fluid, which works in the temperature range from 243K to 453K, a range limited by its freezing and

boiling points. Black VIT (viton) rubber "O" rings and the PTFE delta rings are used as seals between the pistons and the inner cylinder wall in this work. The black VIT (viton) rubber "O" rings work from room temperature up to at least 453K. Using PTFE delta rings, a pressure up to 3.5 kbar can be created at room temperature. Different kinds of seals and pressure transmitting mediums are available for the different working temperature and pressure ranges.

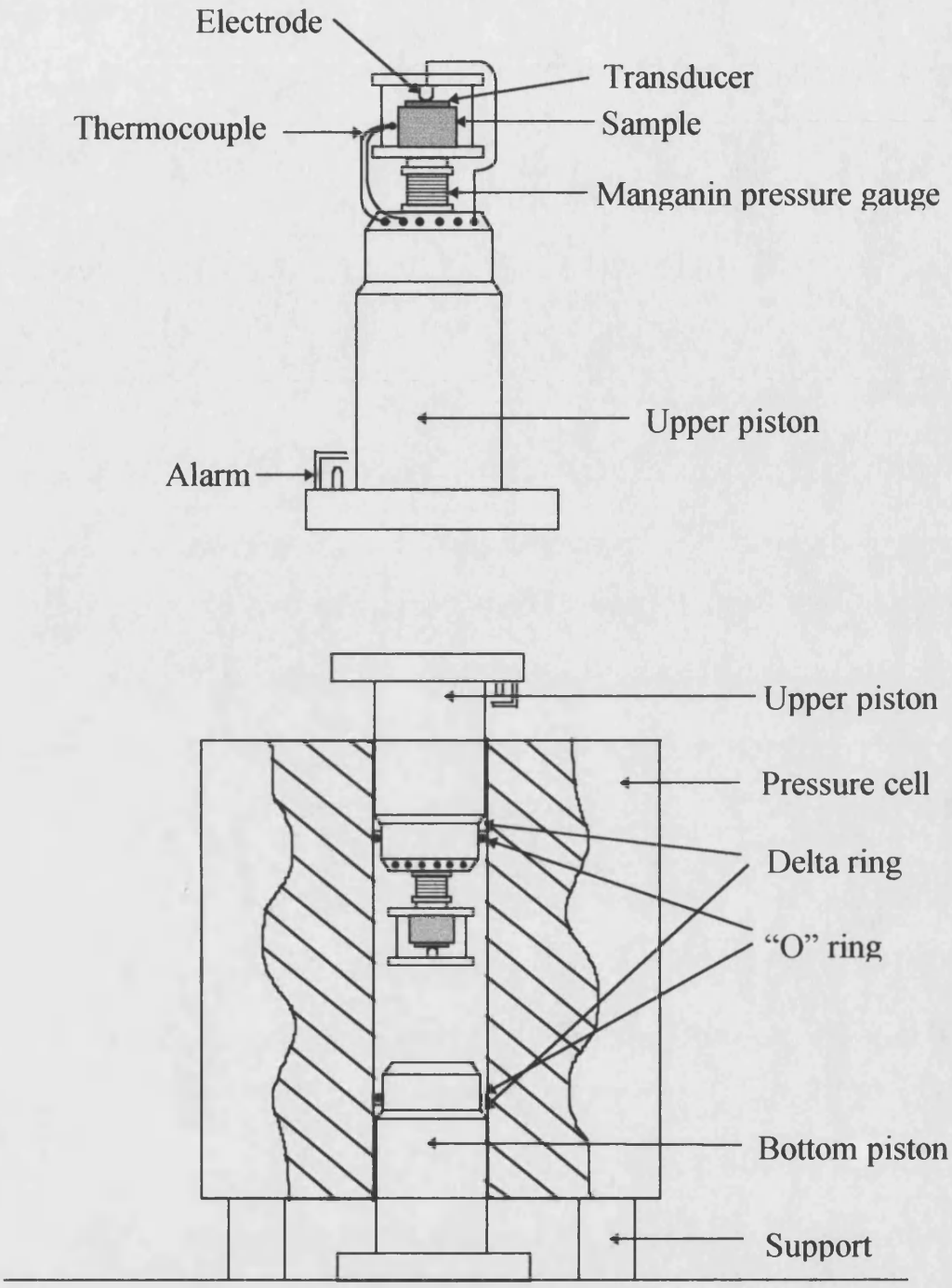

Fig. 4.6 Diagram of the hydrostatic pressure cell and sample holder.

Chapter 5 Techniques for AC Impedance Spectroscopy Experiments

5.1 Instrumentation and sample

Impedance measurements were made with the HP Model 4192A LF Impedance Analyser for all the samples under the same condition. The HP Model 4192A LF Impedance Analyser is a fully automatic, high performance test instrument designed to measure a wide range of impedance parameters as well as gain, phase and group delay. The equipment can provide measuring frequency, OSC level, and dc bias voltage under actual operating conditions. The measurements can be made over the frequency range from 5Hz to 13MHz. The OSC level is variable from 5mV to 1.1Vrms with 1mV resolution (5mV for levels higher than 100mV). The internal dc bias voltage source (impedance measurement only) provides ±35 V in 10mV increments. Measurement frequency or dc bias voltage can be automatically or manually swept in either direction. The measurement range of |Z|, R and X is from 0.1mΩ to 1.2999MΩ; |Y|, G and B is from 1ns to 12.999s; θ is from -180.00° to 180.00°; L is from 0.01mH to 1.00kH; C is 0.1 pF to 100.0mF; D is from 0.0001 to 19.999; Q is from 0.1 to 1999.9. All parameters obtained have a basic accuracy of 0.1% .

A computer-controlled system was set up to enable measurements of the temperature dependence of the impedance spectra. Computer programs were written to collect measurements of the temperature dependence of impedance spectra down to 10 K and above room temperature. A sample-holder was designed and built for the measurements between room temperature and 700°C.

To determine the dielectric properties of a material, a well defined sample geometry must be used (e.g. parallel plate geometry or coaxial). Parallel plate samples were used in this work. To carry out measurements at higher temperatures, electrodes were formed by both gold evaporation and silver paint.

5.2 Impedance spectroscopy measurements above room temperature

The electrodes built in to the sampleholder are two small pieces of hand-fine-polished copper each in the shape of a circular sheet. They were coated by first evaporating on Ag and then Au. Two 0.5 mm diameter Ag wires were used as contacts for high temperature measurements made in a furnace. These Ag wires were about 50cm long. One end of each wire was connected to one of the two electrodes. The other end of the wire was connected to two of the four-terminals of the impedance analyser. In this way a four-terminal arrangement was used. The overall contact resistance plus that of the Ag wires were measured up to 700°C. The contact resistance was about 0.1Ω and independent of the temperature. The sample with electrodes was gripped between the two electrodes of the sampleholder. Temperature was monitored with a chromel-alumel thermocouple adjacent to the sample. A diagram of the sampleholder is shown in Fig. 5.1. The " alumina bar" in Fig. 5.1 was ceramic alumina 99ZA obtained from a German company called "Schunk". The resistance of the alumina bars was 10^{13} Ω at room temperature and 2×10^{7} Ω at 1273K. The admittance of the sampleholder was measured from room temperature up to 682°C. The data were compared with admittance measured on ceramic aluminas. It was found that the largest error due to the sampleholder leakage was about 1%.

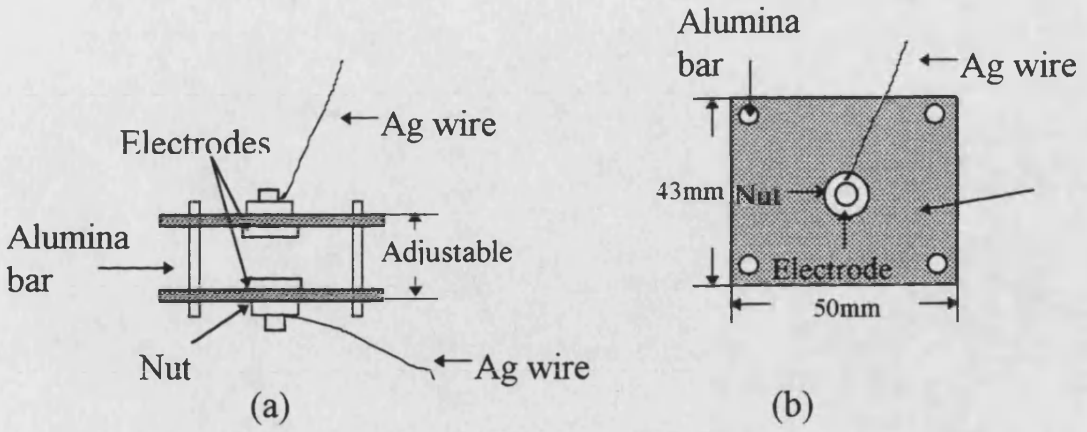

Fig. 5.1 (a) The side view and (b) the top view of the sampleholder used for impedance spectroscopy measurements at high temperature.

5.3 Impedance spectroscopy measurements below room temperature

To make impedance measurements below room temperature a Cryophysics Model 22C cryodyne refrigeration system was used. This system consisted of a Model SC compressor, a Model 22 Cold Head and a Model DRC-91C temperature controller. The temperature was measured by A Model DT-470-CU-12A diode temperature sensor which was mounted on the sampleholder. A rotary pump, together with a diffusion pump, was used to produce an adequate vacuum which was necessary for good temperature control and to enable satisfactory cooling down to 15K. The working temperature range of the system was 15 to 325K and was controlled to an accuracy of 0.1K. For a detailed description of this system see the thesis of Chang (1996). Fig. 5.2 shows the cryodyne sampleholder with the sample mounted and the associated connections. Each electrode of the sample was connected to two of the four coaxial cables which were connected to the four-terminals of the impedance analyser.

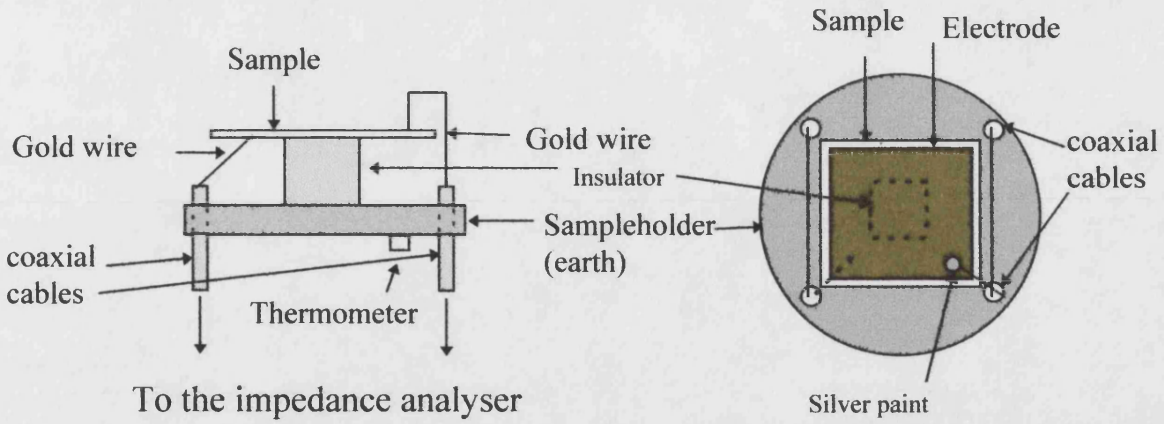

Fig. 5.2 (a) The side view and (b) the top view of the sampleholder with mounted sample as used for impedance spectroscopy measurements below room temperature.

Chapter 6 General Description of Alumina

6.1 Crystallography of single crystal alpha alumina

Aluminium oxide or alumina (Al_2O_3) exists in two principal forms α- and γ-Al_2O_3. α-Al_2O_3, which was investigated in this work, also known as corundum, is the commonest form of alumina and also the most stable; it is yielded when any other form of alumina is heated to a high enough temperature. In single crystal α-Al_2O_3 each Al^{3+} is surrounded by six O^{2-} ions and each O^{2-} ion is surround by four Al^{3+}, which arrangement achieves electrical neutrality, and the net lattice formula is Al_2O_3. The crystallography study shows that α-Al_2O_3 single crystal has rhombohedral symetry with point group of $\bar{3}m$ (Hankey et al. 1969).

The crystallography of α-Al_2O_3 has been described in detail by Kronberg (1957). The large oxygen atoms are arranged in a hexagonal close packed type of lattice, with aluminium atoms occupying two thirds of the available octahedral sites, a third remaining unfilled (Fig. 6.1). The ionic radii are 0.053 nm for Al^{3+} and 0.138 nm for O^{2-} (Kingery, 1976). For the hexagonal cell the lattice parameters a_0 and c_0 are 0.475923 nm and 1.299208 nm at room temperature respectively (Phillips 1980).

6.2 The properties of ceramic and single crystal alpha alumina

With an enthalpy of formation of 1674.4 kJ/mol, α-Al_2O_3 is one of the most strongly bonded compounds in existence. It shows the characteristics common to many strongly bonded compounds such as high electrical resistivity, chemically inert and stable, high melting point and high Young's modulus. In its pure form alumina ceramic is chemically inert and stable up to its melting point of 2050°C, highly resistant to corrosion

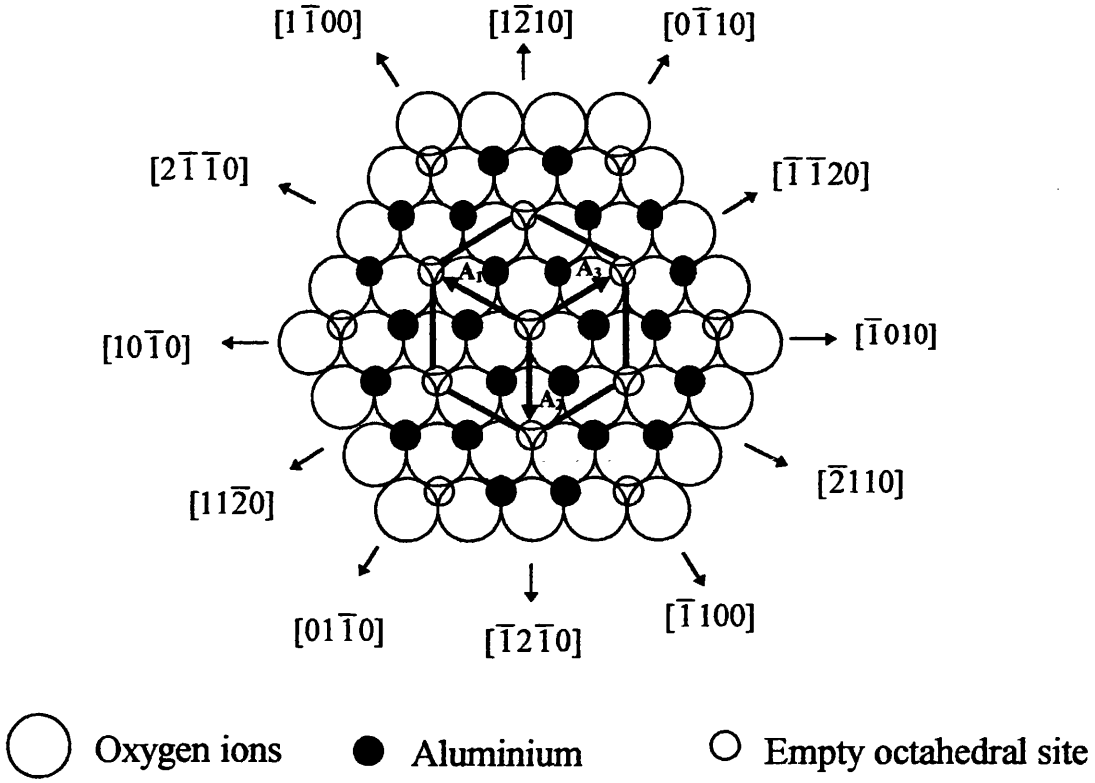

Fig. 6.1 Packing for Al and O ions in the basal plane. The upper layer of O ions is not shown. Basal hexagonal cell vectors and directions are indicated — From Kronberg (1957).

and has a large Young's modulus ($\approx$ 400 GNm^{-2}) (Morrell 1987). It retains its strength even at very high temperature ($\approx$ 1500-1700°C) (Dörre, 1984). One unfavourable property of α-Al_2O_3 is its great brittleness: a complete absence of any plastic deformation until about 1200°C (Dörre, 1984).

In its pure form alumina oxide is a very good insulator and retains its high electrical resistivity up to very high temperatures. The purest α-Al_2O_3 available contains greater than 1ppm per impurity, the electrical properties up to 1600°C are therefore impurity dominated; the intrinsic properties have never been observed and have only been deduced from the properties of doped, compensated material (Kröger, 1984). The electrical conductivity of high purity single crystal α-Al_2O_3 sample was measured along the c-axis in a temperature range from 400°C to 1300°C by Will et al.(1992A). The total impurity content of the sample they used was less

than 35 ppm. This material exhibited a conductivity of 10^{-16} $\Omega^{-1}\cdot cm^{-1}$ at 400°C and 3×10^{-8} $\Omega^{-1}\cdot cm^{-1}$ at 1300°C. It was found that the conductivity of high purity single crystal α-Al_2O_3 parallel to the c-axis is a factor 3.3 higher than that perpendicular to the c-axis (Will et al., 1992B). In ceramic alumina the absolute value of conductivity is considerably greater (up to a factor of 10^4) than in single crystals. A summary of experimental data on the temperature dependence of the electrical conductivity of both single crystal and ceramic α-Al_2O_3 has been given by Dörre (1984).

For a rhombohedral material such as single crystal α-Al_2O_3, distinctly anisotropic thermal and elastic behaviours are expected. Such anisotropic thermal and elastic behaviour accounts for thermal stresses and thermal microcracks found in ceramic aluminas. The relative linear thermal expansions of a ceramic α-Al_2O_3 and of single crystal α-Al_2O_3 parallel and perpendicular to the c-axis were determined between 100 and 1100K by Wachtman et al.(1962). It was found that thermal expansion parallel to the c-axis is about 10% larger than that perpendicular to the c-axis between 100 and 800°C. The elastic constants of single crystal α-Al_2O_3 measured by Wachtman et al.(1960) are listed in table 6.1. A detailed description of the elastic constants of ceramic α-Al_2O_3 is given in Chapter 8.

Table 6.1 The elastic constants of single crystal α-Al_2O_3 measured at room temperature by Wachtman et al. Units are 10^{12} dyn/cm^2.

C_{11}	C_{12}	C_{13}	C_{14}	C_{33}	C_{44}
4.968	1.636	1.109	-0.235	4.981	1.474

Chapter 7 The Effects of Microstructure of Ceramic Aluminas on the Elastic Anisotropy

7.1 Introduction

The microstructure of ceramics can be affected by the manufacturing process; for example, uniaxial pressing can introduce a residual stress with a preferential direction in the sample, which can introduce anisotropic characteristics into the sample. Manufacture involving a uniaxial procedure could also cause the grains to be aligned with a distribution of their c-axes at angles to a particular direction in the sample. Such grain alignment can introduce anisotropy into the sample. The effects of microstructure on the elastic anisotropy of the ceramic aluminas were analysed using a combination of the ultrasonic, X-ray diffraction and scanning electron microscopy.

7.2 The results of X-ray diffraction of alumina ceramics

7.2.1 The samples and experimental procedures

The cubic samples of alumina ceramics D999, AL23, D975, H880 and SINC53 were used in the X-ray diffraction studies. The size of alumina ceramic SINC53 is 13×13×13 mm^3 while the size of others are 15×15×15 mm^3. They are the same samples used in the ultrasonic work. A Philips X-ray diffractometer utilising Philips PW1730/00 4kW x-ray generator, Philips PW1820/00 long fine focus 2kW copper target X-ray tube operated at 40kV and 25 mA and computer controlled vertical diffractometer goniometer were used. All the data were taken at room temperature.

7.2.2 The preferred c-axis orientation of α-Al_2O_3 grains in ceramic aluminas D975 and H880

The X-ray diffraction spectra of samples D975 and H880 taken for different directions at room temperature are shown in Figs. 7.1 and 7.2. Previously the angles between the c-axis and six planes of α-Al_2O_3 were calculated by Akatsu et al. (1994) as follows: $(10\bar{1}4)$: 76.0°; $(11\bar{2}6)$: 71.6°; $(1.0.\bar{1}.10)$: 84.3°; $(11\bar{2}0)$: 0°; $(11\bar{2}3)$: 56.3°; $(03\bar{3}0)$: 0°. From the data shown in Figs. 7.1 and 7.2, it can been seen that planes which make a comparatively large angle to the c-axis of α-Al_2O_3 are preferentially oriented in the Z direction of the sample and planes whose angle to the c-axis is small are preferentially oriented in the direction perpendicular to the Z direction. Therefore, it is concluded that in both D975 and H880 the c-axis of α-Al_2O_3 grains has preferred orientation in the Z direction.

For the X-ray directed onto the sample surface perpendicular to the Z direction, the ratio of peak heights diffracted by $(10\bar{1}4)$ plane, the angle of which between the c-axis is 76.0°, to that of the peak diffracted by $(11\bar{2}0)$ plane, the angle of which between the c-axis is 0°, is 3.01 for D975, while this ratio is 3.44 for H880. Therefore, the degree of anisotropy in sample D975 is smaller than that in sample H880.

7.2.3 The lack of preferred c-axis orientation of α-Al_2O_3 grains in ceramic aluminas D999 and AL23

The X-ray diffraction spectra of samples D999 and AL23 with various directions at room temperature are shown in Figs. 7.3 and 7.4. From the data shown in these two figures it can be seen that within the limits of experimental error (that is $\sqrt{counts}$) the relative peak height is not

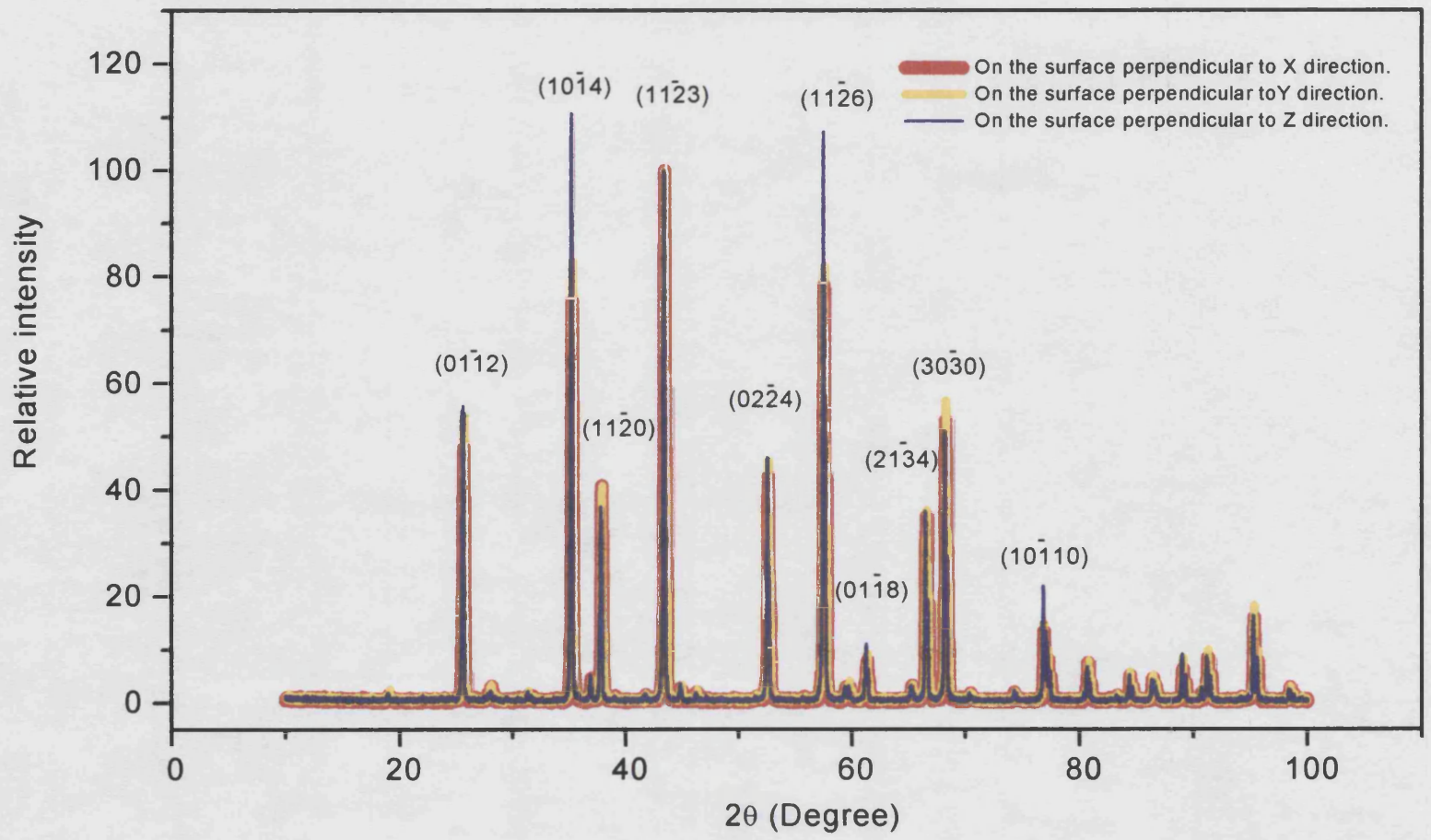

Fig. 7.1 The X-ray diffraction spectrum of ceramic alumina D975 at room temperature.

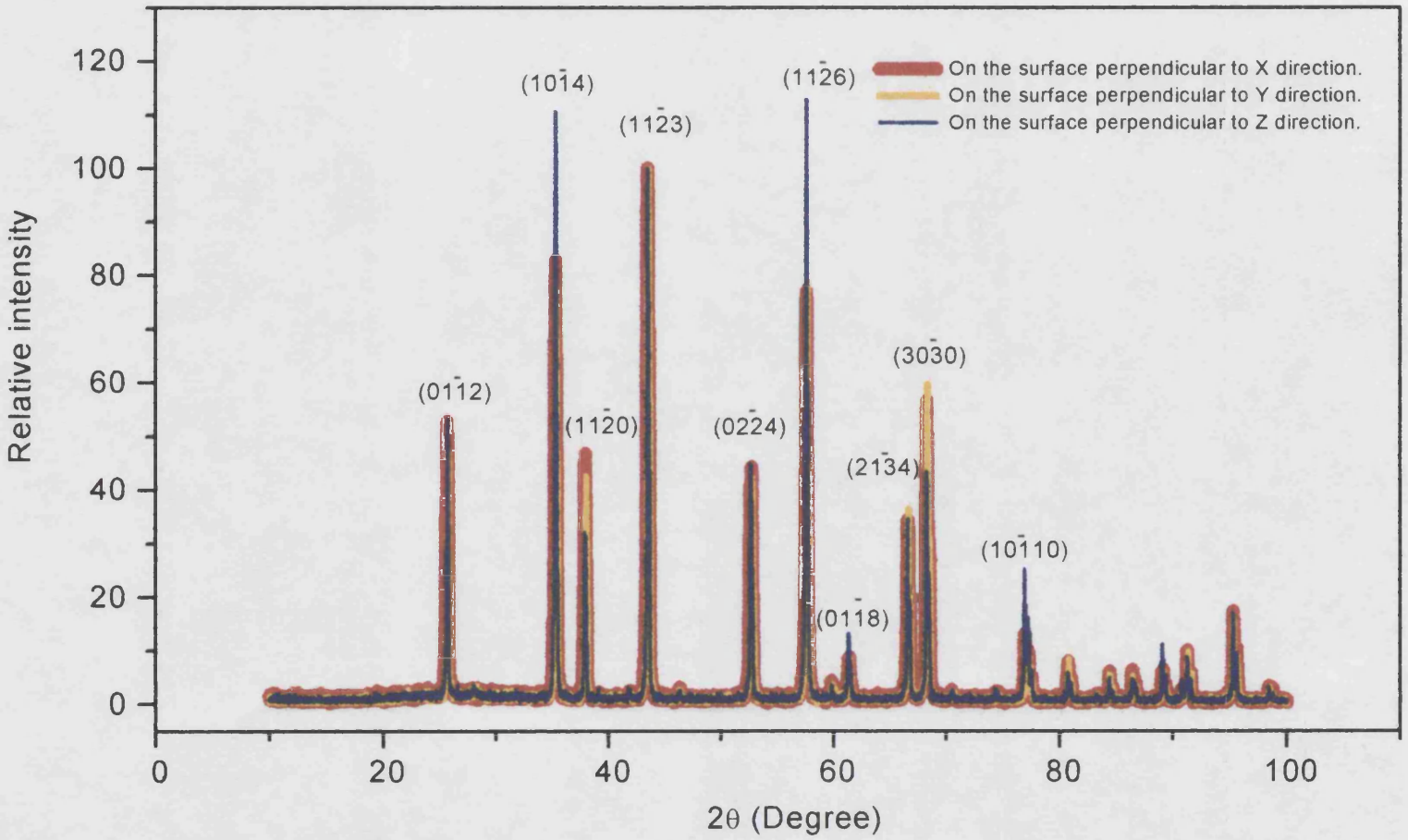

Fig. 7.2 The X-ray diffraction spectrum of ceramic alumina H880 at room temperature.

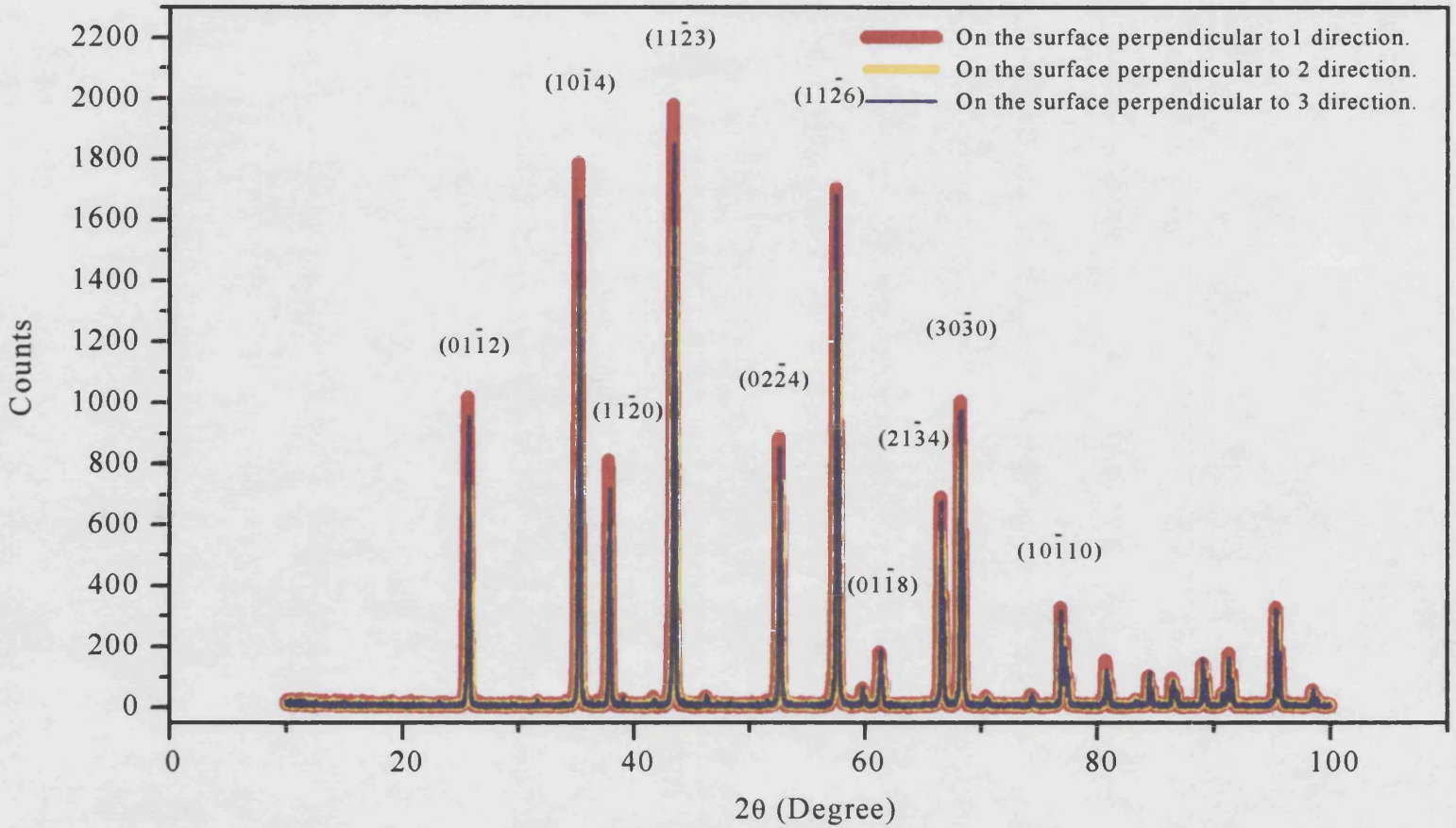

Fig. 7.3 The X-ray diffraction spectrum of ceramic alumina D999 at room temperaure.

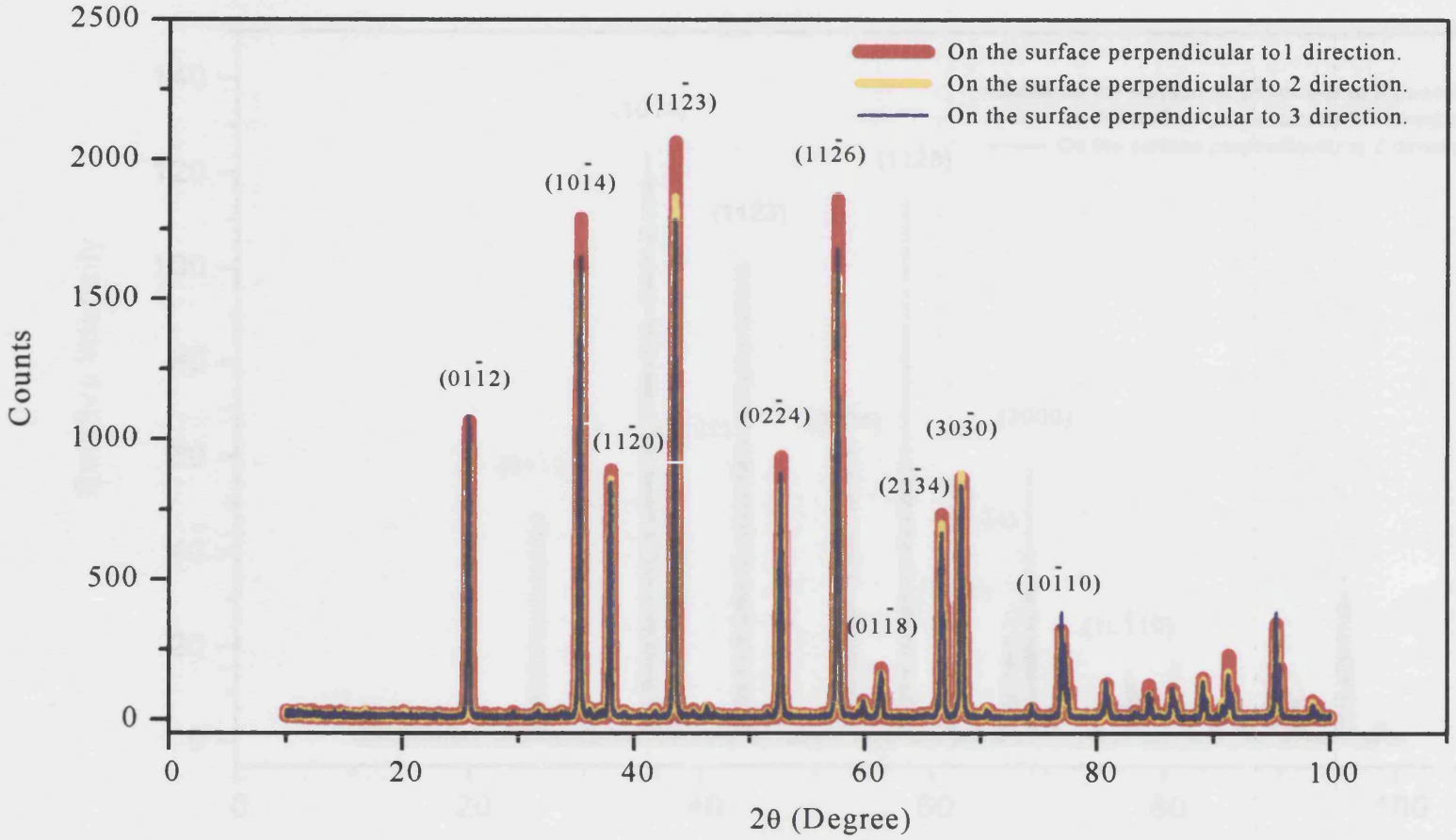

Fig. 7.4 The X-ray diffraction spectrum of ceramic alumina AL23 at room temperature.

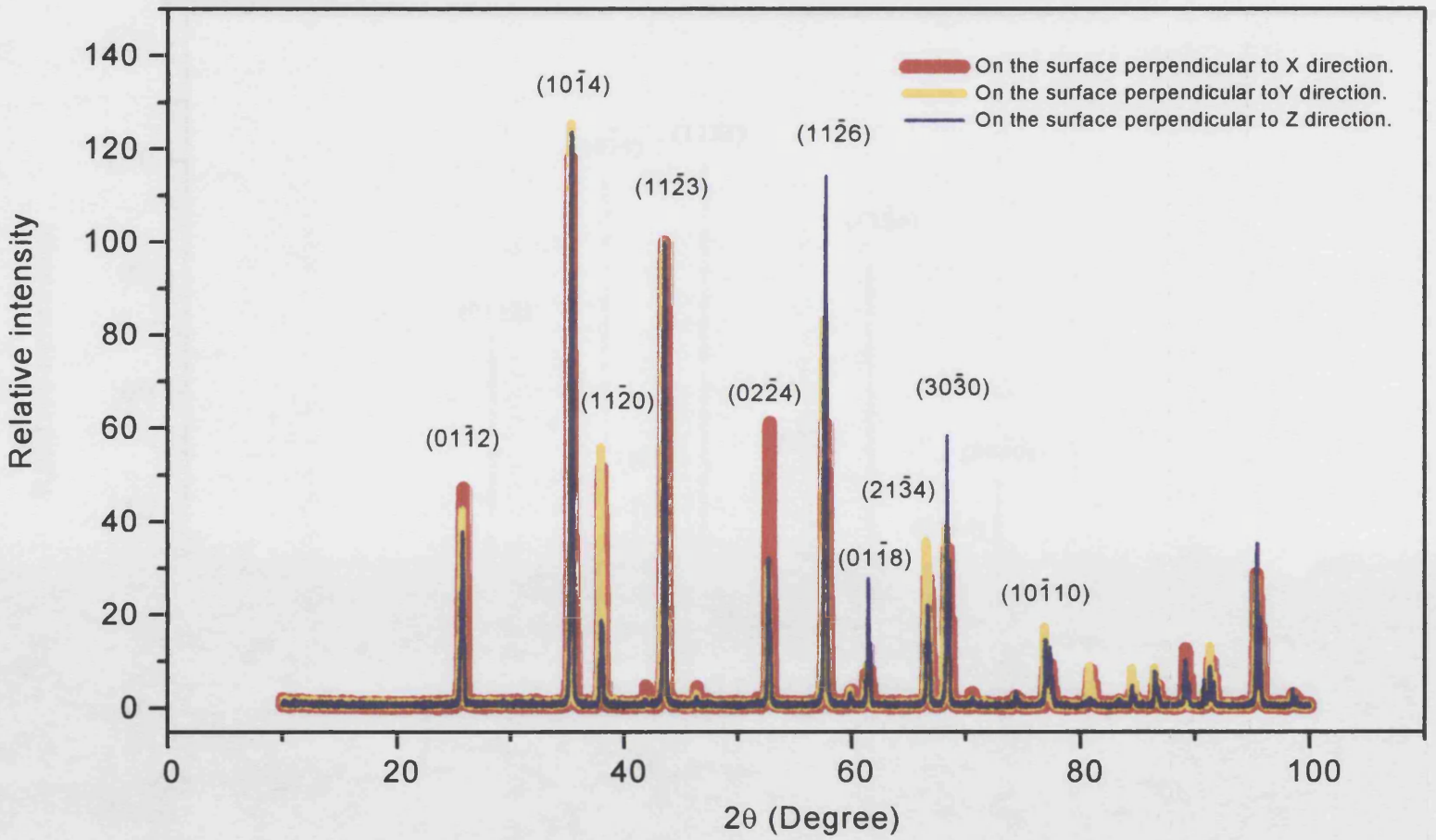

Fig. 7.5 The X-ray diffraction spectrum of ceramic alumina SINC53 at room temperature.

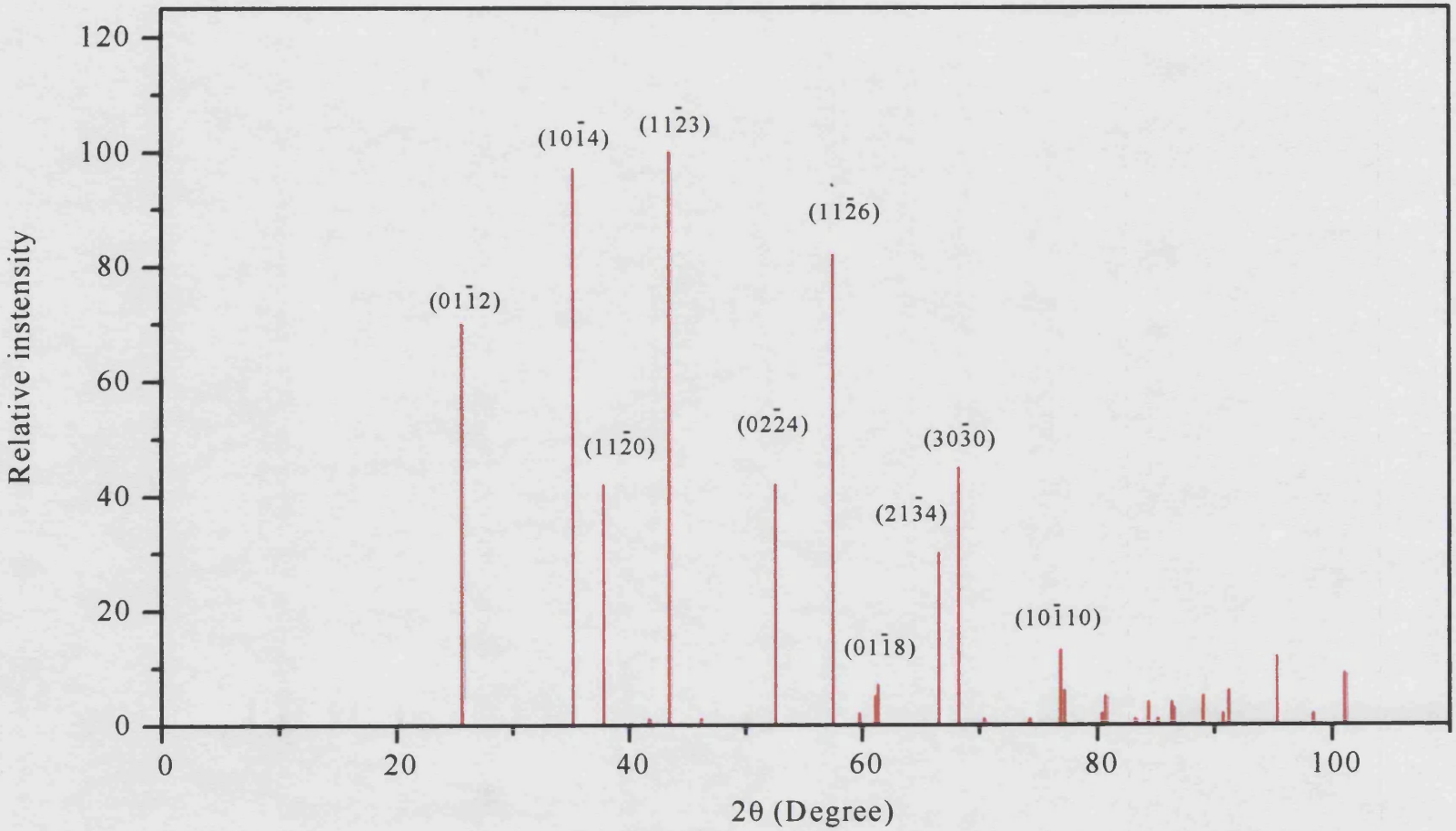

Fig. 7.6 The standard X-ray diffraction spectrum of α-Alumina at room temperature.

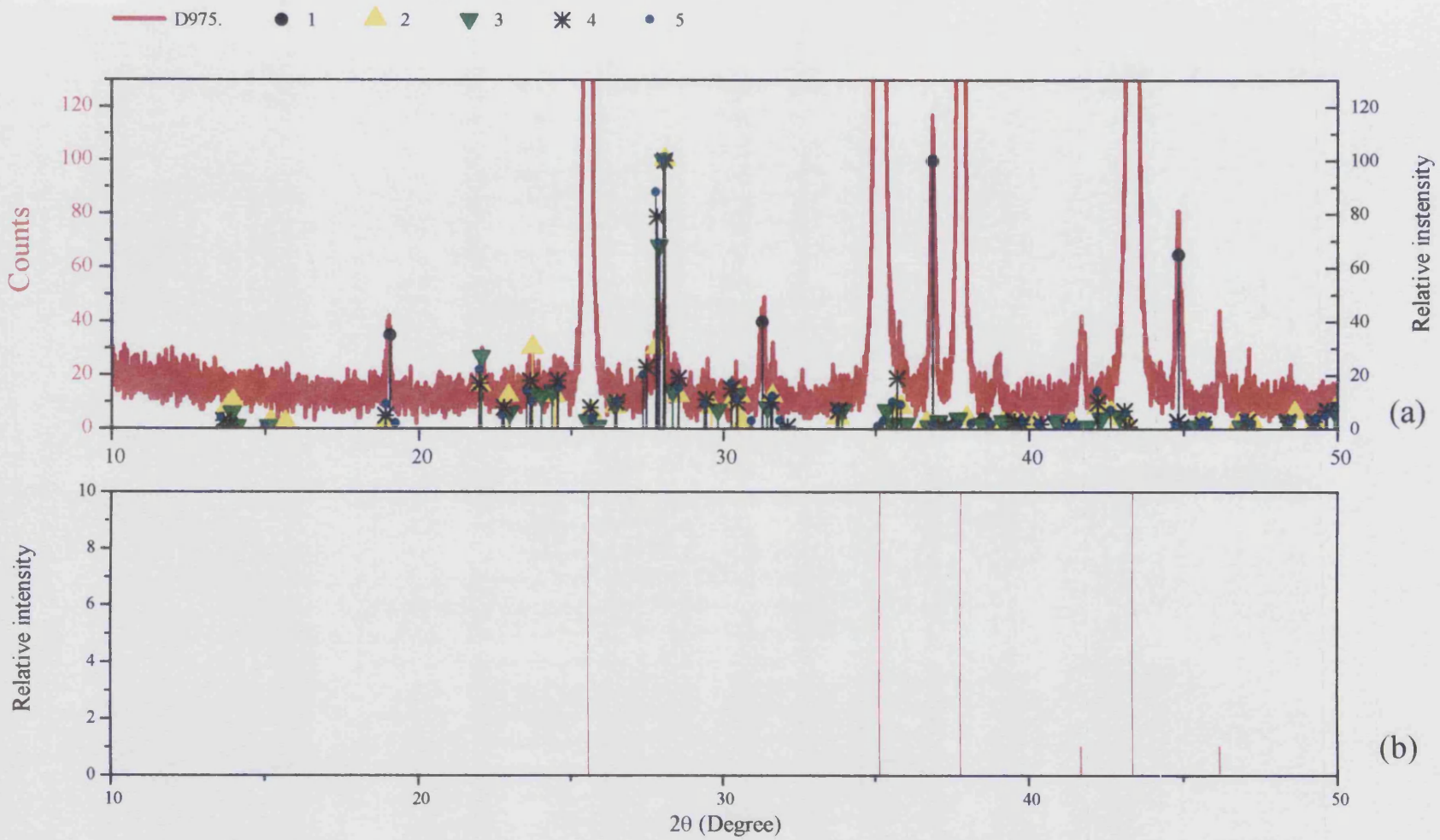

Fig. 7.7 (a) Enlargement of X-ray diffraction spectrum of ceramic alumina D975 and standard X-ray diffraction spectra of five crystallines listed in this report between 10 and 50 degree.
(b) The standard X-ray diffraction spectrum of α-Alumina between 10 and 50 degree.

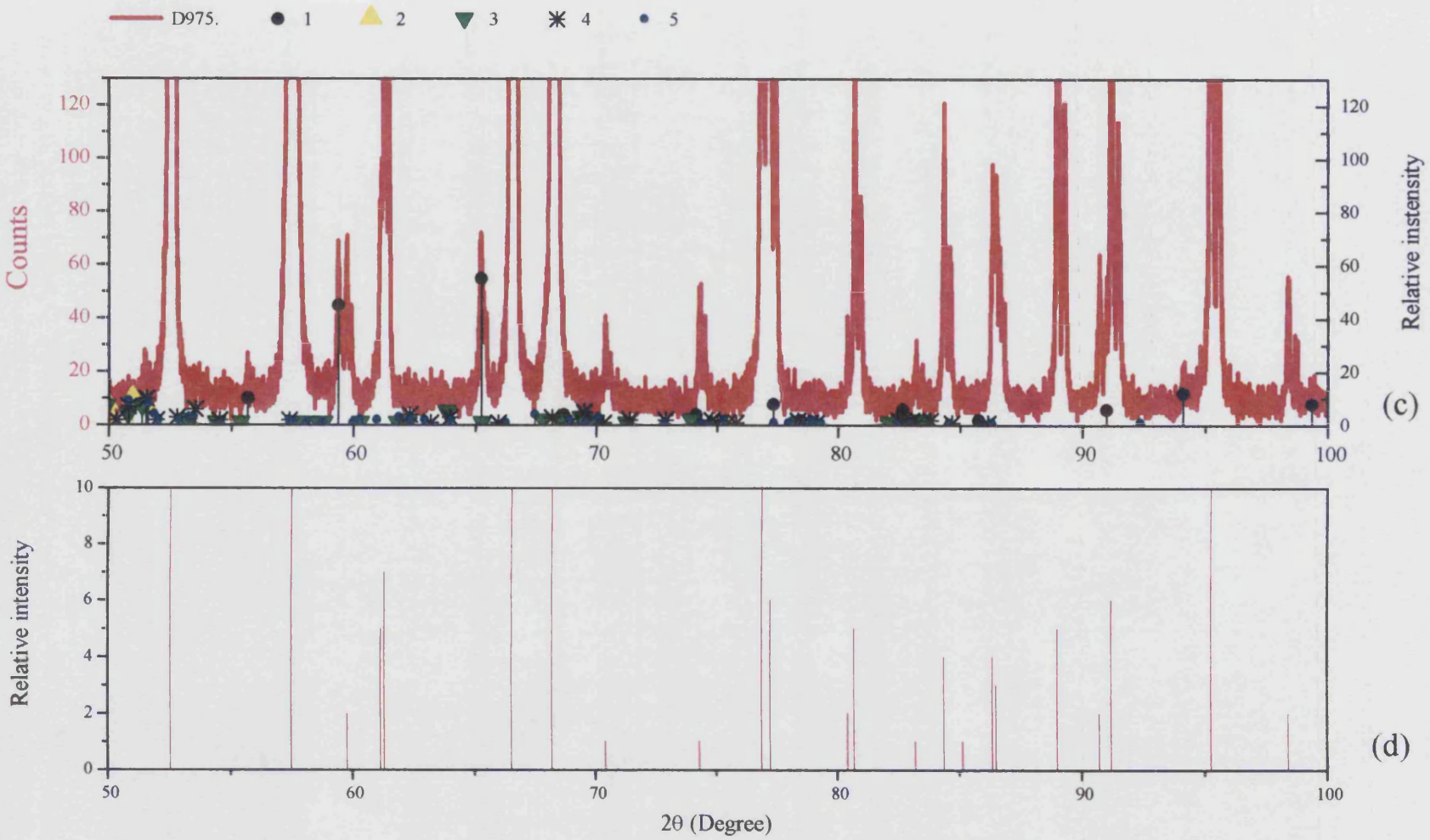

Fig. 7.7 (c) Enlargement of X-ray diffraction spectrum of ceramic alumina D975 and standard X-ray diffraction spectra of five crystallines listed in this report between 50 and100 degree.
(d) The standard X-ray diffraction spectrum of α-Alumina between 50 and100 degree.

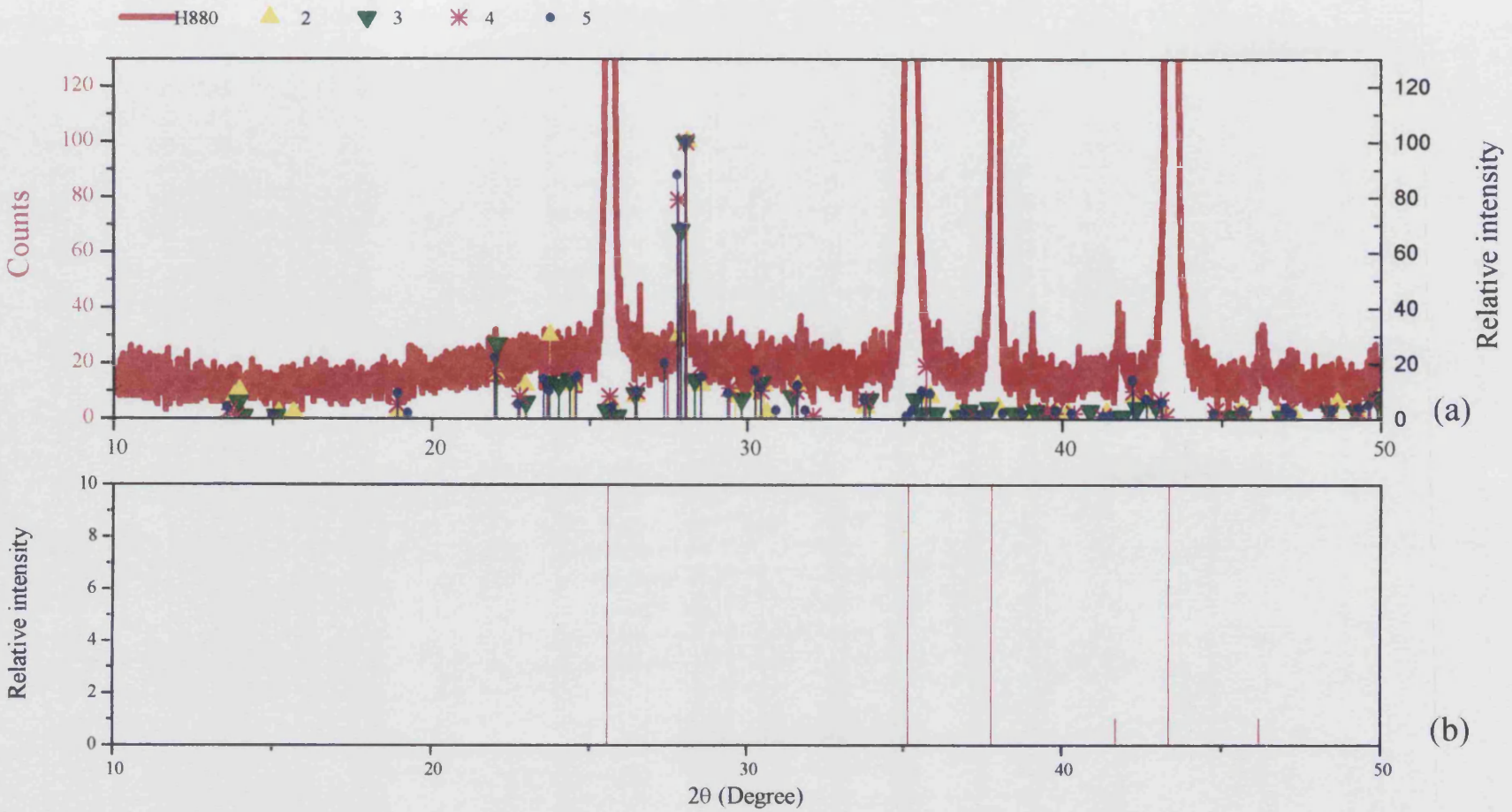

Fig. 7.8 (a) Enlargement of X-ray diffraction spectrum of ceramic alumina H880 and standard X-ray diffraction spectra of four crystallines listed in this report between 10 and 50 degree.
(b) The standard X-ray diffraction spectrum of α-Alumina between 10 and 50 degree.

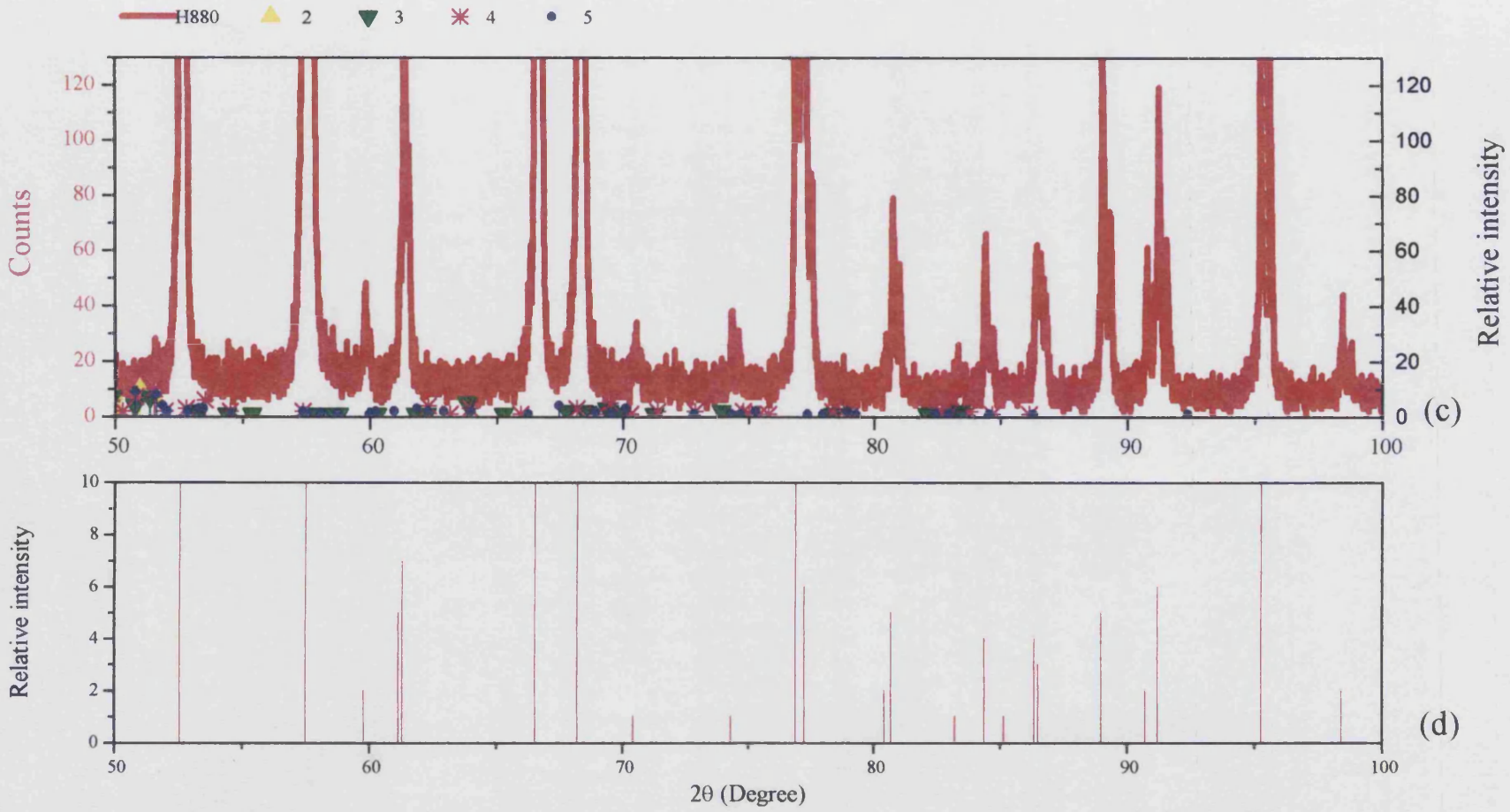

Fig. 7.8 (c) Enlargement of X-ray diffraction spectrum of ceramic alumina H880 and standard X-ray diffraction spectra of four crystallines listed in this report between 50 and 100 degree.
(d) The standard X-ray diffraction spectrum of α-Alumina between 50 and 100 degree.

4. Sodium Calcium Aluminium Silicate /Anorthite, sodian, disordered (Ca,Na) (Si, Al)$_4$O$_8$

5. Calcium Aluminium Silicate / Anorthite, ordered, Ca Al_2 Si_2 O_8

Figs. 7.7(b, d), 7.8(b,d), 7.9(b,d), 7.10(b,d) and 7.11(b,d) each show the standard X-ray diffraction spectrum of α-alumina on an enlarged scale. From the data shown in Fig. 7.7 it has been found that there are at least two crystalline second phases in sample D975. One of them is spinel ($MgAl_2O_4$). It is also possible that in sample D975 there are one or more of 2, 3, 4, and 5 crystalline second phases listed above. As shown by data in Figs. 7.8 the sample H880 has at least one crystalline secondary phase. The crystalline second phases in sample H880 could be one or more of 2, 3, 4, and 5 crystalline second phases listed above. By comparing the data shown in Fig. 7.9 (a,c) to those shown in (b,d), the data shown in Fig. 7.10 (a,c) to those shown in (b,d) and the data shown in Fig. 7.11 (a,c) to those shown in(b,d), it can been found that the samples D999, AL23 and SINC53 have at least one crystalline secondary phase. Due to the shortage of information about the additions included in the samples during manufacture, it is difficult to establish what kind of compounds constitute the crystalline secondary phases in sample AL23. From the data shown in Fig.7.9 and 7.11, it can be shown that ceramic aluminas D999 and SINC53 contain a very small amount of crystalline secondary phase; what kind of compounds may be present is not known: they are at a composition less than the detectable limits of X-ray diffraction spectra measurements.

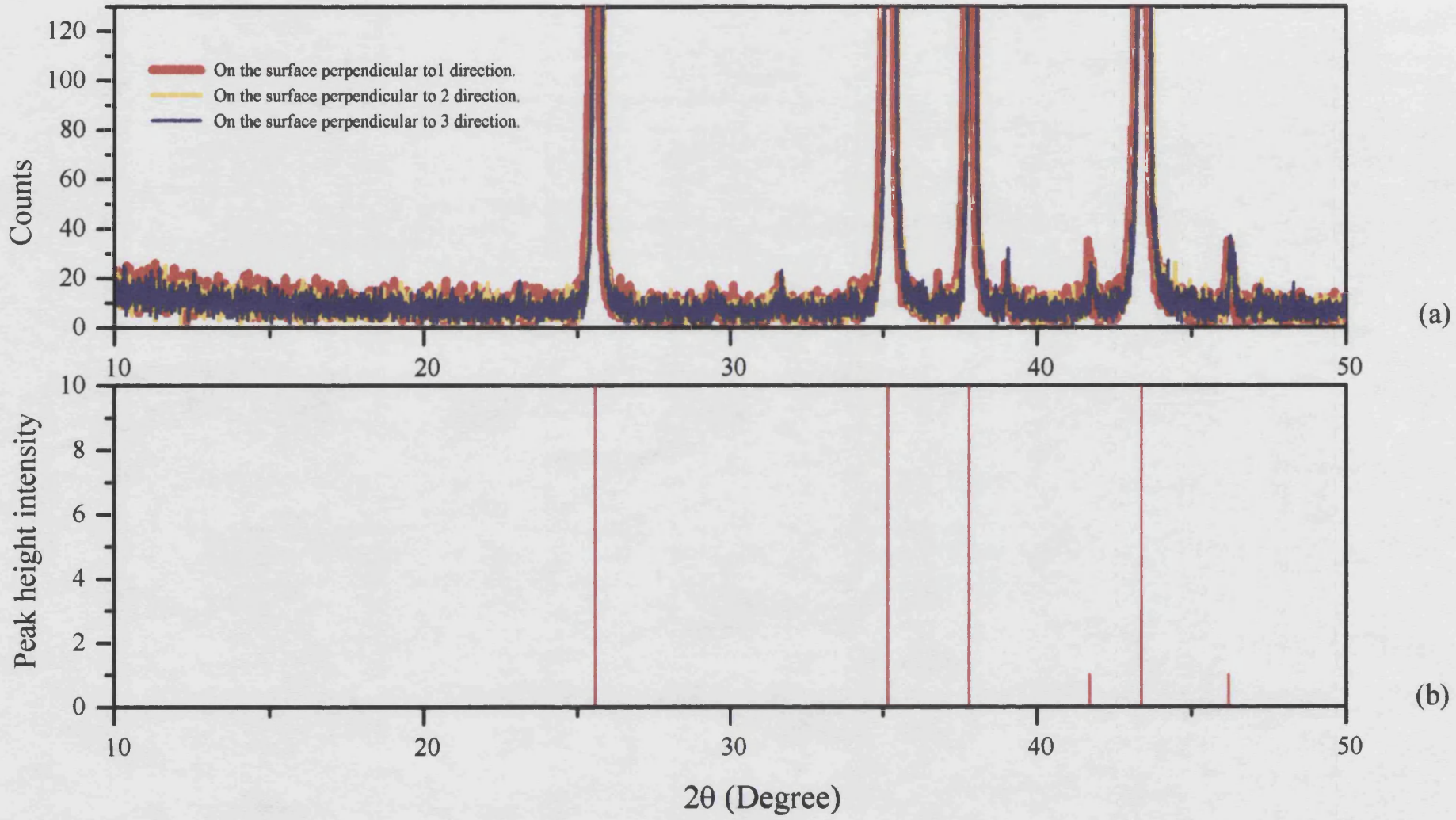

Fig. 7.9 (a) Enlargement of X-ray diffraction spectrum of ceramic alumina D999 between 10 and 50 degree.
(b) The standard X-ray diffraction spectrum of α-Alumina between 10 and 50 degree.

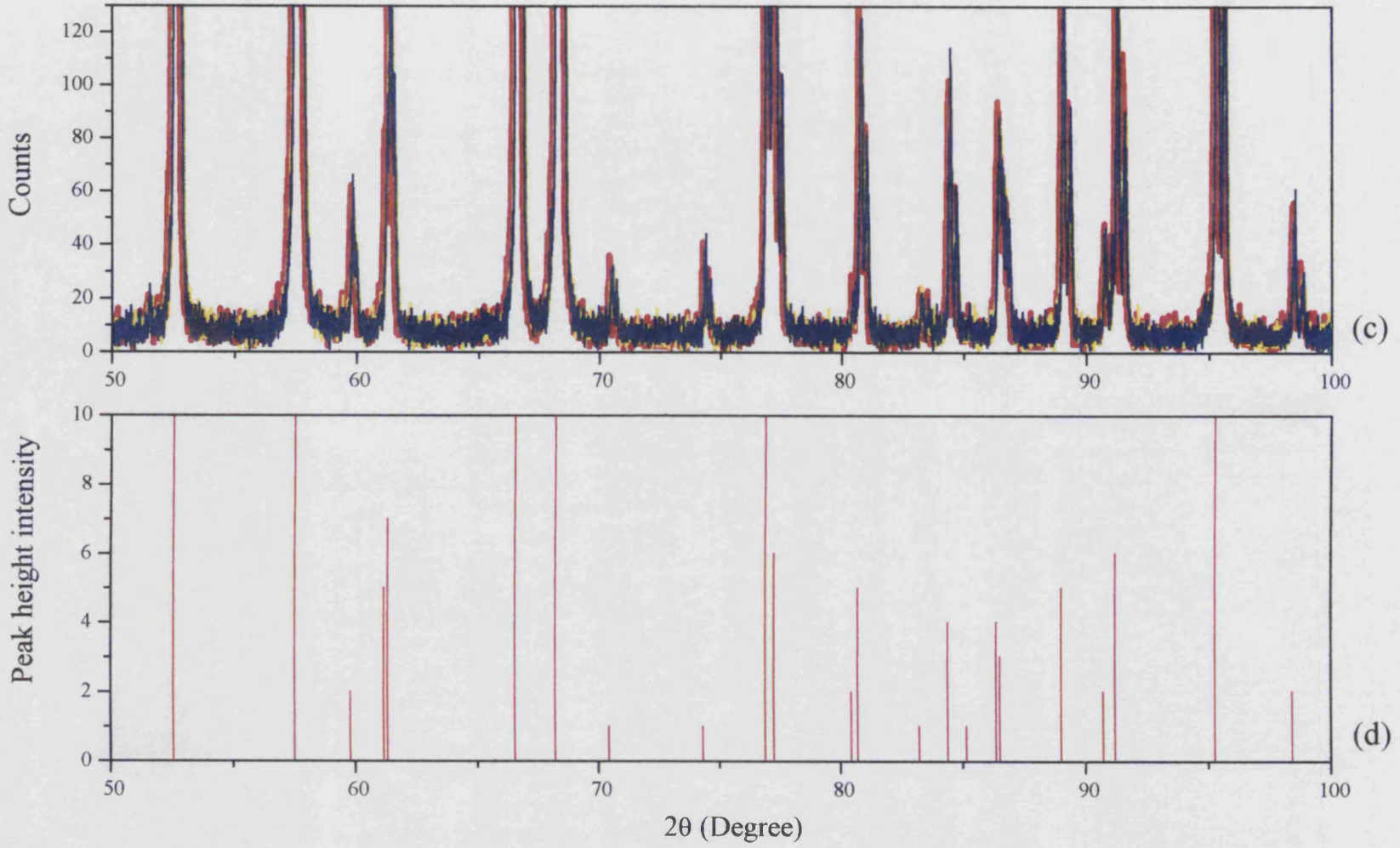

Fig. 7.9 (c) Enlargement of X-ray diffraction spectrum of ceramic alumina D999 between 50 and 100 degree.
(d) The standard X-ray diffraction spectrum of α-Alumina between 50 and 100 degree.

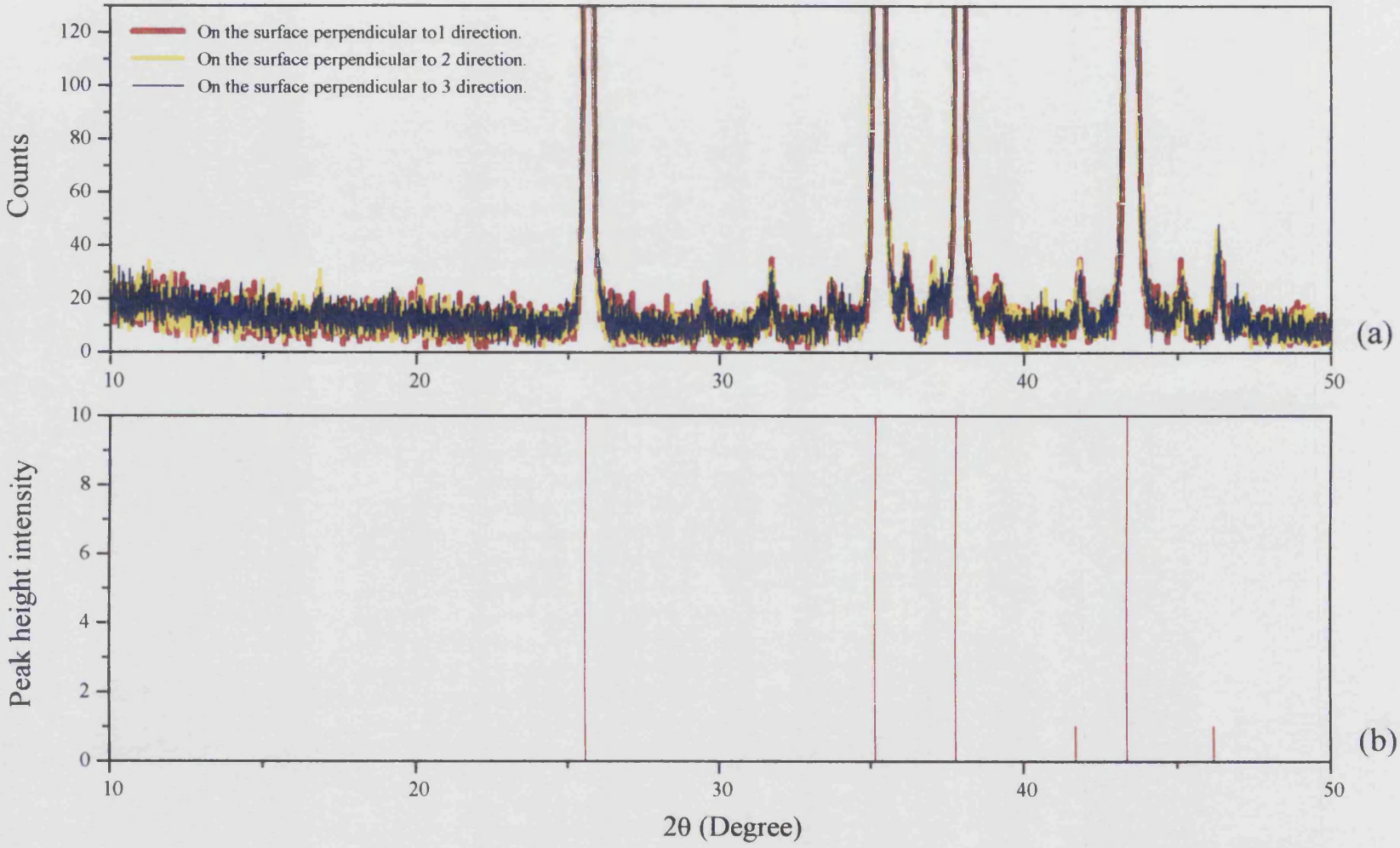

Fig.7.10 (a) Enlargement of X-ray diffraction spectrum of ceramic alumina AL23 between 10 and 50 degree.
(b) The standard X-ray diffraction spectrum of α-Alumina between 10 and 50 degree.

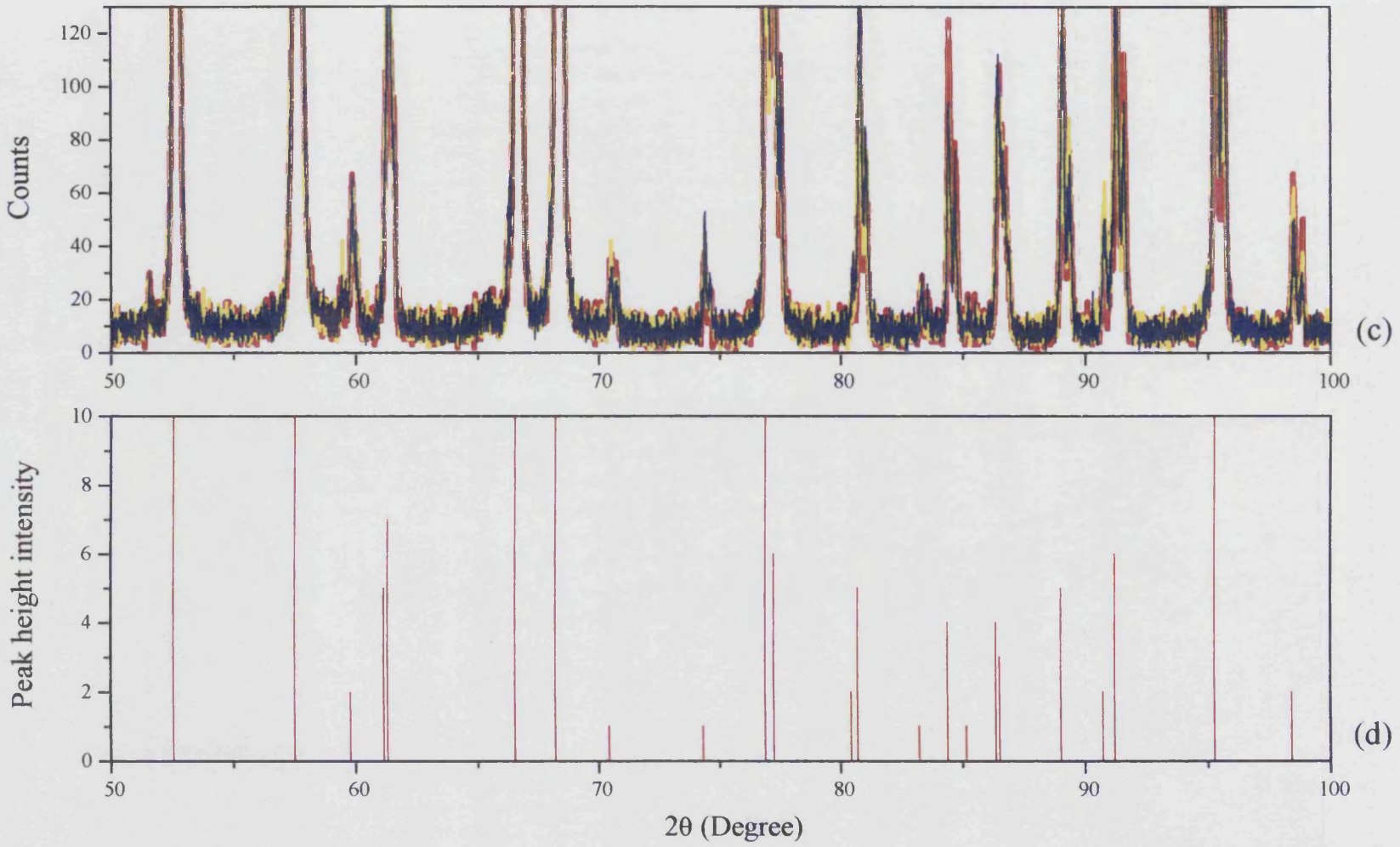

Fig.7.10 (c) Enlargement of X-ray diffraction spectrum of ceramic alumina AL23 between 50 and 100 degree.
(d) The standard X-ray diffraction spectrum of α-Alumina between 50 and 100 degree.

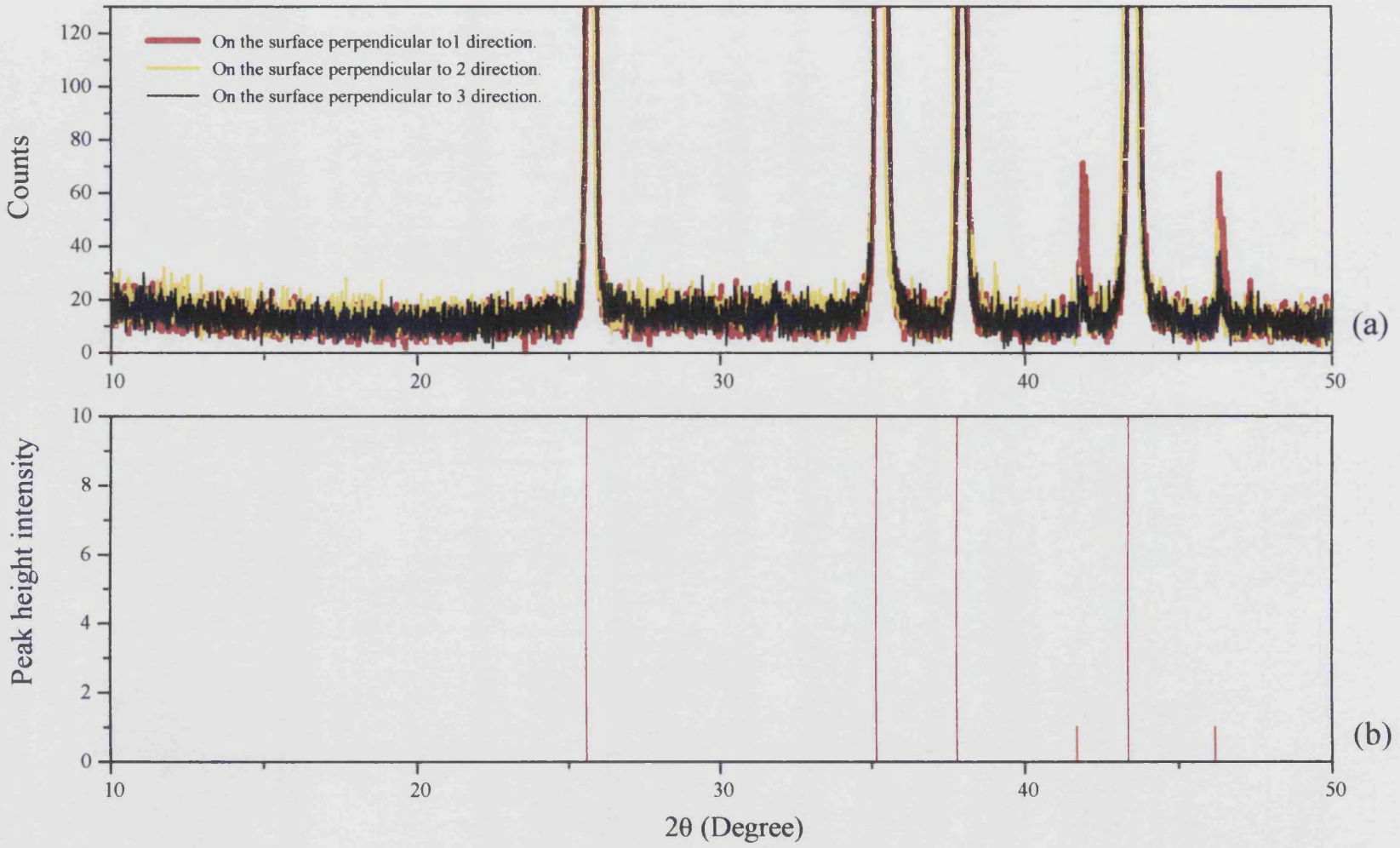

Fig. 7.11 (a) Enlargement of X-ray diffraction spectrum of ceramic alumina SINC53 between 10 and 50 degree.
(b) The standard X-ray diffraction spectrum of α-Alumina between 10 and 50 degree.

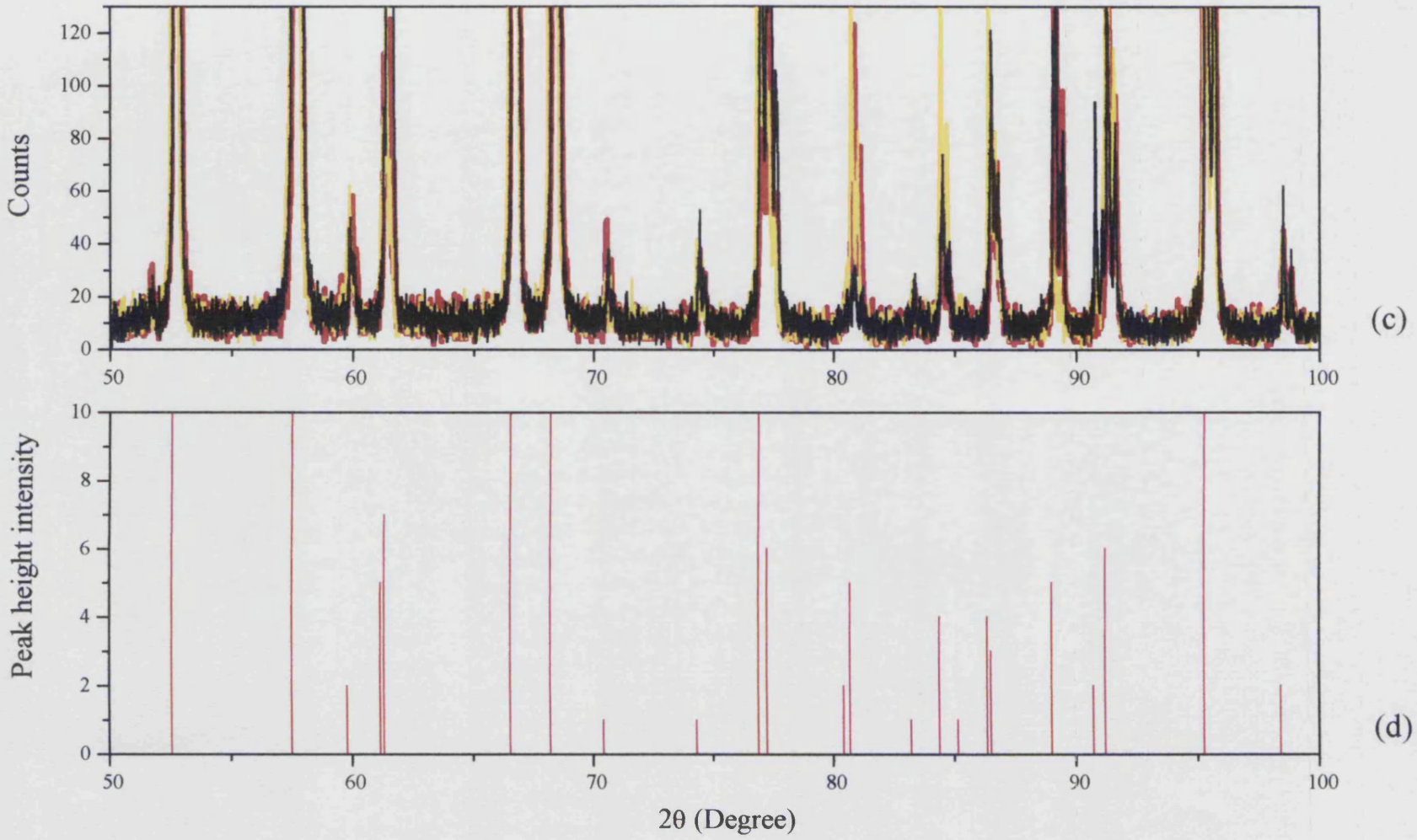

Fig. 7.11 (c) Enlargement of X-ray diffraction spectrum of ceramic alumina SINC53 between 50 and 100 degree.
(d) The standard X-ray diffraction spectrum of α-Alumina between 50 and 100 degree.

7.3 The microstructures of ceramic aluminas observed by using scanning electron microscopy (SEM)

7.3.1 Sample preparation and experimental procedures

The 15×15×15 mm^3 cubic samples of ceramic aluminas D999 and AL23 were cut into three pieces, respectively, with a diamond saw. One of the faces of each piece was polished, finishing with a 0.5μm diamond polish. The polished faces were perpendicular to the directions 1, 2, and 3, respectively. The 15×15×15 mm^3 cubic samples of ceramic alumina D975 and H880 and the 13×13×13 mm^3 cubic sample of SINC53 were cut into two pieces. One of the faces of each piece was polished, finishing with a 0.5μm diamond polish. The polished faces for the samples of D975, H880 and SINC53 were parallel and perpendicular to directions Z, respectively. The polished samples were thermally etched at 1450°C for 30 minutes (Carisey 1995). Because the samples are not good electrical conductors, a thin gold layer (about 10 nm) was sputtered onto the polished surfaces to prevent charging (Cahn, 1992). A JEOL (Japanese Electron Optic Ltd) JSM6310 SEM was used. SEM images were obtained using the secondary electron image mode. All the SEM images are performed at 15kV.

7.3.2 The SEM images of ceramic aluminas D999 and AL23

The SEM images in Fig. 7.12 and 13 show the microstructure of the ceramic alumina D999 and AL23, respectively; (a), (b) and (c) are the images obtained from the surfaces perpendicular to the directions 1, 2, and 3, respectively. In both Figs. 7.12 and 13, the images shown in (a), (b) and (c) have the same characteristics. This means that the microstructures of the ceramic alumina D999 and AL23 are isotropic in the error range of the

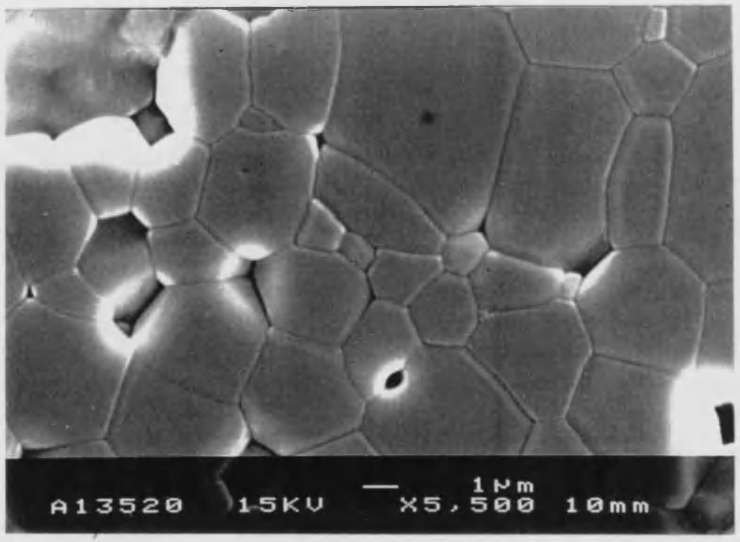

(a)

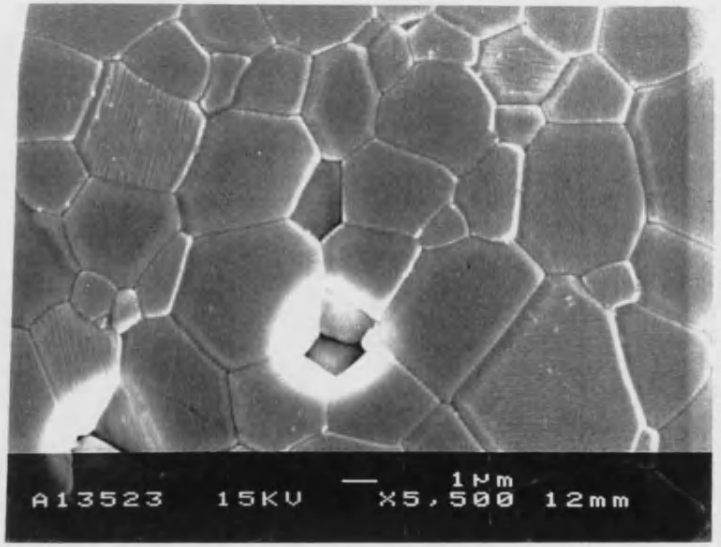

(c)

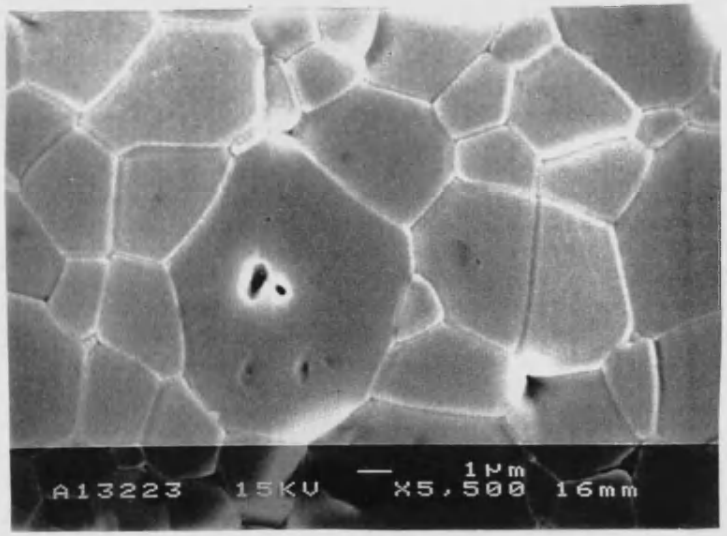

(b)

Fig. 7.12 SEM images showing the microstructure of ceramic alumina D999.

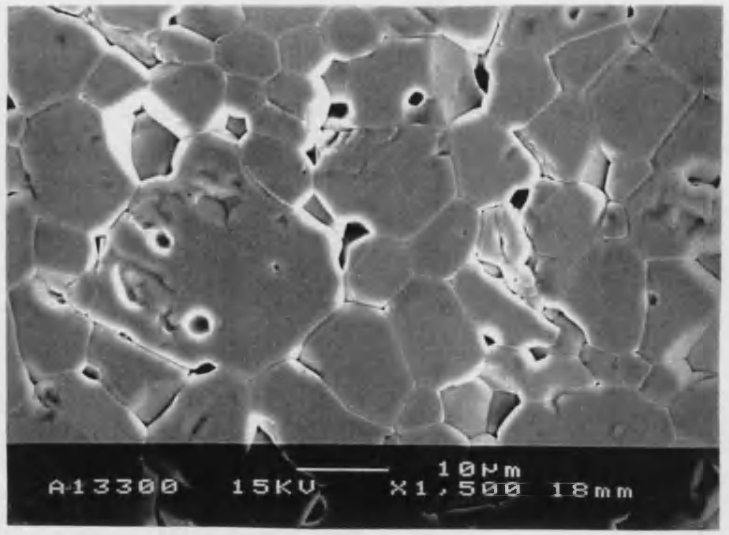

(a)

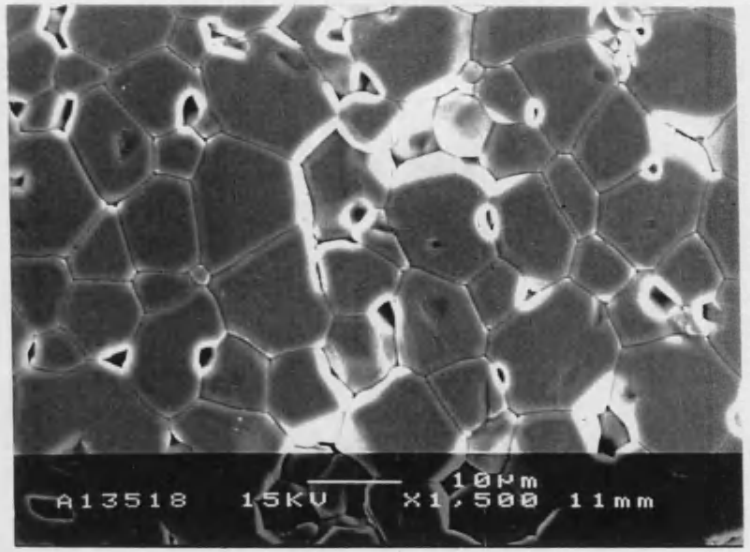

(c)

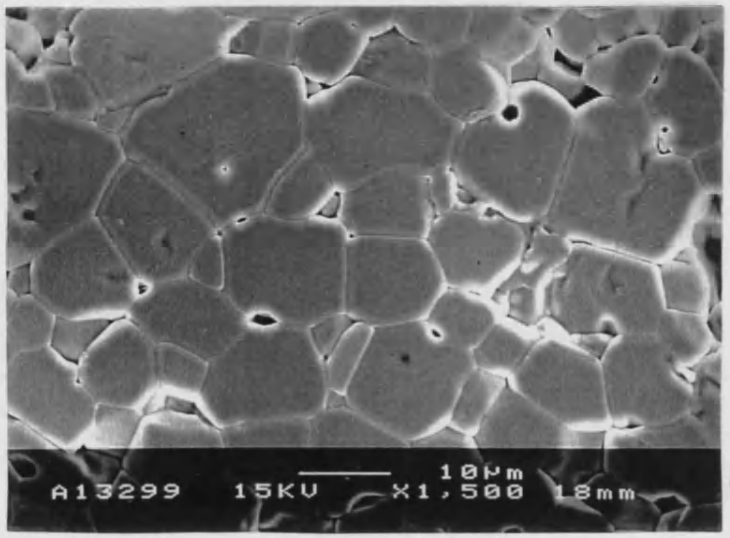

(b)

Fig. 7.13 SEM images showing the microstructure of ceramic alumina AL23.

SEM. The SEM images in Figs.7.12 and 13 show that both the ceramic aluminas D999 and AL23 have equi-axed grains and a rather homogeneous distribution of grain size. The average grain sizes of ceramic alumina D999 and AL23 are approximately 3-4μm and 10 μm respectively (Fig. 7. 12 and 13).

7.3.3 The SEM images of ceramic aluminas D975, H880 and SINC53

Fig 7.14 (a) and (b) show SEM images of the surface perpendicular to direction Z of the ceramic alumina D975, while Fig 7.14 (c) and (d) are images of a surface parallel to this direction. The Z direction is indicated in the figures. These images show that the alumina grains are faceted and elongated. These faceted grains appear tabular in two dimensions and the long edges of the grains are preferentially oriented perpendicular to the Z direction to an observable extent (Fig.7.14 (c) and (d)). The smaller grains in Fig.7.14 (c) and (d) show a preferential orientation more clearly than the larger grains do. It is concluded that the grains or some of the grains are platelet with their basal plane preferentially oriented perpendicular to the Z direction. The ceramic alumina D975 has a rather wide distribution of grain size and the average grain sizes is approximately 2-4μm (Fig. 7. 14).

Fig.7.15 (a) and (b) show the SEM images of a surface perpendicular to direction Z of the ceramic alumina H880, while Fig 7.15 (c) and (d) are the images of a surface parallel to Z direction. The images shown in Fig.7.15 have similar characteristics to those observed in the images shown in Fig.7.14. Using the same analysis as described in the above paragraph, it has been found from the images shown in Fig.7.15 that the ceramic alumina H880 has faceted platelet grains with their basal planes preferentially oriented perpendicular to the Z direction; the images show

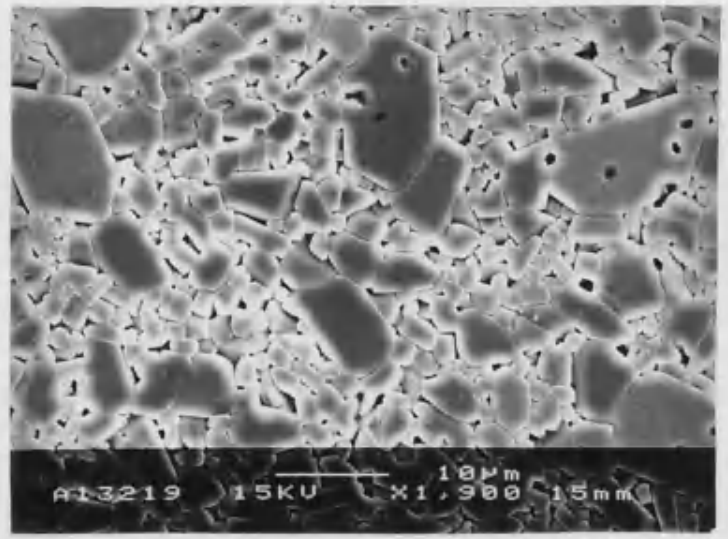

⊗ Z Direction

(a)

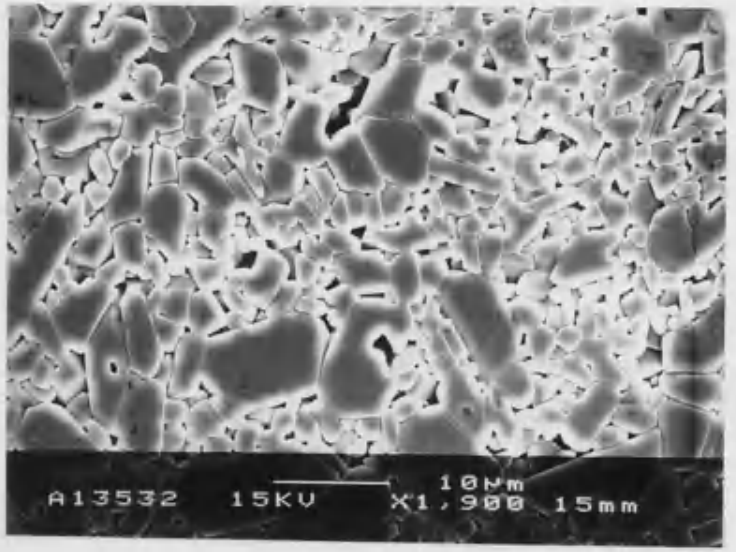

→ Z Direction

(c)

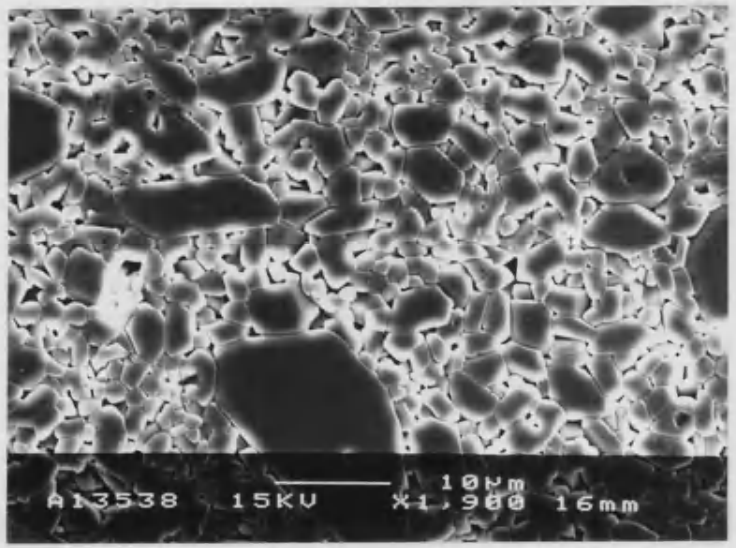

⊗ Z Direction

(b)

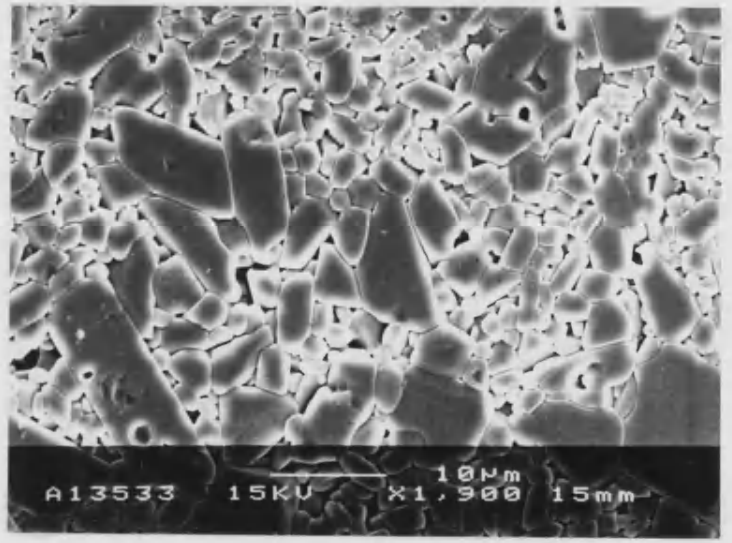

→ Z Direction

(d)

Fig. 7.14 SEM images showing the microstructure of ceramic alumina D975.

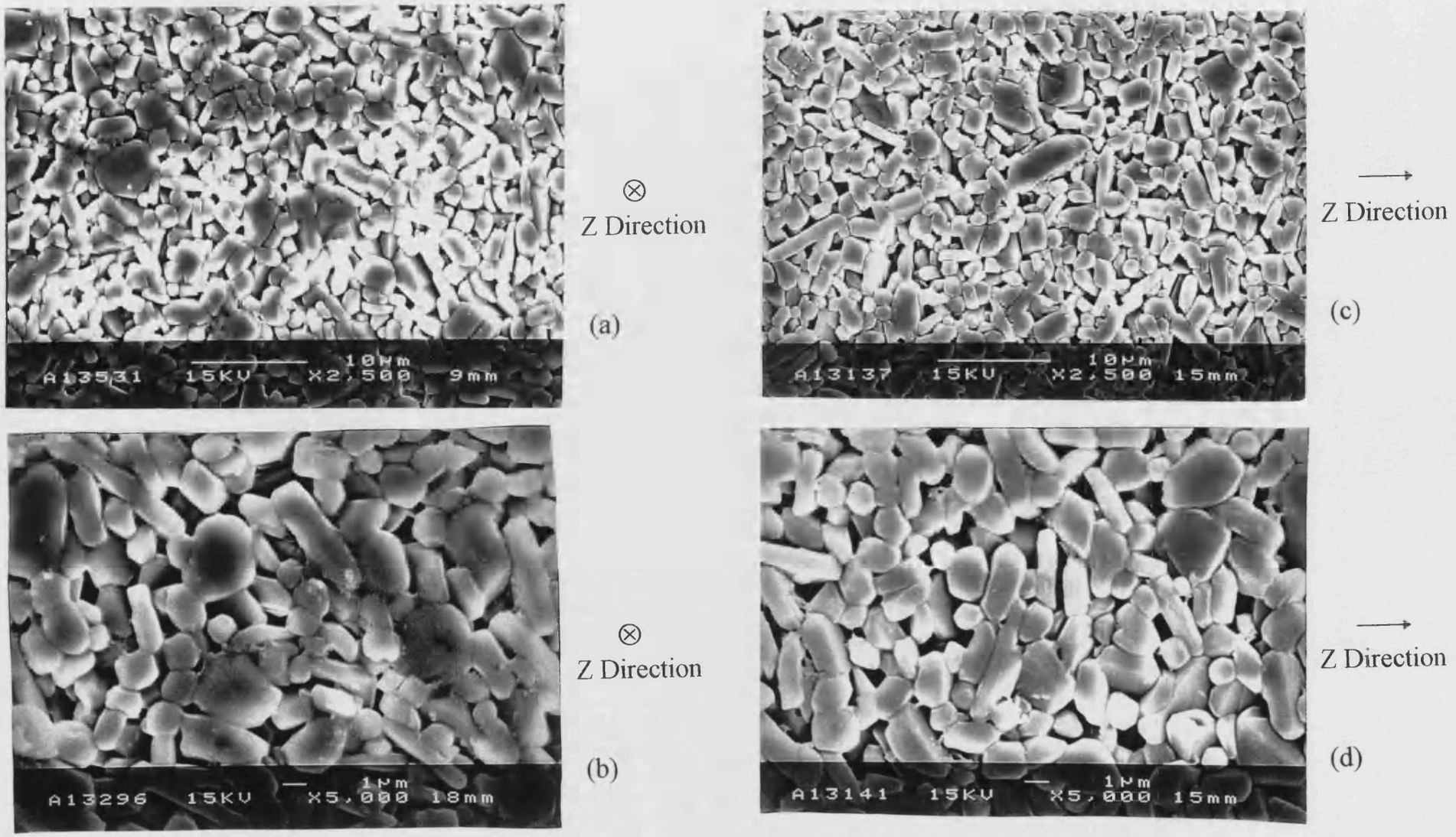

Fig. 7.15 The SEM images showing the microstructure of ceramic alumina H880.

that the ceramic alumina H880 has a rather homogeneous distribution of grain size of about 2-3μm.

Fig.7.16 (a) and (b) show the SEM images of a surface perpendicular to direction Z of the ceramic alumina SINC53; Fig.7.16 (c) and (d) show images of the surface parallel to Z direction. It has been found from the images shown in Fig.7.16 that the ceramic alumina SINC53 has faceted platelet grains with their basal planes preferentially oriented perpendicular to Z direction and the average grain size is about 20-30μm.

7.4 The propagation and polarisation direction dependence of longitudinal and shear velocities in the ceramic aluminas

7.4.1 The samples and experimental procedures

The cubic samples of alumina ceramics D999, AL23, D975, H880 and SINC 53, supplied by the DERA, were used in the this work. The size of alumina ceramic SINC53 is 13×13×13 mm^3 while the size of others are 15×15×15 mm^3. In this part of the work, 10mm X cut and Y cut quartz transducers with fundamental frequencies of 10 MHz have been used to insert and receive ultrasonic pulses. The transducer bonding materials is Dow Resin 276-V9 (Dow-Corp., U.S.A). All the measurements were made at 30±0.5°C. A correction on phase lag caused by multi-reflection between the transducers and the bonding materials (Kittinger 1977) has been applied to the ultrasonic wave velocities.

7.4.2 Propagation and polarisation direction dependence of longitudinal and shear velocities in ceramic alumina D975

Significant modulation in the ultrasonic echo pattern of shear waves has been found when the waves are propagated perpendicular to two pairs of

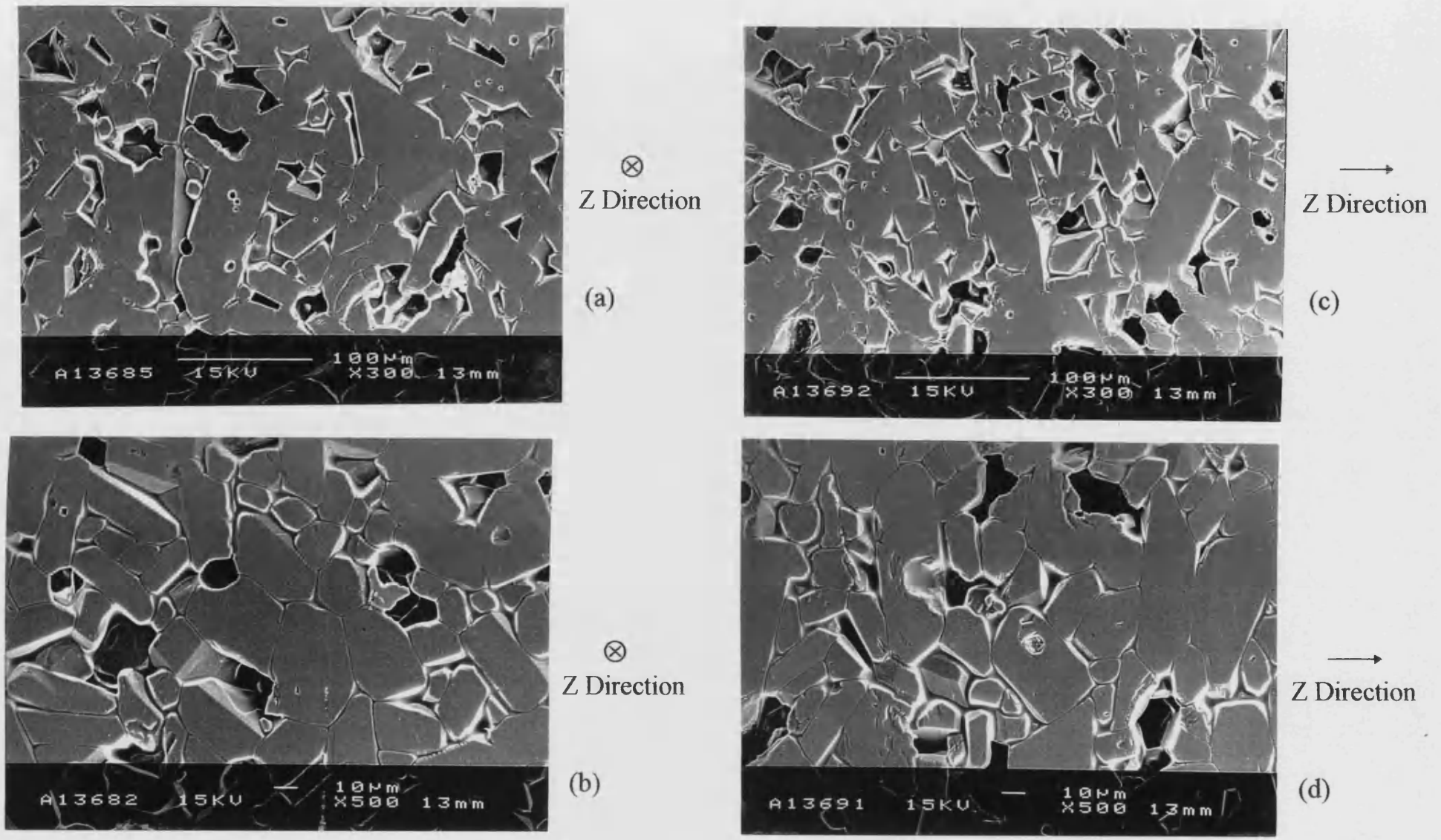

Fig. 7.16 SEM images showing the microstructure of ceramic alumina SINC53.

the faces of sample D975. For convenience, the directions normal to those two pairs are defined as along the X-axis and along the Y-axis respectively. The other direction is defined along the Z-axis.

Fig. 7.17 (a) shows the echo train observed at room temperature on the screen of an oscilloscope when a 30-MHz shear wave is propagated along the X direction with a polarisation parallel to one of the edges of the face of sample D975. The echo pattern is almost exponential. However when the polarisation direction is changed clockwise by 45° about the X-direction, the echo pattern is modulated as shown in Fig. 7.17 (b). A subsequent change of the polarisation direction by 45° clockwise about the X-direction brought back the exponential echo pattern, as shown in Fig. 7.17(c). Fig. 7.17(d) shows the modulated echo pattern when the polarisation direction is changed clockwise by another 45°. The same situation is observed when a shear wave was propagated along the Y axis.

When a shear wave is propagated along the Z axis, the modulation of the echo pattern is less pronounced than along the X and Y axes. Fig. 7.18(a) shows the modulated echo train when the polarisation direction is perpendicular to one of the diagonals of the face in the X-Y plane. After the polarisation direction has been changed anti-clockwise by 45° about the Z axis, i.e. parallel to one of the edges of the sample, the echo pattern in an exponential form is then obtained (Fig. 7.18(b)). The successive change of the polarisation direction by 45° anti-clockwise about the Z axis again causes modulation of the echo train (Fig. 7.18(c)). Fig. 7.18(d) shows the exponential echo pattern when the polarisation direction is changed clockwise by another 45°. The source of signal between echoes in Fig.7.18 is unknown.

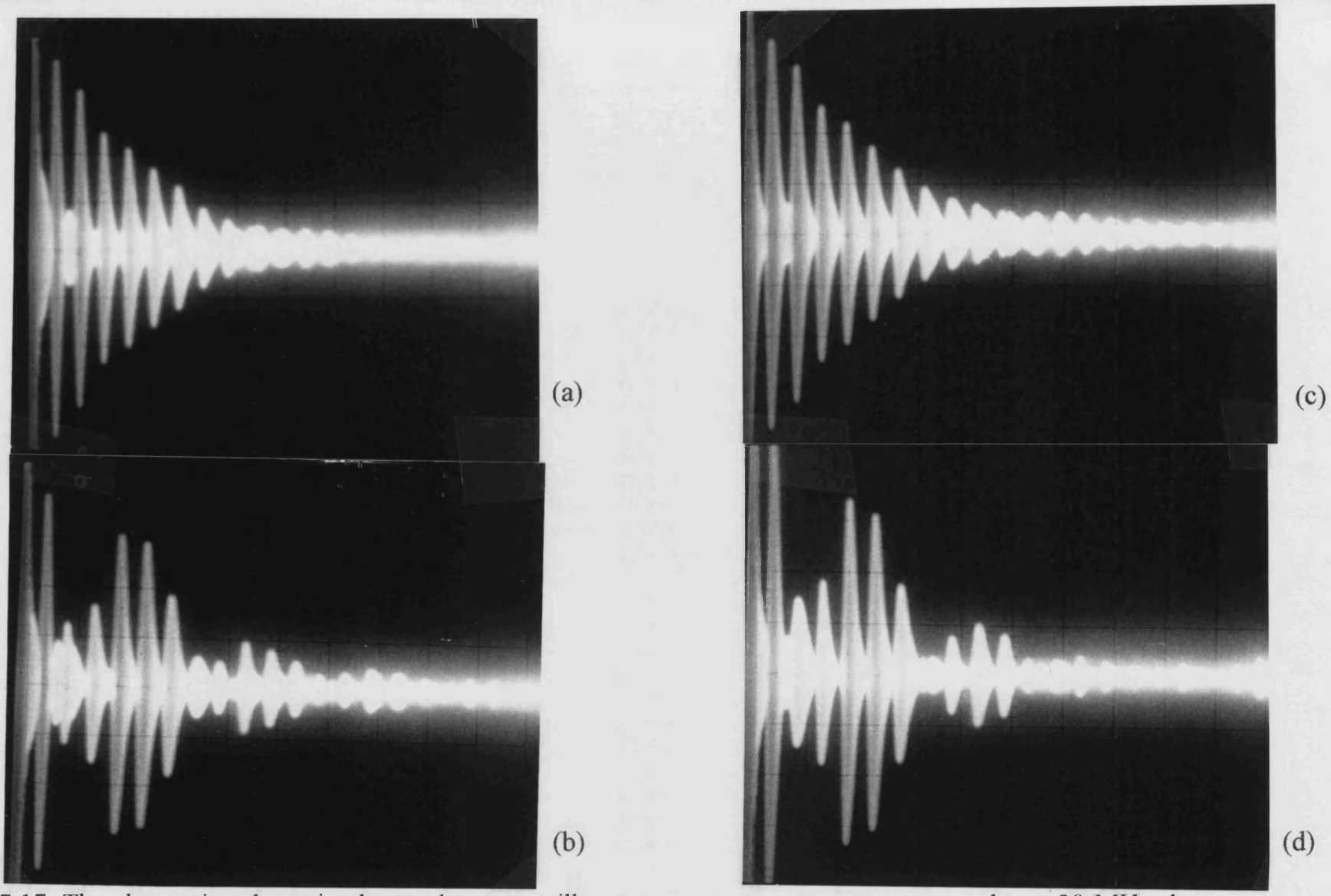

Fig. 7.17 The ultrasonic echo train observed on an oscilloscope screen at room temperature when a 30-MHz shear wave is propagated along the X direction of sample D975 with different polarisation directions.

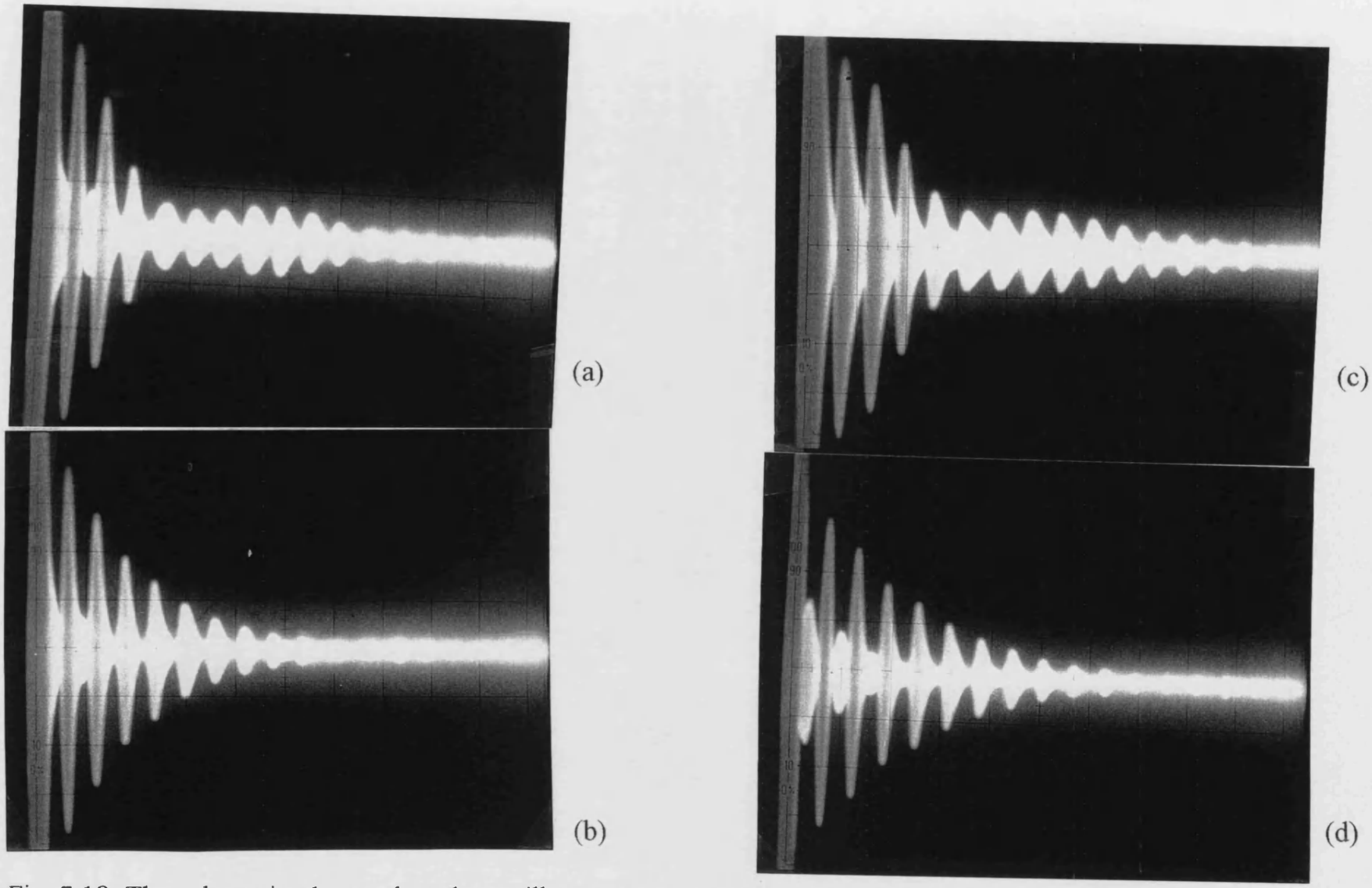

Fig. 7.18 The echo train observed on the oscilloscope screen at room temperature when a 30-MHz shear wave is propagated along the Z direction of sample D975 with different polarisation directions.

Ultrasonic birefringence theory, described in section 2.6, suggests that the D975 sample is anisotropic to some extent. The velocity principal axes are X, Y and Z axes. The difference between the principal shear wave velocities has been evaluated by analysing the modulated echo trains in Fig. 7.17 using ultrasonic birefringence theory. For the modulated echo train shown in Figs. 7.17(b) and (d) the incident shear wave is propagated along the X axis and its polarisation direction is 45° about the Y and Z axes, i.e. in the middle of two principal axes. The anisotropy of the sample causes the wave to split into two components, one polarised parallel to the Y and the other polarised parallel to the Z principal axes. If the attenuation of the two ultrasonic wave components are the same in the sample, the two waves are identical in frequency and amplitude, but have different velocities. The difference between the velocities of the two components causes a phase shift between them. This phase shift increases with path length. Therefore the resultant vibration propagated in the solid is elliptical. Only in two cases does the resultant vibration in the sample become linearly polarised. The first is when the phase shift of the two components reaches $(2n+1)\pi$. The plane of vibration of this resultant wave is perpendicular to the vibration direction of the incident wave. The second is when the phase shift of the two components reaches $2n\pi$. The plane of vibration of this resultant wave is parallel to the vibration direction of the incident wave. After reflection at the opposite surface of the sample, a backwall echo can be detected by a transducer. If at that time the phase shift of the two components reaches $(2n+1)\pi$, the plane of vibration of the resultant wave will be perpendicular to the polarisation direction of the transducer. In this case, the received amplitude of this echo becomes zero. If the phase shift of the two components reaches $2n\pi$, the plane of vibration of the resultant wave will be parallel to the polarisation direction of the transducer. The amplitude of this echo will then be at its maximum value. For a phase shift

between $2n\pi$ and $(2n+1)\pi$, the echo will have an amplitude lower than the maximum depending upon the value of the phase shift between the two components. Fig 7.17 (b) and (d) shows minimum amplitude echoes instead of zero amplitude echoes occurring every fifth received echo. This could be caused by one or more of the following reasons: (1) the attenuations of the two ultrasonic wave components are not the same in the sample, (2) when minimum amplitude echoes reach the transducer, the phase shift between the two components is not exactly $(2n+1)\pi$ but is close to it, (3) the polarisation direction of the transducer is not exactly 45° about the Y and Z axes.

According to the above interpretation of the modulated echo trains shown in Figs. 7.17 (b) and (d) and by using ultrasonic birefringence theory, it is possible to evaluate the difference between the principal shear wave velocities. From Figs. 7.17 (b) and (d), it can be seen that for every five echo returns in the sample, the value of the phase shift between the two components increases by nearly 2π. The normalised difference between the principal shear wave velocities can be calculated as follows:

$$\frac{|V_z - V_y|}{V} = \frac{(5\times 2L+\lambda)/t - 5\times 2L/t}{5\times 2L/t} = \frac{\lambda}{5\times 2L} = \frac{V/\nu}{5\times 2L} \qquad (7.1)$$

with $V = \frac{V_z + V_y}{2}$.

In this equation V_z is the shear velocity when polarised in the Z direction, V_y is the shear velocity when polarised in the Y direction, t is the time for five returns of the echoes, L is the thickness of the sample; ν= 30 MHz. From equation 7.1 the normalised difference between the principal shear wave velocities is evaluated as 0.14%.

The dependence of principal shear wave velocities in sample D975 on polarisation and propagating directions has been measured at 25 MHz and

30±0.5°C and is shown in table 7.1. For the shear wave propagated perpendicular to Z direction the value of the shear wave velocity, when polarised in the Z direction, is 0.14% lower than when polarised in the X or Y direction. This agrees well with the data obtained using birefringence theory. From the data listed in table 7.1, it has been found that for the shear wave propagated in the Z direction the dependence of the wave velocity on the polarisation direction is within the limits of experimental error. The velocities have been measured with the same transducer, the same bounding meterial, and the same equipment setup. For each direction, the deviation of the measured data is very low and within 3 m/s.

Table 7.1 The propagation and polarisation direction dependence of shear velocities in sample D975 at 25 MHz and 30±0.5°C. For experimental error, see the description in the above paragraph.

mode	Direction of propagation	Direction of polarisation	Velocity (m/s)
Shear	X	Y	6086, 6086, 6087
Shear	X	Z	6077, 6077, 6077
Shear	Y	X	6085
Shear	Y	Z	6078, 6077
Shear	Z	X	6079
Shear	Z	Y	6081

Further investigation of the anisotropy in the sample D975 has been carried out by measuring the propagation-direction dependence of longitudinal mode ultrasonic wave velocities at 30±0.5°C. At atmospheric pressure the values of the velocity of the waves propagated along the Z direction are found to be about 0.3 % smaller than those of the waves propagated along other directions. At first this difference in the values of the velocities was

thought to be due to experimental errors resulting from the transducer bonding. However, careful checking carried out later at 16 MHz, 20 MHz, and 30 MHz showed that this difference was always present no matter how many times the transducer was rebonded. The velocities measured at 15 MHz, 16 MHz, 20 MHz and 30 MHz are given in table 7.2. In the table the term "in air" means that the sample was surrounded by air, when the measurement was carried out. "In oil" means that the sample was surrounded by the oil, which acted as the pressure transmitting medium. The velocities in different rows are measured with different transducers and different equipment set-up. The experimental errors thus introduced are within 10 m/s.

Table 7.2 The propagation direction dependence of longitudinal velocities in sample D975 at different frequencies and 30±0.5°C. For the experimental error, see the description in the above paragraph.

Velocity (m/s)	X direction	Y direction	Z direction
16 MHz (in air)	10385	10380	10352
15 MHz (in oil)		10414	10370, 10386
20 MHz (in air)	10185	10186	10159
30 MHz (in air)	10118	10118	10090
31 MHz (in oil)			10090, 10089

7.4.3 Propagation and polarisation direction dependence of longitudinal and shear velocities in ceramic alumina H880

Modulated echo patterns similar to those obtained for the sample D975 have also been observed for shear waves propagated in the sample H880. Here, the directions of wave propagation are defined in the same way as those for the sample D975. Fig. 7.19 (a) shows the echo pattern of a 10 MHz shear wave propagated along the Y direction with the polarisation

direction parallel to one of the edges of the sample. The echo train is clean and exponential. When the direction of the polarisation is turned anti-clockwise 45° about the Y axis, the echo pattern is observed as shown in Fig.7.19 (b), the modulated echo pattern is also produced for this material. Turning the polarisation direction of the transducer by another 45° (i.e. parallel to another edge of the face) leads to the appearance of an exponential echo pattern as shown in Fig. 7.19 (c). After turning the transducer by 45° again, the modulated echo pattern is reproduced (Fig.7.19 (d)). When a 30 MHz shear wave is propagated along the same direction, the modulation on the echo pattern is not seen clearly. Fig .7.20 (a) shows the echo pattern of the 30 MHz shear wave with the polarisation direction as same as that of the 10 MHz shear wave corresponding to the modulated echo pattern shown as Fig. 7.19 (b). Instead of being modulated, the echo pattern (Fig. 7.20 (a)) shows a tail at the right-hand side of each echo. When the ultrasonic wave polarisation direction is turned anti-clockwise about 45° (parallel to one of the edges of the face), the area between the echoes becomes clearer, as shown in Fig. 7.20 (b). After a successive turning by 45° the echo pattern (Fig. 7. 20 (c)) becomes similar to that in Fig.7.20 (a), i.e. a tail appears at the right-hand side of each echo. From the Fig. 7.20 (a)-(c) it can be seen that, for 30 MHz waves, the echo patterns have no obvious polarisation directional dependence.

For the shear waves propagated in the Z direction of sample H880, the modulation of the echo pattern is less pronounced than along the X and Y axes (similar to D975). Fig. 7.21 (a) and (b) show the exponential echo pattern and modulated echo pattern respectively for 10 MHz shear waves propagated in the Z direction.

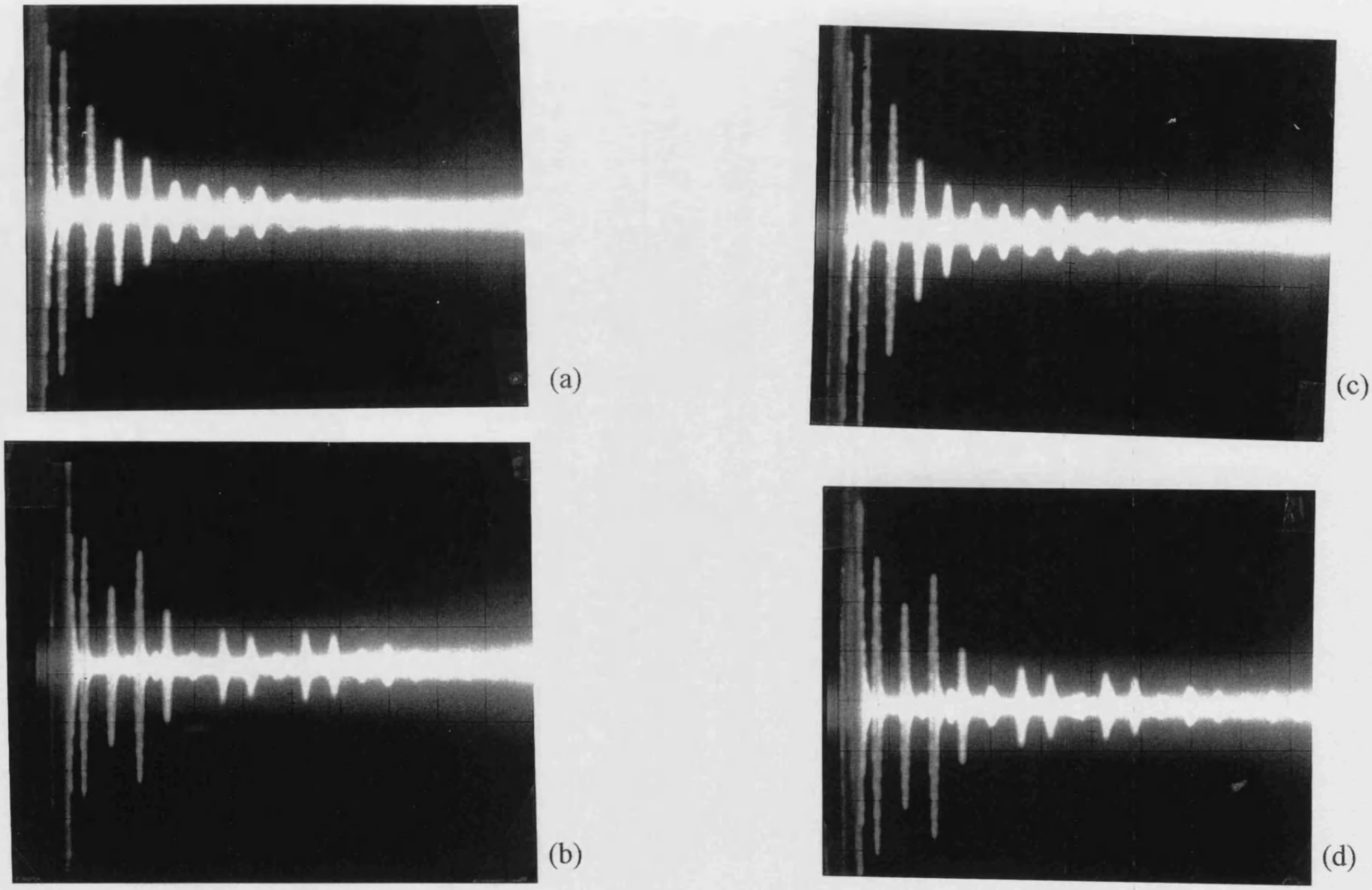

Fig. 7.19 The echo train observed on the oscilloscope screen when a 10-MHz shear wave is propagated along the Y direction of sample H880 with different polarisation directions.

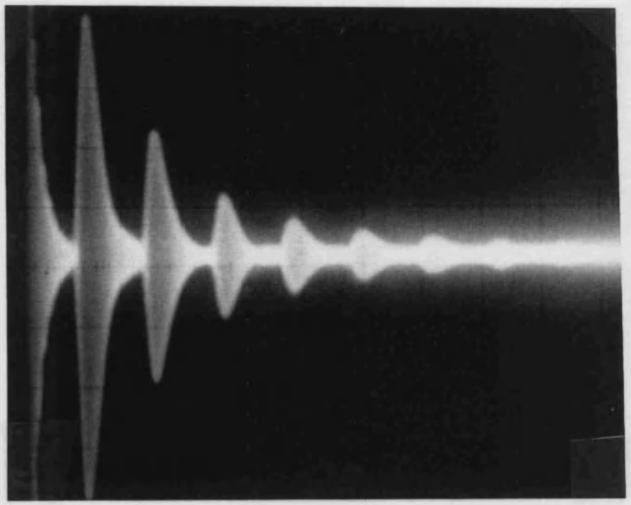

(a)

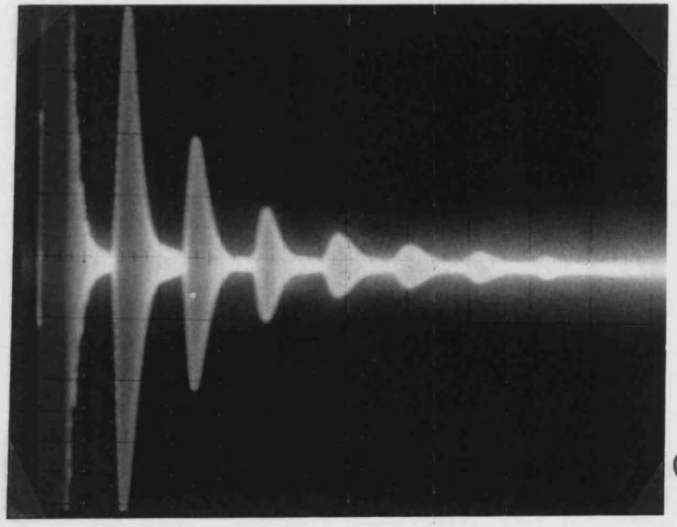

(c)

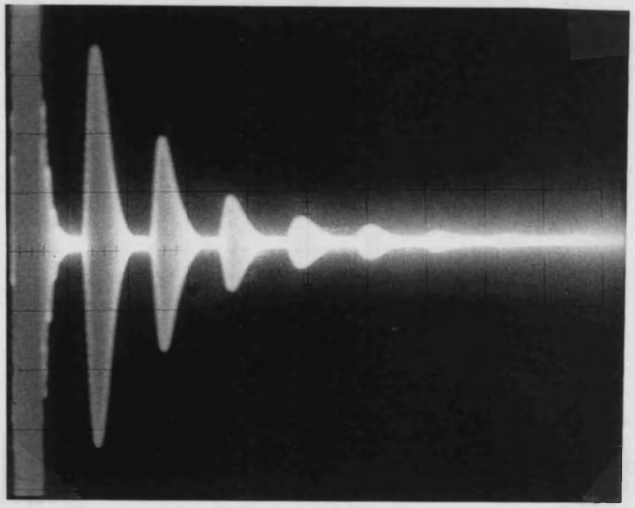

(b)

Fig. 7.20 The echo train observed on an oscilloscope screen when a 30-MHz shear wave was propagated along the Y direction of sample H880 with different polarisation directions at room temperature.

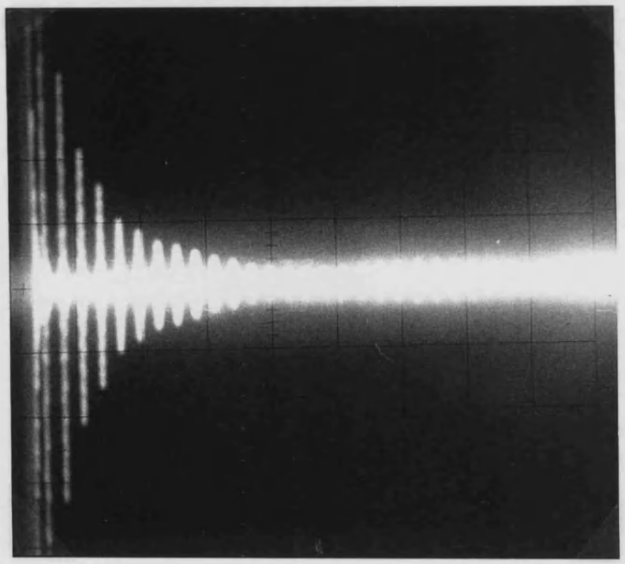

(a)

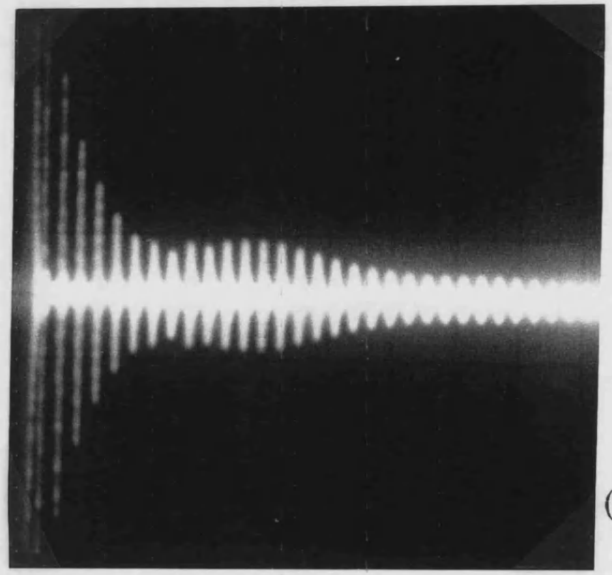

(b)

Fig. 7.21 The echo train observed on an oscilloscope screen at room temperature of when a 10-MHz shear wave is propagated along the Z direction of sample H880 with different polarisation directions.

Analysing Fig. 7. 19 using the same procedure as that adopted for the D975 sample, it is found that the H880 sample is also anisotropic to some degree.

The difference between the principal shear wave velocities of waves propagated along X, Y and Z axes has been evaluated by using the same method as for D975 sample. From Fig. 7.19 (b) and (d), it can be seen that for every three echo returns in the sample, the value of the phase shift between the two components increases by nearly 2π. The normalised difference between the principal shear wave velocities can be calculated as follows:

$$\frac{|V_z - V_x|}{V} = \frac{(3\times 2L+\lambda)/t - 3\times 2L/t}{3\times 2L/t} = \frac{\lambda}{3\times 2L} = \frac{V/\nu}{3\times 2L} \qquad (7.2)$$

with $V = \frac{V_z + V_x}{2}$. In this equation V_z is the shear velocity when the wave is polarised in Z direction; V_x is the shear velocity when the wave is polarised in X direction; t is the time for three returns of the echoes; L is the thickness of the sample; ν is the carrier frequency of 10 MHz. From equation 7.2, the normalised difference between the principal shear wave velocities is evaluated to be 0.6%.

The dependencies of principal shear wave velocities on the polarisation and propagating directions in sample H880 have been measured at 11 MHz and are given in table 7.3. Using the ultrasonic wave velocity data given in this table, it has been shown by calculation that for shear waves propagated perpendicular to the Z direction the value of the velocity of the wave polarised in the Z direction is 0.5% lower than those polarised in the X or Y direction. The analysis, using the birefringence theory, gives a value of 0.6% for this difference. From the data listed in table 7.3, it has been

found that for a shear wave propagating in Z direction the velocity is not dependent upon polarisation direction.

The dependence of longitudinal velocities on the propagation direction in sample H880 for the waves at 12 MHz is given in Table 7.3. From the data listed in the table, it has been shown that the velocity value of the longitudinal wave propagated in the Z direction is 1.2% lower than those of the waves propagated in the X or Y direction.

Table 7.3 The velocities of ultrasonic wave propagated and polarised at different directions at 11 MHz for shear mode and at 12 MHz for longitudinal mode in sample H880 at 30±0.5°C. See P7-34 for explanation of the experimental error.

mode	Direction of propagation	Direction of polarisation	Velocity (m/s)
Longitudinal	X	X	9046±3
Longitudinal	Y	Y	9054±3
Longitudinal	Z	Z	8939±3
Shear	X	Y	5390±3
Shear	X	Z	5365±3
Shear	Y	X	5393±3
Shear	Y	Z	5366±3
Shear	Z	X	5366±3
Shear	Z	Y	5367±3

Fig. 7.20 (a)-(c) shows that for 30 MHz waves the echo patterns have no obvious polarisation direction dependence. The reason is that the wavelength of 30MHz wave is 1/3 of that of the 10 MHz. Every time

when an echo returns, the value of the phase shift between the two polarisation components increases by almost 2π. Hence, amplitude of the echoes has not been modified.

7.4.4 Propagation and polarisation direction dependence of longitudinal and shear velocities in ceramic alumina SINC53

The velocities of 30 MHz ultrasonic waves propagated and polarised in different directions have been measured for ceramic alumina sample SINC53 at 30±0.5°C; the results are given in Table 7.4. The value of longitudinal wave velocity in the x direction is the same as that in the y direction within the experimental error. From the data listed in the table 7.4, it has been shown that the velocity value of the longitudinal ultrasonic wave propagated in the Z direction is 0.7% lower than those of the waves propagated perpendicular to Z direction. It has been shown by calculation that for shear waves propagated perpendicular to the Z direction the value of the velocity of the wave polarised in the Z direction is 0.3% lower than those polarised in the X or Y direction. For a shear wave propagating in Z direction the velocity is not dependent upon polarisation direction (Table 7.4).

Table 7.4 The velocities of longitudinal and shear mode ultrasonic waves propagated and polarised at different directions in ceramic alumina sample SINC53 at 30 MHz and 30±0.5°C. See page 7-34 for explanation of the experimental error.

mode	Direction of propagation	Direction of polarisation	Velocity (m/s)
Longitudinal	X	X	9697±3
Longitudinal	Y	Y	9699±3
Longitudinal	Z	Z	9631±3
Shear	X	Y	5739±3
Shear	X	Z	5725±3
Shear	Y	X	5742±3
Shear	Y	Z	5725±3
Shear	Z	X	5731±3
Shear	z	y	5730±3

7.4.5 The longitudinal and shear velocities propagated and polarised in different directions in Ceramic alumina D999

Table 7.5 is a list of longitudinal and shear mode ultrasonic velocities of waves propagated and polarised at different directions in sample D999 at 31 MHz. From this table it can be seen that there are no significant differences between the velocities of the waves propagated and polarised in different directions, i.e. the differences are within the limits of experimental error.

For the sample D999, 1, 2, and 3 have been used to indicate three wave propagation directions mutually perpendicular to each other (the Z axis has been defined as unique axis of anisotropic materials).

Table 7.5 The velocities of longitudinal and shear mode ultrasonic wave propagated and polarised at different directions in sample D999 at 31 MHz and 30±0.5°C. See page 7-34 for explanation of the experimental error.

mode	Direction of propagation	Direction of polarisation	Velocity (m/s) (±3)
Longitudinal	1	1	10766
Longitudinal	2	2	10766
Longitudinal	3	3	10761
Shear	1	2	6398, 6398
Shear	1	3	6397, 6396, 6396
shear	1	45° to the sample edges	6397, 6397
Shear	2	1	6397
Shear	2	3	6397
shear	2	45° to the sample edges	6396
Shear	3	1	6397, 6396
Shear	3	2	6396
shear	3	45° to the sample edges	6396

7.4.6 The longitudinal and shear velocities propagated and polarised in different directions in ceramic alumina AL23

Table 7.6 provides a list of longitudinal and shear mode ultrasonic velocities of waves propagated and polarised at different directions in ceramic alumina sample AL23 at 30 MHz for longitudinal mode and 25MHz for shear mode. From this table it can be seen that there are no significant differences between the velocities of the waves propagated and polarised in different directions, i.e. the differences are within the limits of experimental error.

For the sample AL23, 1, 2, and 3 have been used to indicate three wave propagation directions mutually perpendicular to each other (the Z axis has been defined as unique axis of anisotropic materials).

Table 7.6 The velocities of longitudinal and shear mode ultrasonic waves propagated and polarised at different directions in sample AL23 at 30±0.5°C. See page 7-34 for explanation of the experimental error.

mode	Direction of propagation	Direction of polarisation	Velocity (m/s)
Longitudinal	1	1	10562
Longitudinal	2	2	10565
Longitudinal	3	3	10566
Shear	1	2	6281
Shear	1	3	6281
Shear	2	1	6281
Shear	2	3	6280
Shear	3	1	6283
Shear	3	2	6284

7.5 Discussion of the effects of microstructure on elastic anisotropy of the ceramic aluminas

The results given in sections 7.4.2 to 7.4.4 reveal that D975, H880 and SINC53 are elastically anisotropic with similar characteristics and the ultrasonic velocity principal axes of D975, H880 and SINC53 are the X, Y and Z axes. Z is the uniaxial axis of the samples. In these three kinds of ceramic aluminas the longitudinal mode velocities along the X have the same values as that along the Y axes; the shear waves along the X axis

show the same polarisation direction dependence as that along the Y axis. Along the Z axis the shear waves show less polarisation direction dependence and the longitudinal velocities have smaller values than those in the directions of X and Y. This is because the Z direction is the uni-pressed direction in the fabrication process. The relative differences between the principal velocities of ultrasonic waves propagated in samples D975, H880 and SINC53 are given in Table 7.7.

Table 7.7 The relative differences between the principal velocities of ultrasonic waves propagated in ceramic alumina samples D975, H880 and SINC53 at 30±0.5°C.

Sample	D_1	D_2
D975	0.3 %	0.14%
H880	1.2%	0.5%
SINC53	0.7%	0.3%
D999	0.0%	0.0%
AL23	0.0%	0.0%

$$D_1 = \frac{V_{L,X} - V_{L,Z}}{V_L} = \frac{V_{L,Y} - V_{L,Z}}{V_L}$$

and

$$D_2 = \frac{V_{S,X} - V_{S,Z}}{V_S} = \frac{V_{S,Y} - V_{S,Z}}{V_S}.$$

The subscript "L" indicates the longitudinal mode; "S" indicates the shear mode; "X", "Y" and "Z" indicate polarisation directions of the waves.

The measured velocities show that H880 has the largest elastic anisotropy in these three kinds of ceramic aluminas while D975 has the smallest. This agrees well with the X-ray results for H880 and D975 samples. From

Table 7.7, it can be seen that, both D_1 and D_2 of H880 are about four times as large as those of D975. However the ratio of D_1 to D_2 is same for those three kinds of ceramic aluminas within the error range of the experiment. Hence, it is possible that the measured elastic anisotropy of those three samples is related to the same effect introduced during manufacture.

The anisotropy of the velocities of these three kinds of ceramic aluminas cannot be attributed to the residual internal compression stress along the Z direction. Compression stress in the Z direction would enhance the velocity of the longitudinal wave propagated in that direction (Schneider 1995). However, our measurements show the opposite situation.

The values of the elastic constants C_{11} (=C_{22}) and C_{33} of single crystal Al_2O_3 are 4.968 and 4.981 GPa (Hankey and Schuele 1969). Therefore, the value of the longitudinal velocity along the c-axis of single crystal is only 0.13% larger than that along the a-axis or b-axis. Hence, the measured smaller longitudinal velocity in the Z direction of the sample H880 and D975 cannot be attributed to the preferred orientation of the grains itself. These lower values could originate from more than one source which have their origin in preferred orientation of the alumina grains. The main source responsible for the decrease of the longitudinal velocity in the Z direction of the samples H880, D975 and SINC53 could be that the total thickness of the grain boundary phase in the Z direction may be larger than that in the X or Y direction. The total thickness of the grain boundary phase cannot be calulated because the imformation needed is not availible. This anisotropy of total grain boundary thickness is caused by preferred orientation of the α-alumina grains due to the following reasons:

1. From the SEM, X-ray diffraction results (sections 7.2 and 7.3), it has been concluded that the α-alumina grains are faceted and that these faceted grains appear tabular in two dimensions, with the long edges usually perpendicular to c-axis of α-alumina grains. This means that grains of D975, H880 and SINC53 grow slower in the c-axis than in all other crystallographic directions. This tendency to facet is linked to the composition of the boundary regions and is a common feature in alumina ceramics (Powell-Dogan and Heuer 1990). It is thought to be an equilibrium structure so that the total surface energy is minimised (Powell-Dogan and Heuer 1990). The texture of faceted grains results in the number of the grain boundary layers in the Z direction being larger than that in the X or Y direction.

2. There is a large difference between the thermal expansion coefficients along the c-axis ($\alpha_{//}=5.7\times10^{-6}$/degree) and in the basal plane ($\alpha_{\perp}=5.0\times10^{-6}$ /degree) (Hankey and Schuele 1969). When the material is cooled down from its sintering temperature before reaching the temperature (about 1000°C) (DERA) at which the glassy phase losesthe ability to flow, grains in the sample contract more in the direction of c-axis than in the basal plane. Hence the distribution of the thickness of the grain boundary layers formed between grains may not be uniform. The texture of faceted grains results in the thickness of the grain boundary layers in the Z direction being larger than that in the X or Y direction.

Chapter 8 Effects of Hydrostatic Pressure on Elastic Properties and Ultrasonic Attenuation of Ceramic Alumina

8.1 Experimental procedures

The samples used in the ultrasonic studies under hydrostatic pressure were supplied by the DERA, Chertsey. There are three kinds of sample sizes: (i) 15×15×15 mm^3 cube, (ii) 7.5×15×15 mm^3 half cube, (iii) 13×13×13 mm^3 cube. The dimensions of each sample have been measured using a MICRO 2000 digital micrometer with resolution of 1μm. The samples used for density measurements are in a regular cubic form. The sample density has been determined by measuring the dimensions and the mass of samples at room temperature. The mass of the samples has been determined using a SARTORIUS electronic analytical balance with standard resolution of ±0.0001g. The measured sample densities are given in table 8.7.

In this part of the work, X cut and Y cut quartz transducers with fundamental frequencies 8 to 15 MHz have been used. Hydrostatic pressure up to 0.35 GPa was applied at 30±0.5°C with the apparatus described in section 4.3. A transducer correction (Kittinger 1977) has been applied to the ultrasonic wave velocities. The echo trains produced by 10 MHz longitudinal waves propagated through D999, D975, AL23 and SINC53 cubic samples show large diffraction effects when 10 mm transducers are used. Inspection of equation 4.4 shows that the diffraction is caused by wall reflection. Therefore, data for 10 MHz longitudinal waves for the D999, D975, AL23 and SINC53 samples are not measurable.

The anisotropy shown by the values of the velocities of ultrasonic waves in the ceramic aluminas D975, H880 and SINC53 is not more than 1.2%; the pressure derivatives of the velocities are found not to depend on the wave propagation direction. Hence it is feasible to treat the materials as isotropic when determining the elastic moduli, the Poisson's ratio, the pressure derivatives of the elastic moduli and the long wavelength acoustic Grüneisen parameters.

8.2 Ceramic alumina D999

In order to check the anisotropy of D999, ultrasonic waves have been propagated in each of three mutually orthogonal directions. For this ceramic D999 there are no significant differences of the velocities and pressure derivatives of the natural velocities of the waves propagated in different directions, i.e. the differences are within the limits of experimental error. Table 8.1 gives pressure derivatives of the natural velocities measured for the three directions. Because this sample is isotropic within the limits of experimental error, the ultrasonic wave velocities and pressure derivatives of natural velocities measured in the three directions were averaged to give mean values for the corresponding parameters. These averaged values were used for the calculation of the elastic moduli, the Poisson's ratio, the pressure derivatives of the elastic moduli and the long wavelength acoustic Grüneisen parameters. The averaged values and calculated results are presented in Table 8.7 in comparison with those of other samples. Figs. 8.1 and 8.2 show the pressure dependences of the relative changes in the natural longitudinal and shear mode wave velocities propagated in the three directions. It can be seen that the natural velocities measured in different directions have the same pressure dependence.

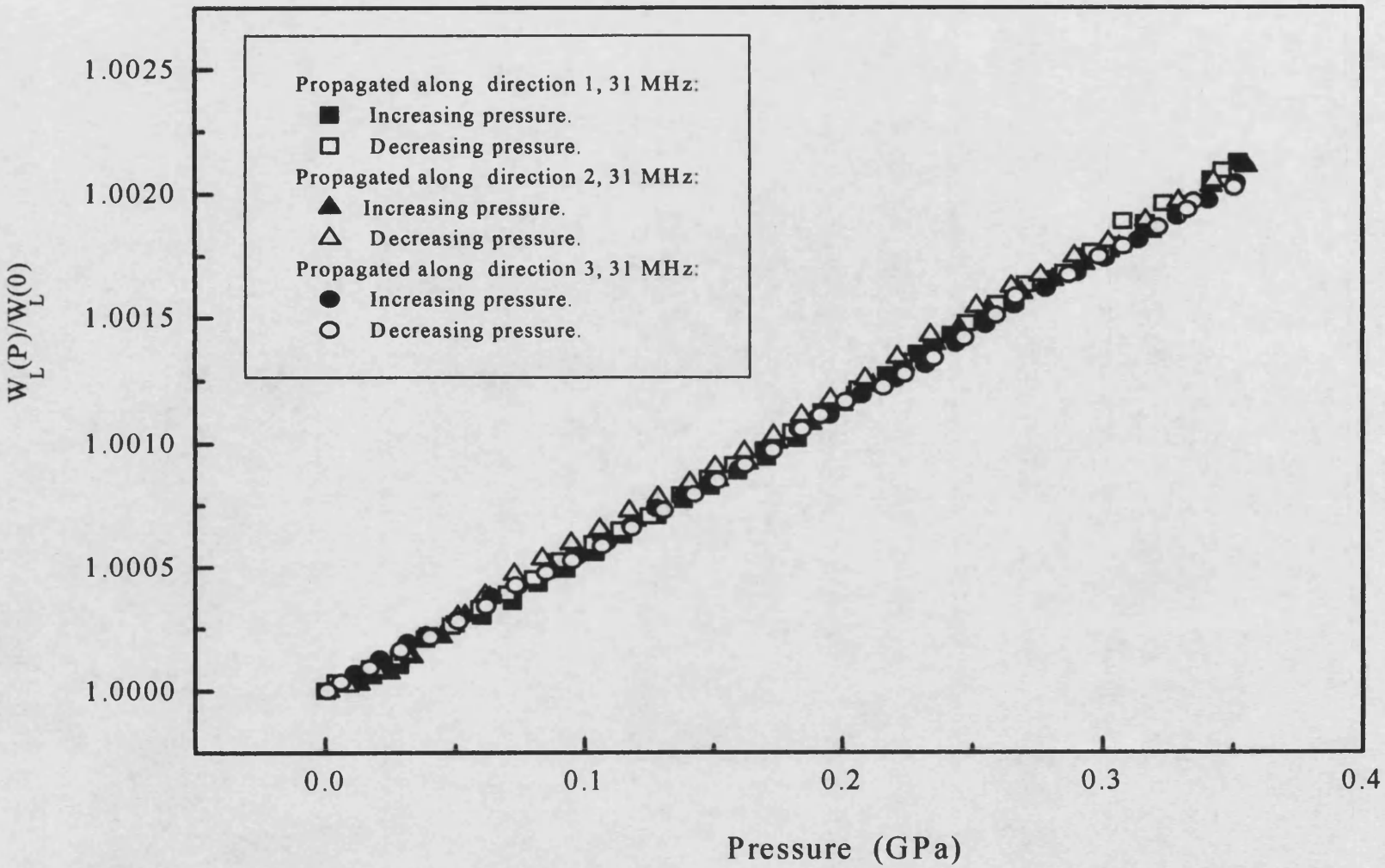

Fig.8.1 The pressure dependence of normalised longitudinal mode ultrasonic natural velocity of ceramic alumina D999 at 30±0.5 °C.

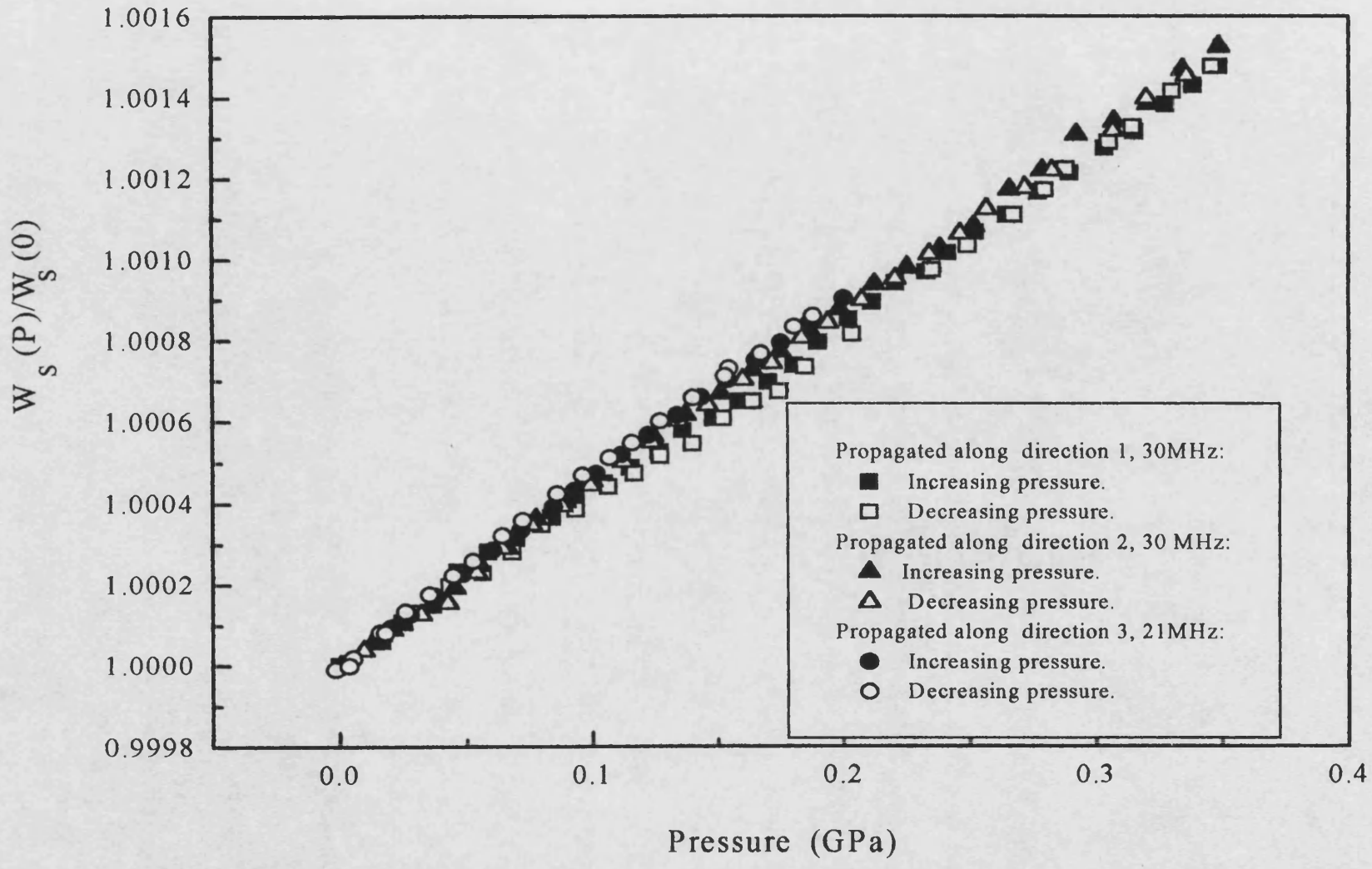

Fig.8.2 The pressure dependence of normalised shear mode ultrasonic natural velocity of ceramic alumina D999 at 30±0.5°C.

The ultrasonic attenuation of longitudinal waves is plotted in Fig. 8.3. No obvious attenuation peak was observed and the attenuation increases almost linearly with increasing pressure.

Table 8.1 The pressure derivatives of ultrasonic natural velocities measured in different directions for sample D999 at atmospheric pressure and 30±0.5°C.

Item	Direction 1	Direction 2	Direction 3
$(\partial W_L/\partial P)_{P=0}$ ($ms^{-1}GPa^{-1}$)	66±2	65±2	63±2
$(\partial W_S/\partial P)_{P=0}$ ($ms^{-1}GPa^{-1}$)	27±2	28±2	30±2

8.3 Ceramic alumina D975

The hydrostatic pressure dependences of velocities and attenuation of ultrasonic waves propagated in the sample D975 have been measured at different frequencies in different directions up to 0.4 GPa. Fig. 8.4 shows the attenuation of 30MHz longitudinal mode waves propagated in the Z direction and 31 MHz waves propagated in the Y direction. The attenuation for the ultrasonic wave propagated in the Z direction is higher than that propagated in Y direction. Fig. 8.5 shows the attenuation of the longitudinal waves propagated in the X direction at 57 MHz and in the Z direction at 50 MHz. The attenuation of the 50-MHz wave along the Z direction is almost constant below about 0.25 GPa with a small peak at about 0.14 GPa. The attenuation of 57-MHz waves propagated along the X direction is lower than that of the 50-MHz wave along the Z direction. From Figs.8.4 and 5, it can be seen that the attenuation of the ultrasonic longitudinal waves propagated in the Z direction is higher than that of the waves propagated in the X or Y directions. To ensure that such differences

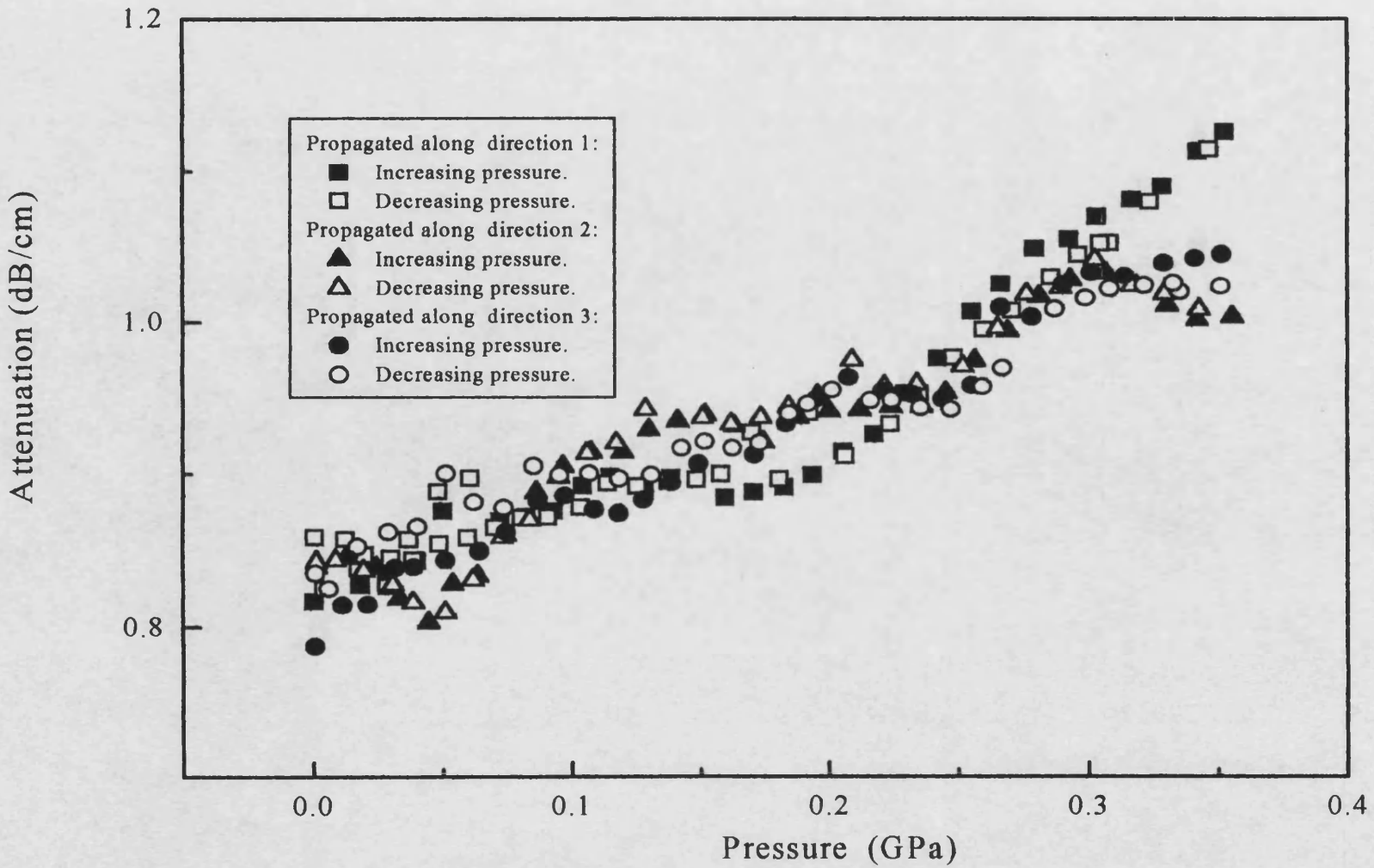

Fig. 8.3 The pressure dependence of attenuation of longitudinal mode ultrasonic wave in ceramic alumina D999 at 31MHz and 30±0.5°C.

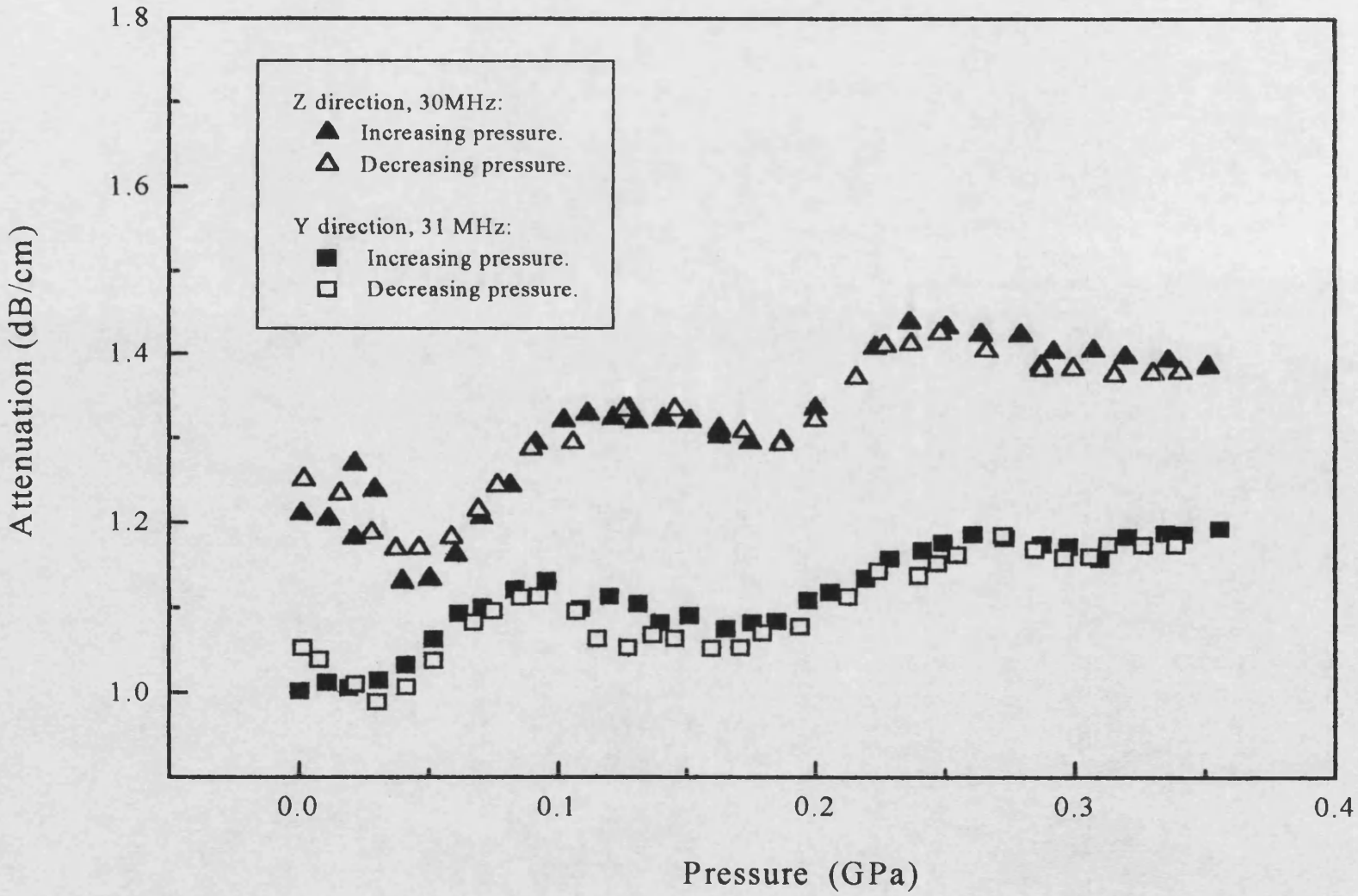

Fig.8.4 The pressure dependence of ultrasonic attenuation in ceramic alumina D975 at 30±0.5°C, propagated in different directions.

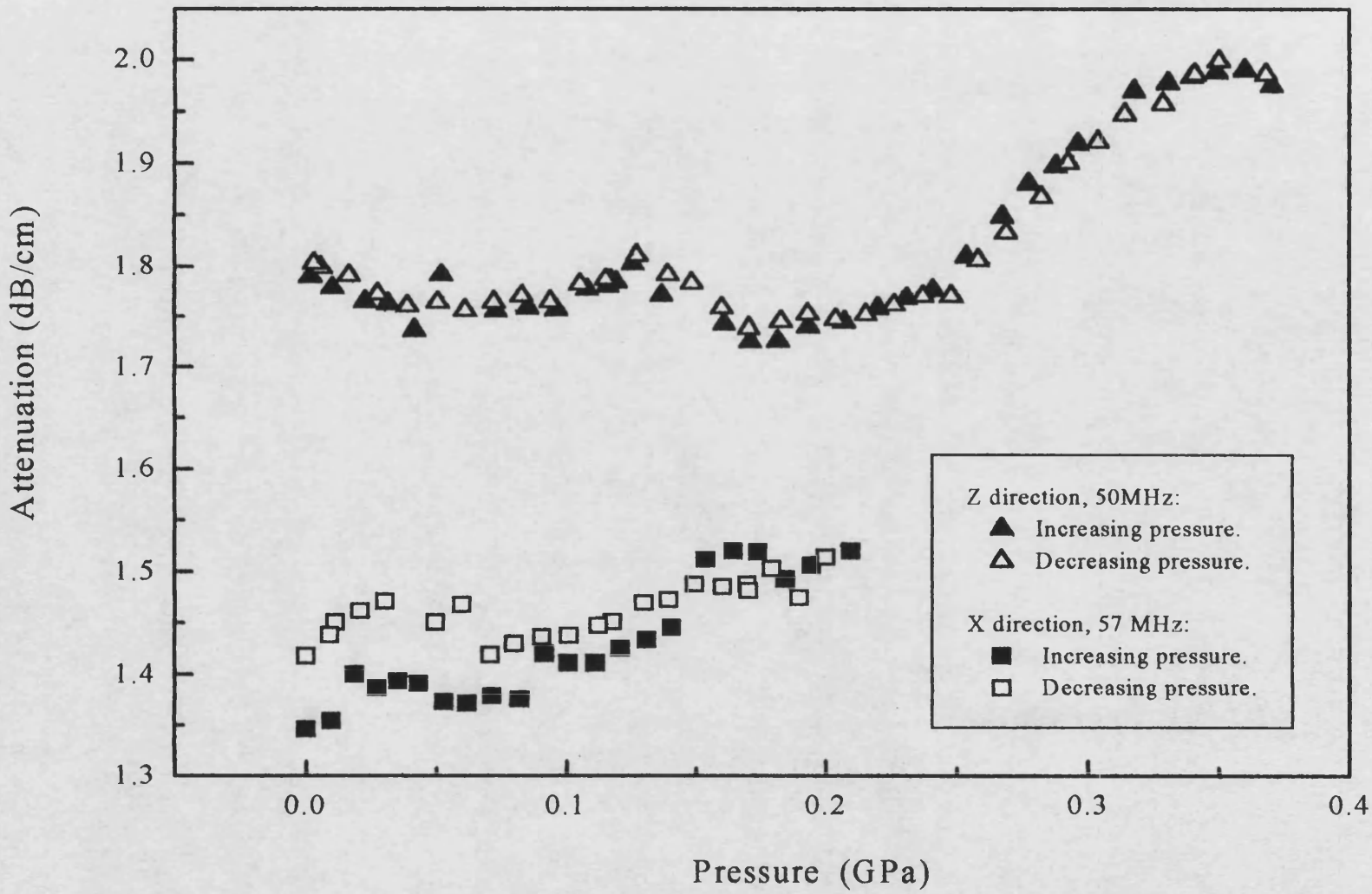

Fig. 8.5 The pressure dependence of ultrasonic attenuation of ceramic alumina D975 at 30±0.5°C, propagated in different directions.

are not caused by the transducer bonding, the attenuation data for ultrasonic waves at 20 MHz and 30 MHz in each of the three directions were checked again with the sample in a furnace kept at 30°C at atmospheric pressure. The results were reproducible. The differences are: 0.24 ±0.04 dB/cm at 30 MHz and 0.2 ±0.04 dB/cm at 20 MHz.

The attenuation data, shown in Figs. 8.4-5, were measured simultaneously with the ultrasonic wave velocities at corresponding frequencies. The normalised longitudinal mode natural velocity $W_L(P)/W(0)$ of ultrasonic waves measured at different frequencies and propagated in the X, Y and Z directions respectively is shown in Fig. 8.6. The ratio $W_L(P)/W(0)$ for all the waves, presented in this figure, increases smoothly as pressure increases. No obvious knees can be seen. All the data in Fig. 8.6 coincide well. That means there is no obvious frequency or directional dependence of pressure derivatives of natural velocities of sample D975. The pressure derivatives of natural velocities of sample D975 at atmospheric pressure and room temperature are listed in table 8.2. For the longitudinal mode, the averaged values measured at 30 and 31 MHz have been used for calculation of the results presented in Table 8.7.

Table 8.2 The pressure derivatives of longitudinal natural velocities of sample D975 at atmospheric pressure and 30±0.5°C.

Frequency and propagating direction	$(\partial W_L/\partial P)_{P=0}$ ($ms^{-1}GPa^{-1}$)
57MHz, in X direction	64±2
31 MHz, in Y direction	68±2
31 MHz, in Z direction	66±2
30 MHz, in Z direction	65±2, 67±2
50 MHz, in Z direction	67±2

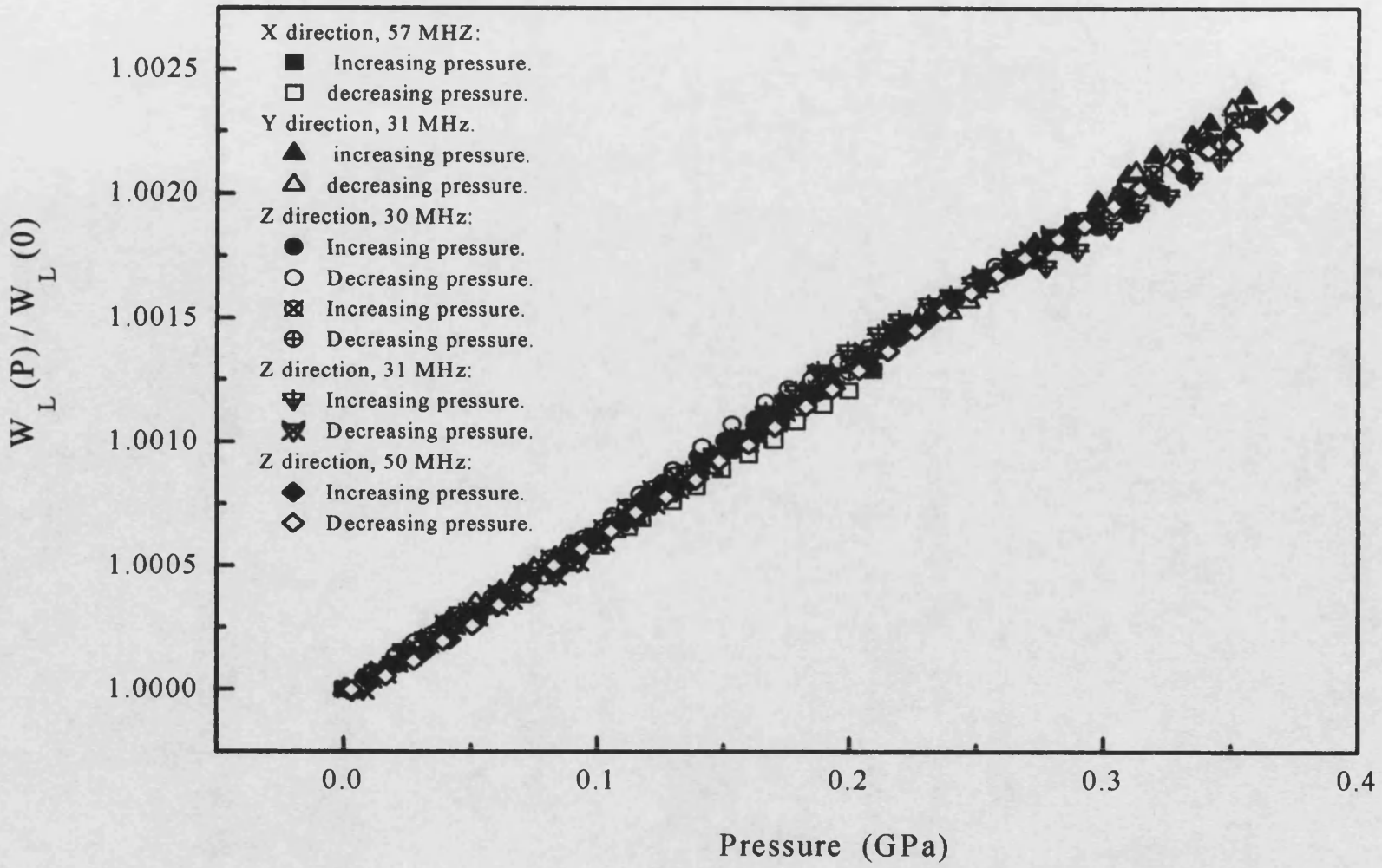

Fig. 8.6 The pressure dependence of normalised longitudinal mode ultrasonic natural velocity of the ceramic alumina D975 at 30±0.5°C.

The pressure dependence of the natural velocity of a shear mode wave at 27.5 MHz propagated in the Y direction is shown in Fig. 8.7. The result is presented in Table 8.7.

8.4 Ceramic alumina H880

To compare the pressure dependence of the natural longitudinal velocity measured along different directions, the data measured along the Z direction at 43 MHz and those measured along the directions perpendicular to Z at 30 and 51 MHz are plotted together in Fig. 8.8. Each set of data is almost linearly dependent on pressure. The pressure derivatives of longitudinal natural velocities of sample H880 at atmospheric pressure and 30±0.5°C listed in Table 8.3. From Fig. 8.8 and Table 8.3 it can be seen the pressure derivatives of longitudinal natural velocities of sample H880 are not dependent upon propagation direction. For the longitudinal mode the velocity measured at 30 MHz has been used for the calculation of the results presented in Table 8.7 in comparison with those for other samples.

Table 8.3 The pressure derivatives of longitudinal natural velocities of sample H880 at atmospheric pressure and 30±0.5°C.

Frequency and propagating direction	$(\partial W_L/\partial P)_{P=0}$ ($ms^{-1}GPa^{-1}$)
30MHz, perpendicular to Z	48±2
43 MHz, in Z direction	46±2
51 MHz perpendicular to Z	45±2

The pressure dependence of the normalised shear mode natural velocity of ultrasonic waves, measured at 30 MHz and 31 MHz, propagated and polarised in different directions at room temperature is shown in Fig. 8.9. The pressure derivatives of the shear mode natural velocities of the sample

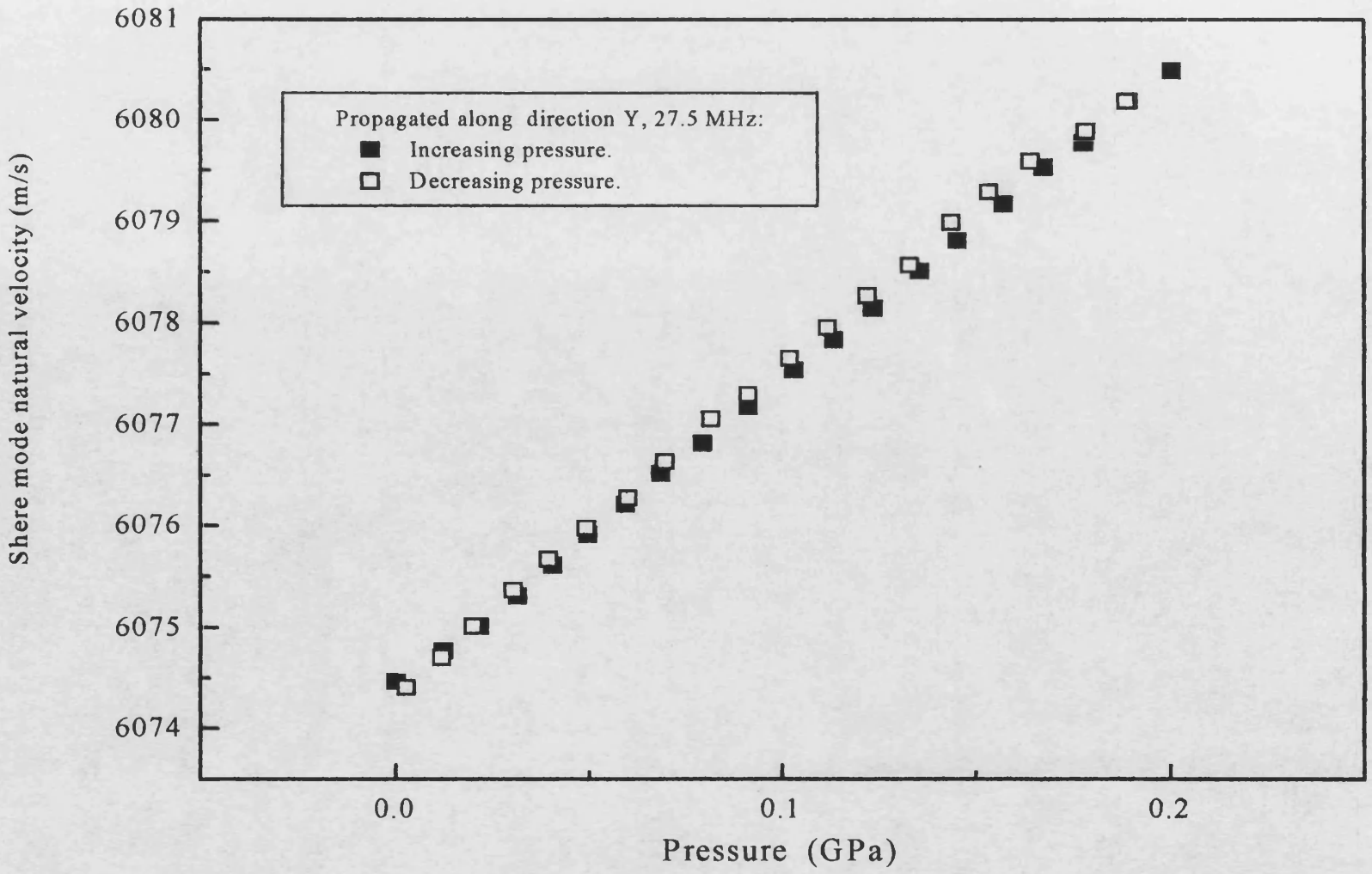

Fig.8.7 The pressure dependence of shear mode ultrasonic natural velocity of ceramic alumina D975 at 30±0.5°C.

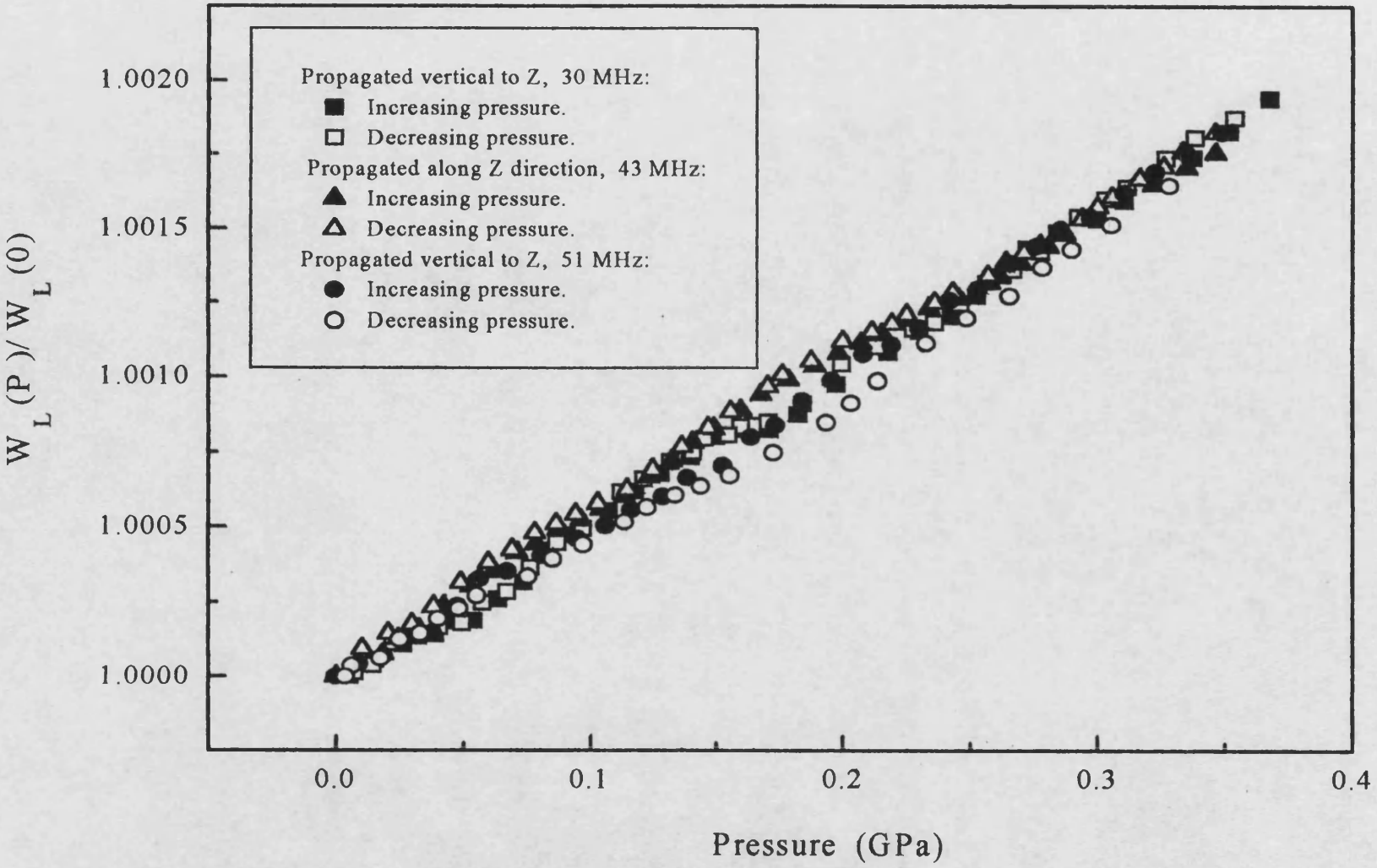

Fig. 8.8 The pressure dependence of normalised longitudinal mode ultrasonic natural velocity of ceramic alumina H880 at 30±0.5°C.

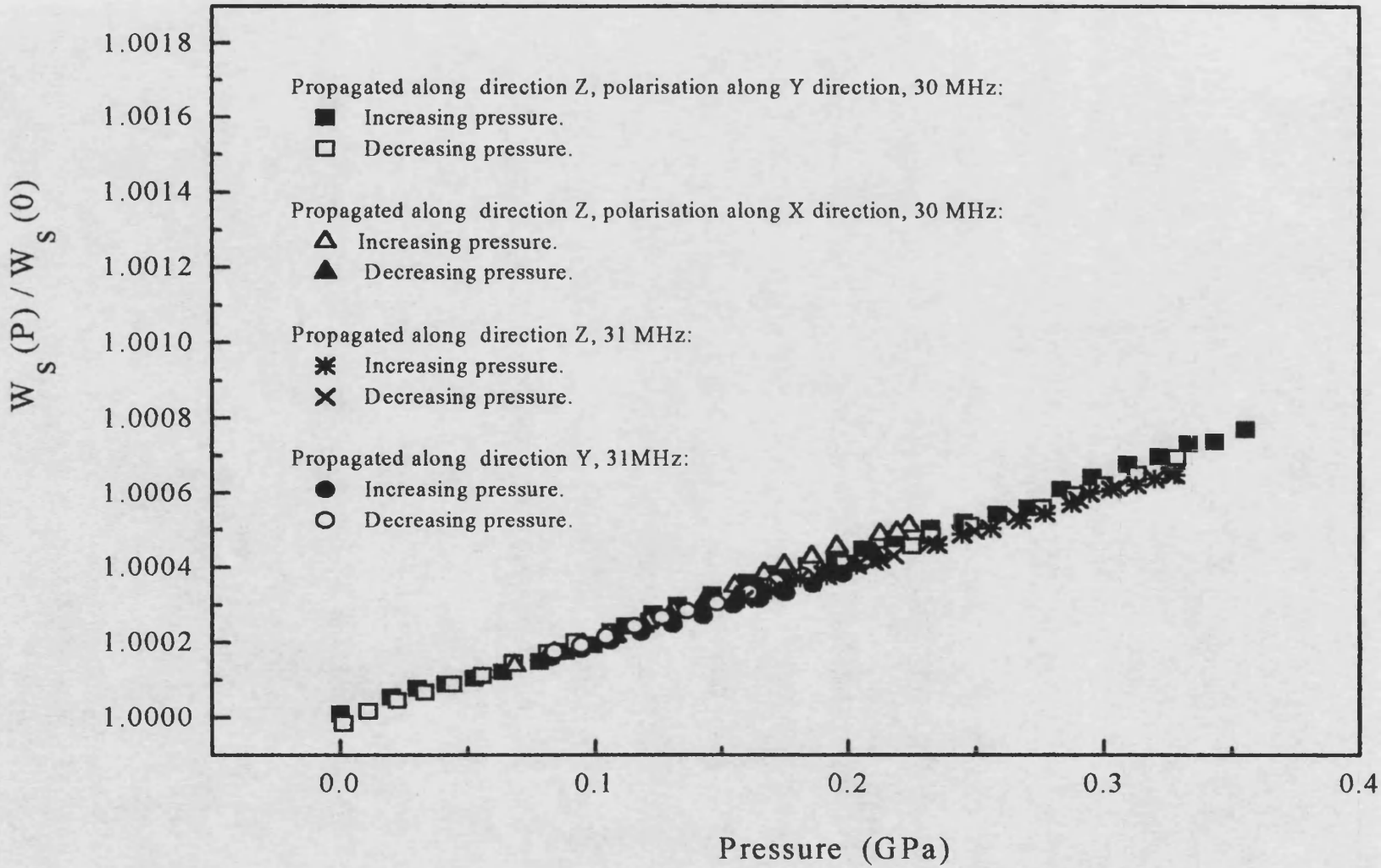

Fig.8.9 The pressure dependence of normalised shear mode ultrasonic natural velocity of ceramic alumina H880 at 30±0.5°C.

H880 at atmospheric pressure and 30±0.5°C are listed in Table 8.4. These averaged values in the table were used for the calculation of the results presented in Table 8.7.

Table 8.4 The pressure derivatives of the shear mode natural velocities of the sample H880 measured at 30 MHz and 31 MHz at atmospheric pressure and 30±0.5°C.

Direction of propagation	Direction of polarisation	$(\partial W_S/\partial P)_{P=0}$ ($ms^{-1}GPa^{-1}$)
Z	X	12±2
Z	Y	11±2
Z		11±2
Y		11±2

The pressure dependence of attenuation of longitudinal waves in sample H880 propagated in different directions is shown in Fig. 8.10. The attenuation of a 44-MHz longitudinal wave propagated along the Z direction is higher than that of a 51-MHz longitudinal wave propagated perpendicular to the Z direction. It seems that the attenuation could be propagation-direction dependent, being larger for a wave propagated along the Z direction.

8.5 Ceramic alumina AL23

Fig. 8.11 gives the pressure dependence up to 0.35 GPa of the normalised 31 MHz longitudinal natural velocities measured in two separate runs at 30±0.5°C. The two sets of the velocity data are consistent with each other, their dependence on pressure being linear. The ultrasonic attenuation of longitudinal mode waves is plotted in Fig. 8.12. The deviations between

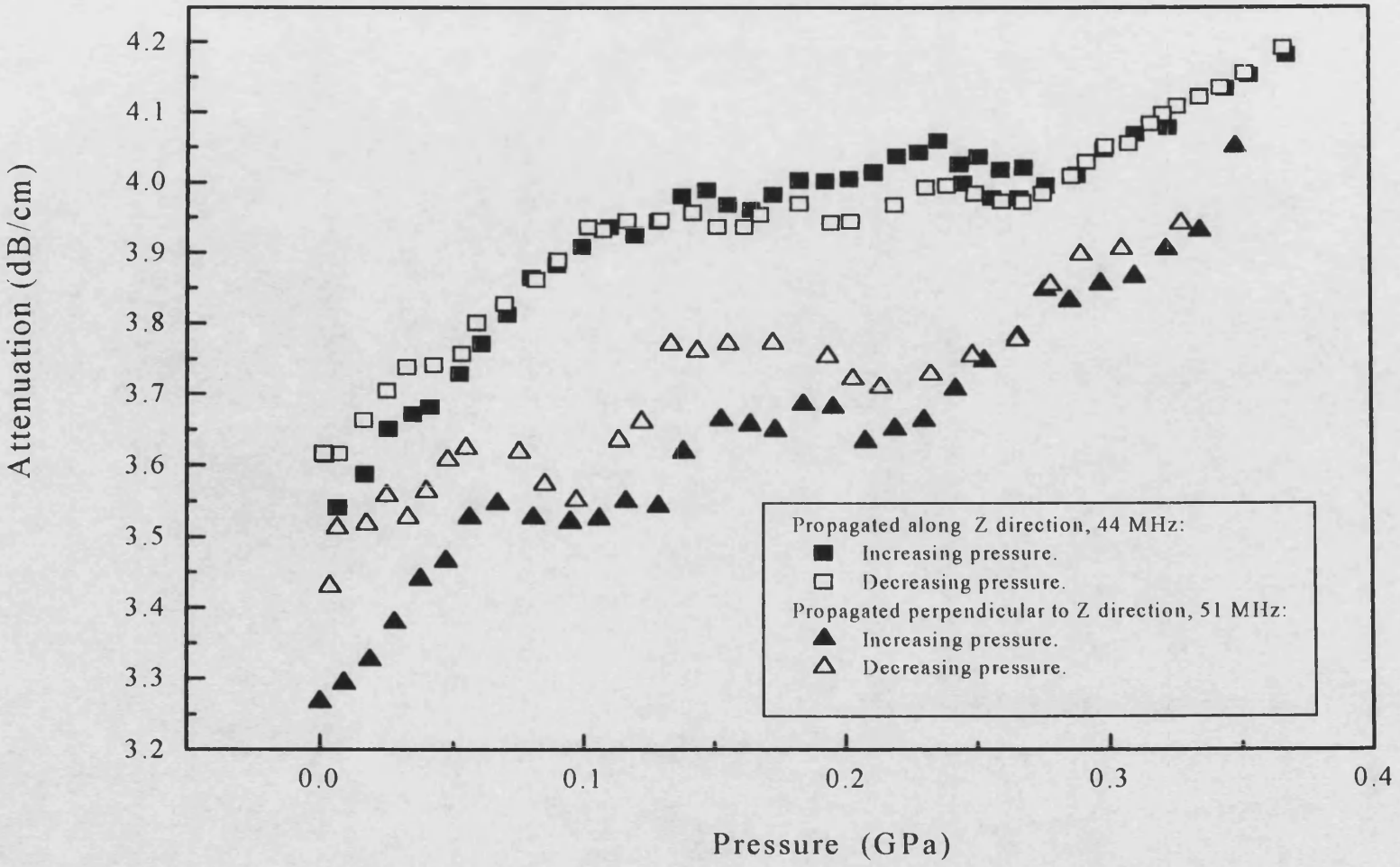

Fig.8.10 The pressure dependence of ultrasonic wave attenuation in ceramic alumina H880 at 30±0.5°C.

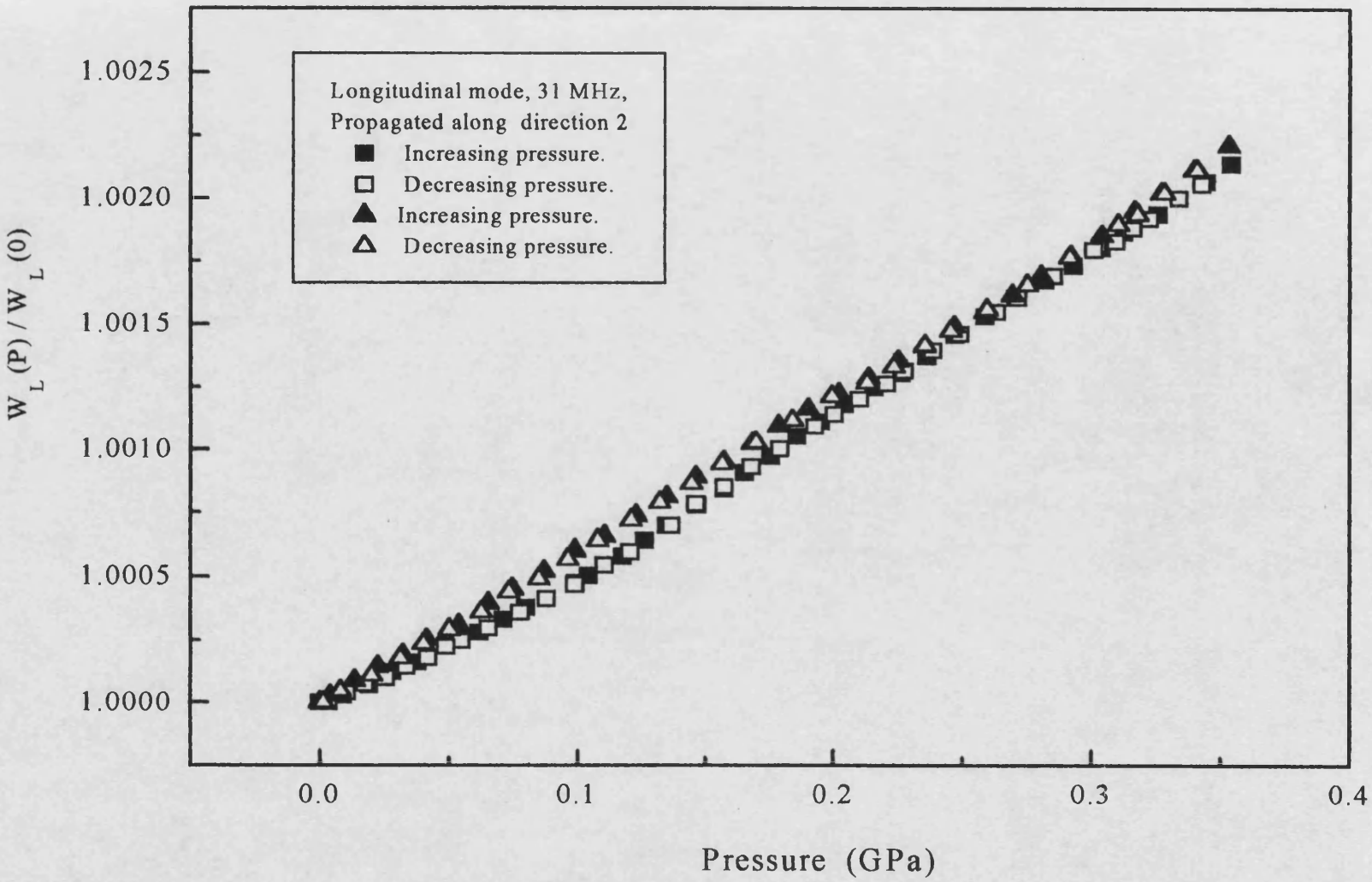

Fig.8.11 The pressure dependence of normalised longitudinal mode ultrasonic natural velocity of ceramic alumina AL23 at 30±0.5°C.

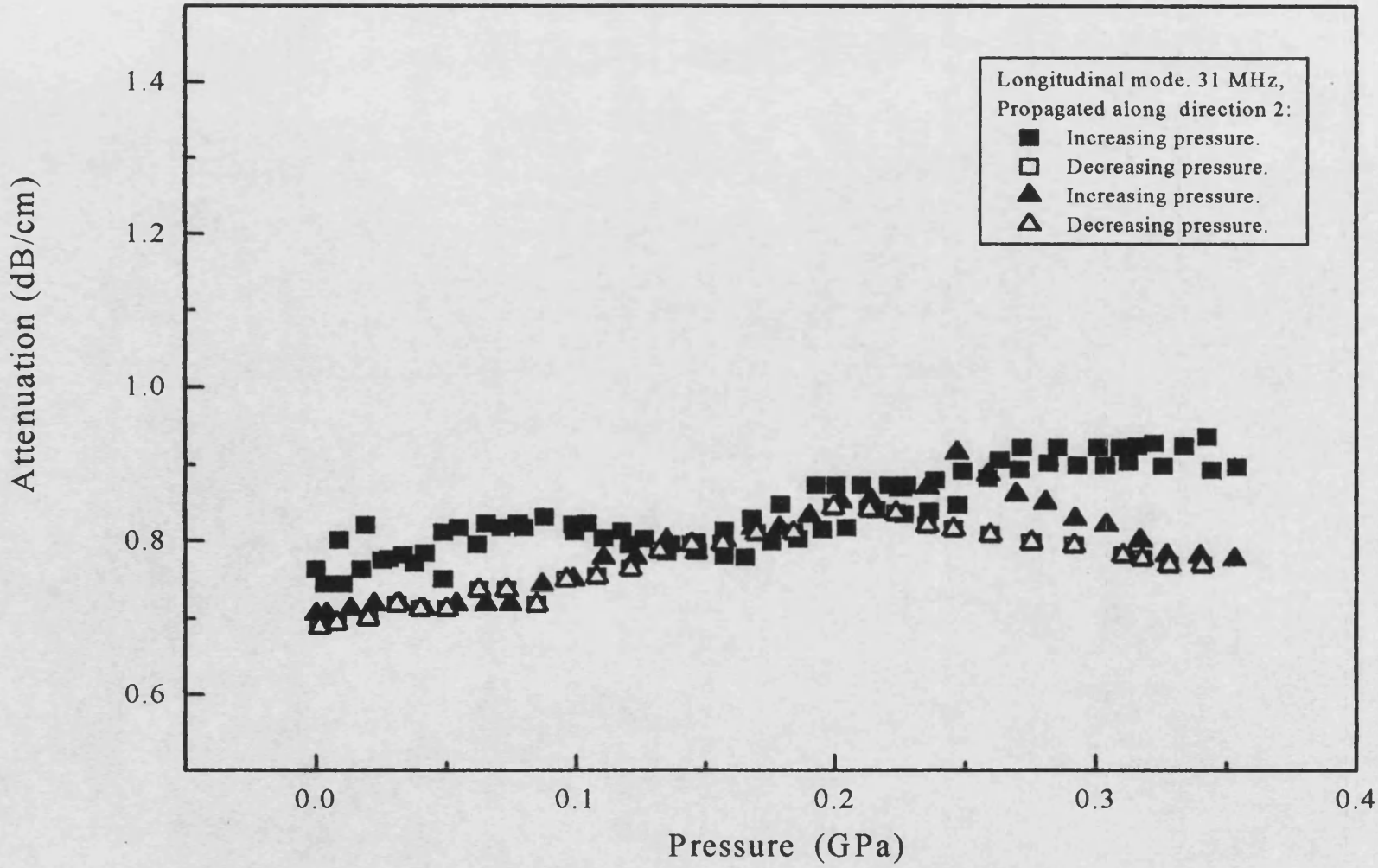

Fig.8.12 The pressure dependence of ultrasonic attenuation of ceramic alumina AL23 at 30±0.5°C.

sets of attenuation data is within the experimental errors (±0.1 dB/cm). The pressure induced changes in the attenuation in this sample are very small compared with those in the samples of D975 and H880. The pressure dependence up to 0.35 GPa of the shear natural velocities measured at 30.5MHz and 30±0.5°C is presented in Fig. 8.13. The pressure derivatives of natural velocities of sample AL23 at atmospheric pressure and 30±0.5°C are listed in table 8.5. The elastic moduli, the Poisson's ratio, the pressure derivatives of velocities and the elastic moduli and the long wavelength acoustic Grüneisen parameters of sample AL23 are given in Table 8.7.

Table 8.5 The pressure derivatives of longitudinal and shear natural velocities of sample AL23 at atmospheric pressure and 30±0.5°C measured at 31 MHz for longitudinal mode and 30.5 MHz for shear mode.

mode	Direction of propagation	Direction of polarisation	$(\partial W/\partial P)_{P=0}$ $(ms^{-1}GPa^{-1})$
Longitudinal	2	2	65±2
Longitudinal	2	2	65±2
Shear	1	2	27±2

8.6 Ceramic alumina SINC53

The hydrostatic pressure dependency of velocities and attenuations of ultrasonic waves propagated in the ceramic alumina SINC53 have been measured in directions parallel and perpendicular to Z for pressure up to 0.25 GPa. The normalised longitudinal and shear mode natural velocities of ultrasonic waves are shown in Fig. 8.14. and 15 respectively. The data for all the waves, presented in Fig.8.14 and 15, increase linearly and smoothly as pressure increases. The data measured in the direction parallel

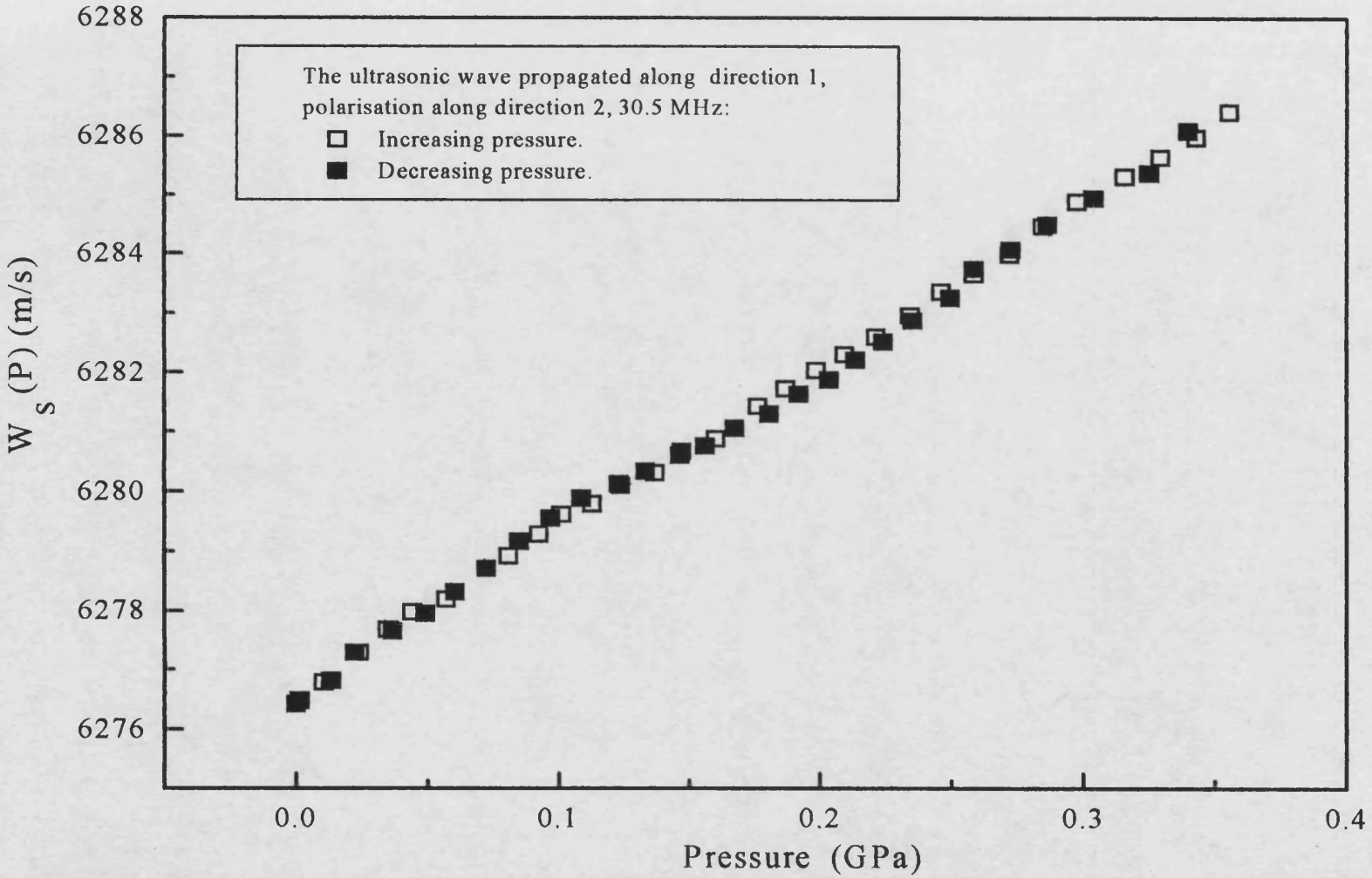

Fig. 8.13 The pressure dependence of shear mode ultrosonic natural velocity of cearmic alumina AL23 at 30±0.5 °C.

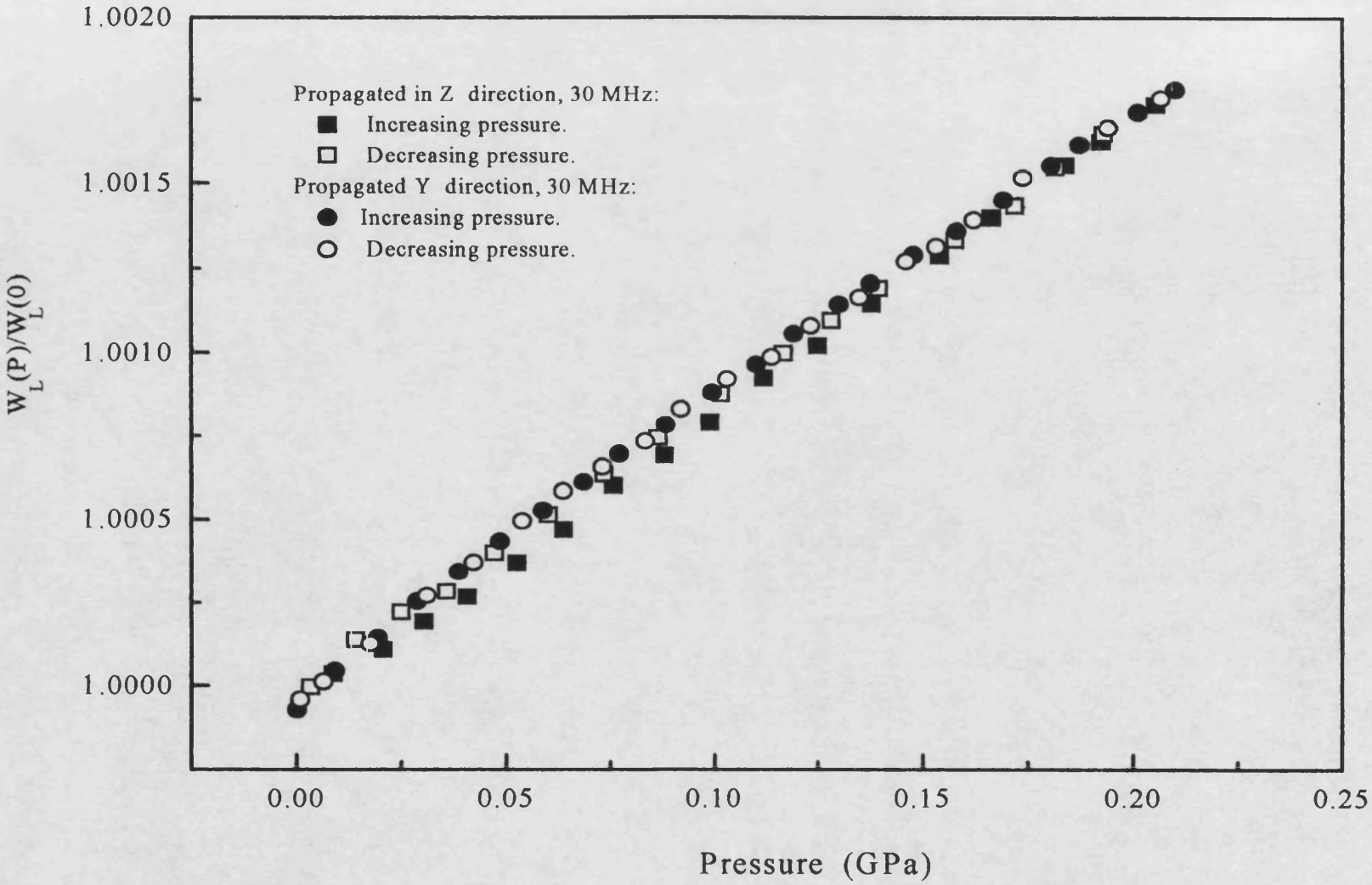

Fig.8.14 The pressure dependence of normalised longitudinal mode ultrasonic natural velocity of ceramic alumina SINC53 at 30±0.5 °C.

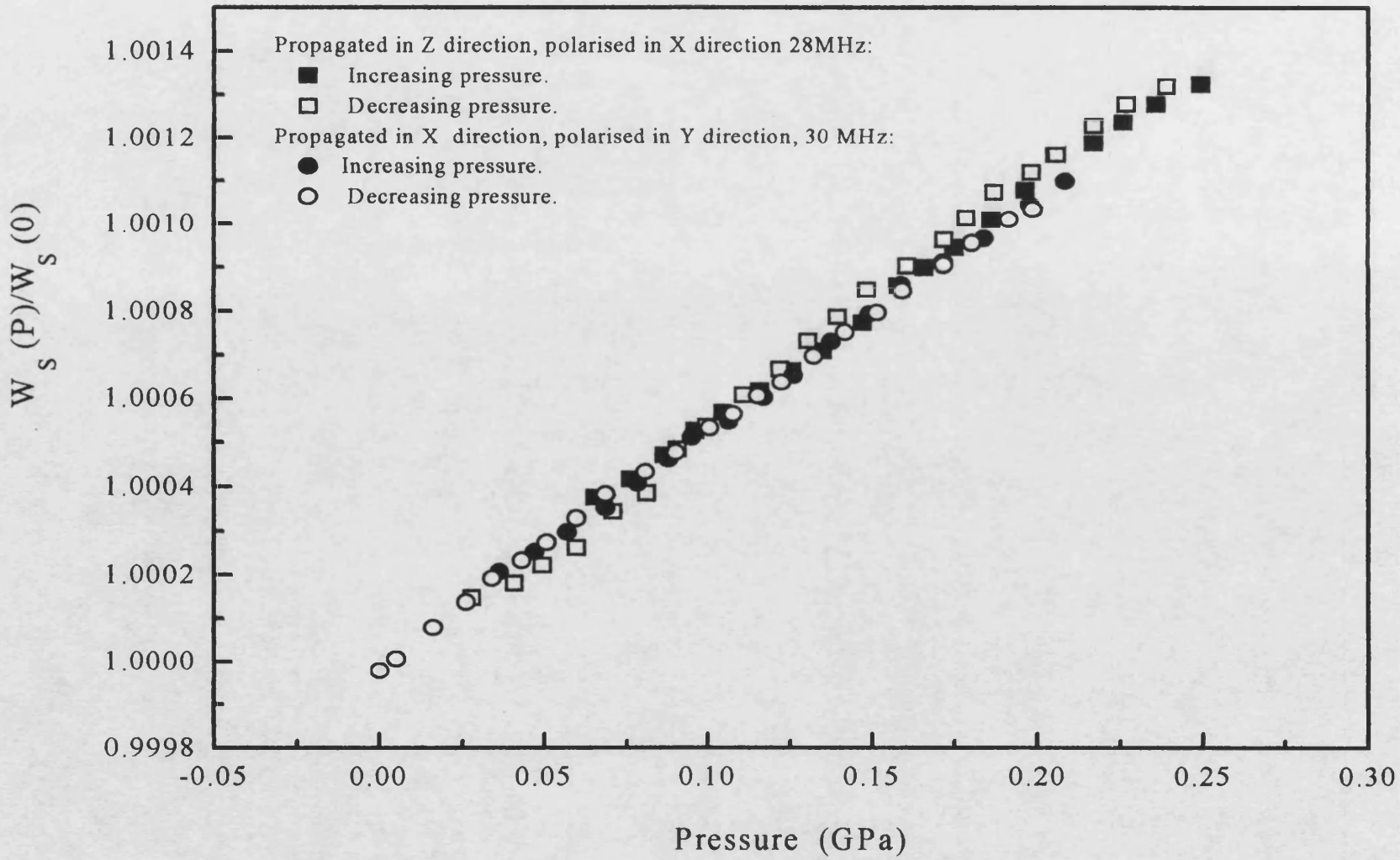

Fig.8.15 The pressure dependence of normalised shear mode ultrasonic natural velocity of ceramic alumina SINC53 at 30±0.50°C.

and perpendicular to Z coincide closely (Fig. 8.14 and 15). That means there is no directional dependence of pressure derivatives of natural velocities of sample SINC53. The pressure derivatives of natural velocities of sample SINC53 at atmospheric pressure and 30±0.5°C are listed in table 8.6.

Table 8.6 The pressure derivatives of longitudinal and shear natural velocities of ceramic alumina SINC53 at a frequency close to 30 MHz measured at atmospheric pressure and 30±0.5°C.

mode	Direction of propagation	Direction of polarisation	$(\partial W/\partial P)_{P=0}$ ($ms^{-1}GPa^{-1}$)
Longitudinal	Y	Y	84±2
Longitudinal	Z	Z	83±2
Shear	X	Y	30±2
Shear	Z	X	33±2

Fig. 8.16 shows the attenuation of 30 MHz longitudinal mode waves propagated in the Z and Y directions. The attenuation for the ultrasonic wave propagated in the Y direction is higher than that propagated in the Z direction.

8.7 Comparison of the data obtained with those reported in the literature and with data calculated for polycrystalline material from single-crystal data

The measured density of the ceramic alumina D999 is 3963±1 kg/m^3, which is comparable with the single-crystal density of α-alumina (3986 kg/m^3). This is a high purity sample (99.4 wt.%). The data for the sample D999 (Table 8. 7) are compared in Table 8.8 with the data calculated from

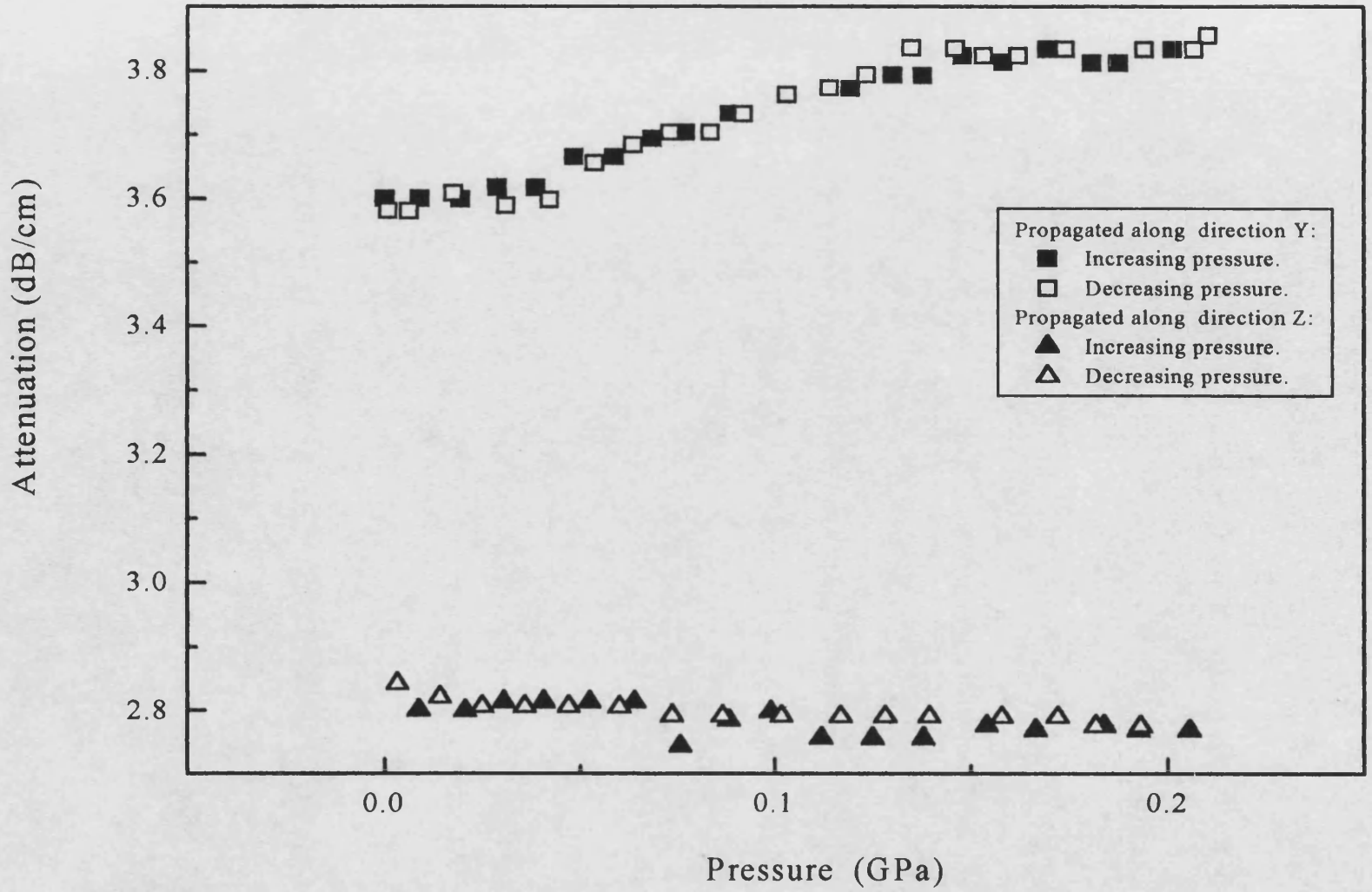

Fig. 8.16 The pressure dependence of attenuation of ultrasonic longitudinal wave in ceramic alumina SINC53 at 30±0.5°C.

the corresponding single-crystal data and the data measured by Chung and Simmons (1968) and Schreiber and Anderson (1966) on high purity, high density α-alumina samples. The results in Table 8.8 make it clear that the data for the sample D999 are in good agreement with measured data for the high purity high density samples in the literature and the polycrystalline data calculated from the corresponding single-crystal data. This scenario means that the data for D999 reflect the nature of the α-alumina grains in the material, although the data are slightly affected by the purity and density. It can be concluded that the large difference of the data of H880 from those of D999 (Table 8.7) arises from the contribution of the additions and the resident impurity that forms the intergrain phase of the ceramic H880.

Table 8.7 The density, ultrasonic wave velocities V, elastic moduli, pressure derivatives of natural velocities, pressure derivatives of the elastic moduli and the long wavelength acoustic mode Grüneisen parameters γ of the ceramic samples at room temperature. σ is the Poisson's ratio. W is the natural velocity.

Material	D999	D975	H880	AL23
Alumina content	99.4 wt.%[(a)]	97.0 wt.%[(a)]	87.1 wt.%[(a)]	99.7 wt.%[(a)]
ρ (kg/m^3)	3963±1	3803±1	3539±1	3877±1
Porosity	0.7%[(a)]	3.5%[(a)]	6.6%[(a)]	2.9%[(a)]
V_S (m/s)	6399±10	6074±10	5423±10	6276±10
V_L (m/s)	10765±10	10104±10	9093±10	10564±10
C_{11} (GPa)	459.2±0.7	388.3±0.7	292.6±0.7	432.6±0.7
C_{44} (GPa)	162±0.4	140.3±0.4	104.1±0.4	152.7±0.4
B^S (GPa)	243±0.9	.201±0.9	154±0.9	229±0.9
E (GPa)	398±2	342±2	255±2	375±2
σ	0.227±0.002	0.217±0.002	0.224±0.002	0.227±0.002
$(\partial W_L/\partial P)_{P=0}$ ($ms^{-1}GPa^{-1}$)	64±2	67±2	48±2	65±2
$(\partial W_S/\partial P)_{P=0}$ ($ms^{-1}GPa^{-1}$)	28±2	31±2	11±2	27±2
$(\partial C_{11}/\partial P)_{P=0}$	6.1±0.1	5.8±0.1	3.7±0.1	6.0±0.1
$(\partial C_{44}/\partial P)_{P=0}$	1.65±0.08	1.66±0.08	0.66±0.08	1.55±0.08
$(\partial B^S/\partial P)_{P=0}$	3.9±0.2	3.5±0.2	2.9±0.2	3.9±0.2
γ_L	1.45±0.04	1.32±0.04	0.82±0.04	1.41±0.04
γ_S	1.07±0.06	1.02±0.06	0.32±0.06	0.99±0.06
γ^{el}	1.20±0.04	1.12±0.04	0.49±0.04	1.13±0.04

Material	SINC53
Alumina content	95.5 wt.% [(a)]
Chromium Sesquioxide	0.14 wt.% [(a)]
ρ (kg/m^3)	3594±1
Porosity	Not available[(a)]
V_S (m/s)	5732±10
V_L (m/s)	9676±10
C_{11} (GPa)	336.5±0.7
C_{44} (GPa)	118.1±0.4
B^S (GPa)	179±0.9
E (GPa)	290±2
σ	0.230±0.002
$(\partial W_L/\partial P)_{P=0}$ ($ms^{-1}GPa^{-1}$)	84±2
$(\partial W_S/\partial P)_{P=0}$ ($ms^{-1}GPa^{-1}$)	32±2
$(\partial C_{11}/\partial P)_{P=0}$	6.5±0.1
$(\partial C_{44}/\partial P)_{P=0}$	1.53±0.08
$(\partial B^S/\partial P)_{P=0}$	4.4±0.2
γ_L	1.55±0.04
γ_S	0.99±0.06
γ^{el}	1.18±0.04

(a) The data marked with "(a)" are supplied by DERA.

Table. 8.8 Comparison of the data of D999 with that reported in the literature and with data for polycrystalline material calculated from the corresponding single-crystal data. All the data are at room temperature.

Item	D999	Chung (1968)[a]	Schreiber (1966)[a]	Chung (1968)[b] (calculated)
Alumina content	99.4 wt.%[e]	99.9%	Lucalox sample[c]	
ρ (kg/m^3)	3963±1	3974	3972	3986
Porosity	0.7%[e]			
V_S (m/s)	6399±10	6377	6373.0	
V_L (m/s)	10765±10	10845	10845	
C_{11} (GPa)	459.2±0.9	467.39	467.15	466.01-468.96
C_{44} (GPa)	162±0.5	161.6	161.32	160.02-164.45
B^S (GPa)	243±1	251.92	252.0	247.99-252.29
E (GPa)	398±3		398.8	395.66-404.21
σ	0.227±0.002		0.2363	
$(\partial V_L/\partial P)_{P=0}$ ($ms^{-1}GPa^{-1}$)		53.5	51.75	
$(\partial V_S/\partial P)_{P=0}$ ($ms^{-1}GPa^{-1}$)		22.0	22.07	
$(\partial W_L/\partial P)_{P=0}$ ($ms^{-1}GPa^{-1}$)	64±2	67.9[d]	66.12[d]	
$(\partial W_S/\partial P)_{P=0}$ ($ms^{-1}GPa^{-1}$)	28±2	30.5[d]	30.51[d]	
$(\partial C_{11}/\partial P)_{P=0}$	6.1±0.1	6.51		6.58
$(\partial C_{44}/\partial P)_{P=0}$	1.65±0.06	1.77		1.73
$(\partial B^S/\partial P)_{P=0}$	3.9±0.1	4.16	3.98	4.27
γ_L	1.45±0.03	1.58	1.528	
γ_S	1.07±0.05	1.22	1.201	
γ^{el}	1.20±0.03	1.34	1.31	

(a) Measured data in literature.

(b) Data calculated from the corresponding single-crystal data by Chung (1968).

(c) Lucalox alumina is a high pure high-density polycrystalline alumina. It contains 99% Al_2O_3 with small amounts of MgO as the major impurity.

(d) In the literature only $(\partial V_L/\partial P)_{P=0}$ and $(\partial V_S/\partial P)_{P=0}$ were given. $(\partial W_L/\partial P)_{P=0}$ and $(\partial W_S/\partial P)_{P=0}$ listed here with superscript "(d)" are calculated from the values $(\partial V_L/\partial P)_{P=0}$, $(\partial V_S/\partial P)_{P=0}$ and the relative change in the linear dimension as a function of hydrostatic pressure.

(e) Supplied by DERA.

8.8 Comparison of the ultrasonic attenuation between different ceramic aluminas

To provide a comparative view of the difference in the ultrasonic attenuation between different ceramic aluminas, the pressure dependences of the ultrasonic longitudinal wave attenuation measured at 30 or 31MHz in different ceramic aluminas are plotted in Fig.8.17. It can be seen that the ultrasonic longitudinal wave attenuation in the ceramic aluminas D999 and AL23 is lower than those in ceramic aluminas D975 and H880 and SINC53. For D999 and AL23 the changes in the attenuation induced by application of pressure are less pronounced than those of the ceramic aluminas D975 and H880. These differences can be attributed to the different grain boundaries in different ceramic aluminas. The ultrasonic longitudinal wave attenuation in the ceramic alumina SINC53 is much higher than for the other four ceramic aluminas. The scanning electron microscopy images shows that the largest grain size of ceramic alumina SINC53 is about 60-80μm (Page 7-28). The size is comparable with the wavelength used; that is, about 330μm for longitudinal mode. Therefore the contribution of gain scattering to attenuation in sample SINC53 is more

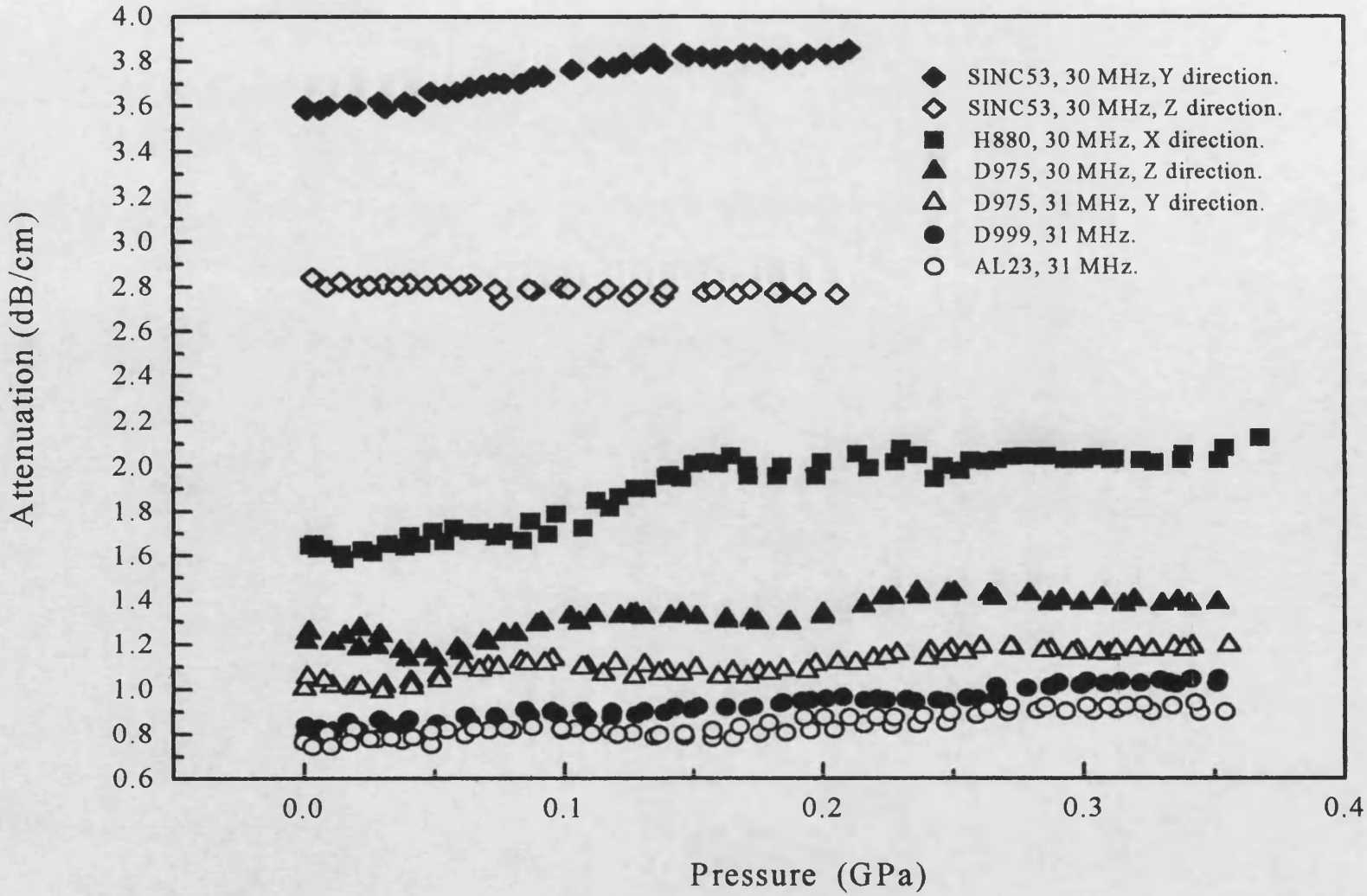

Fig. 8.17 The pressure dependence of attenuation of longitudinal ultrasonic wave in ceramic aluminas at 30±0.5°C and near 30MHz.

significant than that in the other four ceramic aluminas.

For H880 (Page 8-16) and D975, the attenuation for the ultrasonic wave propagated in the Z direction is higher than that propagated in the X or Y direction. This could be due to the fact that the texture of faceted grains results in the thickness of the grain boundary layers in the Z direction being larger than that in the X or Y direction. For sample SINC53 the situation is opposite. The attenuation for the ultrasonic wave progated in the Y direction of ceramic alumina SINC53 is higher than that propagated in the Z direction. The reason could be that there are attenuation mechanisms in ceramic alumina SINC53, which are related to large grains in the material.

8.9 Volume compression extrapolated to higher pressure

The volume compression V(P)/V(0) of the samples D999, D975, AL23, SINC53 and H880 has been extrapolated up to 20 GPa using Murnaghan's equation-of-state (equation 2.32), the bulk modulus B^S and its pressure derivative $(\partial B^S/\partial P)_{P=0}$. The sets of data are presented in Fig. 8.18. The volume compression of these materials, due to their large elastic stiffness, is very small compared with that of many solids (Wang et al. 1992, Anderson 1966). Sample H880 is the most compressible of the five ceramic aluminas.

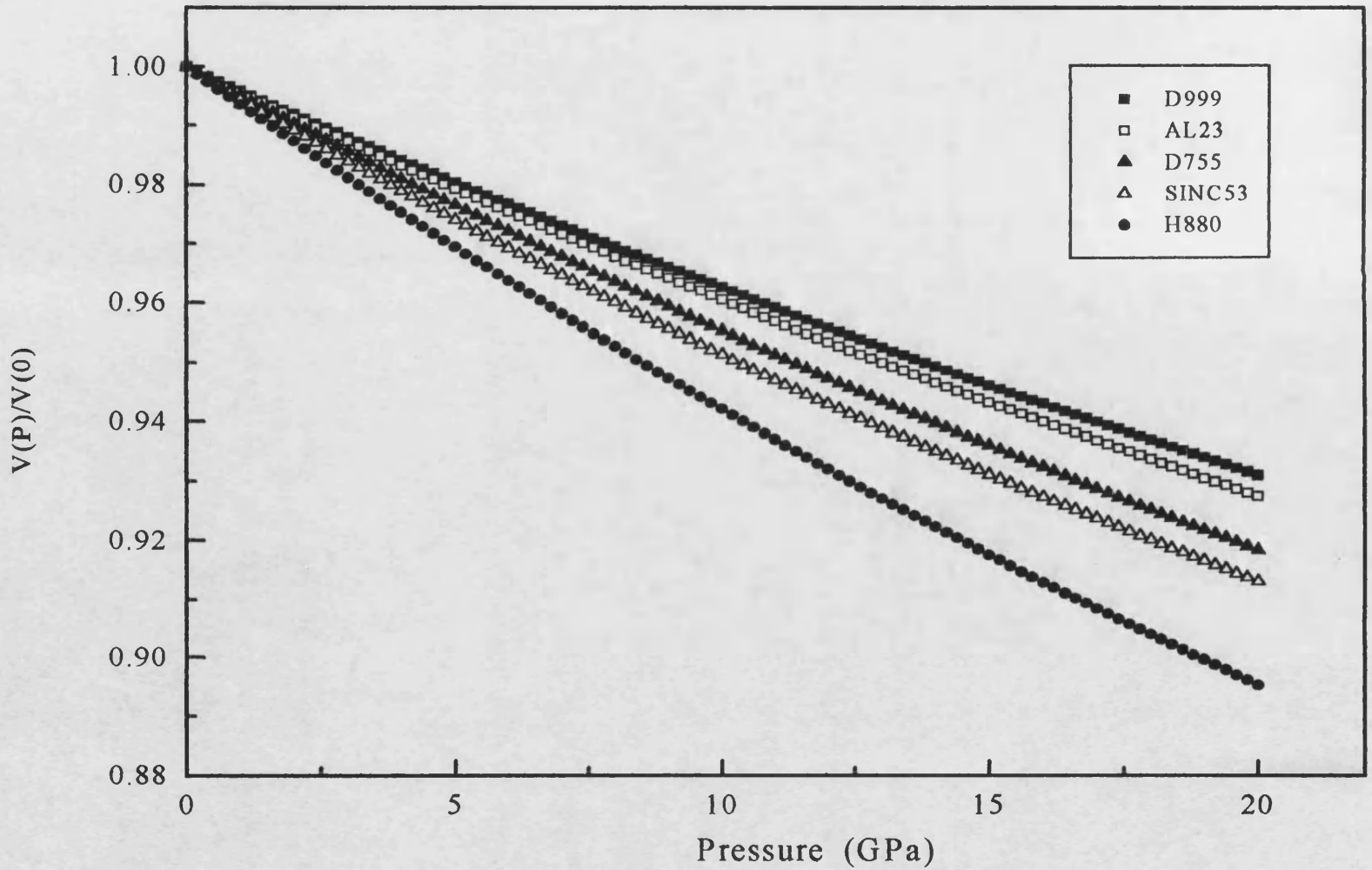

Fig.8.18 The volume compression of the ceramic aluminas extrapolated from the bulk modulus B and (dB/dP) measured under moderate pressures and 30±0.5°C.

Chapter 9 The Results and Discussion of the AC Impedance of Ceramic Aluminas

9.1 The experiment procedures and the samples

Impedance measurements have been made on four types of materials: ceramic alumina D999, AL23, D975 and H880, with the sizes of $30\times30\times0.5mm^3$. The density, purity and porosity of samples are listed in table 8.7. To carry out measurements at higher temperatures, the electrodes were formed by either golden evaporation or silver paint. The results are not electrode dependent. For the ceramic alumina D999 above room temperature results measured with silver paint are included here. The results shown here for D975, H880 and AL23 and for D999 below room temperature have been measured with golden evaporated electrodes. The sizes of the electrodes and the thicknesses of the samples are listed in table 9.1. The Z directions of the sample H880 and D975 are perpendicular to the electrodes. Impedance spectroscopy measurements were made in the temperature ranges between 17°C and 600°C~ 704°C at intervals of 10°C ~50°C and between 20K and 320K at an interval 10K. The frequency range used was 5 Hz up to 10MHz. The OSC level used was 1Vrms. After each measurement the overall contact resistance, which was about 1 Ohm at room temperature, was checked again.

The impedance analyser is set to measure the conductance G and susceptance B as a function of frequency. The dielectric constant and dielectric loss are calculated from

$$\varepsilon' = \frac{d}{A\varepsilon_o}\frac{B}{\omega} \tag{9.1}$$

and

$$\varepsilon'' = \frac{d}{A\varepsilon_o}\frac{G}{\omega} \tag{9.2}$$

respectively. Here d is the thickness and A the area of the sample. The real and imaginary parts of the complex impedance are calculated from

$$Z' = \frac{G}{G^2 + B^2} \tag{9.3}$$

and

$$Z'' = \frac{B}{G^2 + B^2} \tag{9.4}$$

respectively.

For the impedance analyser, parameters obtained have a basic accuracy of 0.1%. Due to the fact that the sample area is much larger than the thickness; the error arising from the edge effect should not be significant. The relative error of the dielectric constant ε′ and dielectric loss ε″ arises from the thickness and area measurements and can be calculated from

$$\left|\frac{\Delta\varepsilon'}{\varepsilon'}\right| = \frac{1}{\varepsilon'}\left(\frac{\partial\varepsilon'}{\partial A}\Delta A + \frac{\partial\varepsilon'}{\partial d}\Delta d\right) = \left|\frac{\Delta A}{A}\right| + \left|\frac{\Delta d}{d}\right|$$

and

$$\left|\frac{\Delta\varepsilon''}{\varepsilon''}\right| = \frac{1}{\varepsilon''}\left(\frac{\partial\varepsilon''}{\partial A}\Delta A + \frac{\partial\varepsilon''}{\partial d}\Delta d\right) = \left|\frac{\Delta A}{A}\right| + \left|\frac{\Delta d}{d}\right|$$

respectively which have been estimated as 1.5% using the ΔA and Δd listed in table 9.1. This was the main error of the dielectric constant ε′ and the main error of the dielectric loss ε″ below room temperature. Above room temperature the error of admittance arising from the sampleholder leakage was about 1% (Chapter 5). Therefore above room temperature relative error of dielectric loss ε″ was 2.5%.

Table 9.1 The sizes of the electrodes and the thicknesses of the alumina samples at room temperature.

Sample	Electrode	Electrode size (mm^2)	Sample thickness (mm)
D999	Silver paint	714±5	0.504±0.004
D999	Golden	743±5	0.511±0.004
AL23	Golden	748±5	0.498±0.004
D975	Golden	743±5	0.505±0.004
H880	Golden	716±5	0.503±0.004

9.2 Complex plane profiles

9.2.1 The complex plane profiles of sample D999

Examination of a series of complex impedance profiles in order of increasing measurement temperature reveals three distinct regions. Fig. 9.1 shows the complex plane profile of impedance data of sample D999 obtained at 280°C; the results consist of a half semicircle (the first arc) and a small part of a second arc. The half semicircle occurs at low values of Z′ (i.e. at high frequency) and it passes through the origin. As the temperature is increased, the diameter of the half-semicircle decreases and the second arc moves gradually into the available frequency range, as shown in Fig. 9.2. From this figure it can be seen that the diameter of the first arc decreases and the frequency at which the two arcs join increases with increasing temperature. Fig. 9.3 and 9.4 show the complex plane profiles of the impedance data between 410°C and 450°C. Fig. 9.4, a 400-times enlargement of the lower left corner of Fig. 9.3, shows the first arc while the Fig. 9.3 shows the second. The ratio of diameters of the second to the first arc is about 500. That is the reason why the first arc cannot be seen in

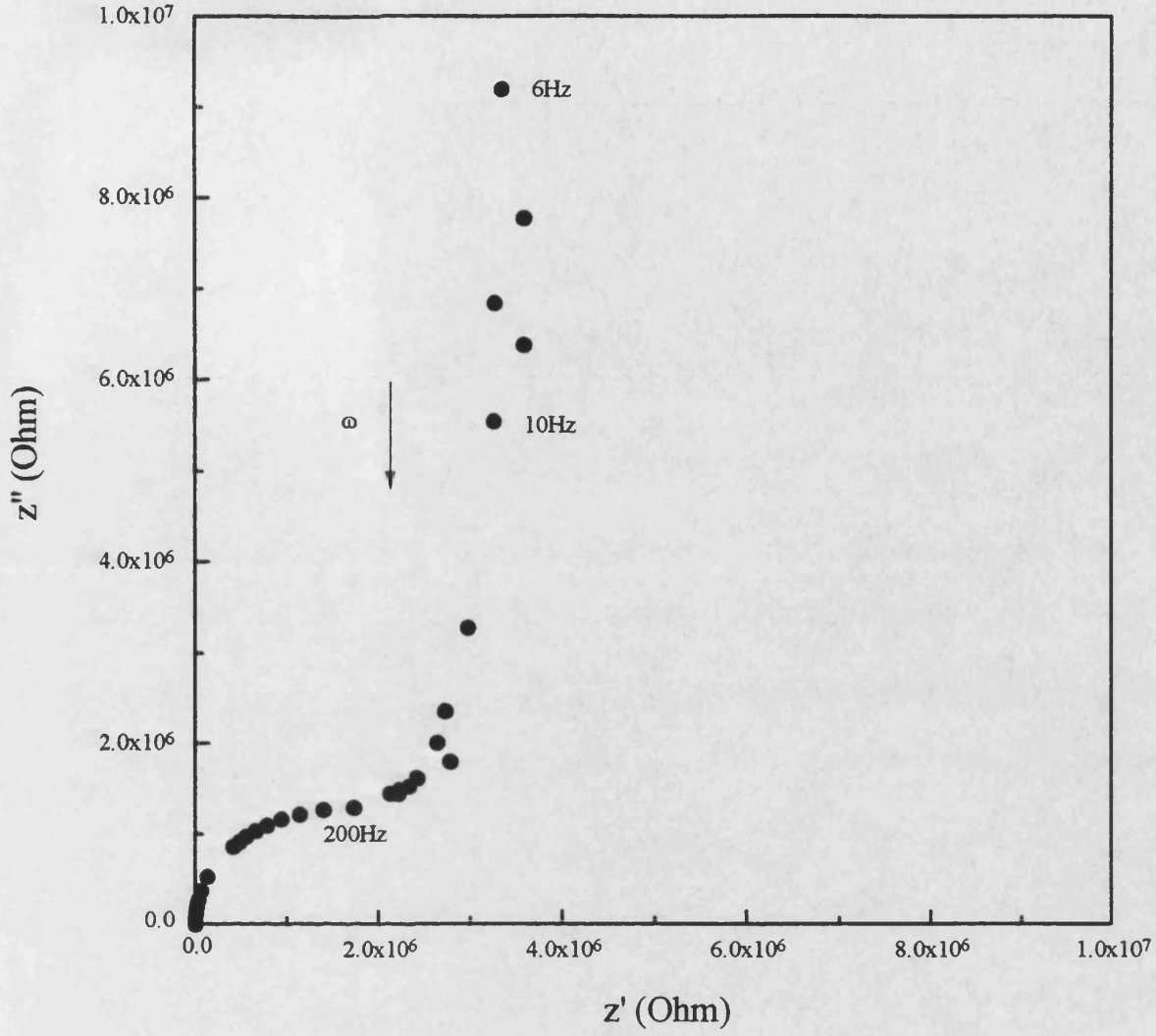

Fig. 9.1 Complex plane profile of the impedance data for the ceramic alumina D999 at 280°C.

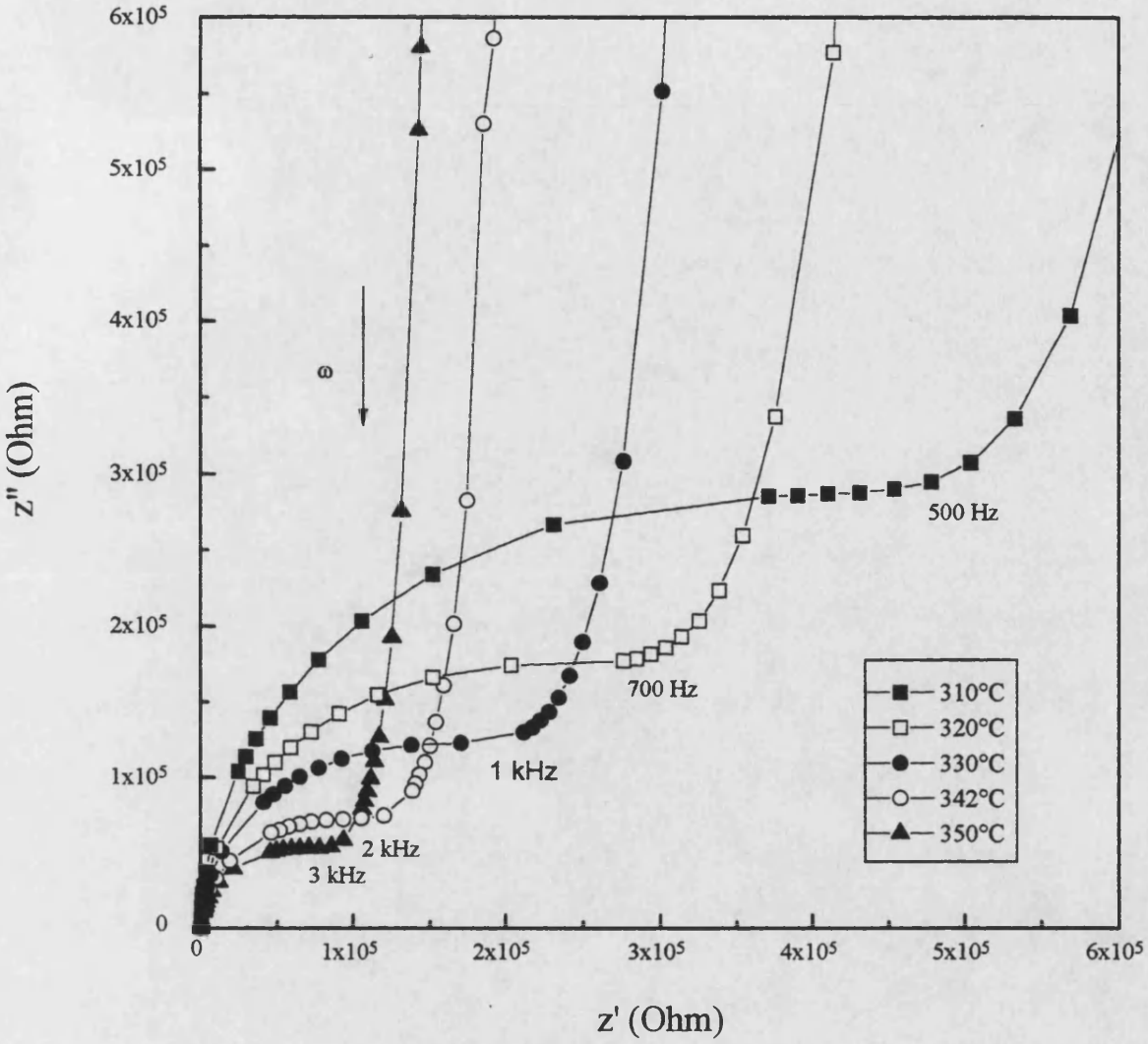

Fig.9.2 Complex plane profiles of the impedance data for the ceramic alumina D999 between 310°C and 350°C.

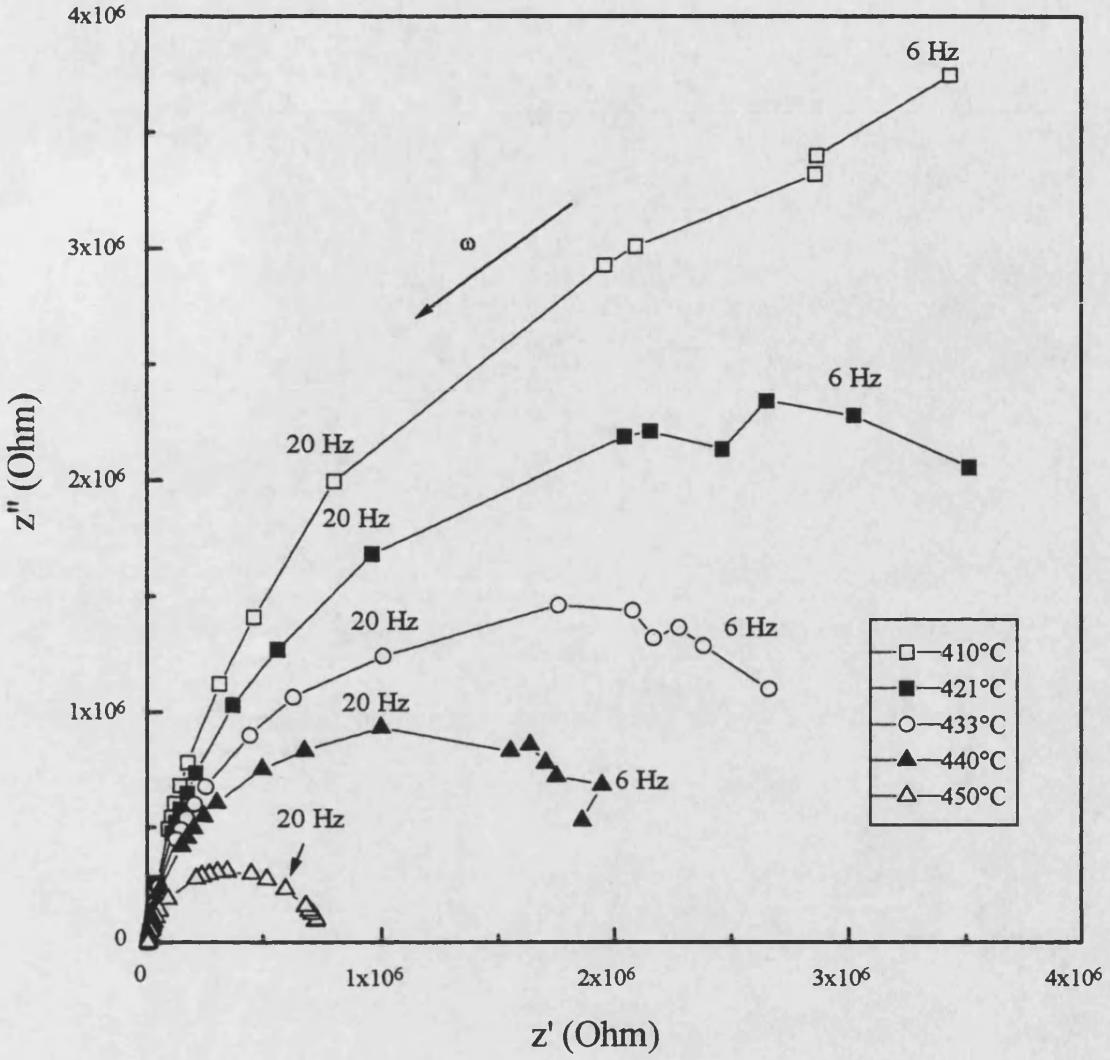

Fig.9.3 Complex plane profiles of the impedance data for the ceramic alumina D999 between 410°C and 450°C.

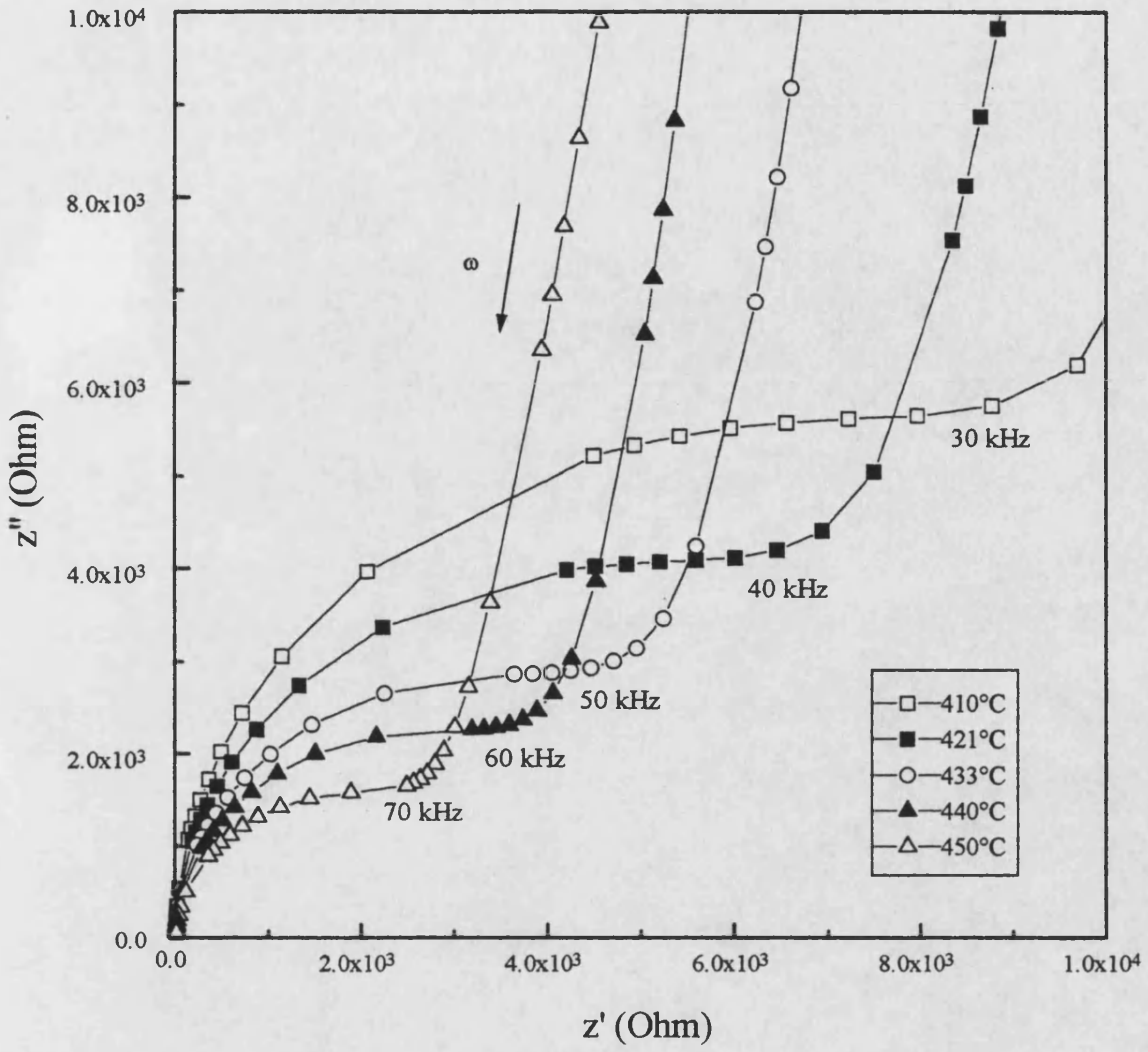

Fig.9.4 The enlarged graph of Fig.9.3 for Z' from 0 to 10^4 Ohm.

Fig. 9.3. From Fig. 9.3 it can be seen that at 410°C about 1/4 of the semicircle of the second arc is in the available frequency range. As the temperature increases to 450°C, almost the whole semicircle of the second arc comes into the available frequency range. The diameters of both arcs decrease with increase of temperature. From these figures 9.3 and 9.4 it can be seen that the first semicircle is partially overlapped with the second one. Fig. 9.5 shows the complex plane profiles of the impedance data between 500°C and 620°C. At about 550°C a small part of a third semicircle appears in the lowest frequency range; when the temperature increases, this semicircle moves gradually into the available frequency range. As temperature increases to 620°C, almost the whole of the third semicircle comes into the available frequency range. The third semicircle partially overlaps the second one. From the enlarged graph (Fig. 9.6) of Fig. 9.5, it can be seen that the first arc gradually moves out of the available frequency range as temperature increases. On a log-log scale, the behaviour described above can be seen more clearly. On the log-log scale the shapes of the three arcs are changed (Fig. 9.7-9.8). From Fig. 9.7-9.8, it can be seen that at 240°C only one arc lies in the available frequency range. At about 280°C the junction A of the first and second arcs appears at the low frequency end of the available frequency range. As temperature increases, the frequency of this point increases. At about 550°C the junction B of the second and third arcs appears at the low frequency end. As the temperature increases, these two junctions A and B move towards higher frequency with A getting nearer the high frequency end of the available frequency range. This means that if temperature were to be increased further, the first arc would move out of the available frequency range. This case illustrates that performing impedance measurements in an appropriate temperature and frequency range is very important for a

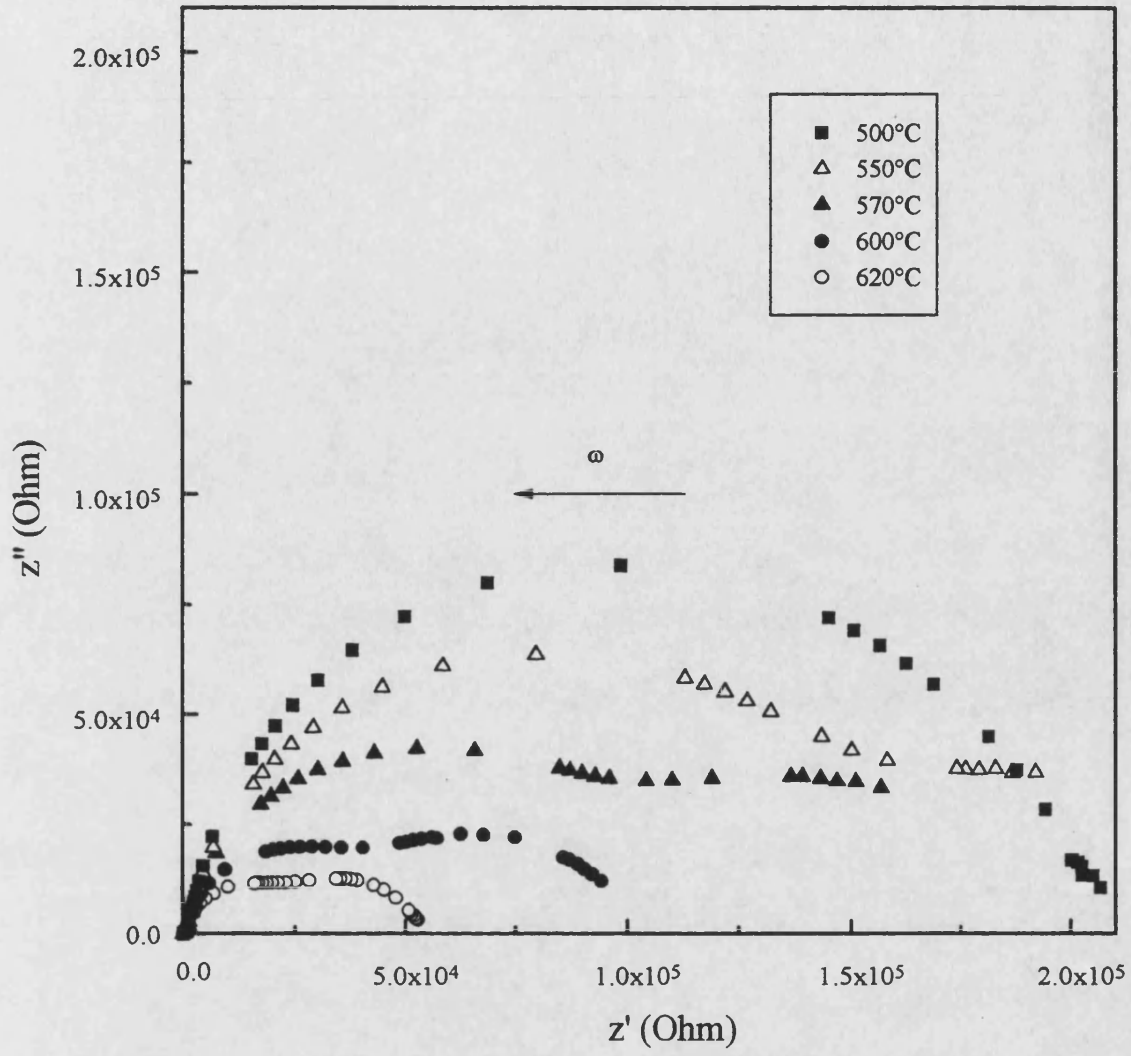

Fig. 9.5 Complex plane profiles of the impedance data for the ceramic alumina D999 between 500°C and 620°C.

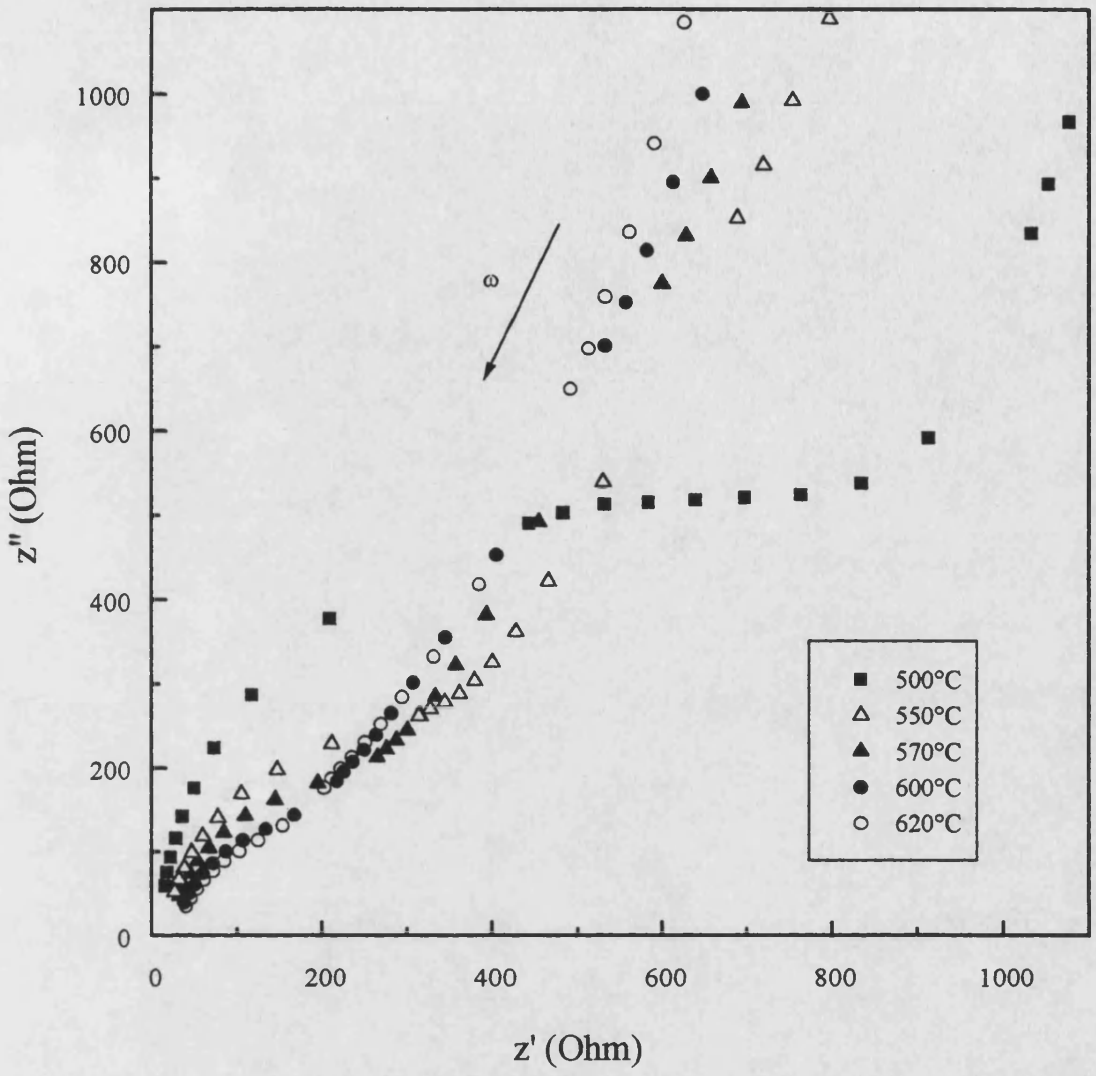

Fig. 9.6 The enlarged graph of Fig.9.5 for Z' from 0 to 1100 Ohm.

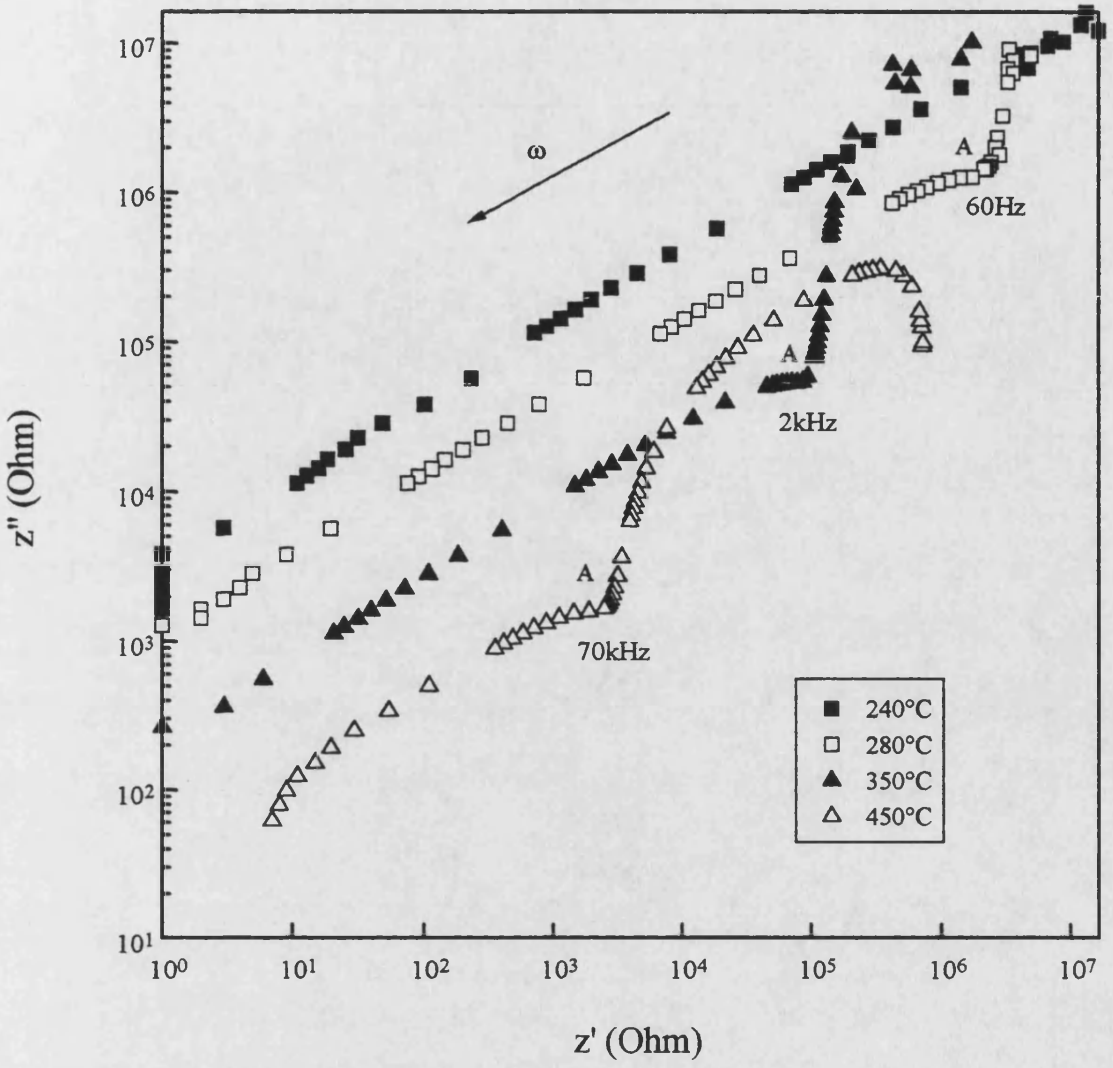

Fig. 9.7 Complex plane profiles of the impedance data of the ceramic D999 between 240°C and 450°C in log-log scale.

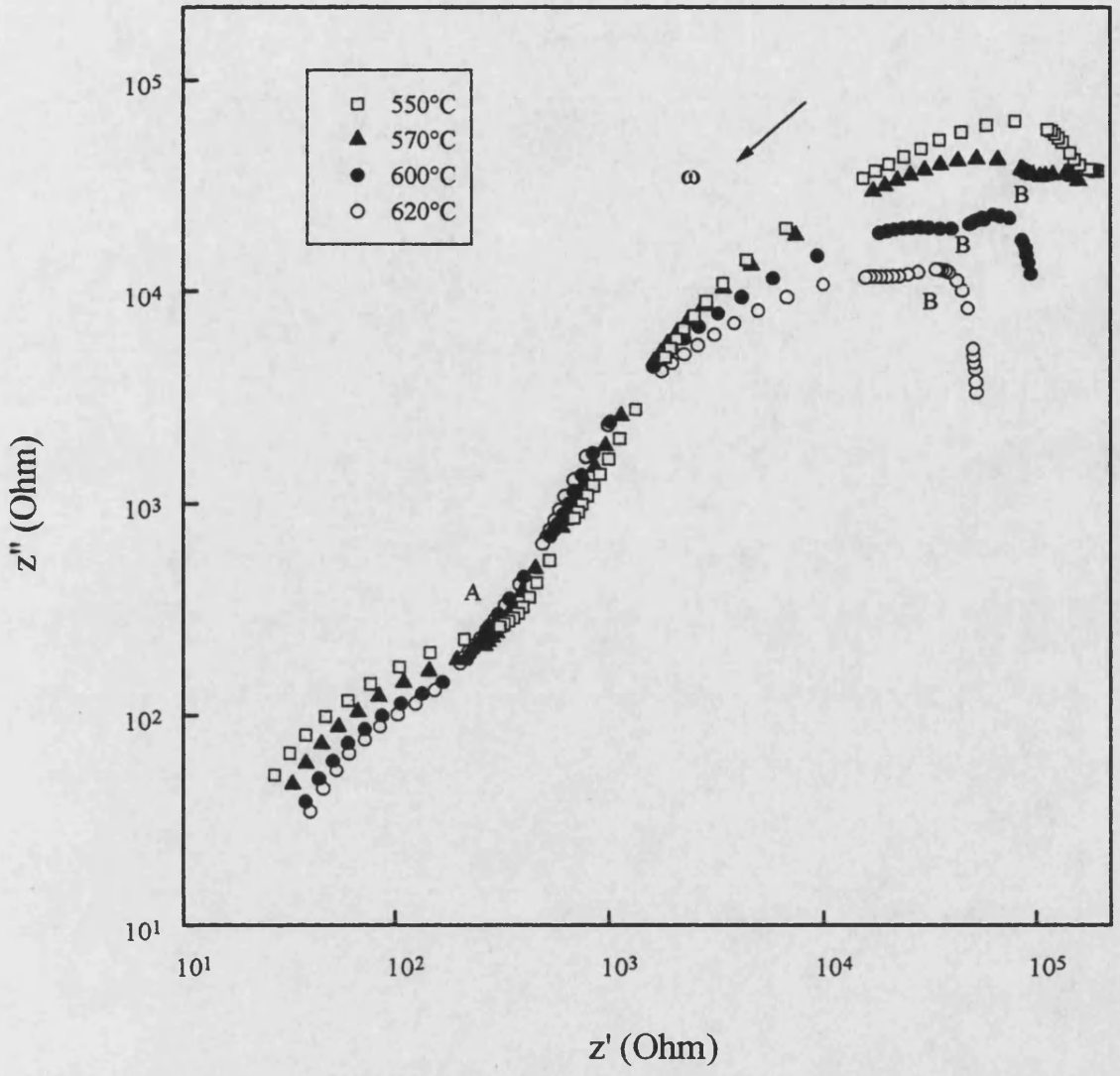

Fig.9.8 Complex plane profiles of the impedance data for the ceramic alumina D999 between 550°C and 620°C in log-log scale.

systematic analysis of the impedance of these materials.

9.2.2 The complex plane profiles of sample AL23

Examination of a series of complex impedance profiles in order of increasing measurement temperature reveals two distinct regions. Fig. 9.9 shows the complex plane profile of impedance data of sample AL23 obtained between 399°C an 500°C; below 500°C there is only one arc (part of first semicircle) in the available frequency range; at 500°C a small part of a second arc (part of a second semicircle) comes into the available frequency range. Fig. 9.10 and Fig. 9.11 show the complex plane profiles of impedance data obtained for sample AL23 between 521°C and 640°C; Fig. 9.12 presents a 5-times enlargement of the lower left corner of Fig. 9.11. Those figures show that as the temperature is increased, the second arc moves gradually into the available frequency range; the frequency of the junction point of the first and second semicircle increases; the diameter of both the first and the second semicircle decreases. Also it can be seen from these figures that the first and second semicircles are partially overlapped and the first semicircle passes through the origin. From the log-log scale plots (fig. 9.13 and 14) of the data from Fig. 9.10 and 11 the behaviour described above can be seen more clearly. As temperature increases to 687°C, the whole of the second semicircle comes into the available frequency range (Fig. 9.15). From Fig. 9.15 only the second semicircle can be seen clearly. To display the first semicircle clearly the lower left corner of Fig. 9.15 is enlarged in Fig. 9.16. The log-log scale plots (Fig. 9.17) of the data from Fig. 9.15 show that the complex impedance profiles of AL23 have two distinct regions more clearly than the linear profiles do. From these complex impedance profiles, similar common characters to those found in complex impedance profiles (described above for both AL23 and D999) are shown clearly;

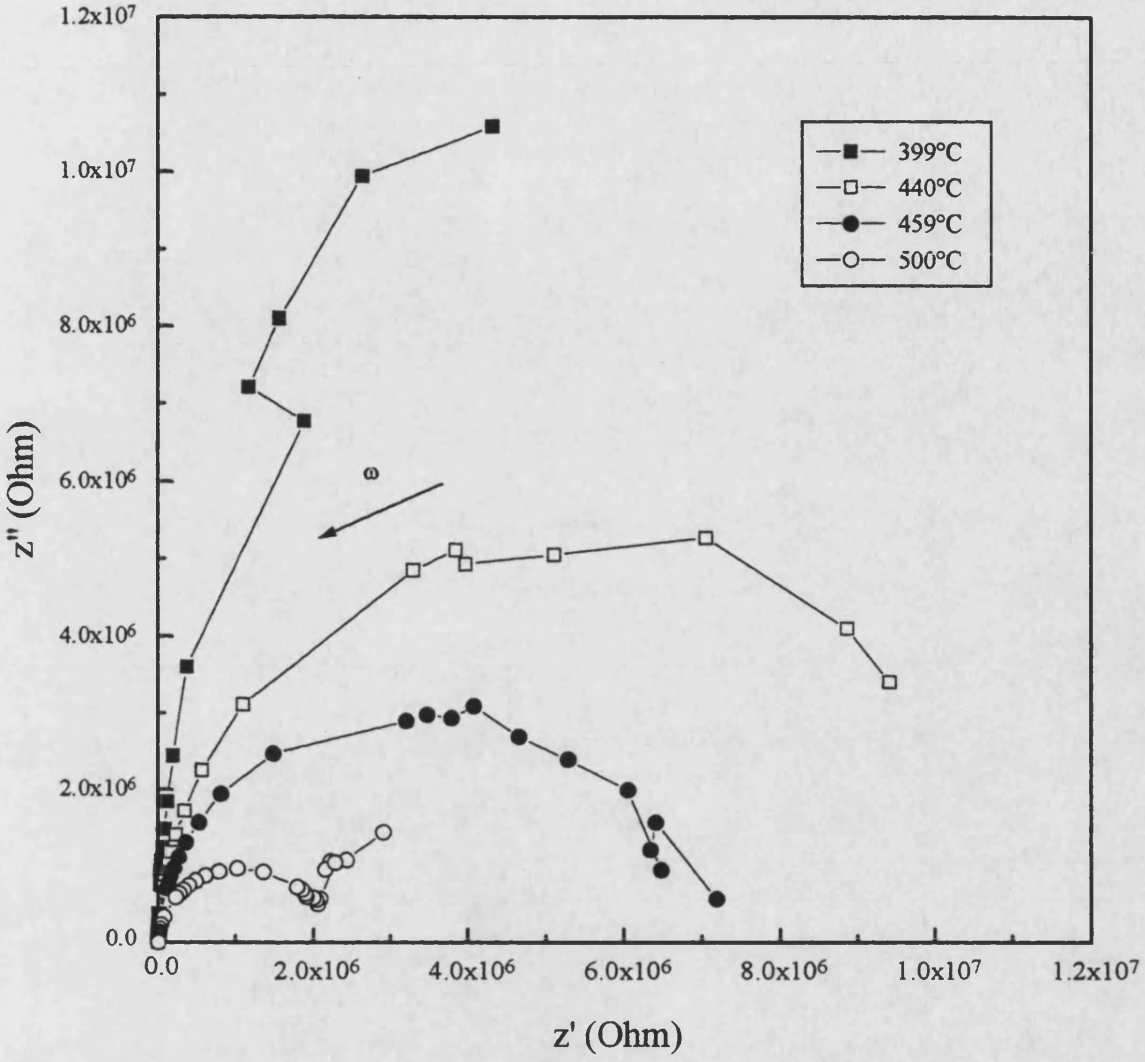

Fig.9.9 Complex plane profiles of the impedance data for the ceramic alumina AL23 between 399°C and 500°C.

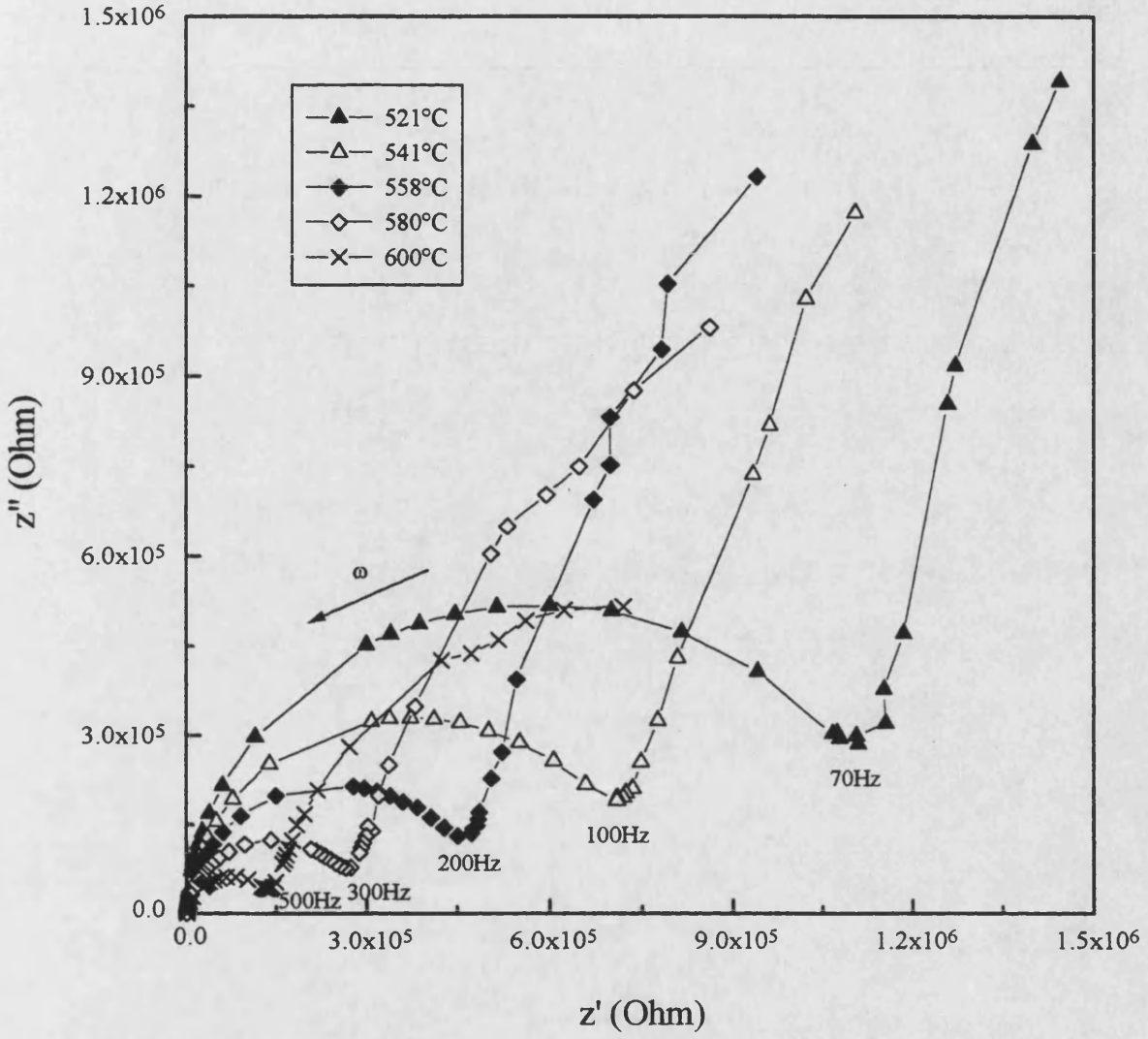

Fig.9.10 Complex plane profiles of the impedance data for the ceramic alumina AL23 between 521°C and 600°C.

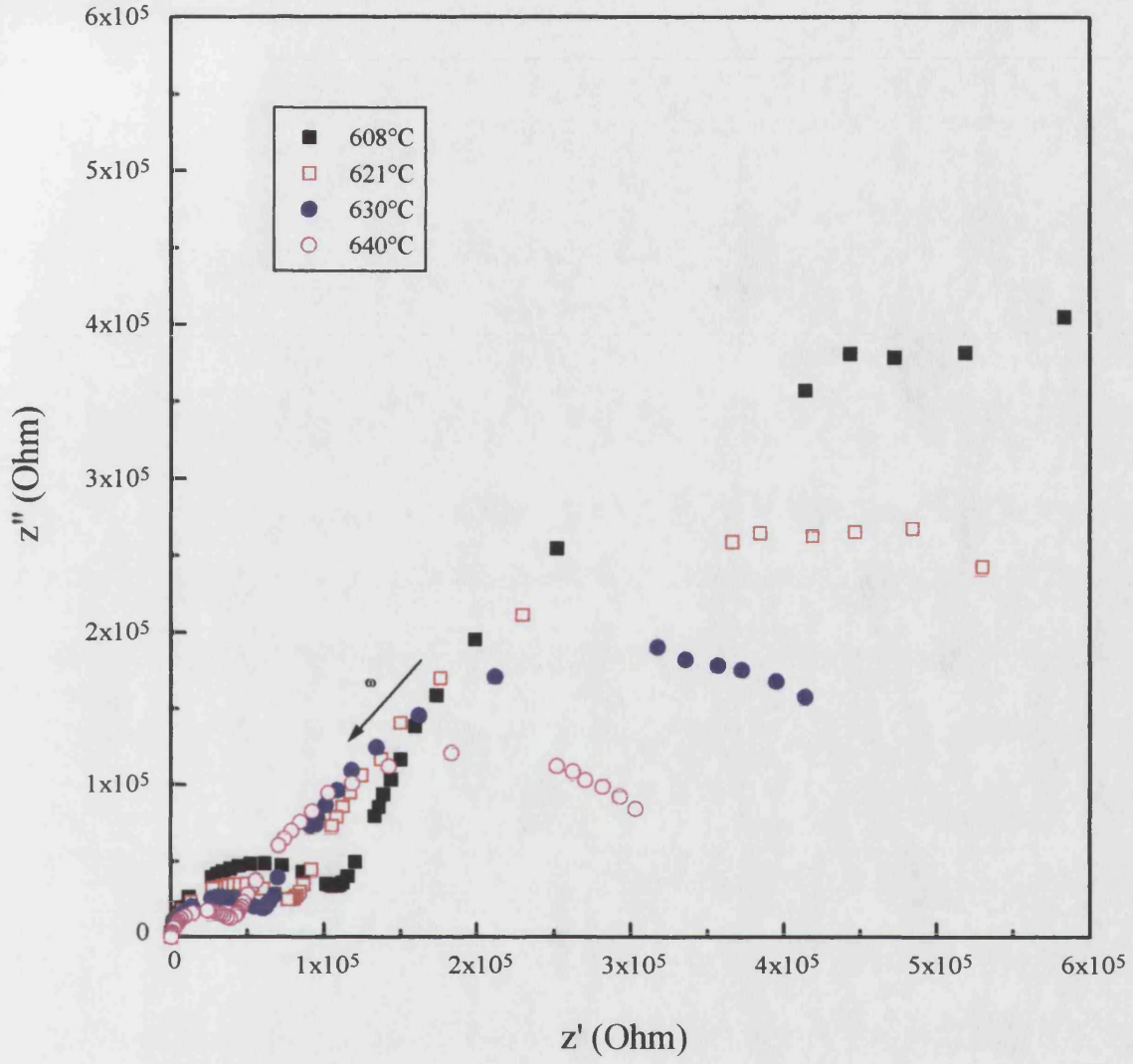

Fig.9.11 Complex plane profiles of the impedance data for the ceramic alumina AL23 between 608°C and 640°C.

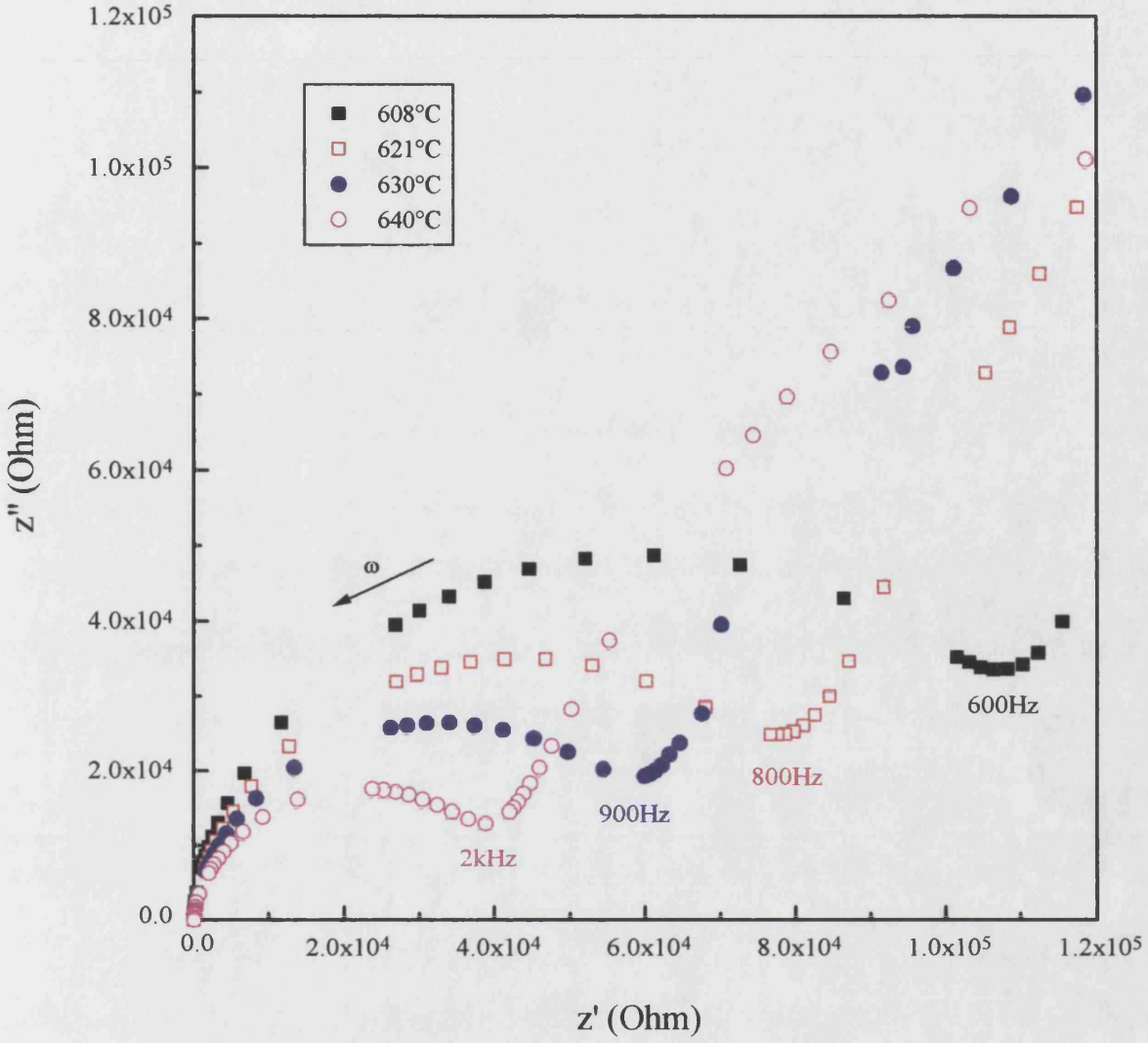

Fig.9.12 The five-times enlargment of the lower left corner of fig.9.11.

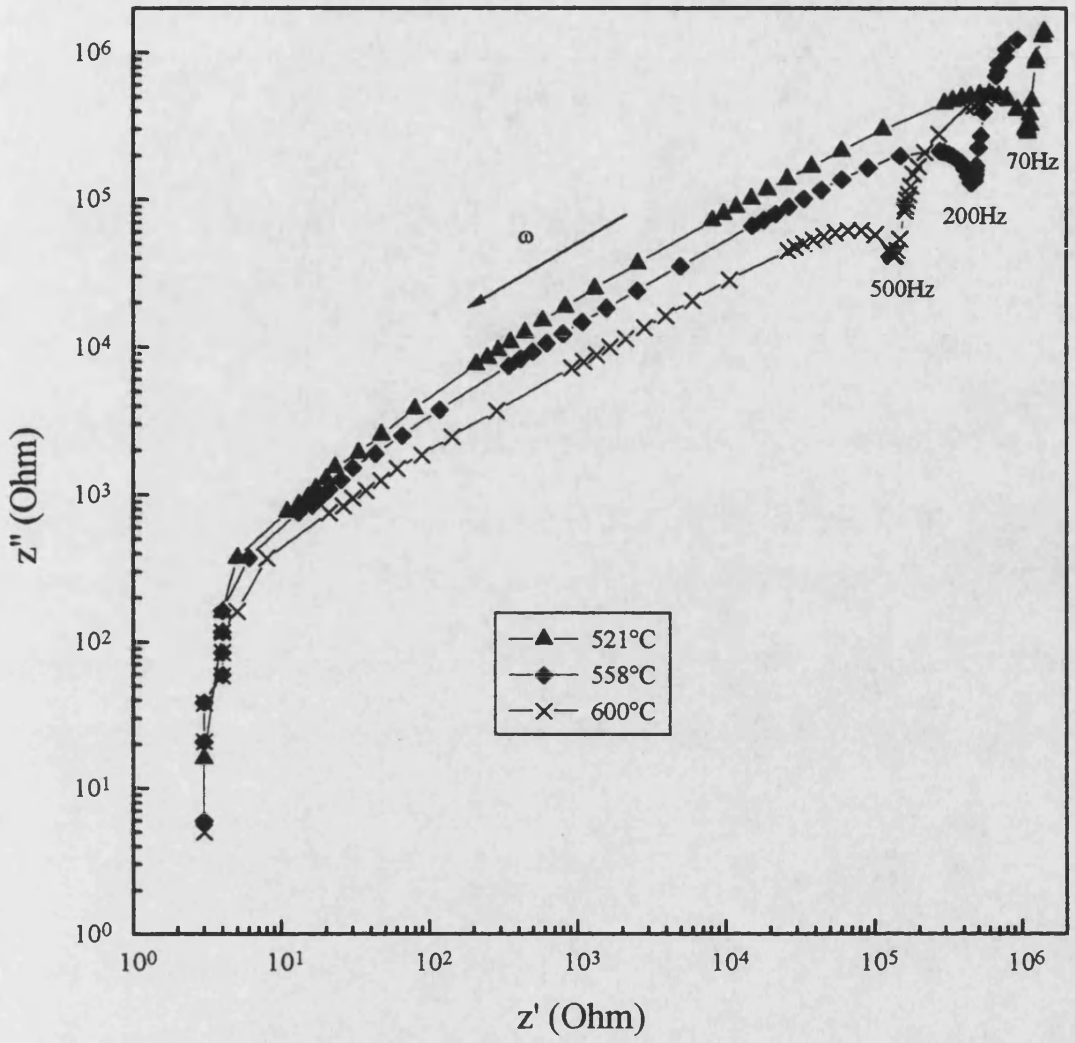

Fig.9.13 Log-log scale complex plane profiles of the impedance data for the ceramic alumina AL23 between 521°C and 600°C.

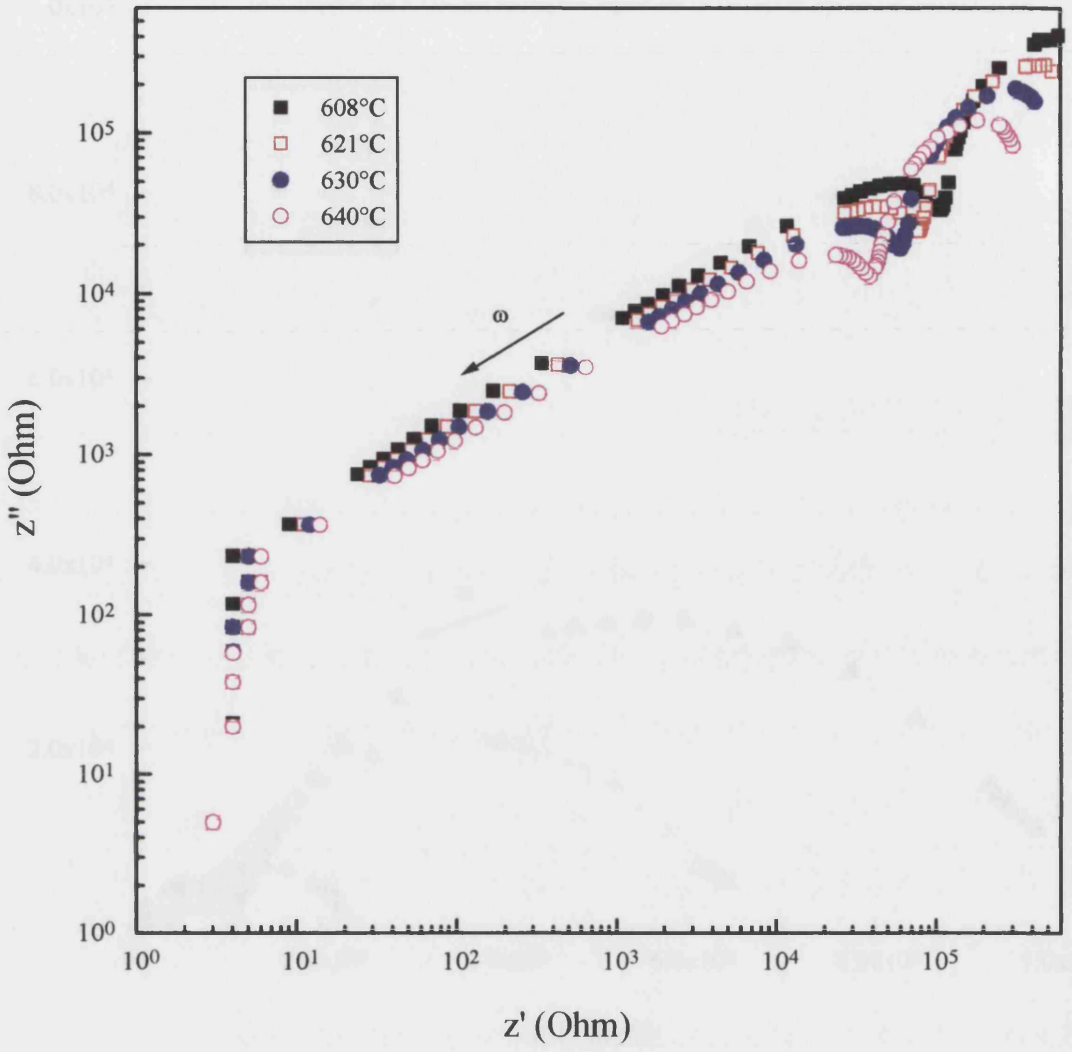

Fig.9.14 Complex plane profiles of the impedance data for the ceramic alumina AL23 between 608°C and 640°C.

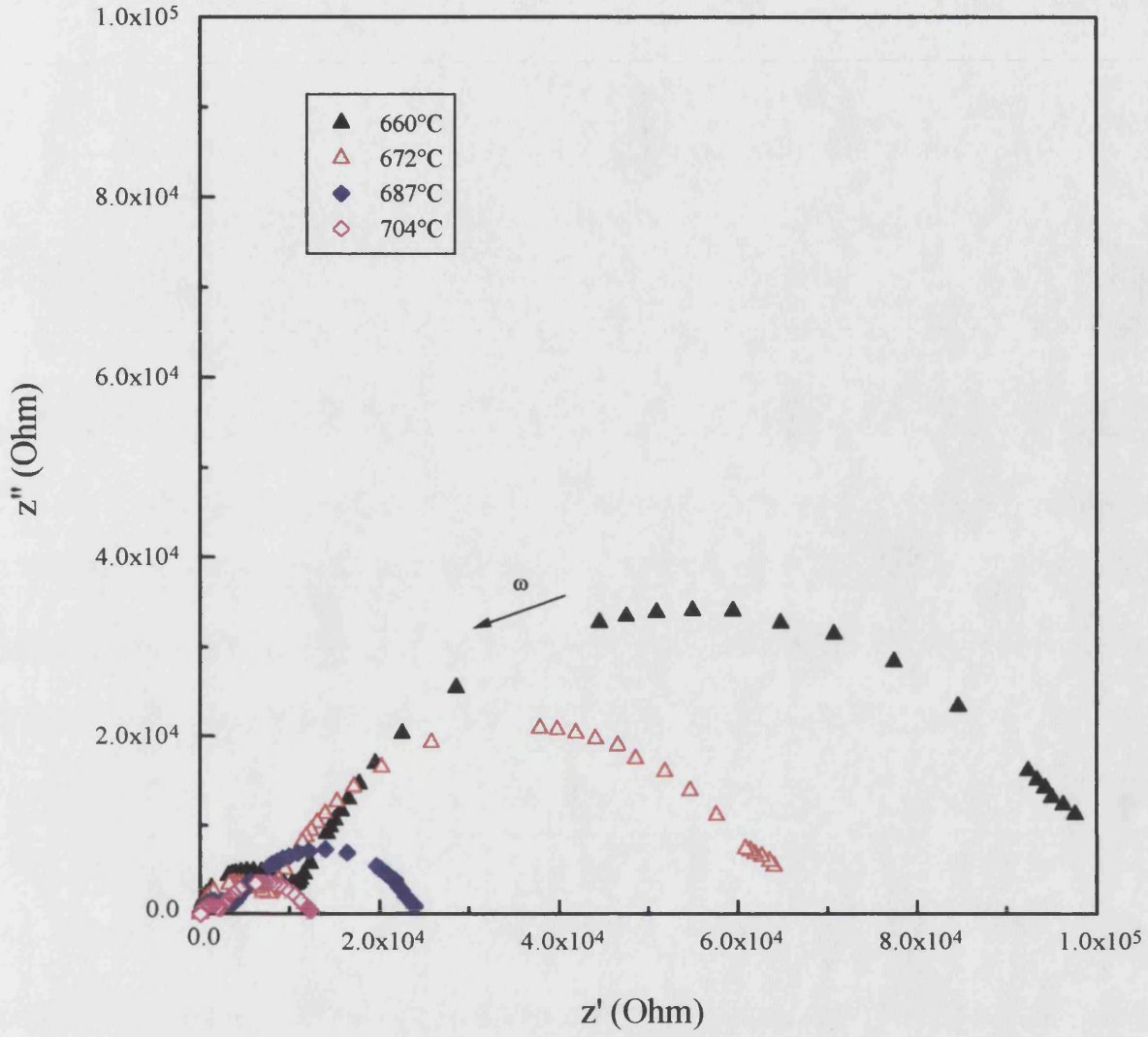

Fig. 9.15 Complex plane profiles of the impedance data for the ceramic alumina AL23 between 660°C and 704°C.

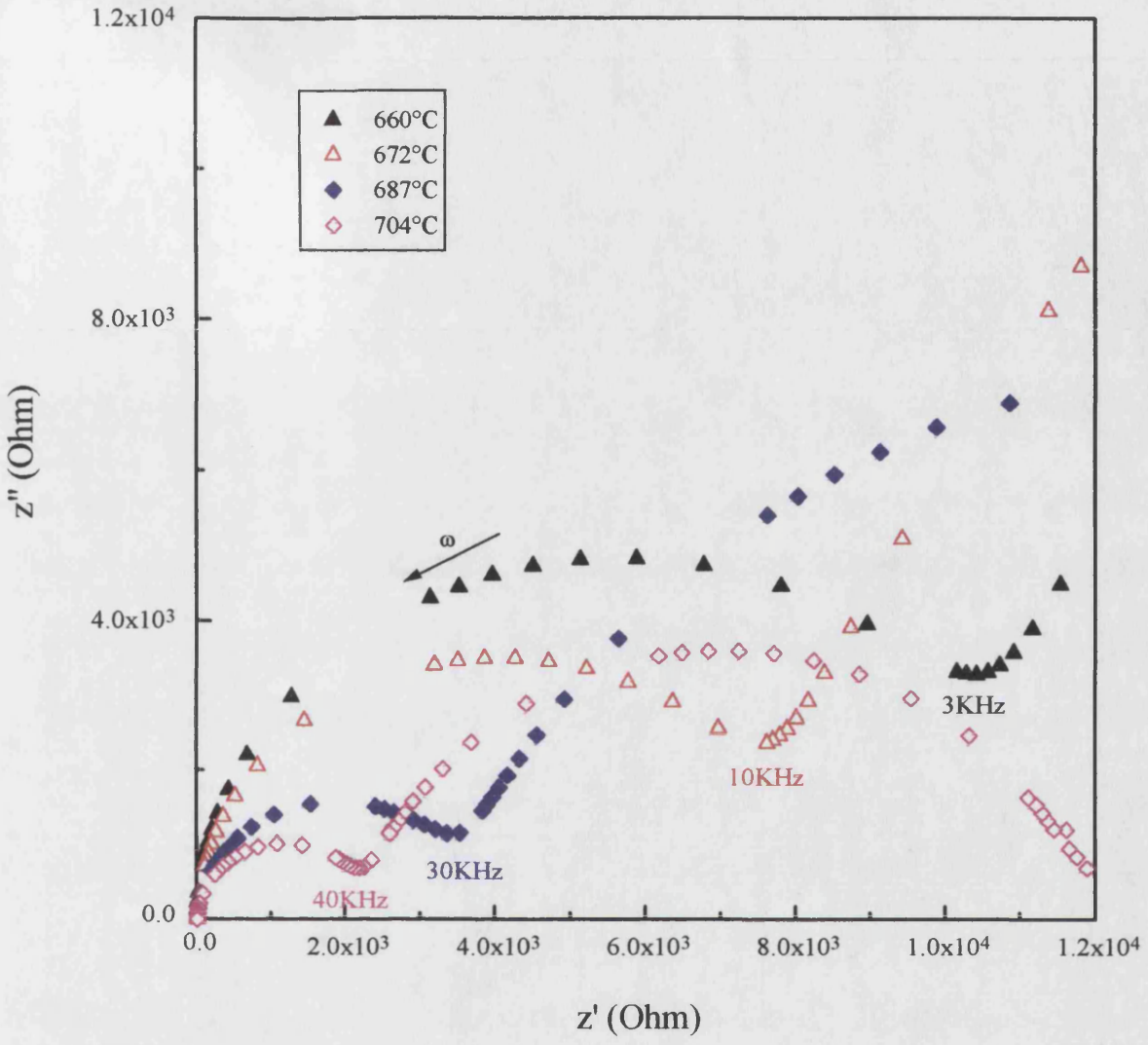

Fig. 9.16 The enlargement of the lower left corner of fig.9.15.

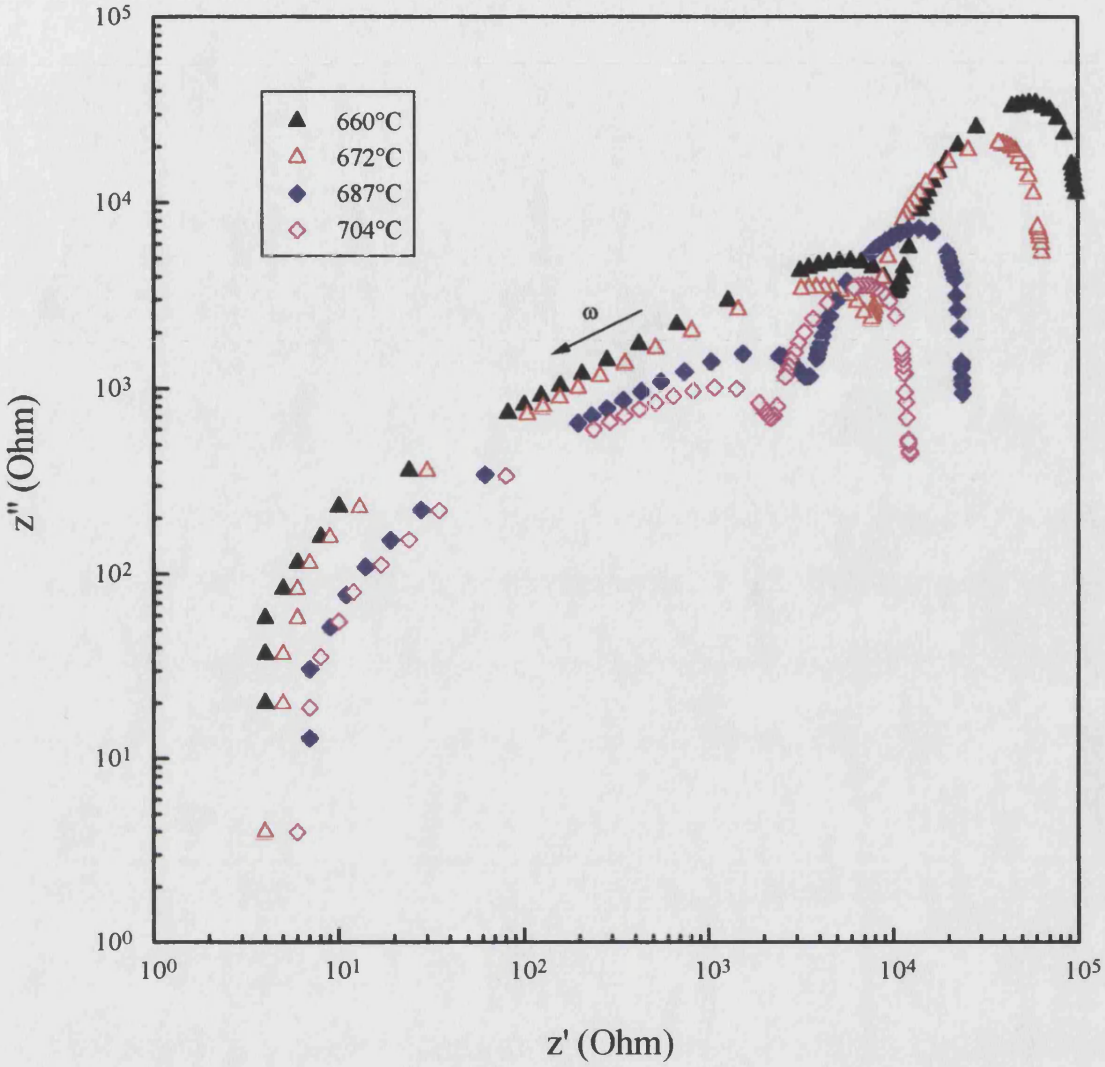

Fig.9.17 Log-log scale Complex plane profiles of the impedance data for the ceramic alumina AL23 between 660°C and 704°C.

namely that (i) as temperature is increased the frequency of junction point of the first and second semicircle increases and (ii) the diameter of both first and second semicircle decreases.

9.2.3 The complex plane profiles of sample D975 and H880

The complex impedance profiles of both of sample D975 and H880 show one semicircle only in the available frequency and temperature range (Figs. 9.18-20 for D975 and Fig. 9.21-23 for H880). These semicircles pass through the origin. At lower temperature only part of a semicircle can be seen in the available frequency range (Fig. 9.18 for D975 and Fig. 9.20 for H880). As temperature increases, this semicircle gradually moves into the available frequency range until at about 352°C for D975 sample and 400°C for H880 sample the whole semicircle can be seen (Fig. 9.18 for D975 and Fig. 9.21 for H880). The measurements were made up to 620°C. The diameters of semicircles decrease with increase of temperature. The lower frequencies parts of Fig 9.20 and Fig. 9.23 show that no more semicircles appear. The complex impedance profiles for both of the sample D975 and H880 show only one semicircle. To examine whether the semicircle is associated with the electrode response, it is useful to make a measurement of the impedance spectra at different DC bias. The barrier height of the electrode polarisation is dependent on DC bias. Hence R_e and C_e in the Fig. 3.8(A) are dependent on DC bias; the arc that is associated with the electrode response should show a significant DC-bias-voltage dependence. The DC bias dependence of impedance was measured at 400°C for ceramic alumina D975 and 627°C for ceramic alumina H880. The complex impedance profiles of impedance data of ceramic alumina D975 and H880 at different DC bias are shown in Fig. 9.24 and 25. No visible bias dependence was found. This proves that the impedance profiles of ceramic alumina H880 and D975 are not associated with an electrode

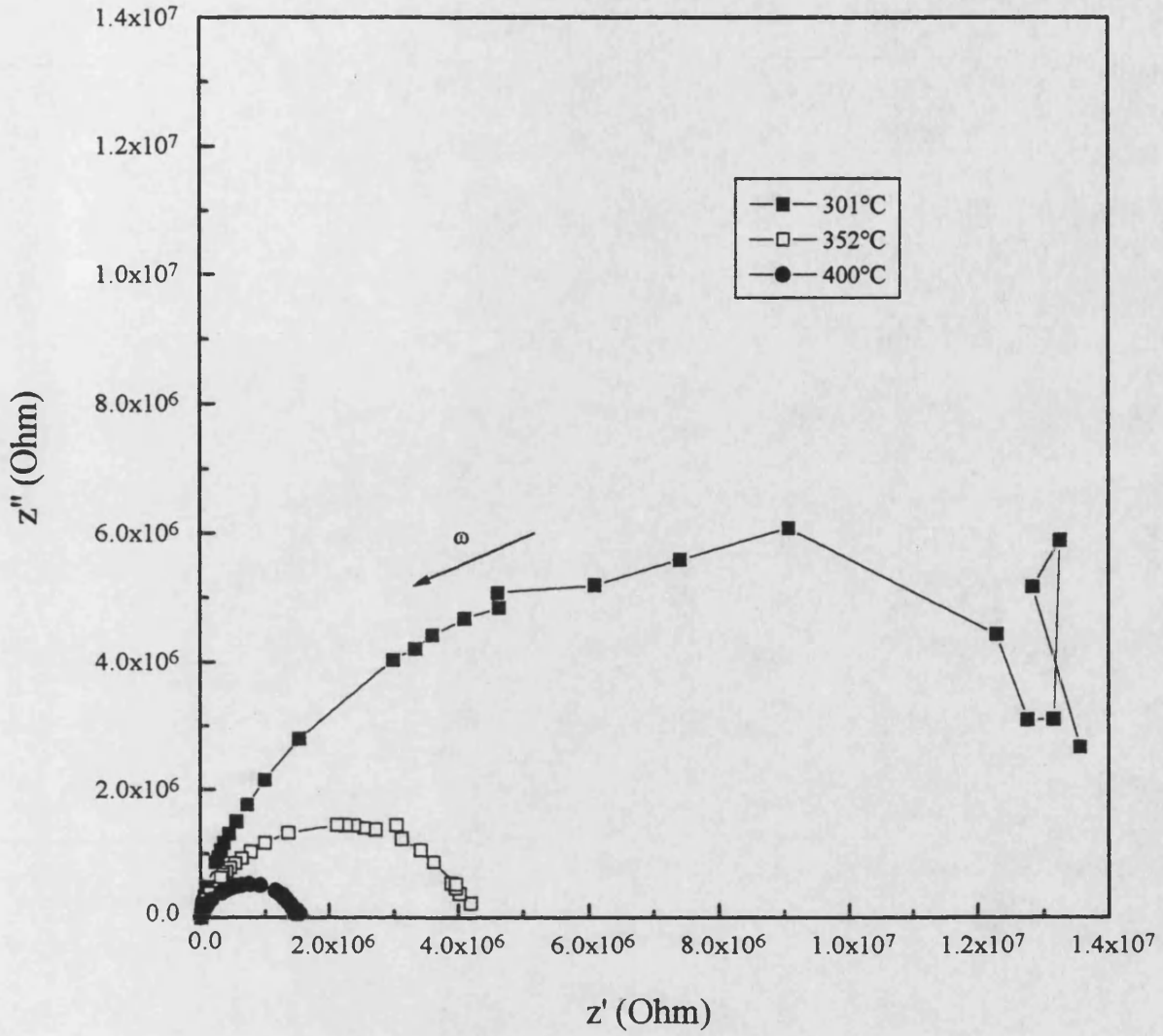

Fig.9.18 Complex plane profiles of the impedance data for the Ceramic alumina D975 between 301°C and 400°C.

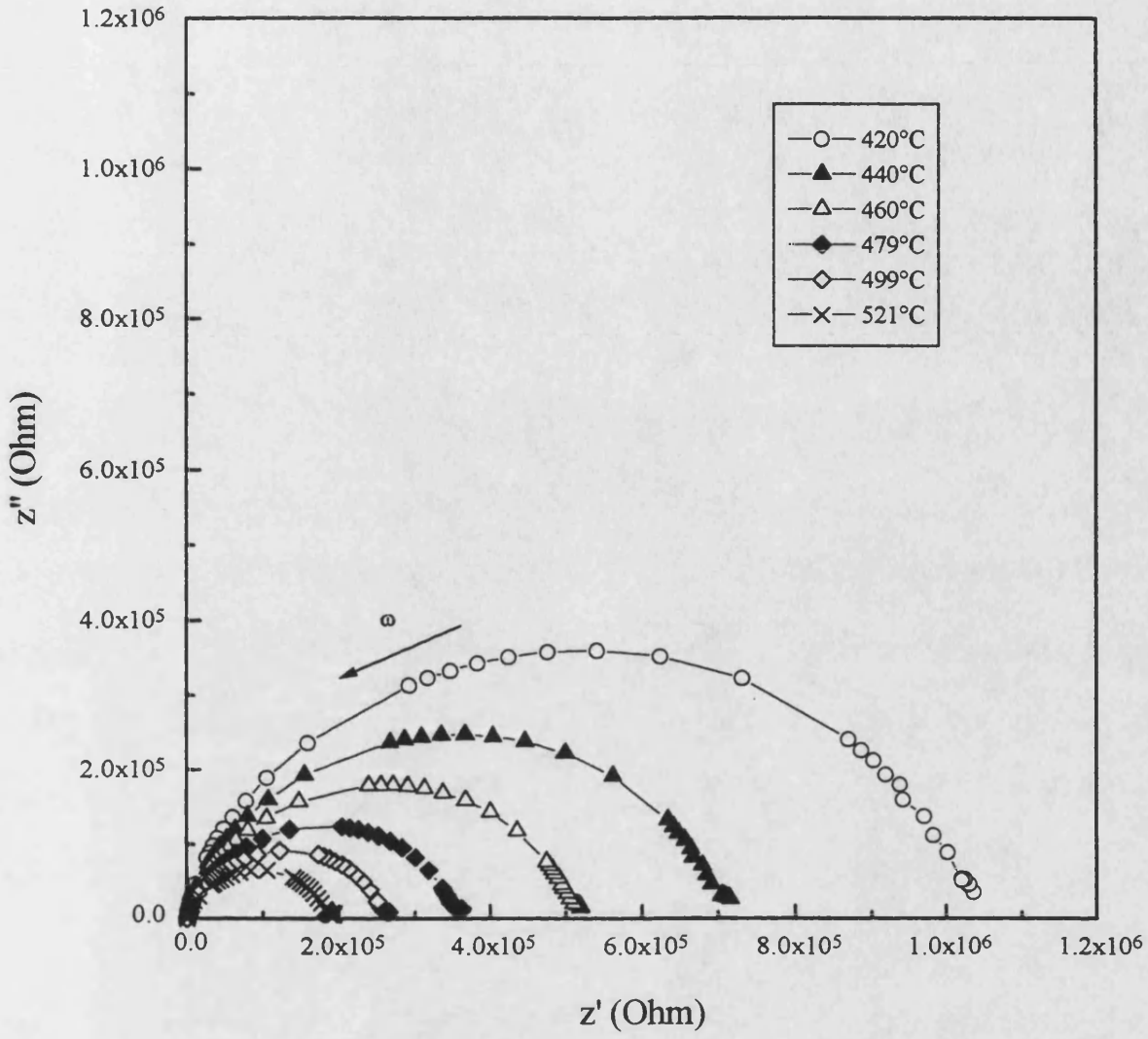

Fig.9.19 Complex plane profiles of the impedance data for the ceramic alumina D975 between 420°C and 521°C.

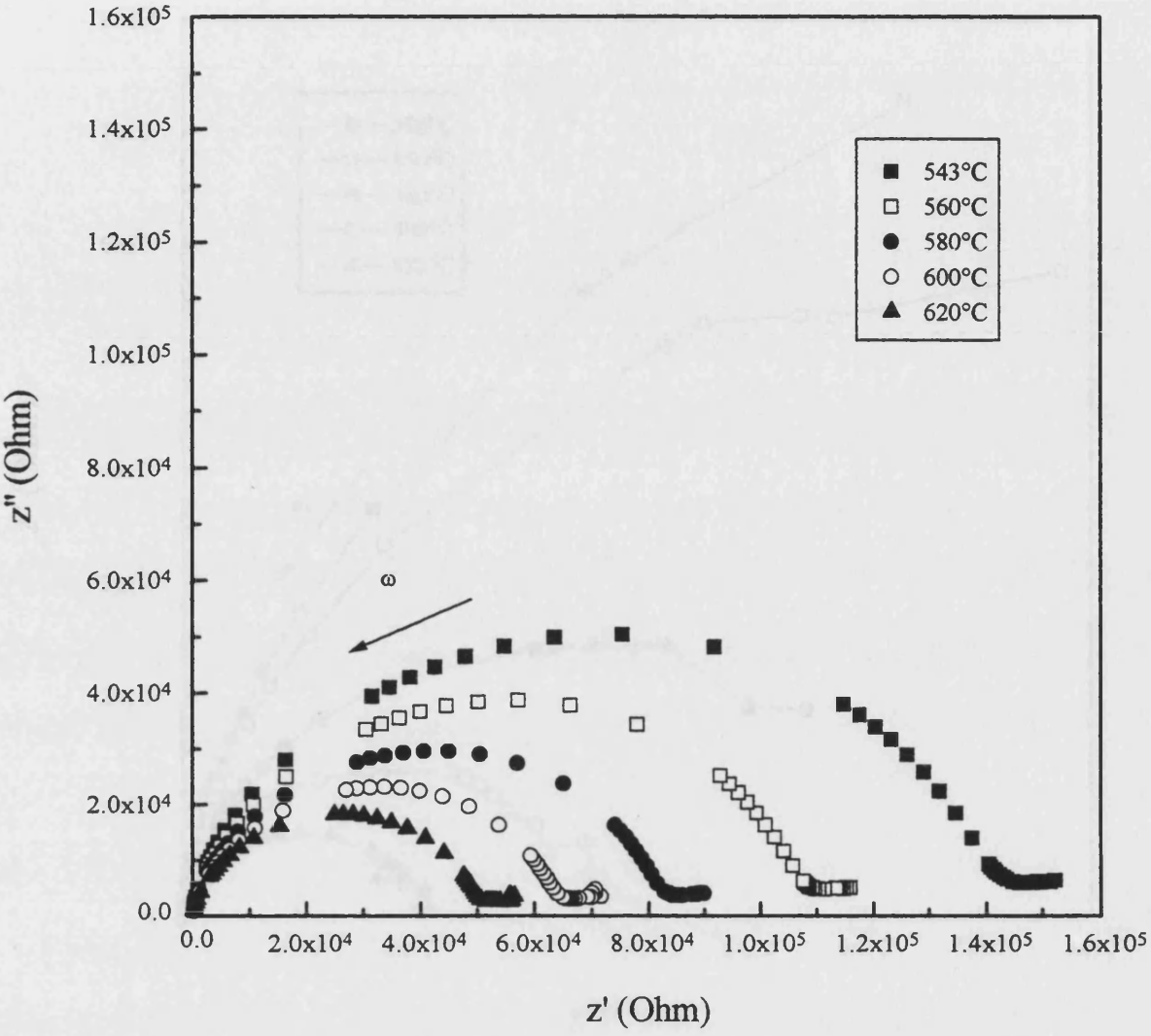

Fig.9.20 Complex plane profiles of the impedance data for the ceramic alumina D975 between 543°C and 620°C.

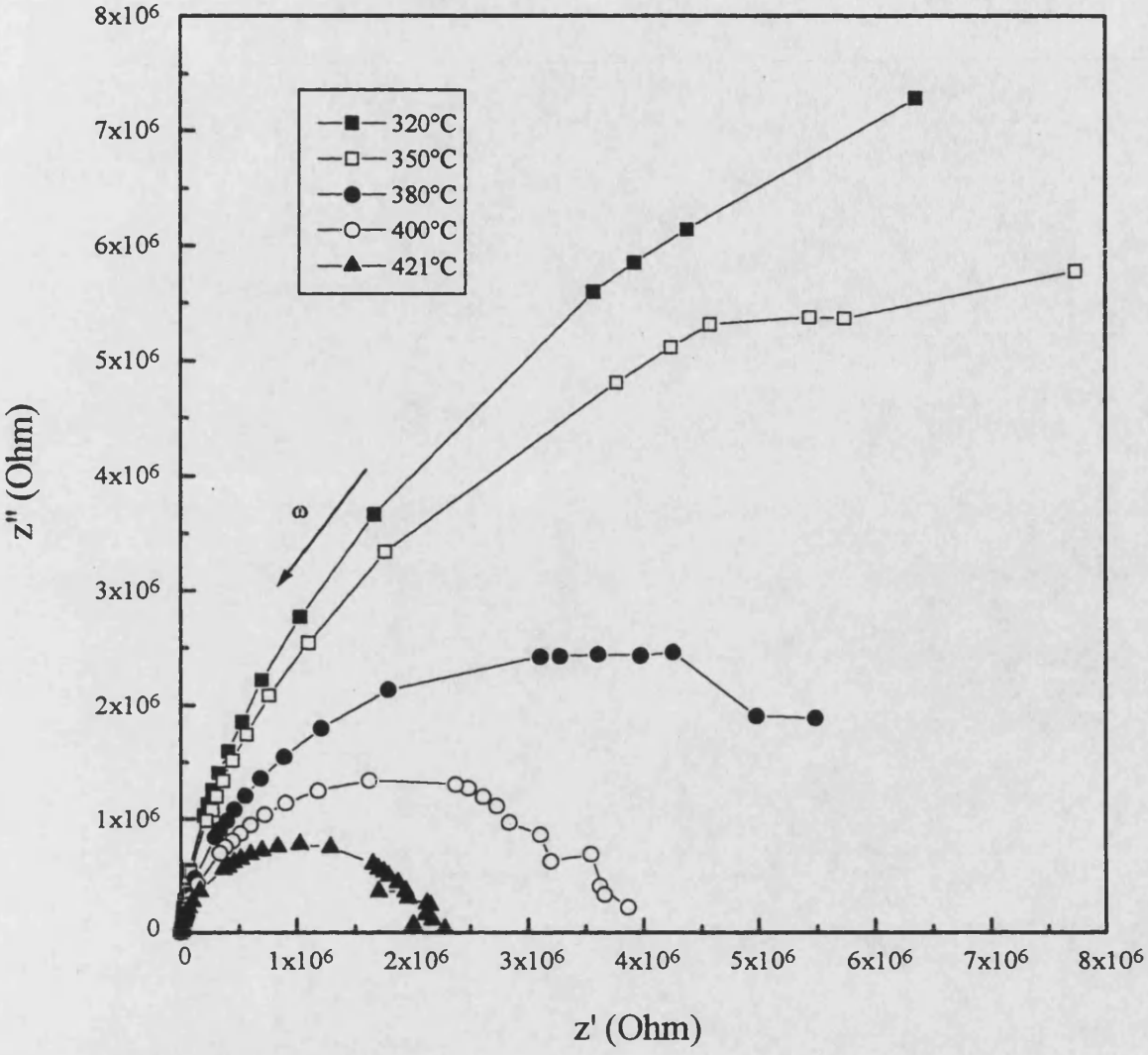

Fig.9.21 Complex plane profiles of the impedance data for the cearmic alumina H880 between 320°C and 421°C.

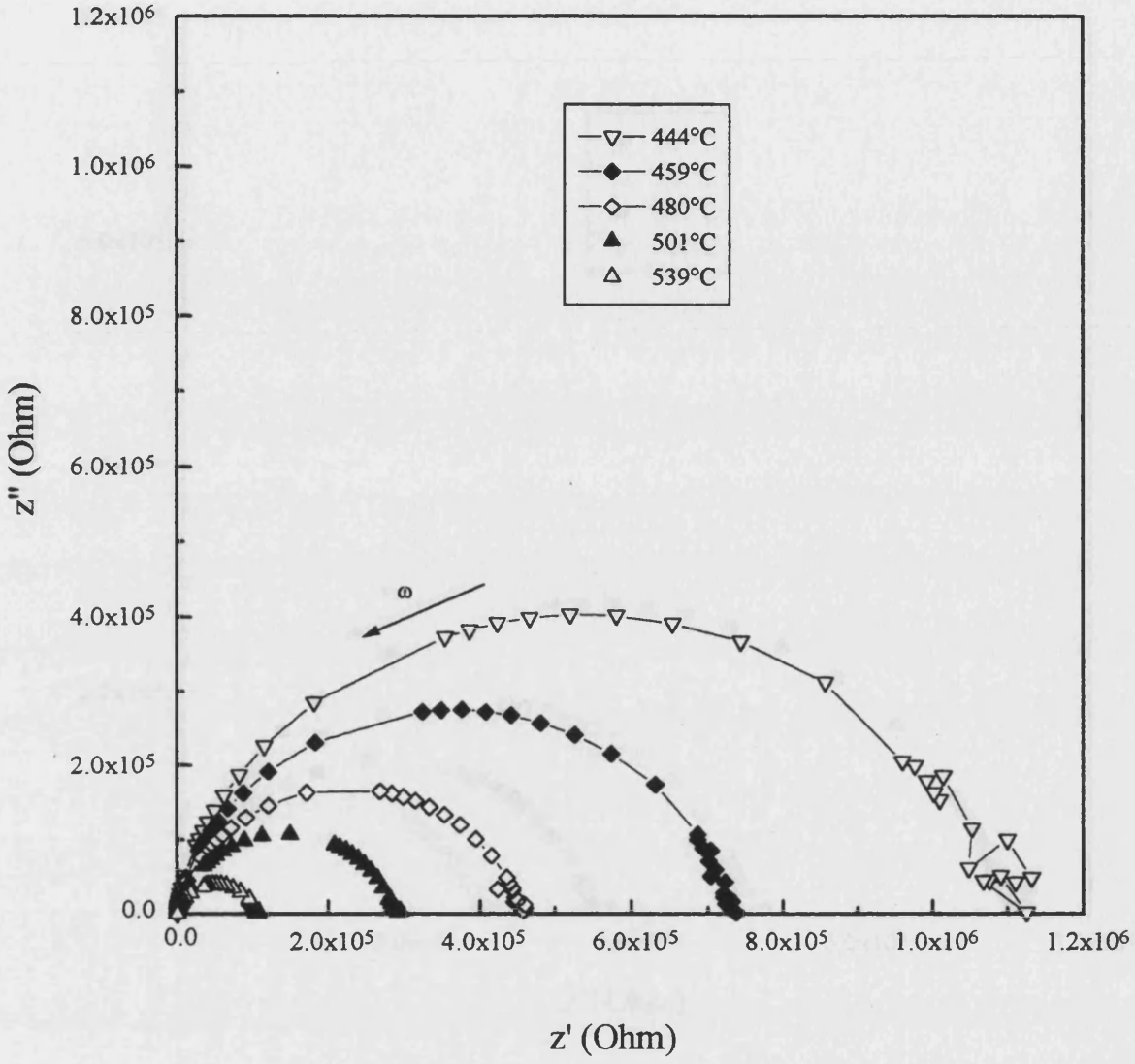

Fig.9.22 Complex plane profiles of the impedance data for the ceramic alumina H880 between 444°C and 539°C.

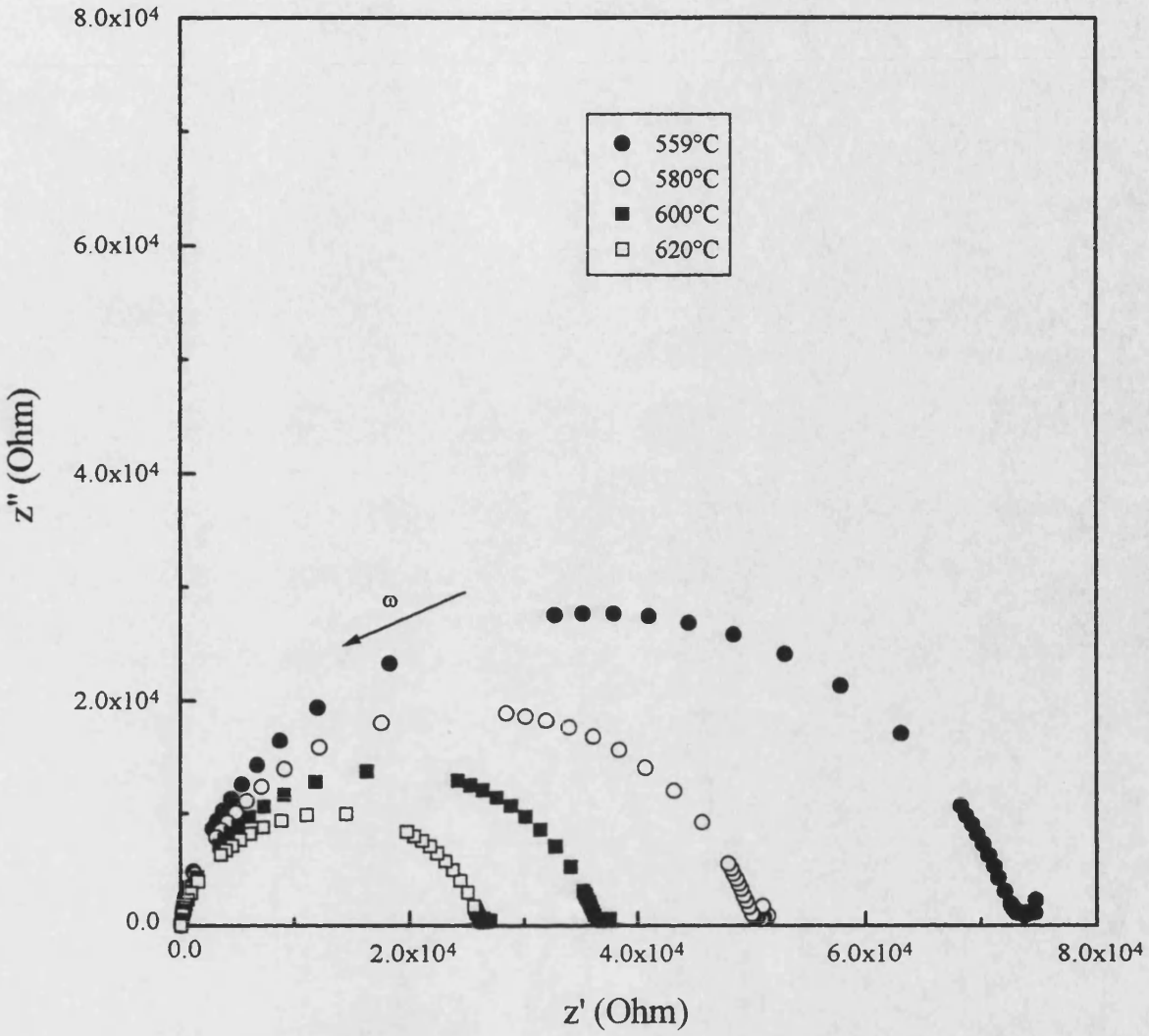

Fig.9.23 Complex plane profiles of the impedance data for the ceramic alumina H880 between 559°C and 620°C.

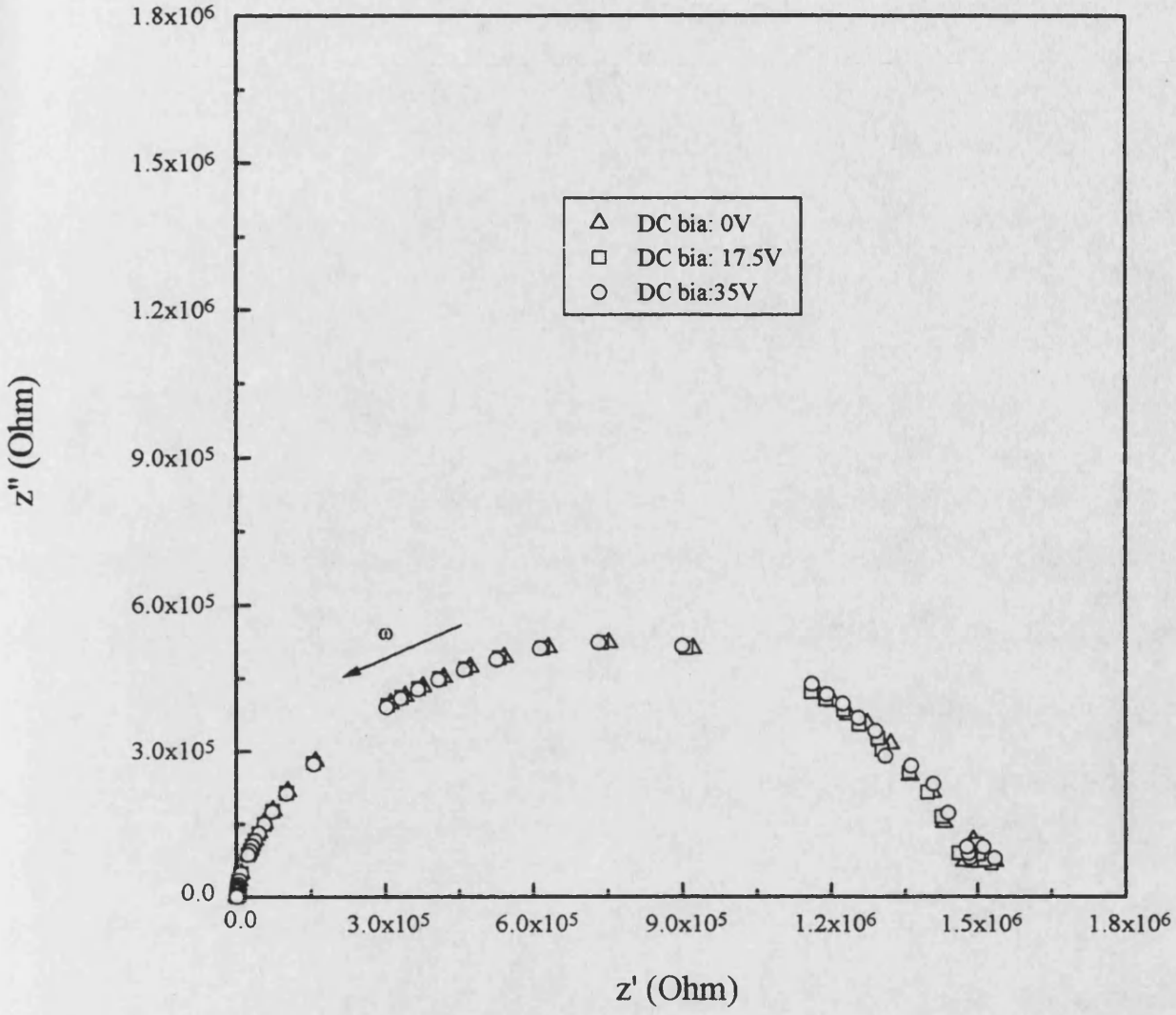

Fig.9.24 Complex plane profiles of the impedance data for the ceramic alumina D975 at different DC bias and at 400°C.

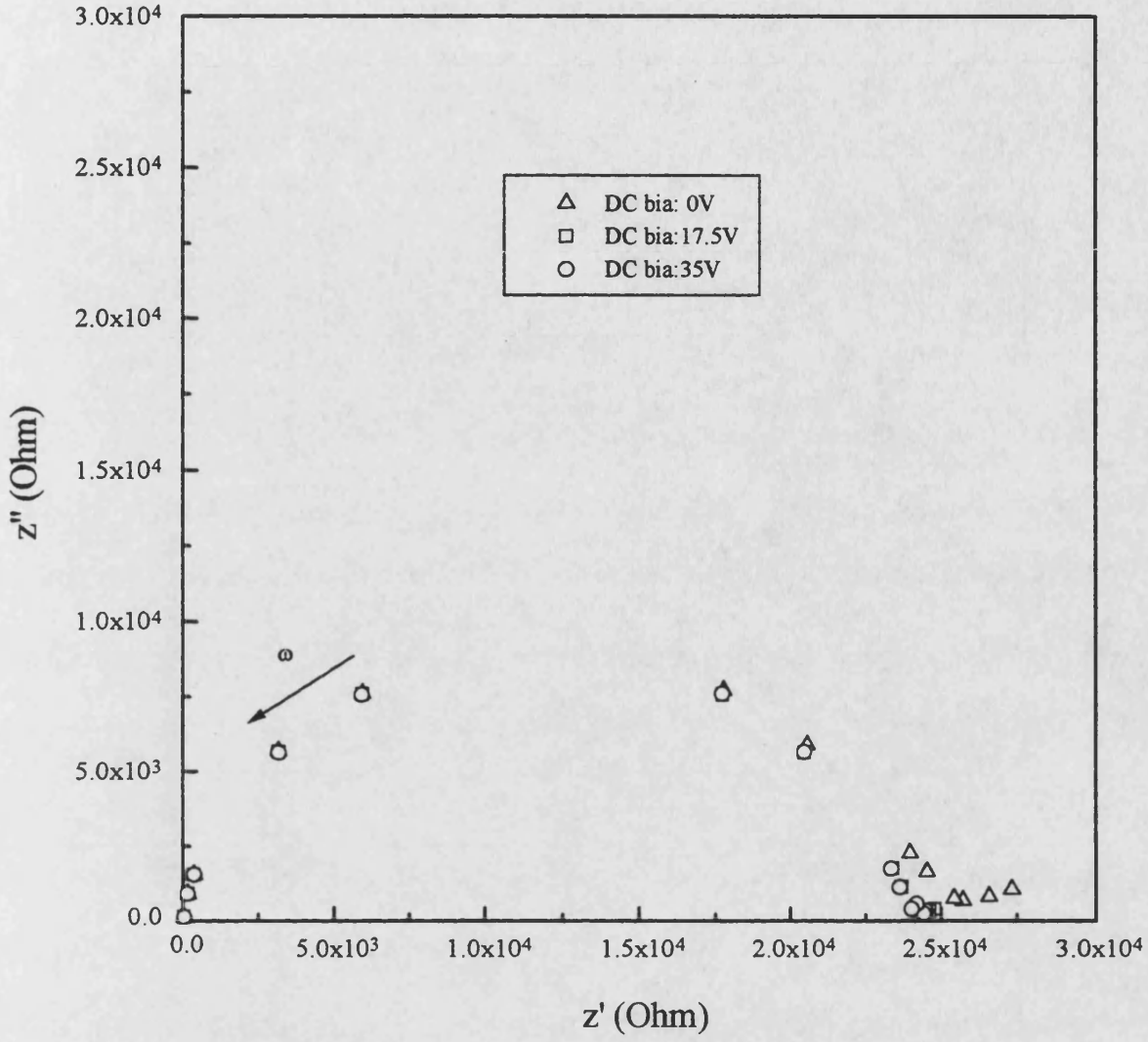

Fig.9.25 Complex plane profiles of the impedance data for the ceramic alumina H880 at different DC bias at 627°C.

effect but reflect the nature of the material.

9.3 The equivalent circuits of D999 and AL23

The impedance behaviour of a real sample will never be exactly the same as that of an idealised equivalent circuit, but it appears reasonable on the basis of the brick model, and on the basis of the shape of the impedance graphs of D999 and AL23 measured in this work, to use the equivalent circuit given in Fig. 3.8(A). It is now necessary to link the arcs in the complex plane profile to the bulk (grain), grain boundary and electrode responses. The order in which the arcs come in the complex plane profile is determined by the relative magnitudes of the circuit time constants RC. It is sensible to assume that the highest frequency portion will be associated with the bulk effects because that is the largest component and should have the smallest RC value. Due to the intermediate size of the ratio A/d (the effective area /the thickness) of the grain boundaries between the electrode and bulk values, it is expected that the second semicircle of the complex plane profile for D999 is associated with the grain boundary effects. The complex plane profiles of ceramic alumina AL23 consist of only two semicircles in the available temperature and frequency range under zero DC bias. To examine whether the second semicircle is associated with the electrode response, it is useful to make a measurement of the impedance spectra at different DC bias. The DC bias dependence of the impedance of sample AL23 was measured at 671°C (Fig. 9.26 and 27). From Fig. 9.26 and 27 it can be seen that under DC bias the complex impedance profiles reveals three distinct regions; the third region (the low frequency part) is DC bias dependent. Analysing the Fig. 9.26 and 27, we can conclude that the third region is a part of a third semicircle which is partially overlapped with the second semicircle; the third semicircle is associated with the

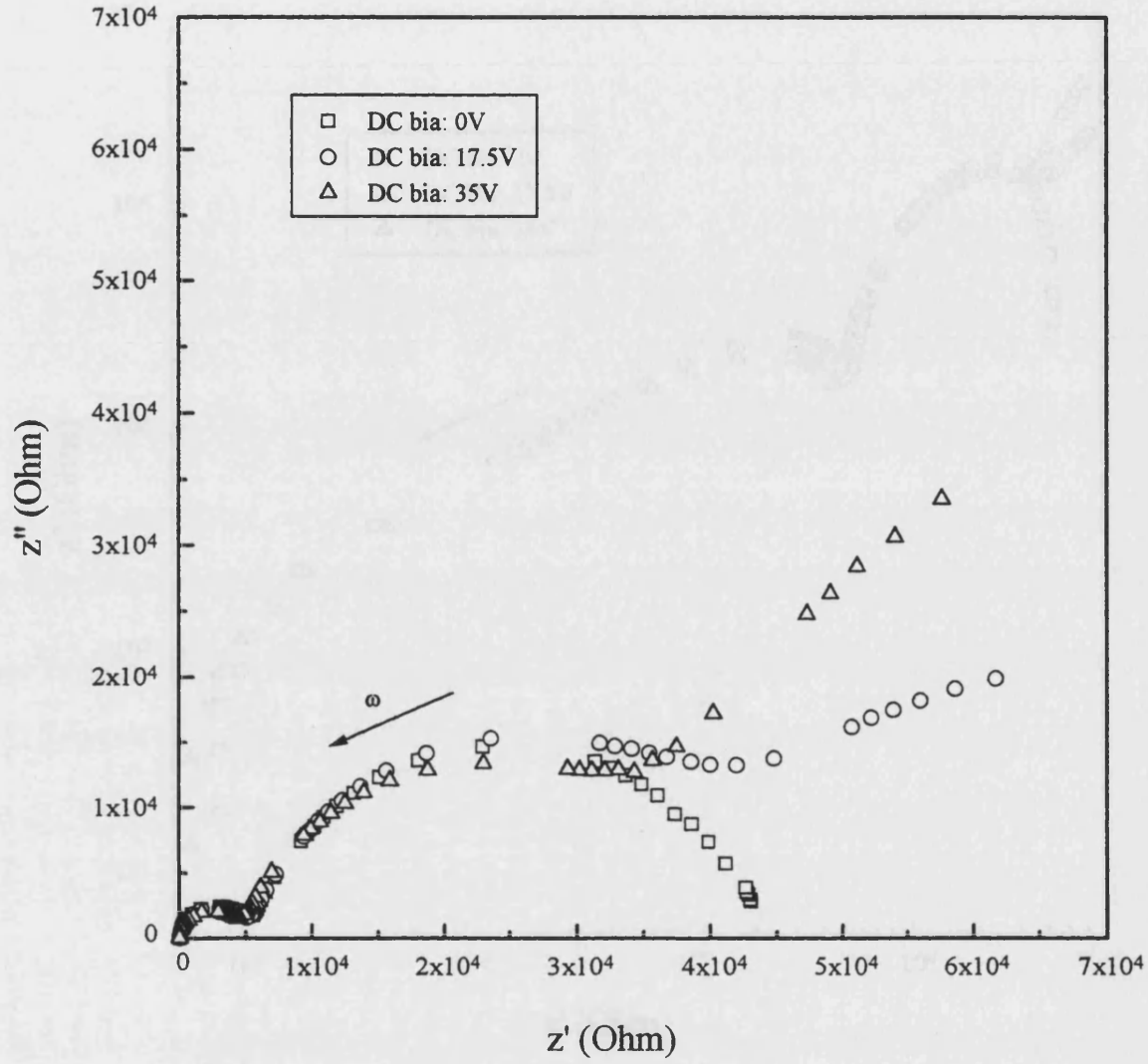

Fig.9.26 Complex plane profiles of the impedance data for the ceramic alumina AL23 at different DC bias and at a temperature of 671^{0}C.

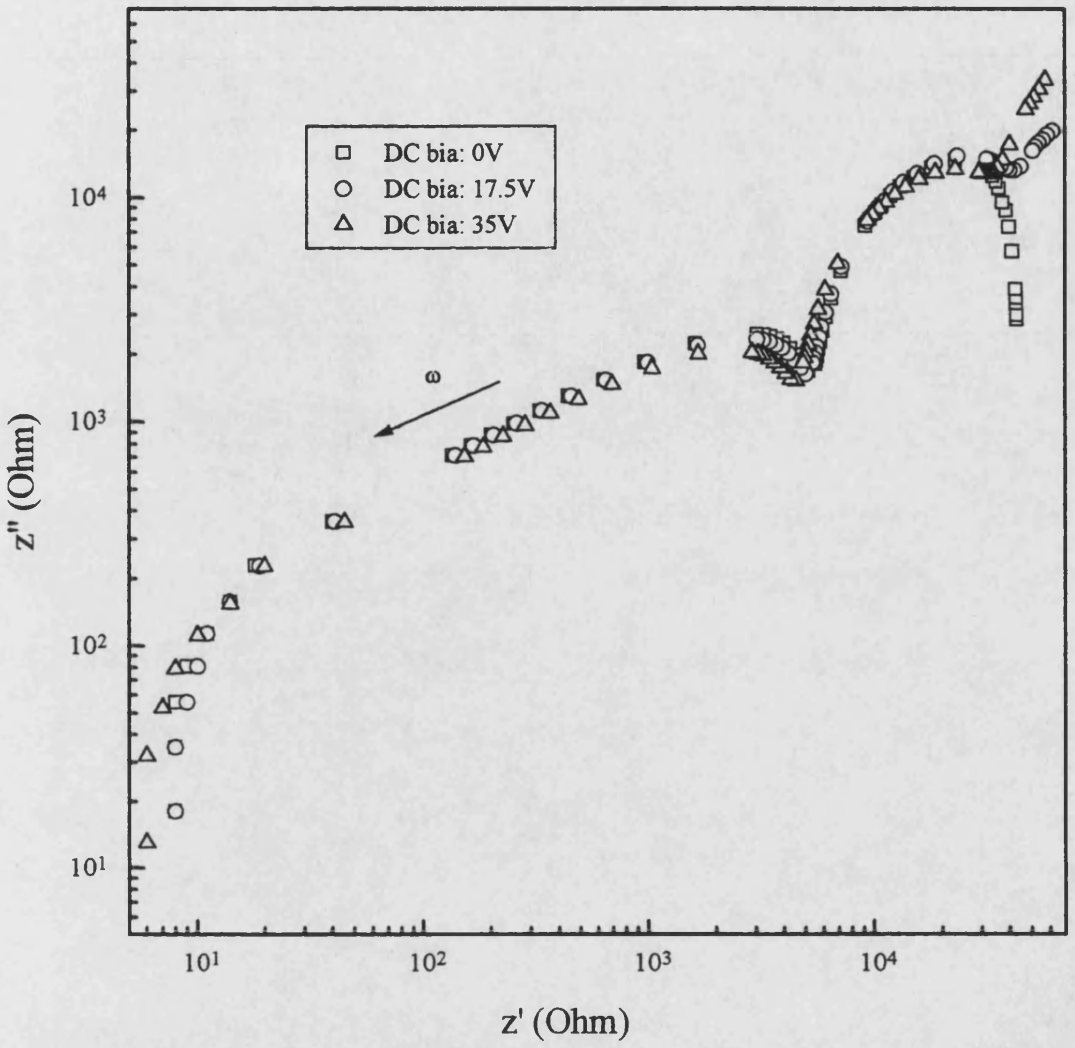

Fig.9.27 The Log-log scale complex plane profiles of the impedance data for the ceramic alumina AL23 at different DC bias and at 671°C.

electrode response; the slight inconsistency with each other in the second region is not DC bias direction dependence but is due to the temperature instability in the process of measurement. Second semicircle of the complex plane profile for AL23 is associated with the grain boundaries. We can conclude that the equivalent circuit for bath D999 and AL23 are the same as that given in Fig. 3.8(A).

9.4 Analysis of microstructure of the ceramic aluminas D999 and AL23 using the "brick model"

By using the "brick model" it is possible to obtain crude estimates of some microstructural properties from the measured electrical responses. Since three arcs in the complex plane are found, it can be assumed that, for both D999 and AL23 samples, the conductivity σ_b in the grains is much greater than that σ_{gb} across the grain boundaries (i.e. $\sigma_b >> \sigma_{gb}$). An estimate of the ratio of grain boundary thickness (d) to grain size (D) can now be made using the results in equation (section 3.4.2)

$$\frac{d}{D} = \frac{C_b}{C_{gb}} \frac{\varepsilon_{gb}}{\varepsilon_b} . \qquad (3.20)$$

In following analysis for both D999 and AL23 the effects of the microcracks and the porosity are neglected and it is assumed that the dielectric constants of the bulk (ε_b) and the grain boundary material (ε_{gb}) are equal (Macdonald 1987).

The volume fraction X_{gb} of grain boundary can be estimated by using equation (see section 3.4.2)

$$X_{gb} = \frac{3d}{D} = 3\frac{C_b}{C_{gb}} \frac{\varepsilon_{gb}}{\varepsilon_b} \qquad (3.19)$$

The weight fraction of grain boundary phase would be calculated from the volume fraction and the mass densities of the phases as follows:

$$W_{gb} = X_{gb}\frac{\rho_{gb}}{\rho_b} . \qquad (9.5)$$

The equivalent circuit parameters from the complex plane profiles and the calculated ratio of the grain boundary thickness (d) to grain size (D) is listed in Table 9.2 for ceramic alumina D999 and in Table 9.3 for ceramic alumina AL23. The calculations show that the ratio of grain boundary thickness (d) to grain size (D) is about 5% for the ceramic alumina D999 and 1% for ceramic alumina AL23. The estimated volume fractions X_{gb} of grain boundary are about 15% for sample D999 and 3% for AL23.

The main error of estimated volume fractions X_{gb} and ratio of the grain boundary thickness (d) to grain size (D) are introduced by the assumption that the dielectric constants of the bulk (ε_b) and the grain boundary material (ε_{gb}) are equal. In practice, the thickness of a grain boundary phase may easily vary along one boundary by more than the uncertainty introduced by the assumption of $\varepsilon_b=\varepsilon_{gb}$ (Macdonald 1987).

Table 9.2 Equivalent circuit parameters from the complex plane profiles of D999 and the ratio of grain boundary thickness (d) to grain size (D).

T (C°)	R_b (Ohm)	C_b (10^{-10} F)	$\omega_b=1/\tau_b$ ($\times10^{-3}$)	R_{gb} (kΩ)	C_{gb} (10^{-10} F)	$\omega_{gb}=1/\tau_{gb}$	d/D (%)
450	3300	1.93	1571	758.3	44.66	295	4
460	2820	1.95	1822	508	39.14	503	5
471	2230	2.04	2199	365	39.65	691	5
480	1820	2.06	2670	298	41.07	817	5
490	1420	1.96	3644	244	38.37	1068	5
500	1200	1.98	4210	208.8	42.35	1131	4
510	905	1.95	5655	177	42.8	1320	5

Table 9.3 Equivalent circuit parameters from the complex plane profiles of AL23 and the ratio of grain boundary thickness (d) to grain size (D).

T (C°)	R_b (Ohm)	C_b (10^{-10} F)	$\omega_b=1/\tau_b$ ($\times10^{-3}$)	R_{gb} (kΩ)	C_{gb} (10^{-10} F)	$\omega_{gb}=1/\tau_{gb}$	d/D (%)
630	58218	3.11	55.3	438.21	304	75	1
640	41719	3.18	75.4	298.62	296	113	1
650	28780	3.08	113	197	288	176	1

9.5 The activation energies of electrical resistance of grain and grain boundary in ceramic alumina D999 and AL23

The published literature on electrical conductivity of alumina was reviewed by Cohen (1959), who classified alumina as a semiconductor at high temperatures. The conductivity data reported for alumina has been found to obey an equation of the form (Cohen,1959):

$$\sigma = Ae^{-E_{act}^{\sigma}/kT} \tag{9.6}$$

with A being a constant, E_{act}^{σ} the activation energy, k the Boltzmann constant and T temperature in Kelvin. The equation 9.6 is set up on the basis of band conduction of a semiconductor. The measured activation energy is due to a contribution from a binding energy. For ceramics, the activation energy and the pre-exponential factor are strongly affected by the presence of impurities, the diffusion path for the charge carriers and the partial oxygen pressure.

This conduction would then be described by the resistors R_b and R_{gb} in the equivalent circuit model Fig. 3.8(a). From the equation (9.6), the resistor in the equivalent circuit is given by

$$\frac{1}{R} = Be^{-E^{\sigma}_{act}/kT} \tag{9.7}$$

with B being a constant. From Equation 9.7 we have:

$$\ln(\frac{1}{R}) = -\frac{E^{\sigma}_{act}}{kT} + \ln(B) \tag{9.8}$$

The equivalent circuit resistances from the complex plane profiles of D999 and AL23 are listed in Table 9.4 and 9.5 respectively. The Arrhenius plots described by equation 9.8 are shown in the Fig. 9.28-31. The activation energies for R_b and R_{gb} of ceramic alumina D999 and AL23 are listed in Table 9.6. The grain electrical conductivity behaviour $\ln(1/R_{gb})$ of ceramic alumina D999 shows a distinct and unexpected change of gradient starting in the temperature range approximately 520-570°C (Fig. 9.29).

Table 9.4 Equivalent circuit resistances from the complex plane profiles of D999.

T (C°)	280	290	300	310	320	330	342
R_b (KΩ)	2600	1520	975	570	390	257	154

T (C°)	350	360	370	379	390	400	410
R_b (KΩ)	105	70	49.7	33.5	22.5	16.4	11

T (C°)	421	433	440	450	460	471	480
R_b (Ohm)	9080	6300	4840	3300	2820	2230	1820
R_{gb} (KΩ)				758.3	508	365	298

T (C°)	490	500	510	520	528	541	550
R_b (Ohm)	1420	1200	905				
R_{gb} (KΩ)	244	208.8	177	130	195	110	140

T (C°)	570	580	591	600	612	620	630
R_{gb} (KΩ)	105	82	59	46	32	24	17

Table 9.5 Equivalent circuit resistances from the complex plane profiles of AL23.

T (C°)	459	482	500	511	521	532	541
R_b (KΩ)	6710	6170	2160	1540	1160	875	735

T (C°)	558	569	580	590	600	608	621
R_b (KΩ)	485	376	295	200	147	106	85

T (C°)	630	640	650	660	672	687	704
R_b (Ohm)	58218	41719	28780				
R_{gb} (KΩ)	438.21	298.62	197	88.06	55.59	20.83	9.927

Table 9.6 The activation energies for R_b and R_{gb} of ceramic alumina D999 and AL23

	Activation energy E_{act}^{σ} (eV)
Bulk of D999	1.30±0.01
Grain boundary for D999 (570-630°C)	1.99±0.07
Grain boundary for D999 (450-520°C)	1.13±0.06
Bulk of AL23	1.71±0.06
Grain boundary for AL23	4.1±0.2

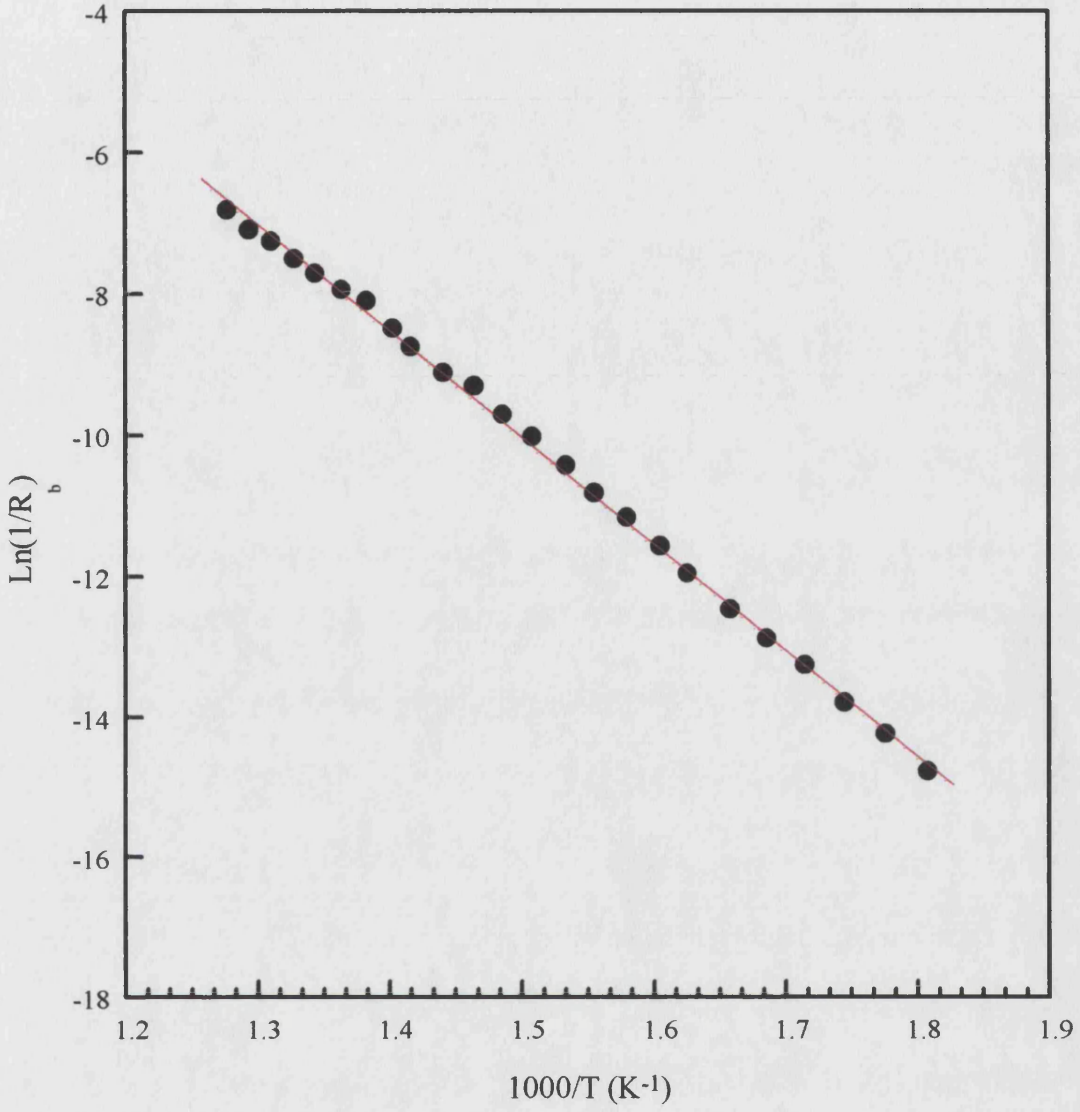

Fig.9.28 The Arrhenius plot of bulk resistance of the ceramic alumina D999, indicating an average activation energy of 1.30±0.01eV.

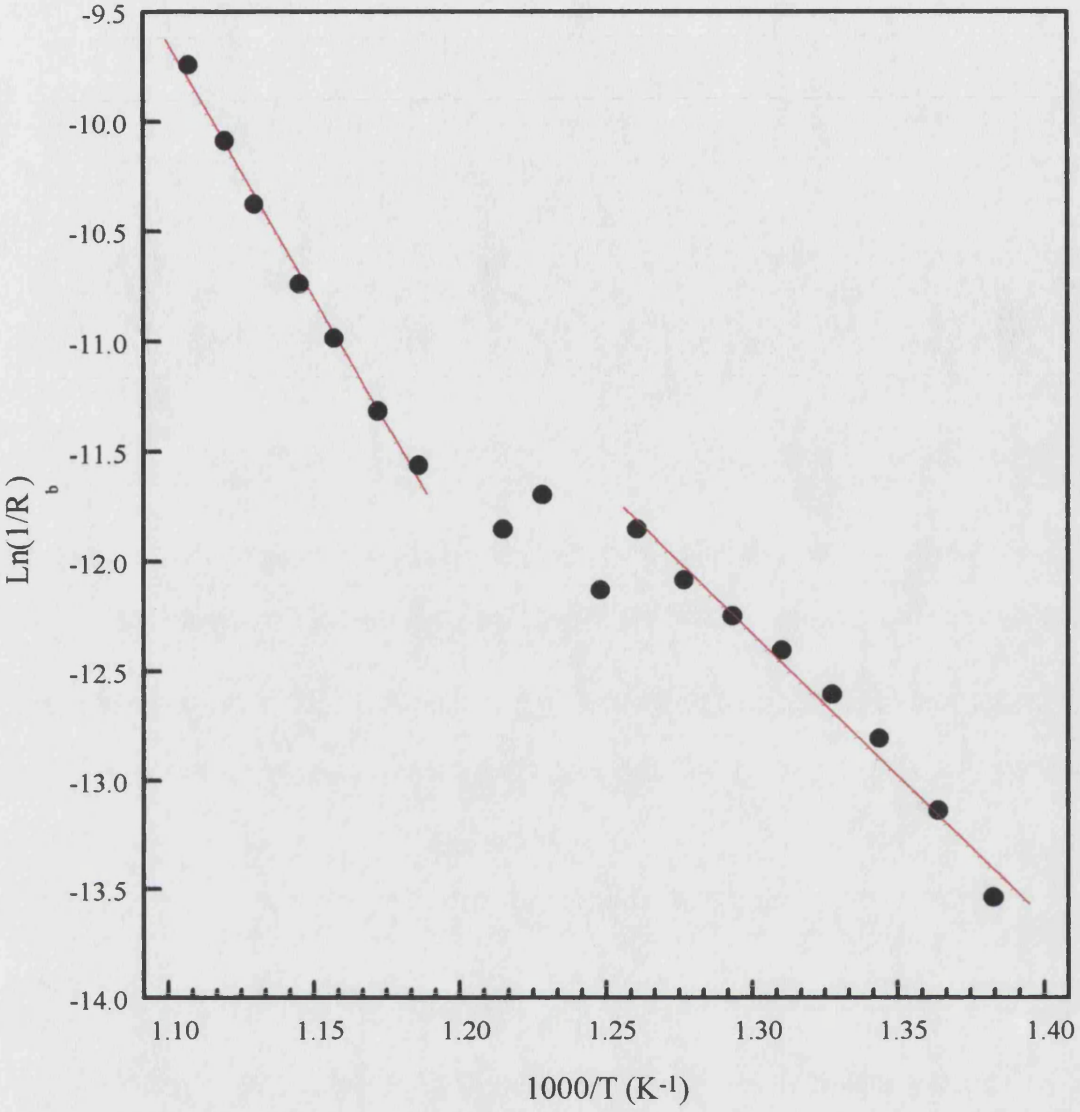

Fig.9.29 The Arrhenius plot of grain boundary resistance of the ceramic alumina D999, indicating an average activation energy of 1.13±0.06eV between 450°C and 520°C and 1.99±0.07eV between 570°C and 630°C.

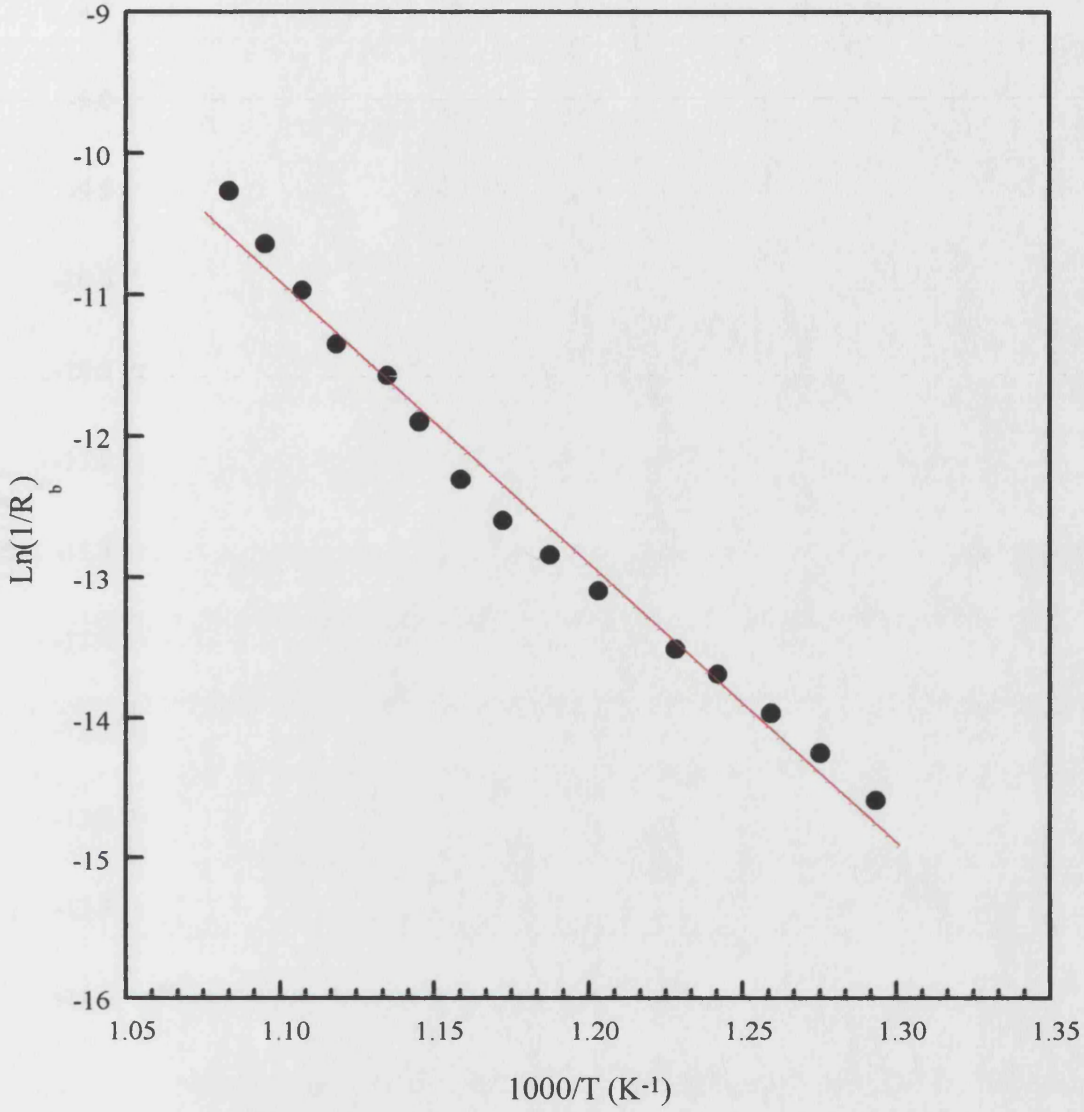

Fig.9.30 The Arrhenius plot of bulk resistance of the ceramic alumina AL23, indicating an average activation energy of 1.71±0.06eV.

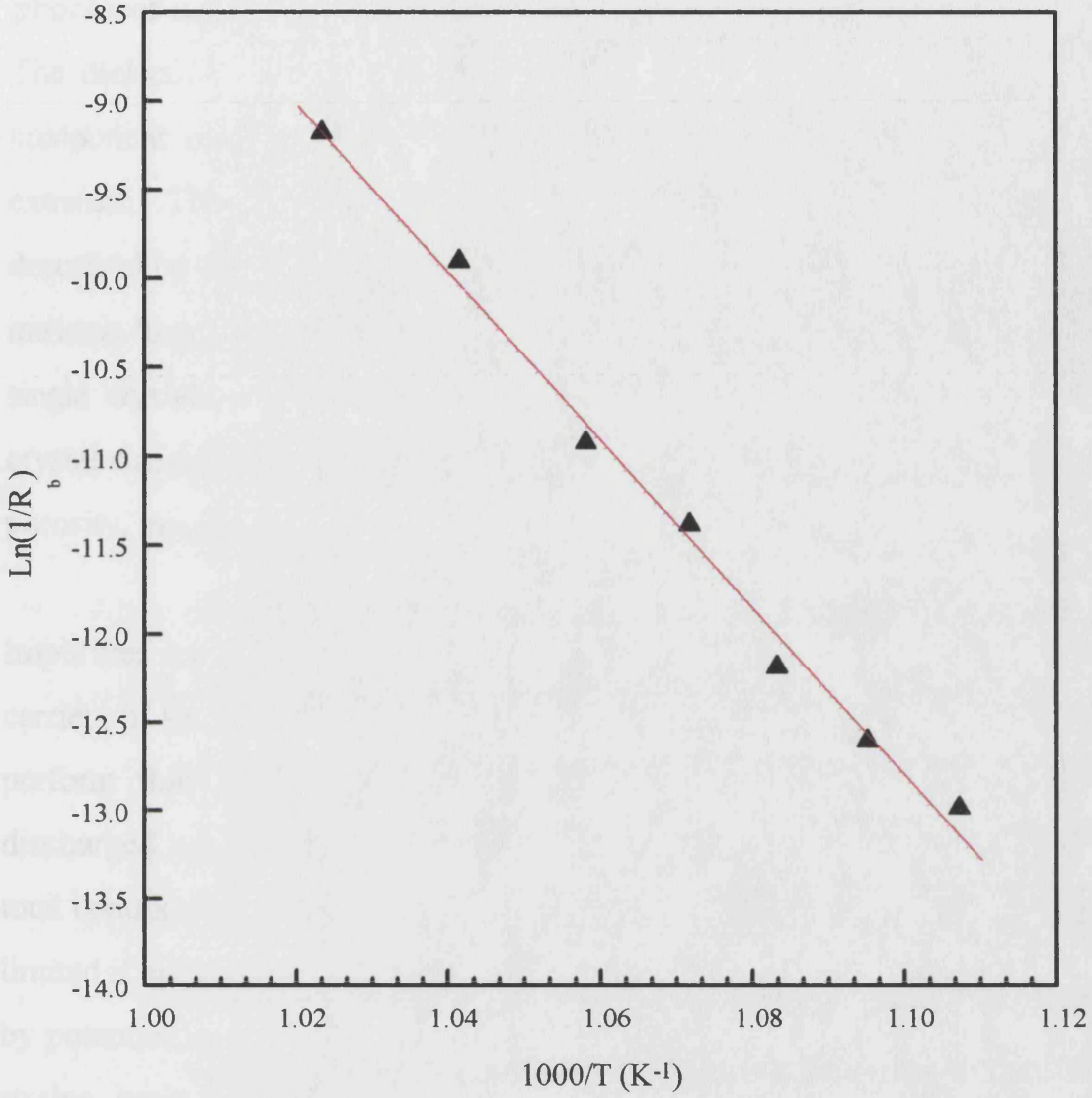

Fig.9.31 The Arrhenius plot of grain boundary resistance of the ceramic alumina AL23, indicating average activation energy of 4.1±0.2eV.

9.6 The dielectric constant, dielectric loss, dielectric relaxation processes and the Maxwell-Wagner effect of ceramic aluminas

The dielectric loss, which is conventionally described by the imaginary component of the permittivity, falls into two categories: intrinsic and extrinsic. The intrinsic losses depend on the crystal structure and can be described by the interaction of the phonon with the ac electric field. These intrinsic losses set the lower limit of the losses found in pure "defect-free" single crystals. Extrinsic losses are associated with imperfections in the crystal structure, e.g., impurities, microstructural defects, grain boundaries, porosity, microcracks and random crystallite orientation.

Impurities are effective agents for increasing the number of mobile charge carriers in an insulator. Different impurities vary widely in their ability to perform this function. Carriers may be entirely free to enter or be discharged on contact with metal electrodes. In this case they add to the total conduction through the dielectric. The motion of a carrier can also be limited if either it is associated with others to form dipoles, or it is confined by potential barriers introduced by lattice defects, impurity centres, voids, strains, grain boundaries or electrode surfaces. In such cases the limited oscillatory movement of carriers that occurs in an ac field does not affect the dc conductivity, but the consumed energy becomes part of the dielectric loss. Moreover, the charge displacement involved in this motion adds to the polarisation and therefore increases the apparent dielectric constant.

The relaxation processes are always related to the movement of the charges between different equilibrium positions separated by a potential barrier due to the different phenomena such as: (1) electrode potential, (2)interfacial polarisation, (3) dipolar relaxation. All these process are thermally activated. The related activation energy can be obtained by an Arrhenius

plot of the frequency of the loss peak versus the inverse of temperature.

The purest ceramic alumina used in this work is AL23, which is composed of 99.7% Al_2O_3. From the semiconductor point of view 0.3% impurities are more than enough to produce drastic electrical changes.

9.6.1. The dielectric constant, dielectric loss, dielectric relaxation processes and the Maxwell-Wagner effect in ceramic alumina D999

9.6.1.1 The dielectric constant, dielectric loss in ceramic alumina D999 above room temperature

Fig. 9.32 is a plot of the frequency dependence of dielectric constant between 17°C and 170°C. Fig. 9.32 shows an increasing dielectric constant with temperature at all frequencies and a small frequency dependence of dielectric constant. No sign of a mechanism of either dipole rotation or interfacial polarisation of grain boundaries is found in the data shown in Fig. 9.32. The results given in Fig 9.33 show the temperature dependence of dielectric constant of ceramic alumina D999 at 10^5 Hz and between 17°C and 170°C. In this temperature range the dielectric constant increases linearly with the temperature, indicating a temperature coefficient ($\partial\varepsilon'/\partial T$) of $(1.39\pm0.02)\times10^{-3}$/°C. Between 17°C and 170°C the dielectric loss is small being out of the measurable range of impedance analyser used. Fig. 9.34-9.37 are a series of plots of the frequency dependence of dielectric constant and dielectric loss of ceramic alumina D999 in order of increasing measurement temperature above 180°C. At temperatures below 250°C, the dielectric constant has much smaller frequency dependence than that above 250°C. At 200°C the dielectric

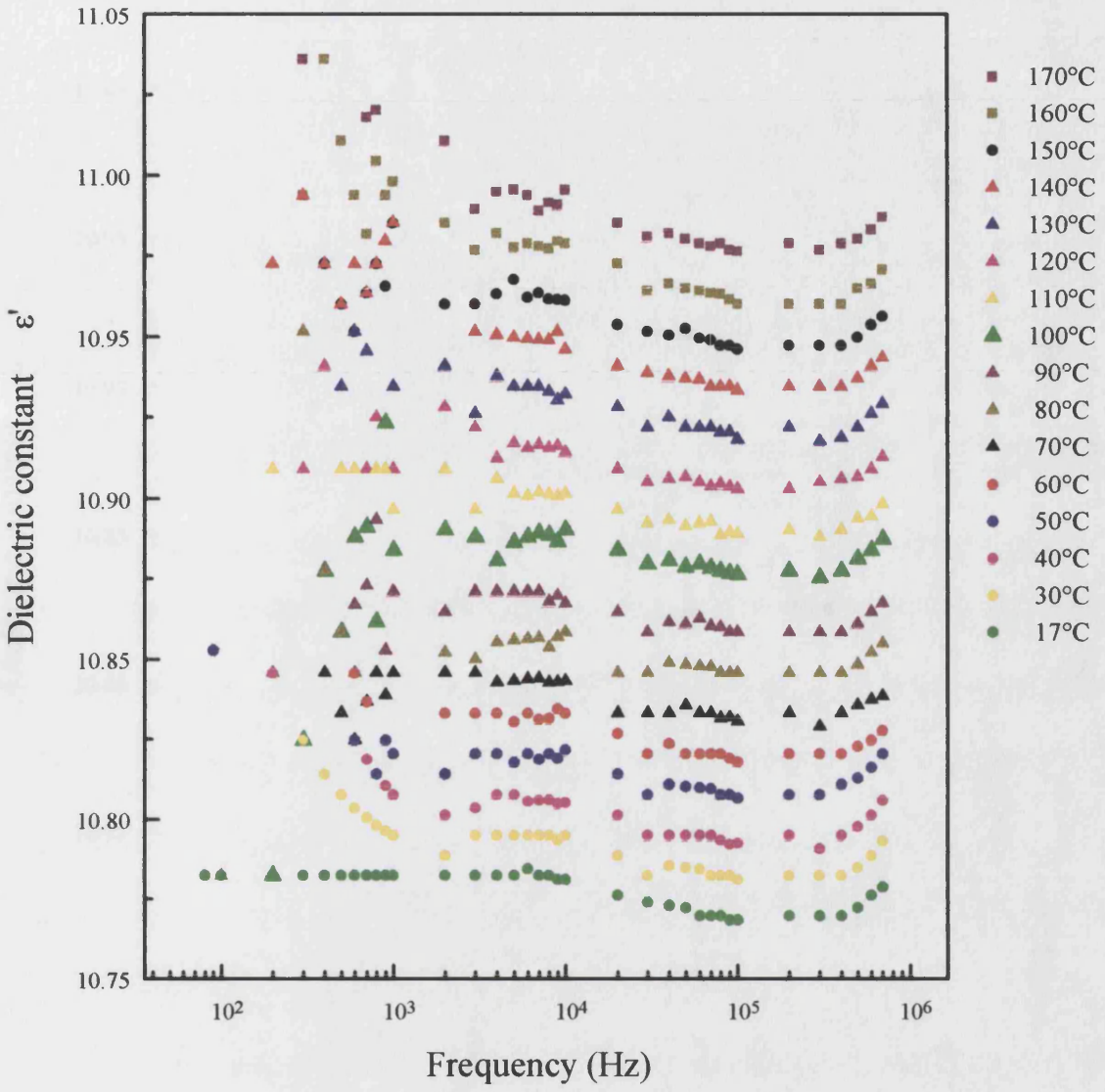

Fig.9.32 The frequency dependence of dielectric constant of the ceramic alumina D999 between 17°C and 170°C.

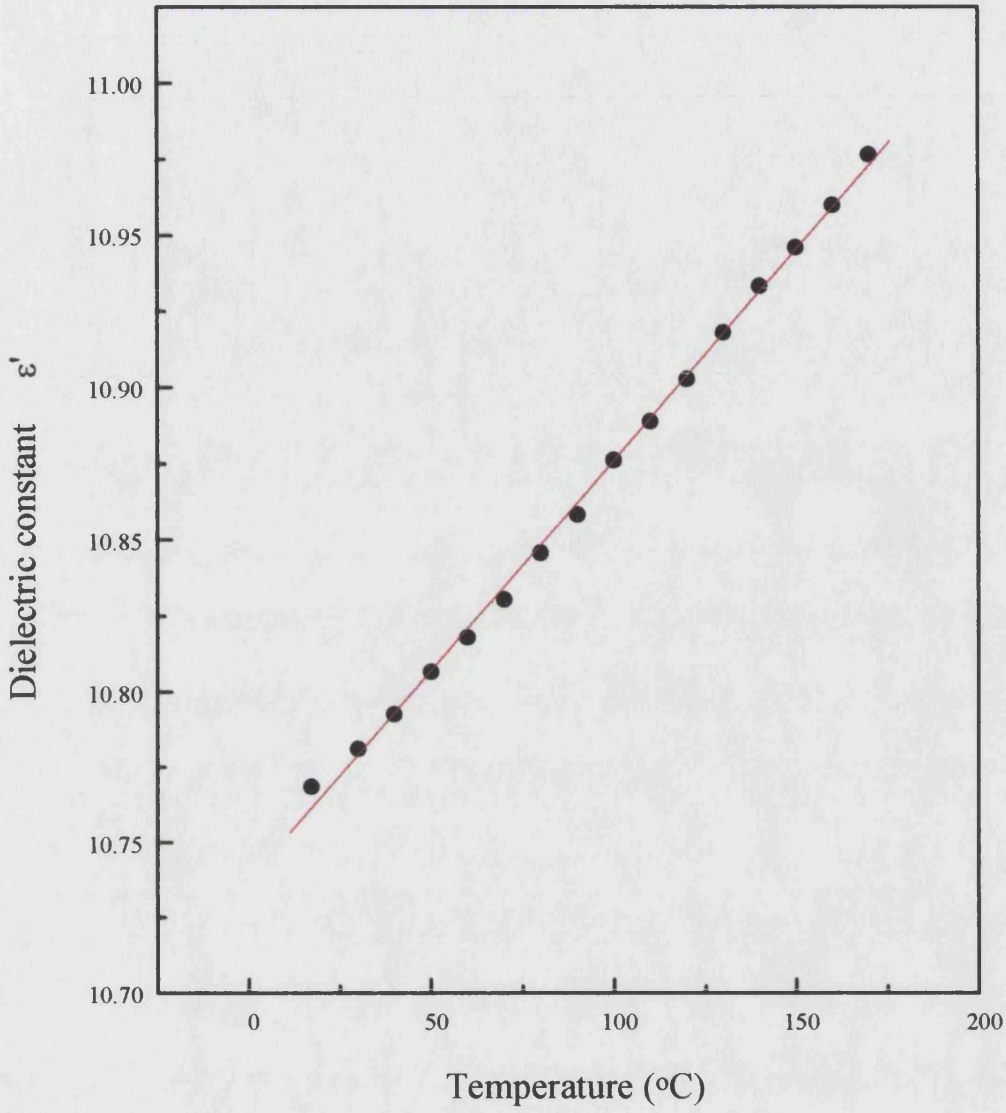

Fig.9.33 The temperature dependence of dielectric constant of the ceramic alumina D999 at 10^5Hz and between 17°C and 170°C.

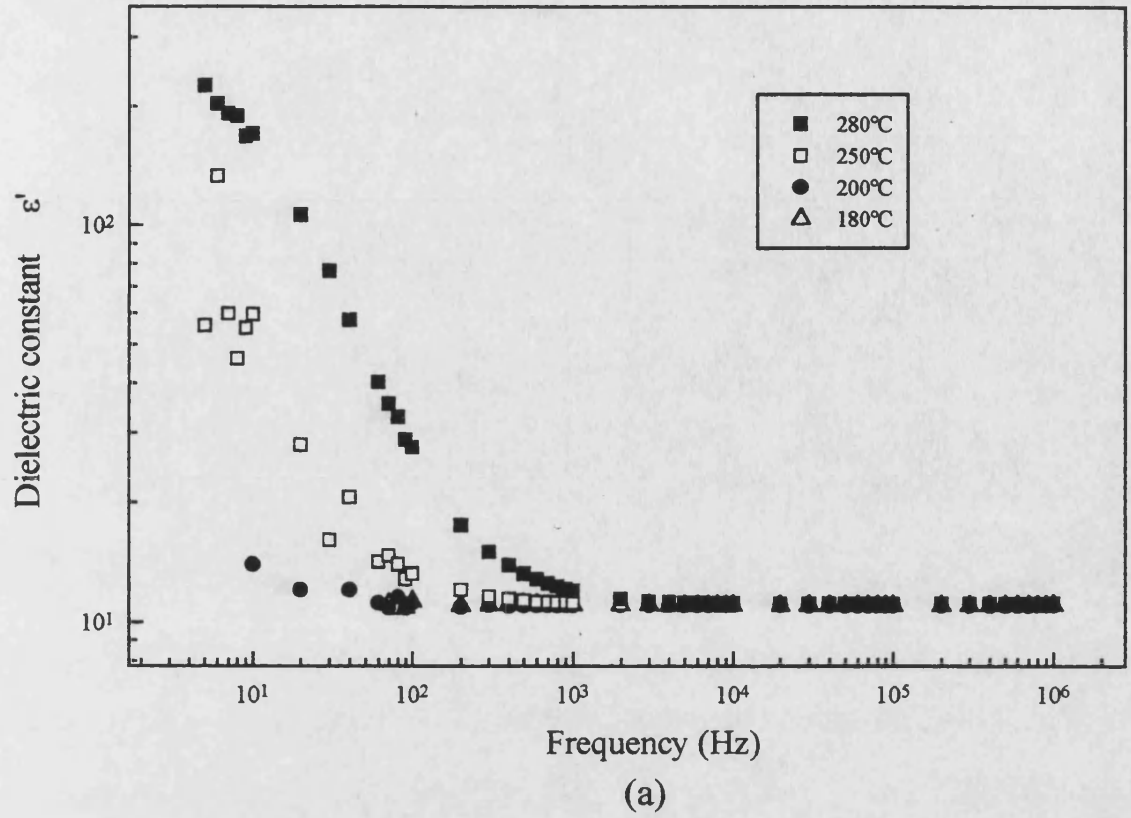

(a)

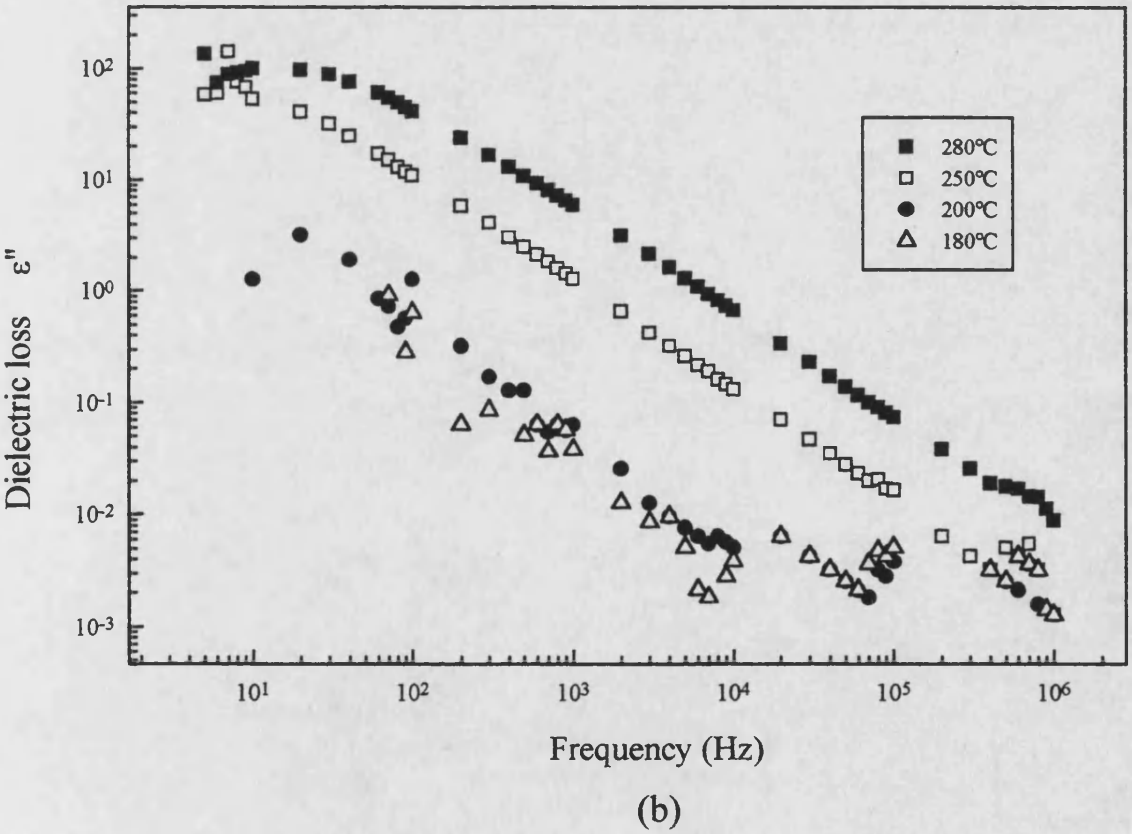

(b)

Fig.9.34 The frequency dependence of (a) dielectric constant (b) dielectric loss of the ceramic alumina D999 between 180°C and 280°C.

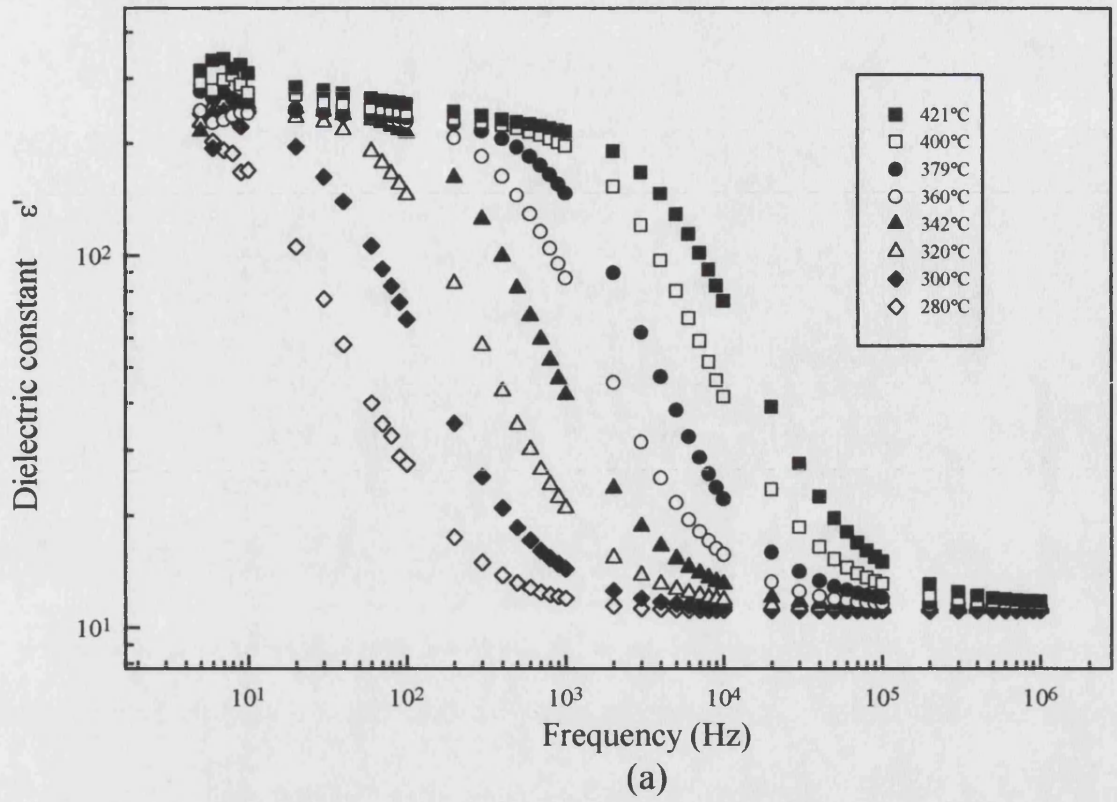

(a)

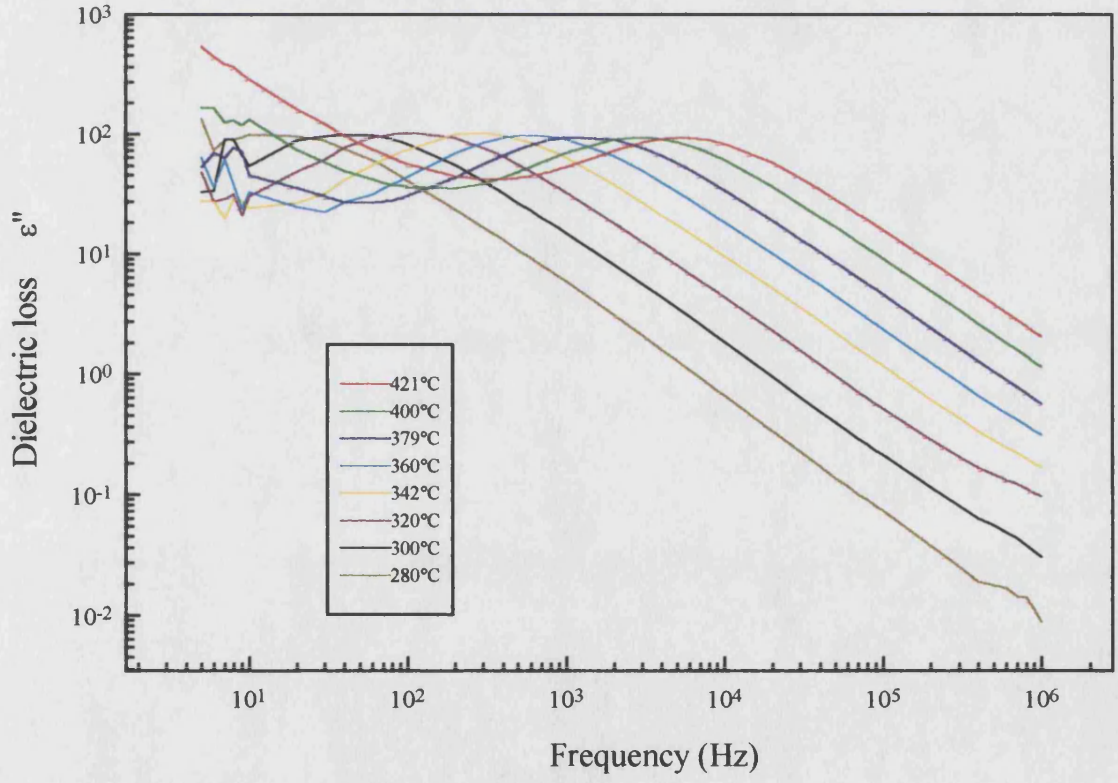

(b)

Fig.9.35 The frequency dependence of (a) dielectric constant (b) dielectric loss of the ceramic alumina D999 between 280°C and 421°C.

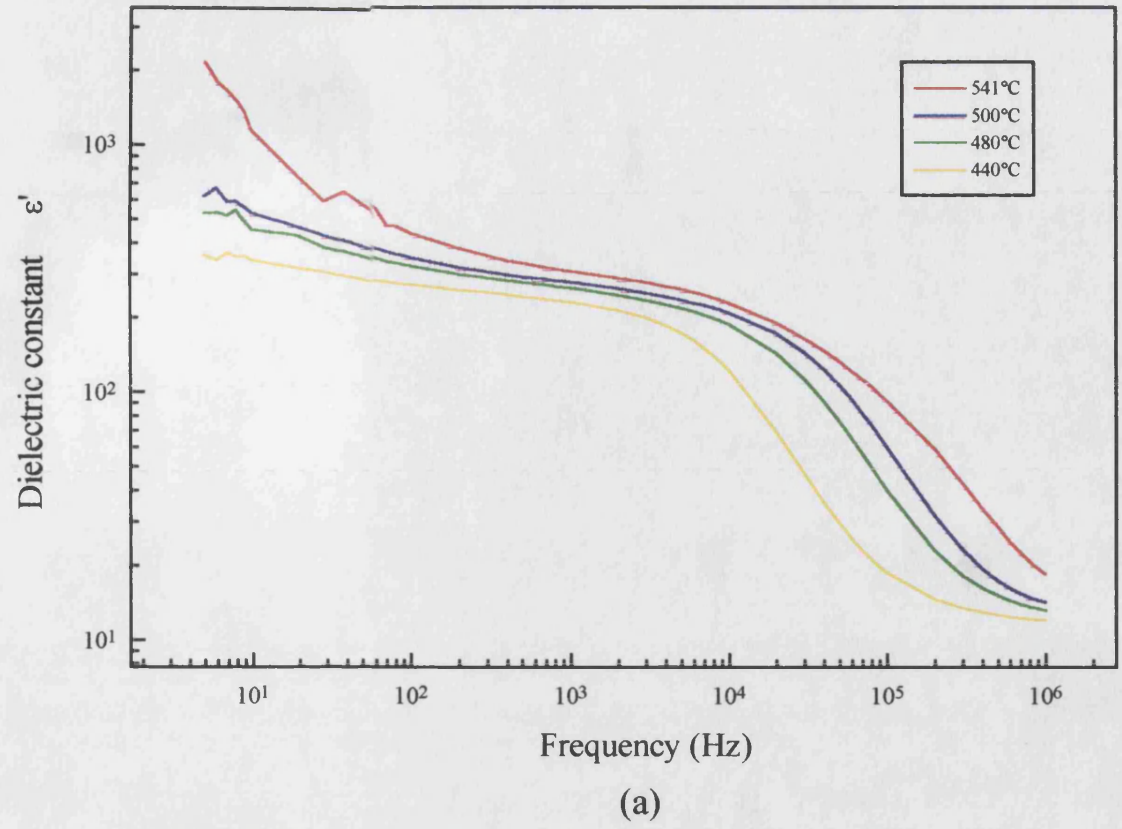

(a)

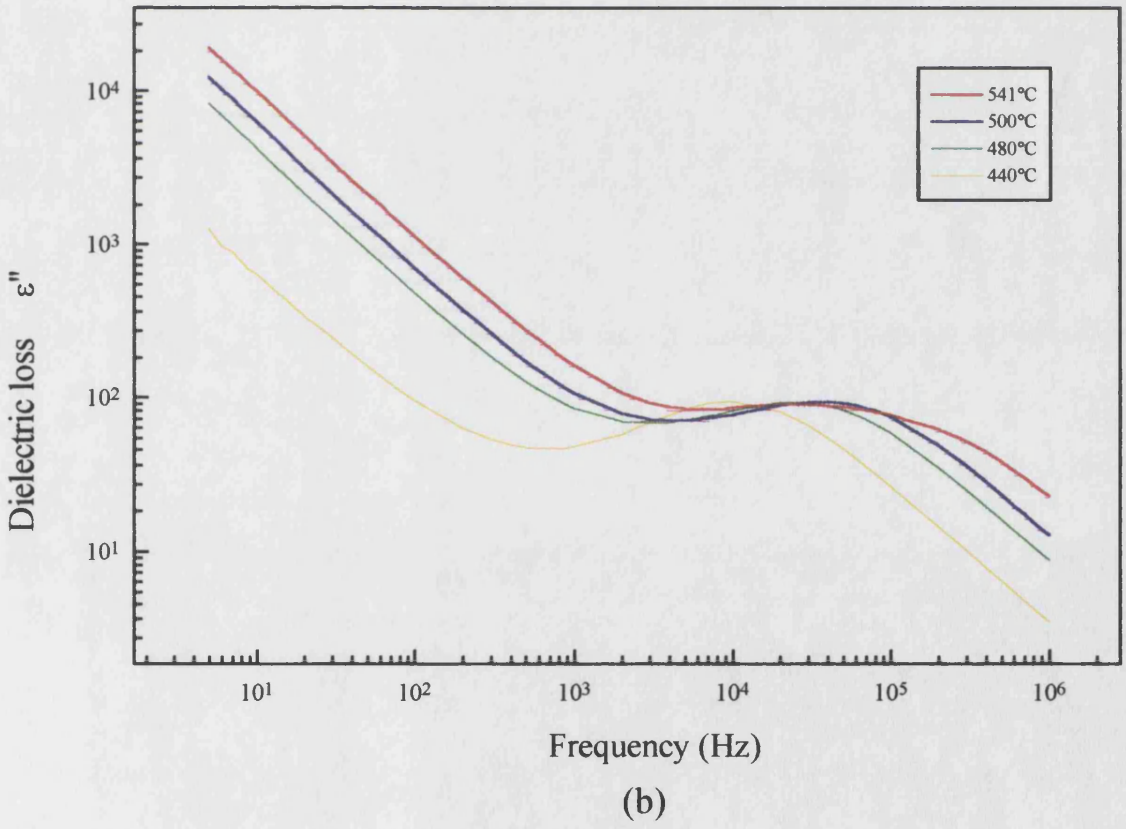

(b)

Fig.9.36 The frequency dependence of (a) dielectric constant (b) dielectric loss of the ceramic alumina D999 between 440°C and 541°C.

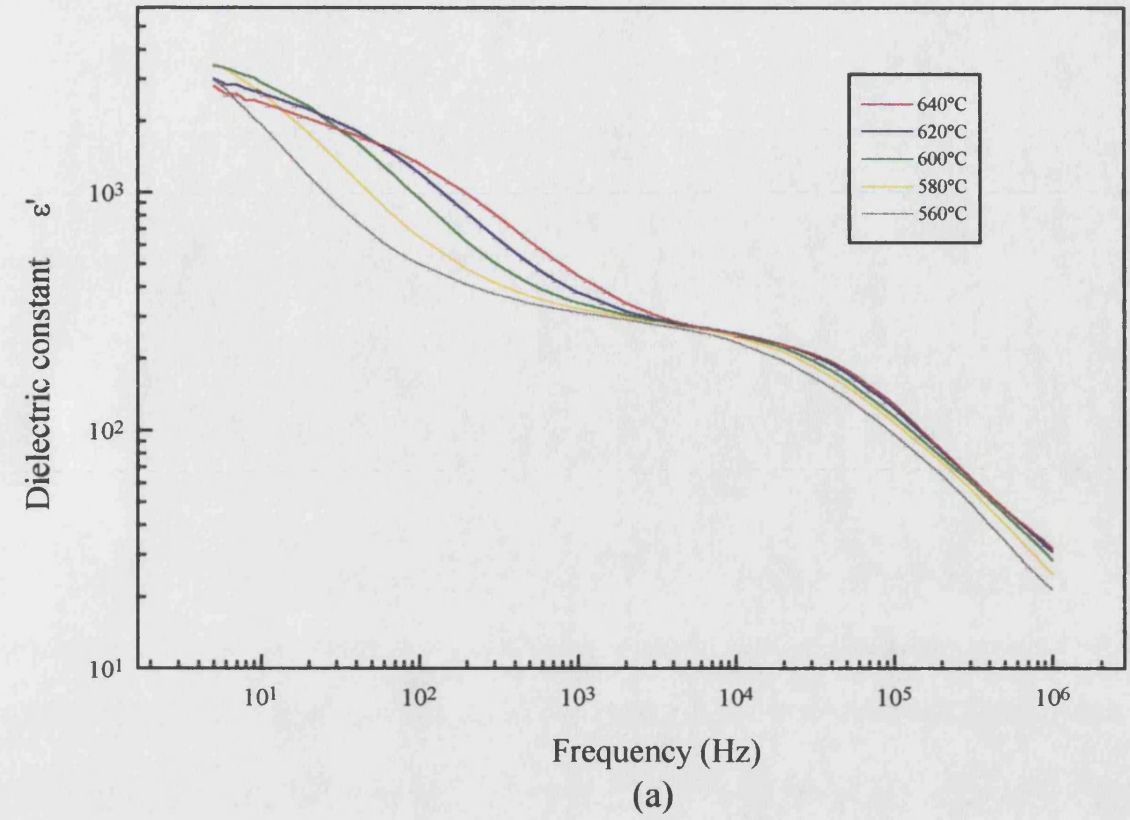

(a)

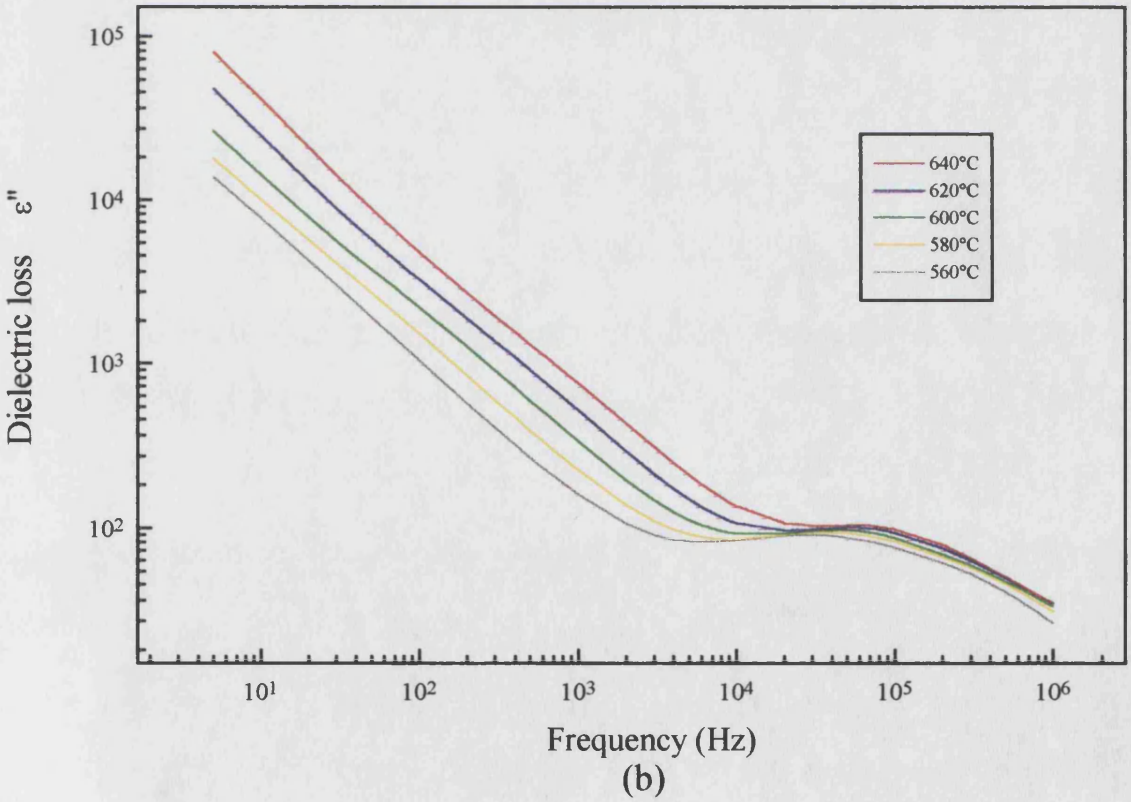

(b)

Fig.9.37 The frequency dependence of (a) dielectric constant (b) dielectric loss of the ceramic alumina D999 between 560°C and 640°C.

constant is 11.2 at 100Hz and 11.02 at 10^6Hz. The strongly dispersive behaviour of the dielectric constant begins to come into the available frequency range at about 250°C (Fig. 9.34(a)). In the dielectric loss plots, a peak begins to come in to the available frequency range at about 250°C (Fig. 9.34(b)). As the temperature is increased, this dispersion behaviour of the dielectric constant and dielectric loss peak moves gradually to higher frequency, as shown in Fig. 9.34-35. From the results shown in these figures it can be seen that the peak height in the dielectric loss remains constant with increasing temperature. As the temperature increases to 541°C (Fig. 9.36), another dispersion behaviour of the dielectric constant appears within the available frequency range; no corresponding peak was found in the dielectric loss plots. As the temperature is increased, this dispersion behaviour of the dielectric constant moves gradually to the higher frequency (Fig. 9.36(a) and 37(a)).

9.6.1.2 The master curves of dielectric constant and dielectric loss plots of ceramic alumina D999 between 280°C and 520°C

It is found quite generally that the frequency dependence does not change very drastically with temperature, at least over temperature ranges in which the material does not alter its structure in any significant way. This means that it is often possible to normalise the data for different temperatures by shifting the frequency spectra laterally into coincidence to obtain a single "master curve" which gives a complete description of the behaviour when accompanied by the locus of the reference point.

The master curves were drawn by using the graph-making software package "Origin". The log-log graphs of frequency dependence of ε' and ε'' of ceramic alumina D999 between 280°C and 520°C are shown in Figs.

9.38(a) and 9.39(a). In these figures A and B are reference points which indicate the shift of the logarithmic frequency in each curve needed to form the master curve. The reference points were created by inserting the same set of data into the data worksheets for each temperature (see Figs. 9.38(a) and 9.39(a)). Before shifting the reference points for different curves overlap together. It can be seen that the dielectric loss (ε") (Fig. 9.37 (a)) peaks have the same height at different temperatures. It is only necessary to shift the logarithmic frequency. The shifting of the curves was done by adding an appropriate value to the logarithmic frequency data column in the data worksheets until the curve under consideration overlapped with the reference curve. Each reference point was then shifted by the same value as its associated curve. The same logarithmic frequency shift was used for ε" (Fig. 9.39) and ε' (Fig. 9.38). This means that the shift of the curves needed along the X axis to make the master curves is the same for the ε' and ε" curves. Fig. 9.40 is an enlarged plot of Fig. 9.39 to show the dielectric peak more clearly.

The data in Fig. 9.38 (b) and Fig. 9.40 (b) are plotted together in Fig. 9.41. A comparison of the curve shape expected from the ideal Debye model (Fig. 3.2) with those in the master curves for ε" and ε' (Fig. 9.41) suggests that a Maxwell-Wagner effect (section 3.3.4) is involved in ceramic alumina D999. Fig. 9.41 shows that below the relaxation frequency, the dielectric losses alter to a branch rising steeply towards lower frequencies, instead of going to zero at zero frequency. Observing the variation of ε'' below the relaxation frequency can distinguish interfacial polarisation from the Debye relaxation. The dielectric loss ε'' of interfacial polarisation tends to infinity as ω tends to zero while in the Debye relaxation case ε'' drops towards zero as frequency is lowered (section 3.3.4). The interfacial

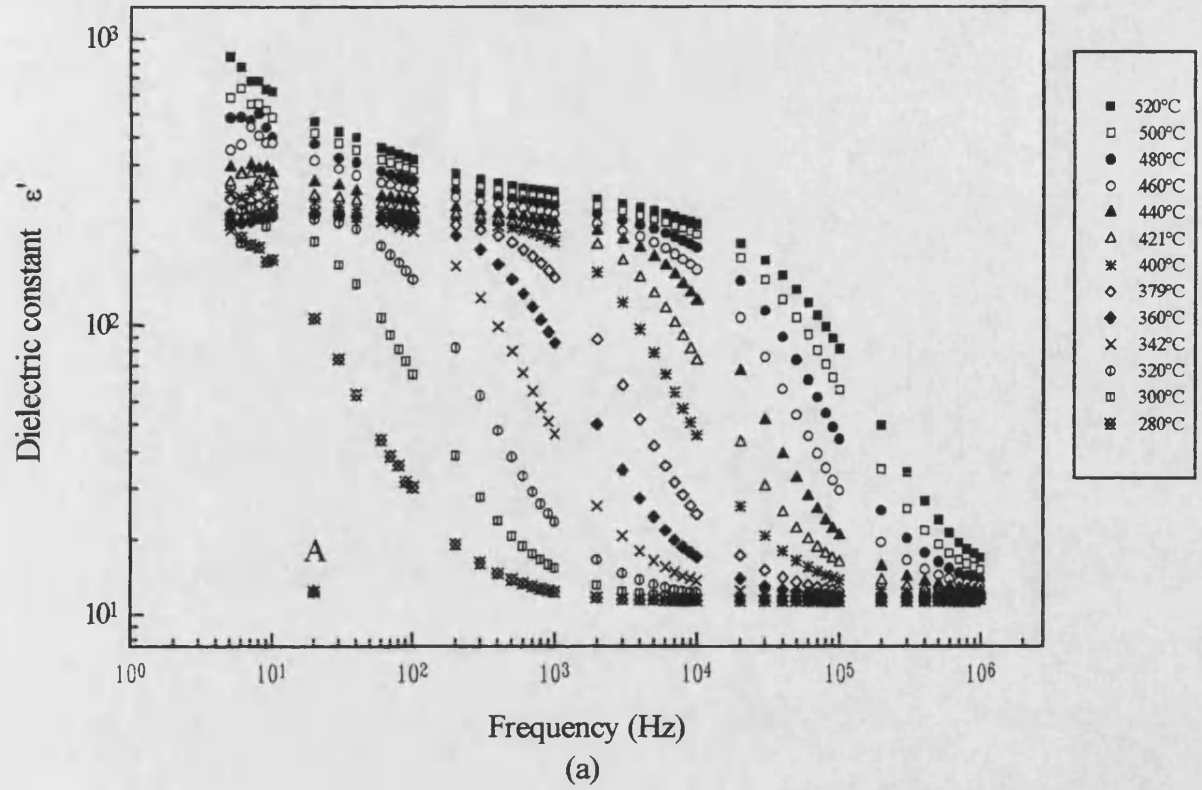

(a)

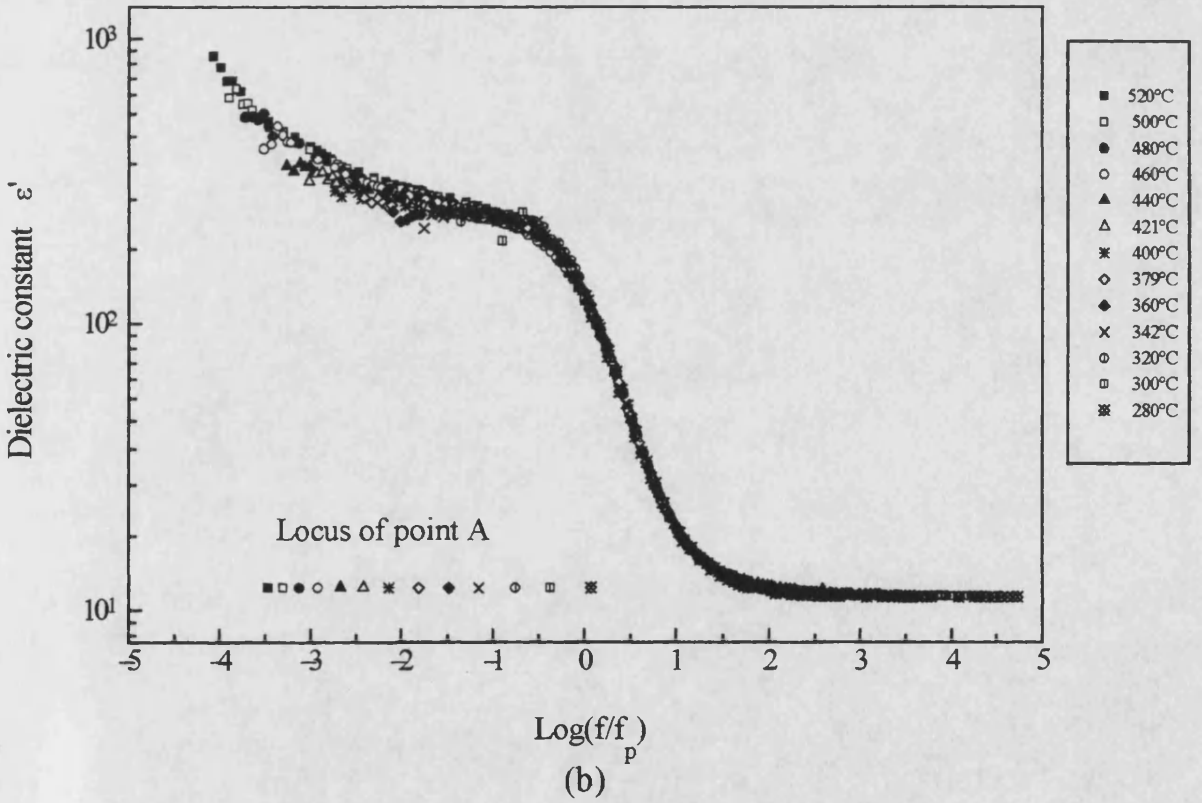

(b)

Fig.9.38 (a) Dielectric constant of the ceramic alumina D999 between 280°C and 520°C.
(b) The master curve of (a).

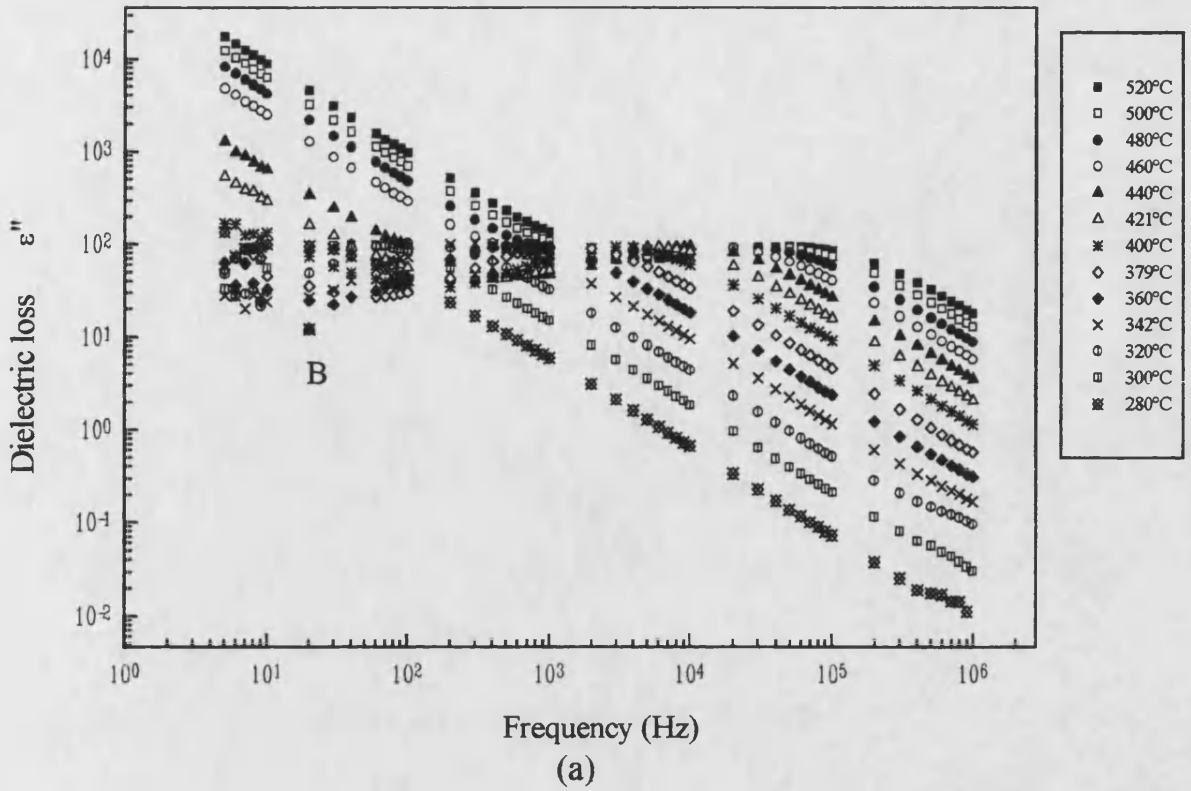

(a)

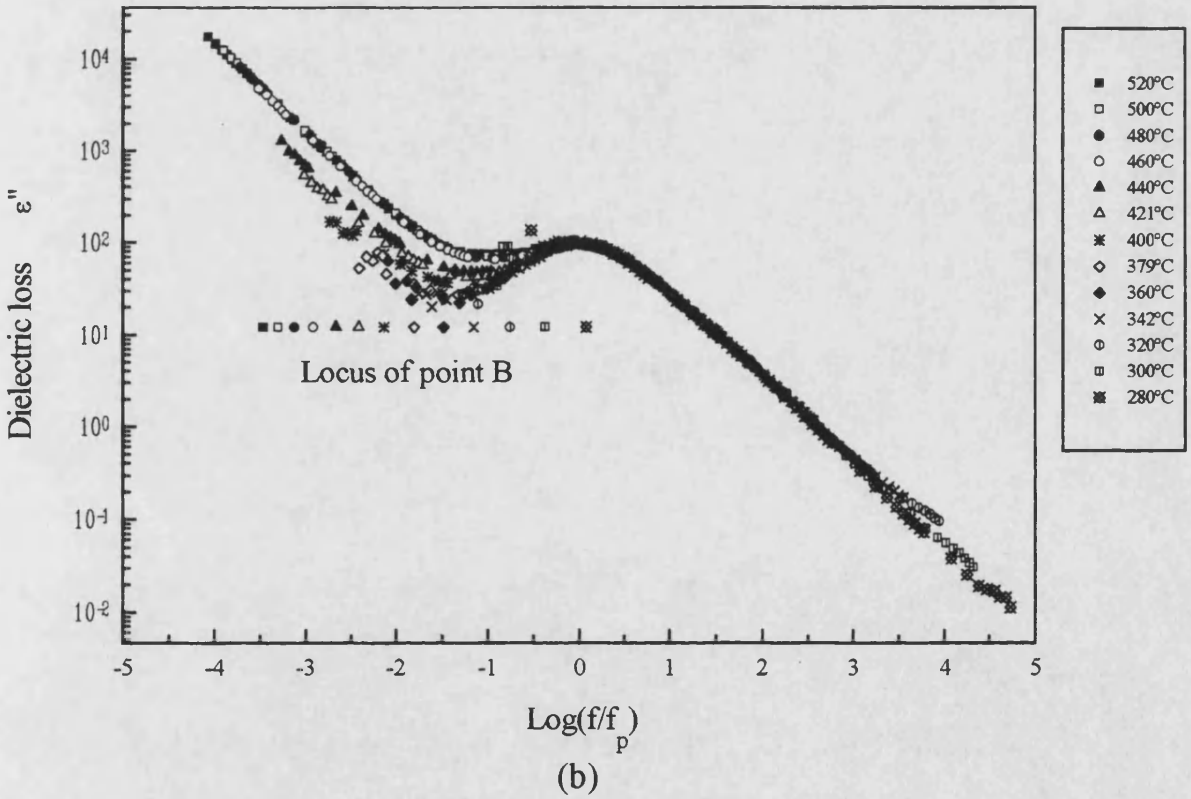

(b)

Fig.9.39 (a) Dielectric loss of the ceramic alumina D999 between 280°C and 520°C.
(b) The master curve of (a).

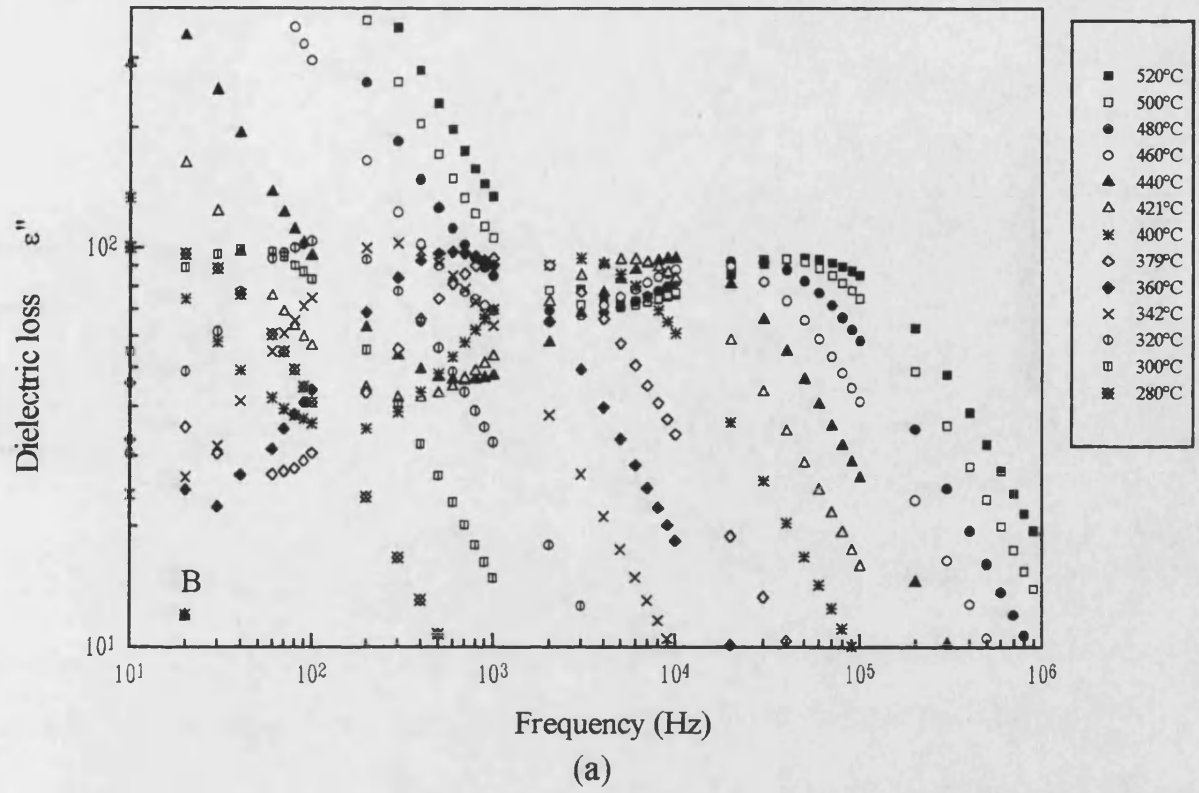

(a)

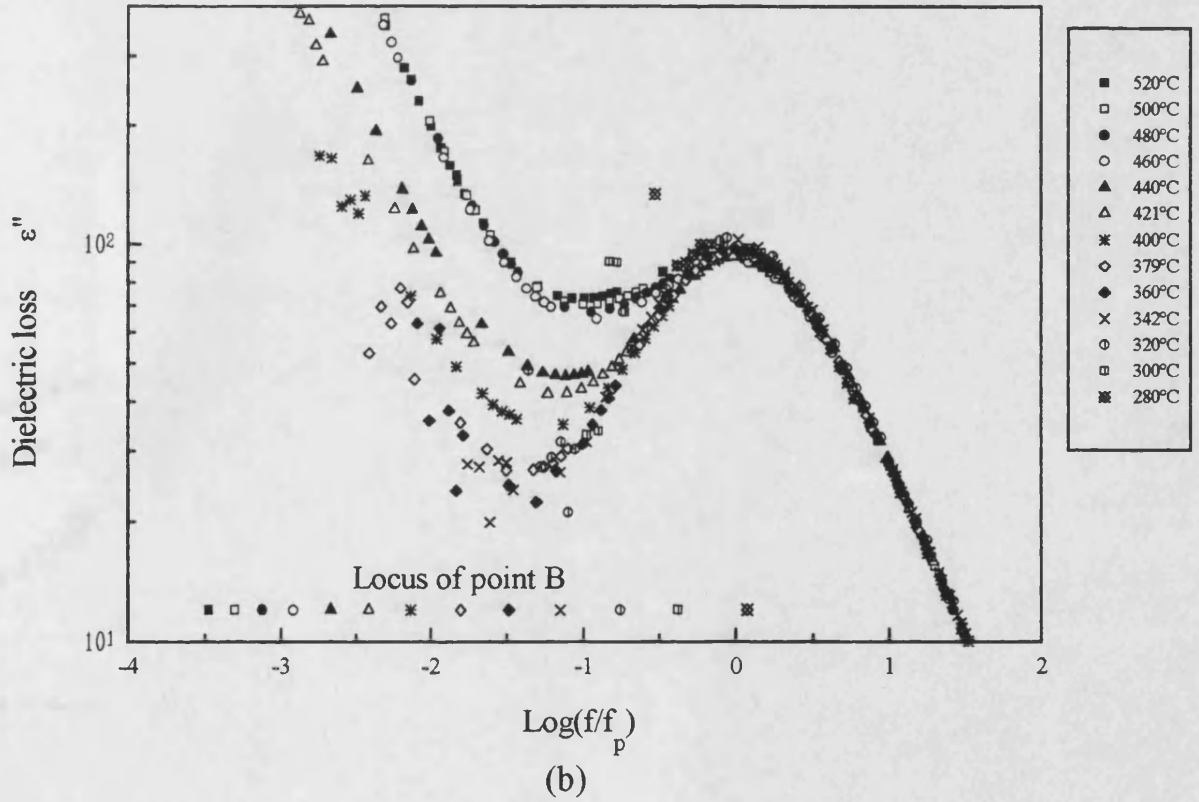

(b)

Fig.9.40 (a) The enlarged graph of fig. 9.39 (a).
(b) The enlarged graph of fig. 9.39 (b).

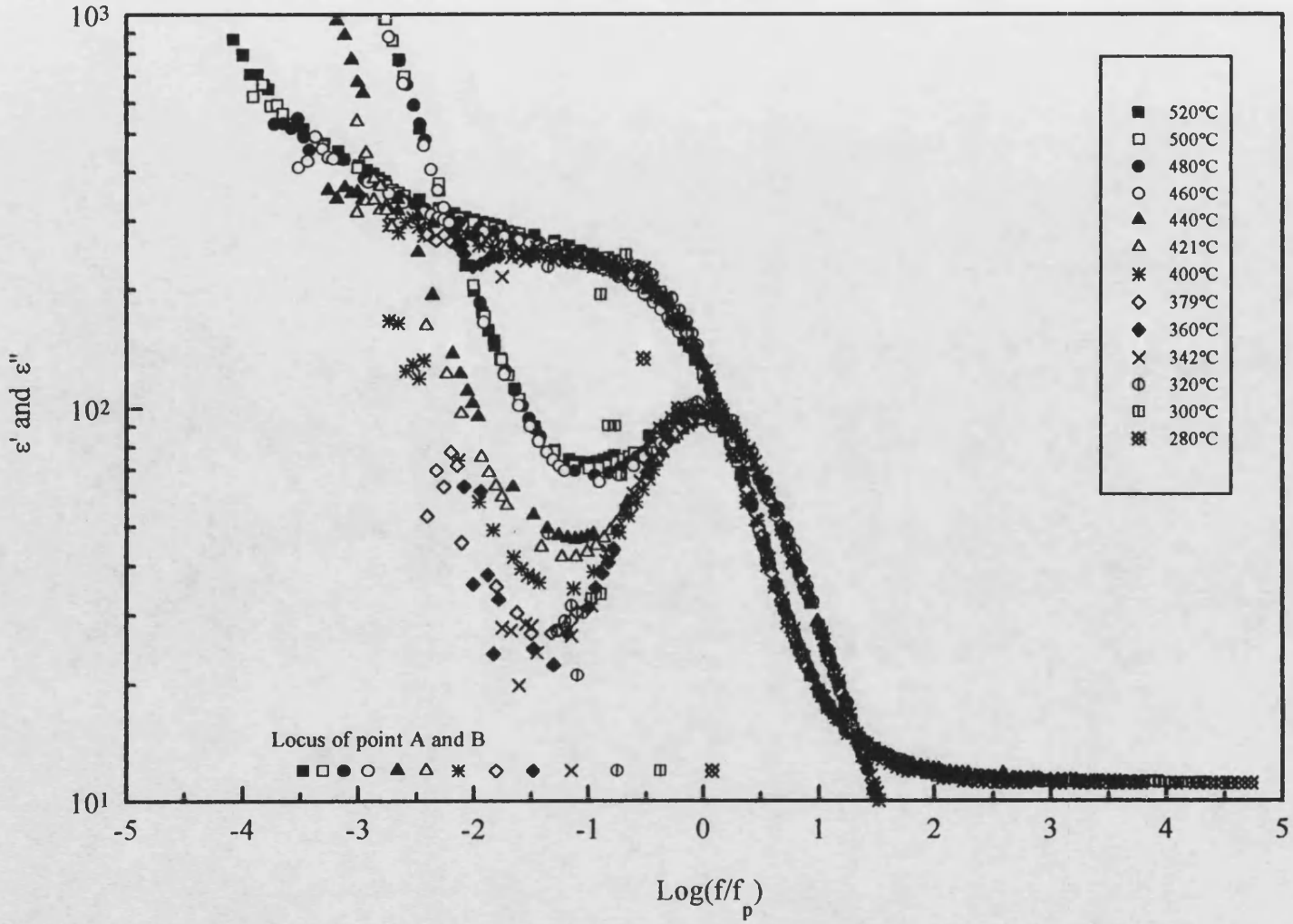

Fig.9.41 The master curvers of ε' and ε" for ceramic alumina D999.

polarisation is due to the differences in the electrical conductivity of the grains and grain boundaries. The charges can build up on the surfaces which separate the grains and grain boundaries. The conducting phase becomes polarised. Using the ratio of grain boundary thickness (d) to grain size (D) (table 9.2) and the values of R_b and R_{gb} (table 9.4), it has been shown by calculation that the electrical conductivity of the grains is about 3500 larger than that of the grain boundaries.

The logarithm of the peak frequency f_p of dielectric loss ε'' against reciprocal temperature between 280°C and 520°C is plotted in Fig. 9.42. It has been found that the relaxation process is thermally activated and the peak frequency f_p of the dielectric loss ε'' obeys an equation of the form:

$$f_p(T) = A\exp(-W/kT) \qquad (9.9)$$

with A being a constant, W the activation energy, k the Boltzmann constant and T temperature in Kelvin. The almost linear relationship between log (f_p) and the reciprocal temperature (1000/T) gives an average activation energy of 1.30 ±0.01eV. Extending the line in Fig. 9.42 towards lower temperature, it is found that at room temperature (20°C) the relaxation process is very slow and the relaxation frequency (f_p) is about 10^{-9} Hz. This suggests again that a Maxwell-Wagner effect is involved (section 3.3.4).

9.6.1.3 The dielectric constant, dielectric loss in ceramic alumina D999 below room temperature

Fig. 9.43(a) shows the dielectric constant of ceramic alumina D999 obtained in the temperature range 20K to 320K. Between 170K and 320K, the dielectric constant increases with temperature at all frequencies and has a small frequency dependence. No signs of relaxation processes for dipole

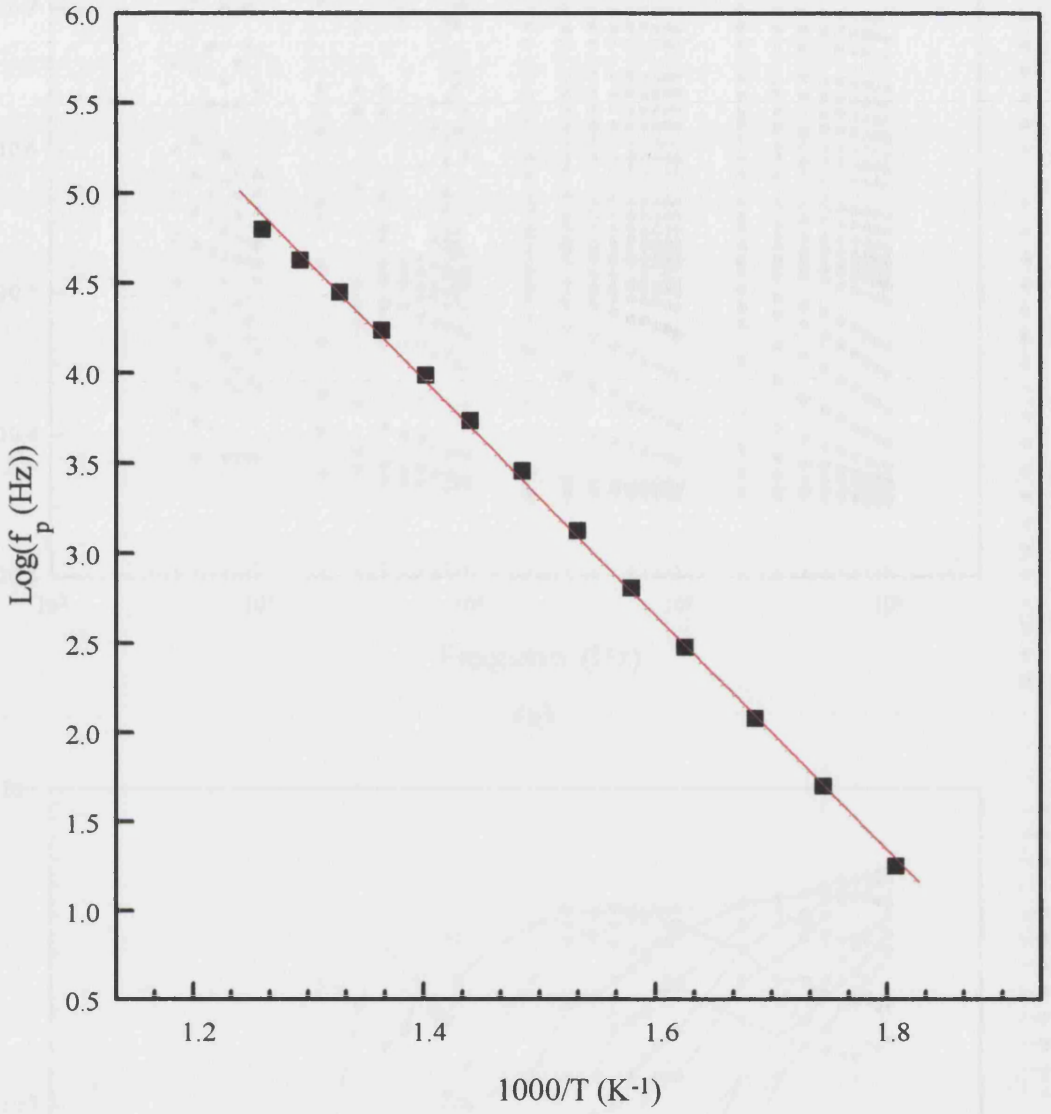

Fig.9.42 The plot of the logarithm of the peak frequency of dielectric loss against reciprocal temperature of the ceramic alumina D999 between 280°C and 520°C, indicating an average activation energy of 1.30±0.1eV.

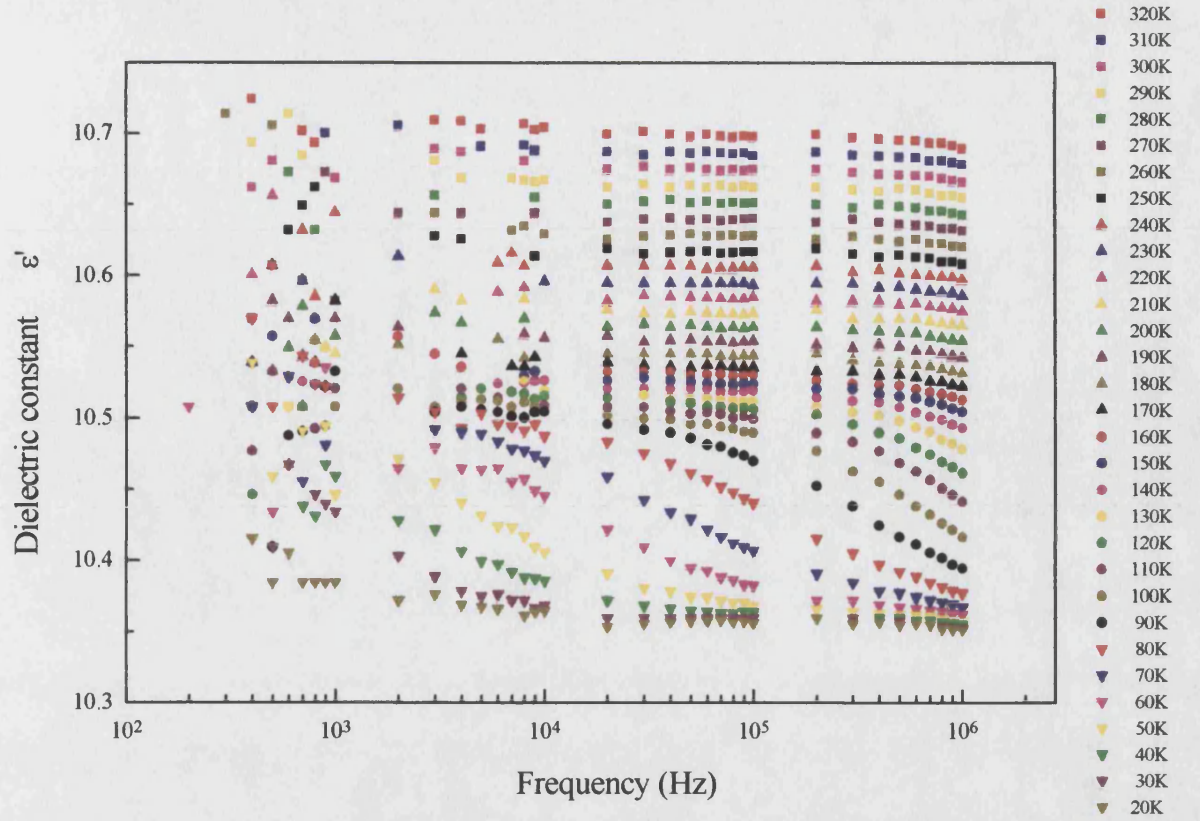

(a)

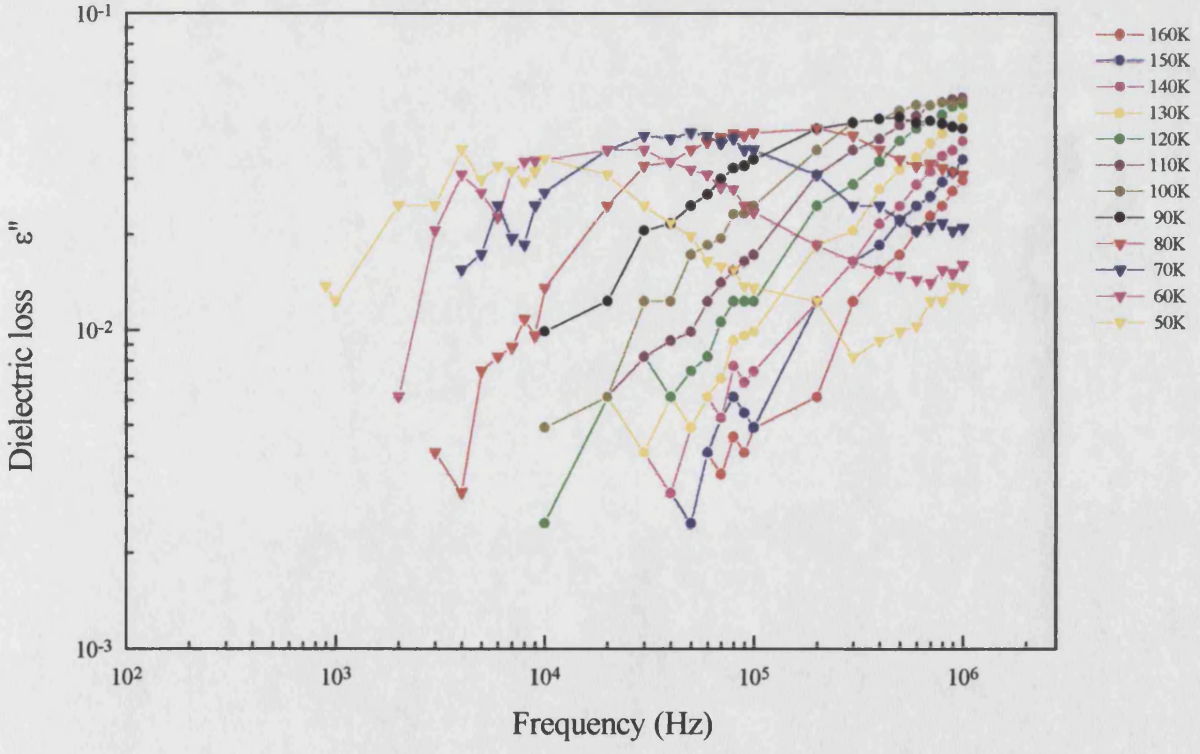

(b)

Fig.9.43 The frequency dependence of (a) dielectric constant (b) dielectric loss of the ceramic alumina D999 at different temperatures.

rotation or interfacial polarisation of grain boundaries are observed between 170K and 320K. Fig. 9.44 shows the temperature dependence between 170K and 320K of the dielectric constant of ceramic alumina D999 at 10^5 Hz. In this temperature range the dielectric constant increases linearly with the temperature with a temperature coefficient ($\partial\varepsilon'/\partial T$) of $(1.09\pm0.01)\times10^{-3}$/K. Between 170K and 320K the dielectric loss is small being out of the measurable range of the impedance analyser. Fig. 9.43(b) shows the dielectric loss obtained in the temperature range 50K to 160K. A dielectric loss peak and a dispersion behaviour of dielectric constant begins to come into the high end of available frequency range at about 160K (Fig. 9.43). As the temperature is decreased, this dispersion behaviour of dielectric constant and dielectric loss peak moves gradually to the lower frequency (Fig. 9.43). As the temperature decreases to 50K, this dispersion behaviour of dielectric constant and dielectric loss peak move out of the available frequency range at the lower end.

The graphs of frequency dependence of dielectric constant and dielectric loss of ceramic alumina D999 between 50K and 160K are shown in Figs. 9.45 (a) and 9.46 (a). The master curves are shown in Figs. 9.45 (b) and 9.46 (b). In these figures A and B are reference points to indicate the shift made of the logarithmic frequency in each curve to form the master curve. The shift of the curves needed along the X axis to make the master curves is the same for the dielectric constant and dielectric loss curves. It can be seen that the height of dielectric loss (Fig. 9.46 (a)) peaks are temperature dependent. It is necessary to shift the logarithmic dielectric loss as well to make the master curve.

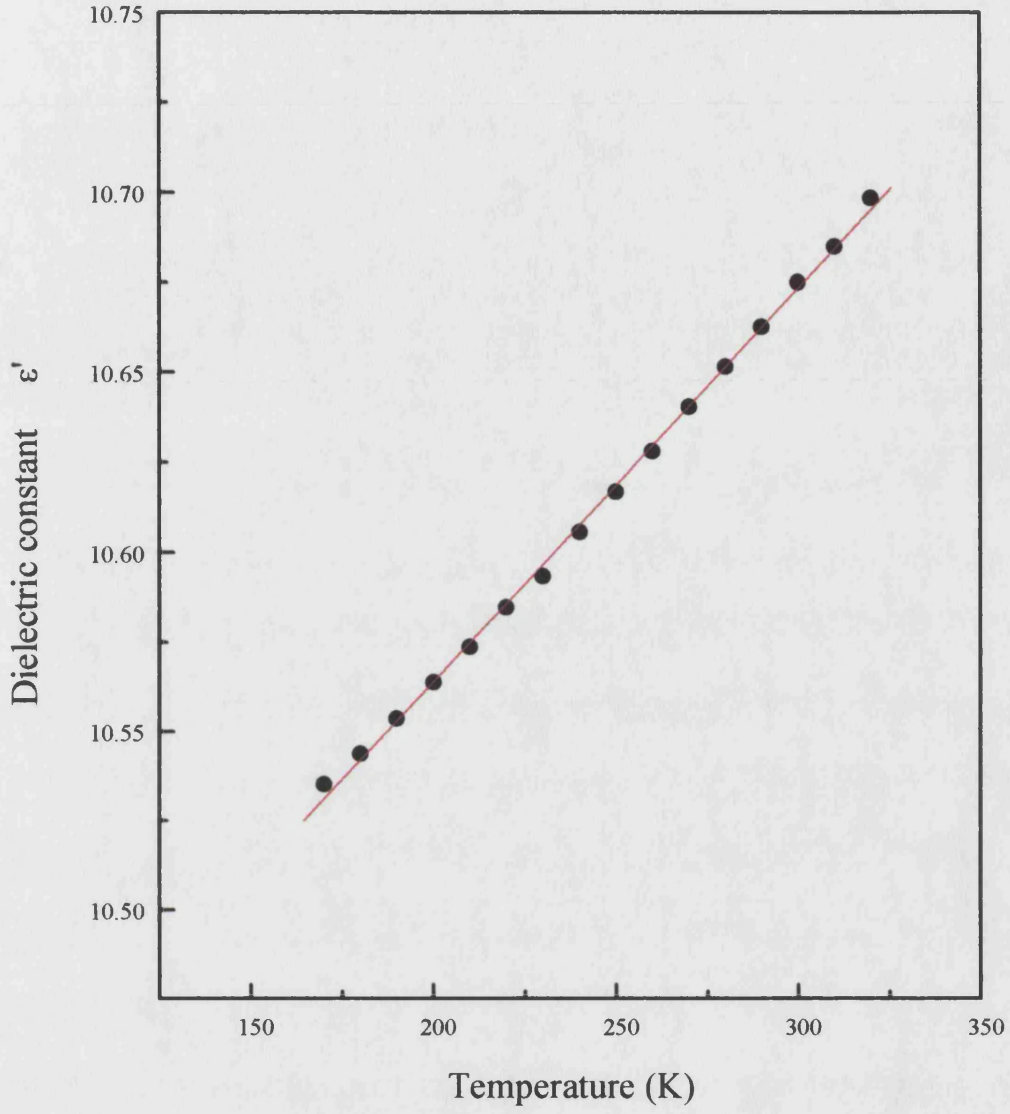

Fig.9.44 The temperature dependence of dielectric constant of the ceramic alumina D999 at 10^5Hz and between 170K and 320K.

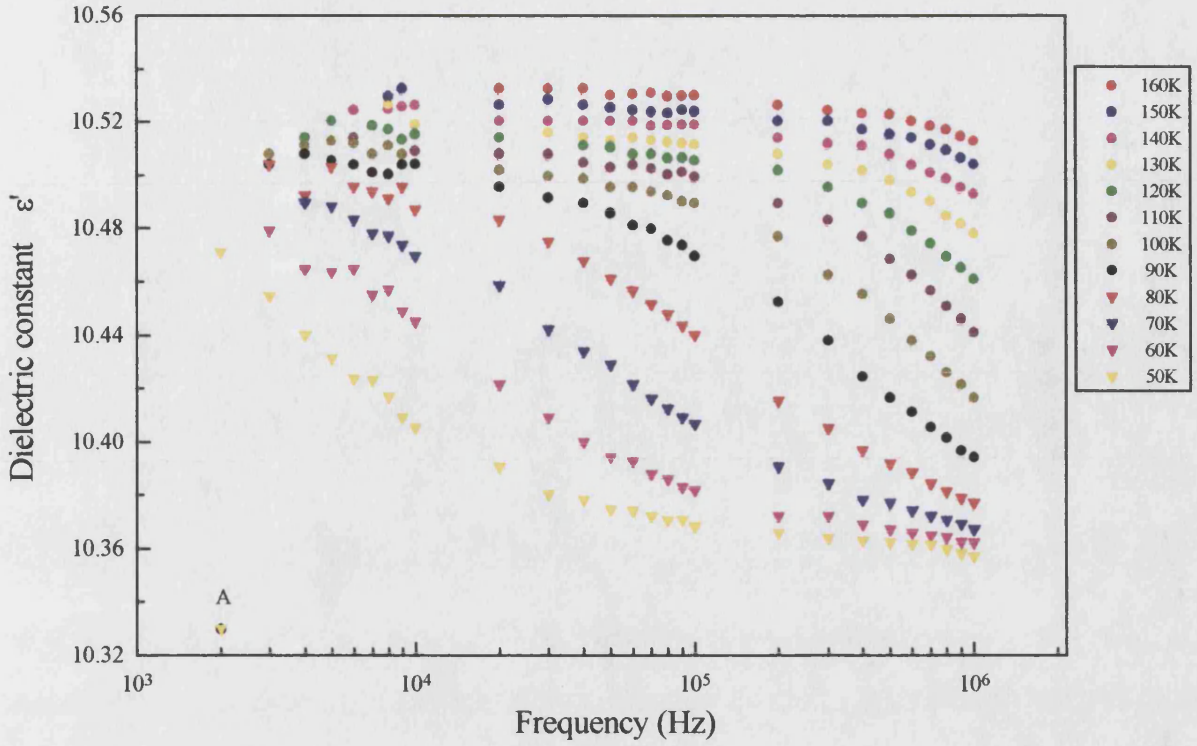

(a)

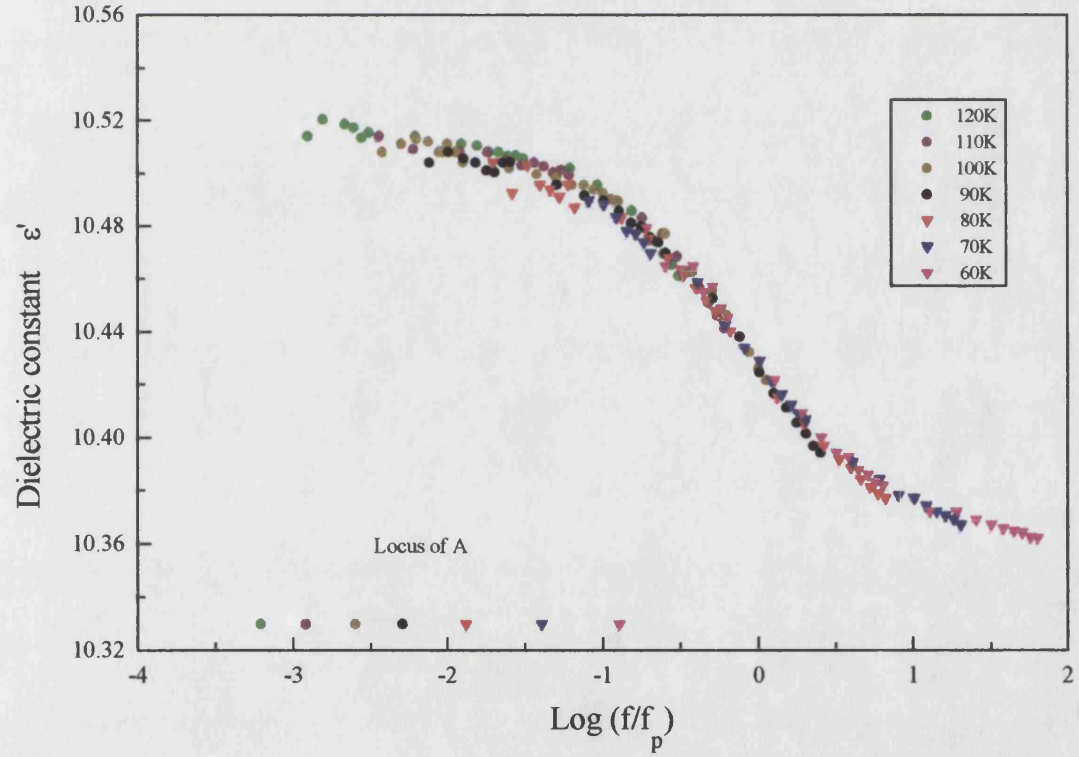

(b)

Fig.9.45 (a) The frequency dependence of dielectric constant of the ceramic alumina D999 between 50K and 160K.
(b) The master curve of (a) between 60K and 120K..

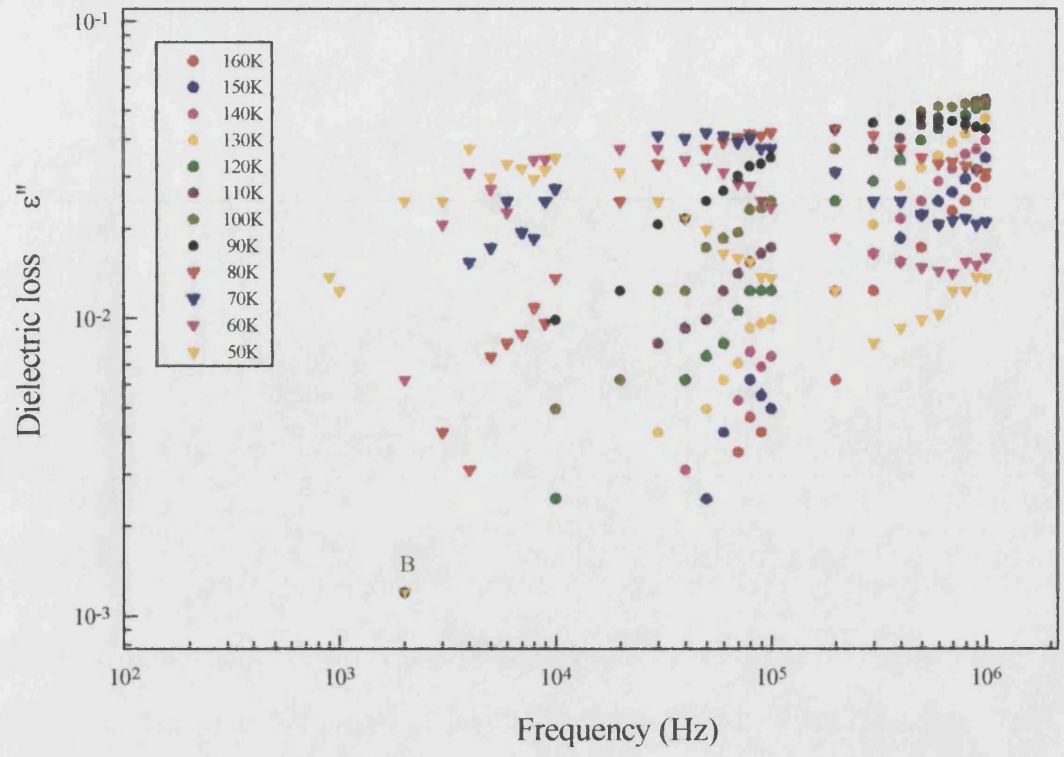

(a)

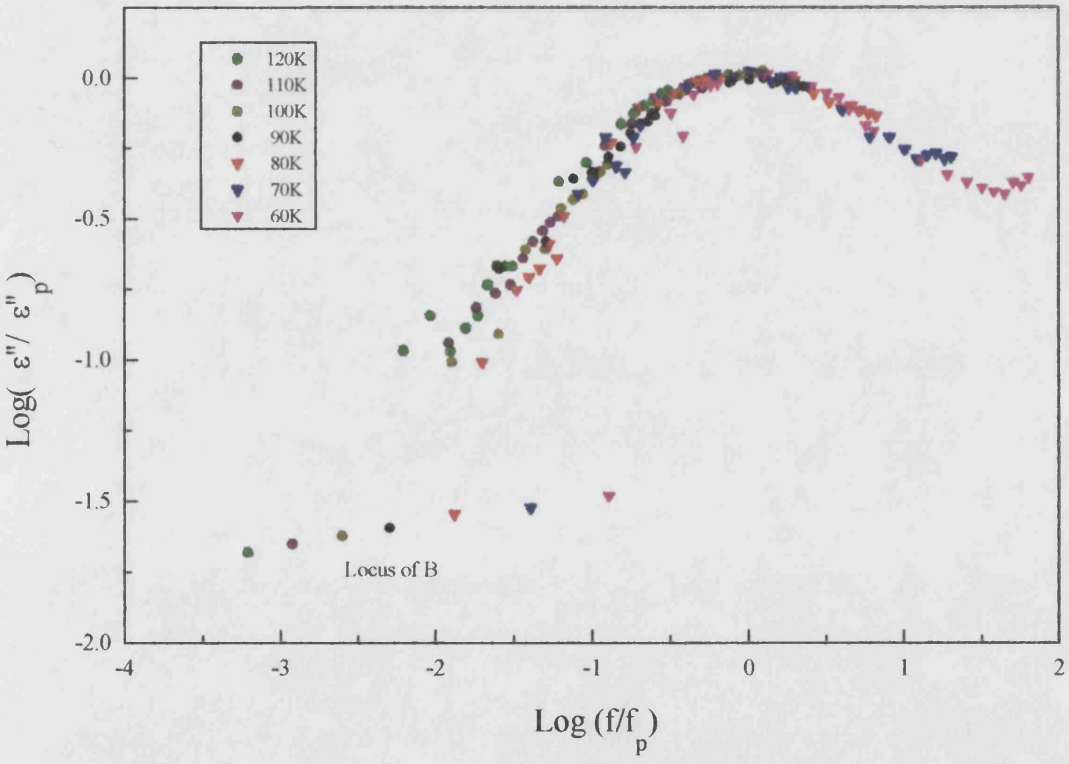

(b)

Fig.9.46 (a) The frequency dependence of dielectric loss of the ceramic alumina D999 between 50K and 160K.

(b) The master curve of (a) between 60K and 120K.

The data given in Fig. 9.45 (b) and Fig. 9.46 (b) are plotted together with the theoretical curves for a Debye relaxation in Fig. 9.47. Fig. 9.47 shows that below the relaxation frequency, the dielectric losses go to minimum at low frequency and that the peak is broader than that of the theoretical curve for a Debye relaxation. This suggests that a dipolar relaxation process with a distributed relaxation time is involved. It is common that the real measured relaxation peak is wider than the ideal Debye peak: the response of most dielectrics cannot be described by assuming a single relaxation time.

The logarithm of the peak frequency f_p of dielectric loss ε'' of ceramic alumina D999 against reciprocal temperature (1000/T) between 50K and 160K is plotted in Fig. 9.48. The almost linear relationship between log (f_p) and the reciprocal temperature (1000/T) suggest that the relaxation process is thermally activated and the peak frequency f_p dielectric loss ε'' obeys equation 9.9. From the result of the linear fit, shown in Fig. 9.48, an average activation energy of 0.060±0.002eV is obtained. Extrapolating the line in Fig. 9.48 towards higher temperature, it is found that at room temperature (20°C) the relaxation frequency (f_p) is about 10^8 Hz. This suggests again that a dipolar relaxation process is involved (section 3.3.3).

9.6.2 The dielectric constant, dielectric loss, Maxwell-Wagner effect and relaxation processes in ceramic alumina AL23

9.6.2.1 The dielectric constant, dielectric loss in ceramic alumina AL23 above room temperature

The frequency dependencies of dielectric constant and dielectric loss obtained in the temperature range 19°C to 200°C are shown in Fig. 9.49. From the results given in Fig. 9.49 it can be seen that the dielectric loss

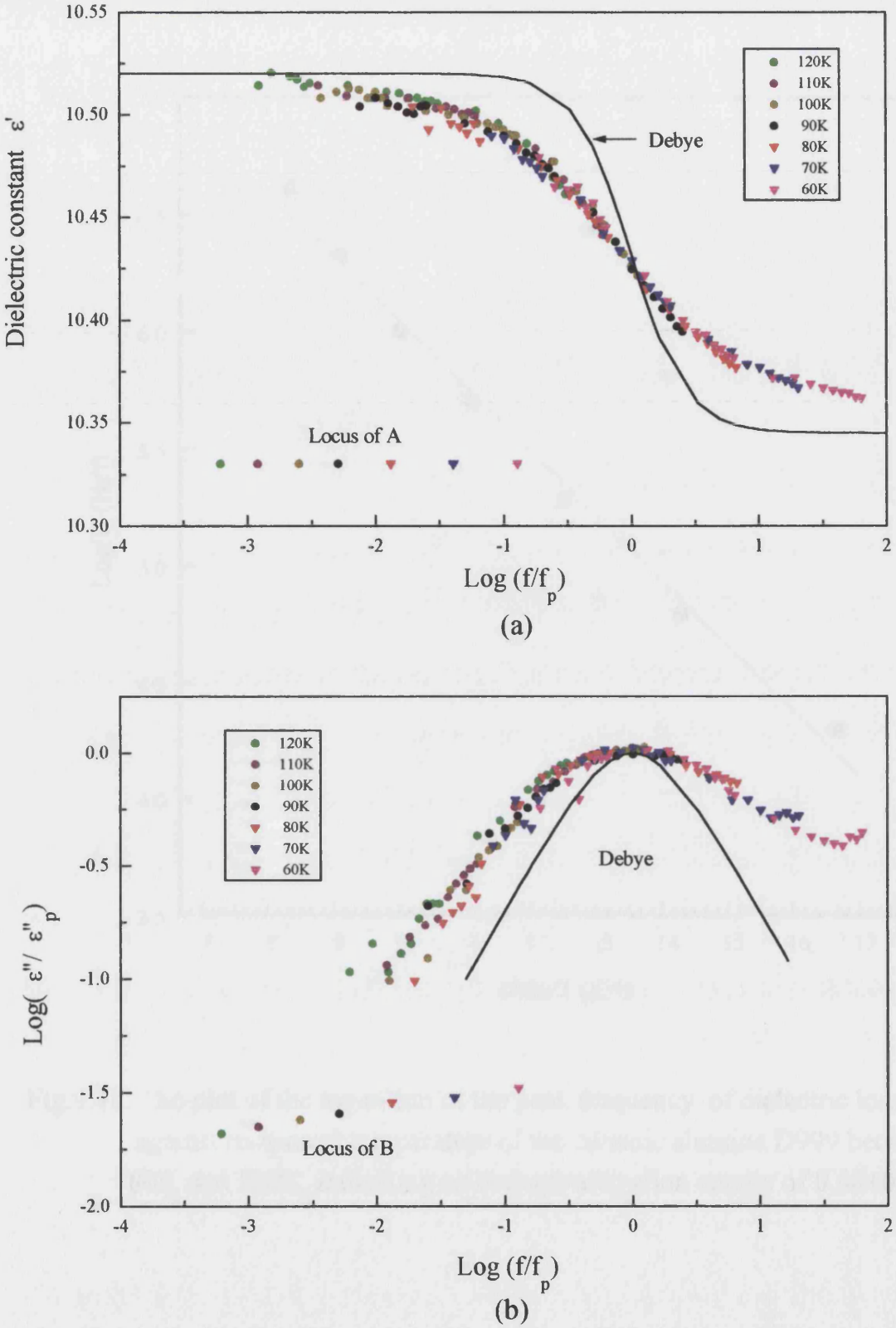

Fig.9.47 The master curve of (a) dielectric constant (b) dielectric loss of the ceramic alumina D999 between 60K and 120K plotted together with that of a debye system.

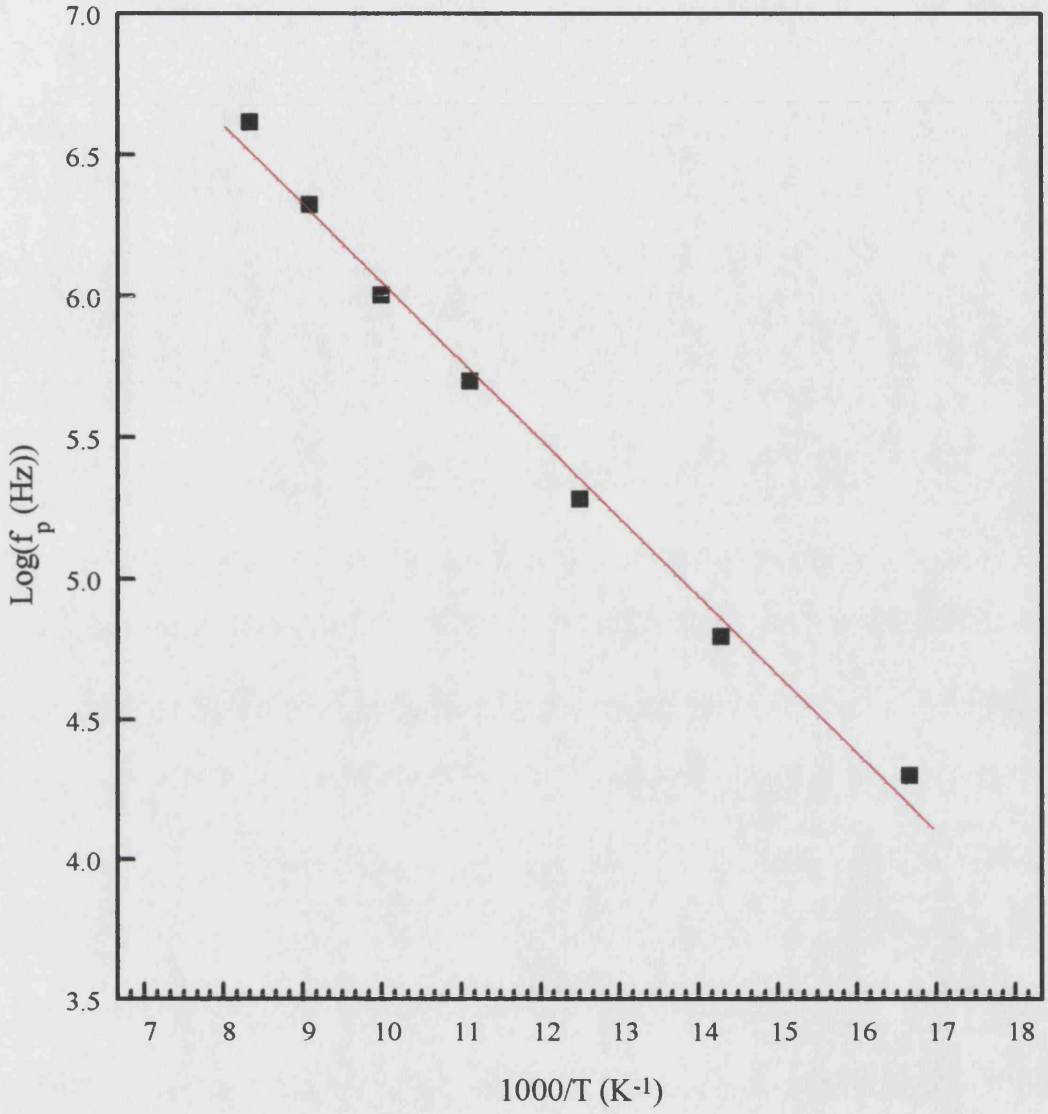

Fig.9.48 The plot of the logarithm of the peak frequency of dielectric loss against reciprocal temperature of the ceramic alumina D999 between 60K and 120K, indicating an average activation energy of 0.06±0.002eV.

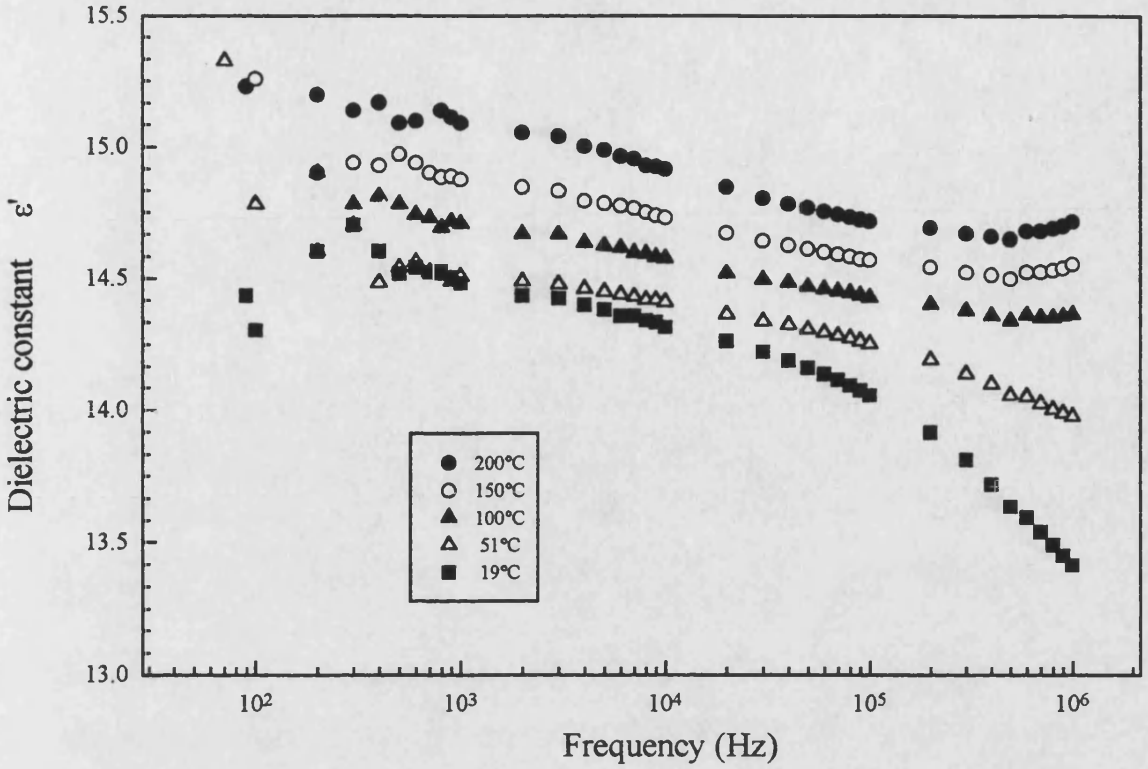

(a)

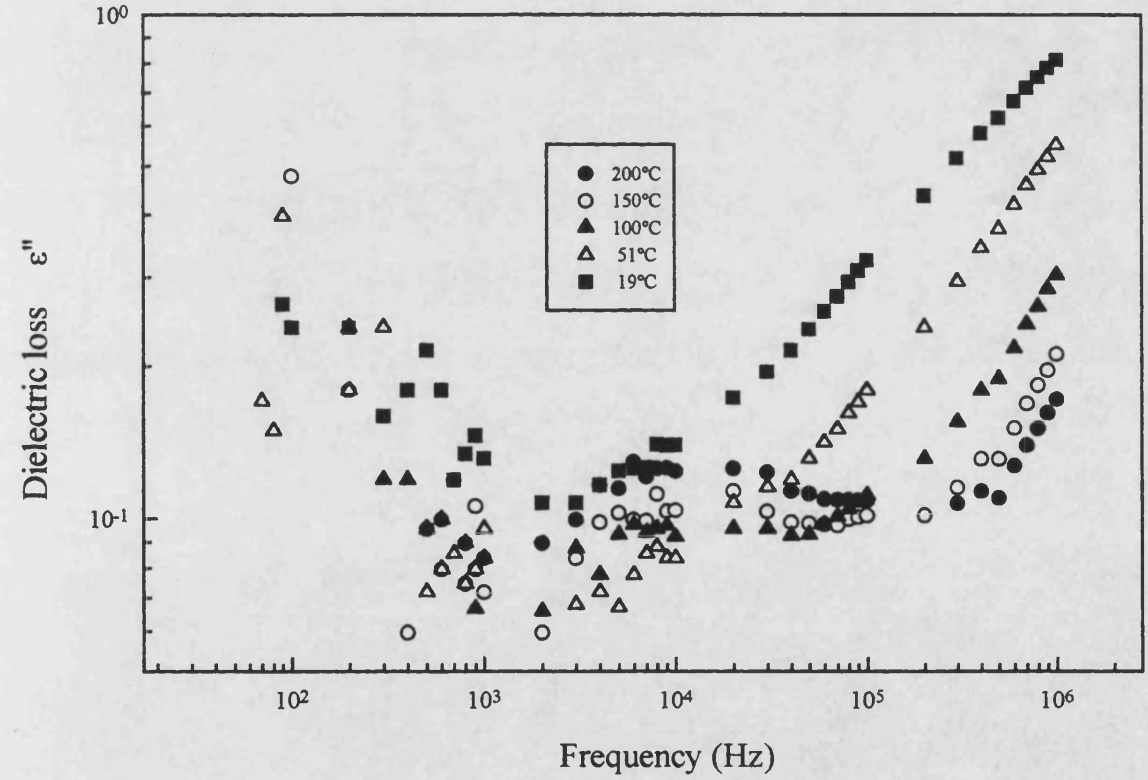

(b)

Fig.9.49 The frequency dependence of (a) dielectric constant and (b) dielectric loss of the ceramic alumina AL23 between 19°C and 200°C.

increases with decrease of the temperature and a relaxation process may begin to come into the available frequency range. This will be described in detail in the next section.

Fig. 9.50. shows the frequency dependence of dielectric constant and dielectric loss obtained in the temperature range 200°C to 399°C. The peaks, which are just visible in the dielectric loss versus frequency curves, shift to higher frequencies when the temperature increasing. The temperature dependence of dielectric loss peak frequency is very small. It is known that any relaxation process is associated with a decrease of the dielectric constant as frequencies are raised above the relaxation rates. At 399°C the dielectric constant is 16.3 at 10^2Hz and 15.1 at 3×10^5Hz. Hence the associated dielectric constant decrease is only 1.2. A relaxation process is observed with a small activation energy (about 0.2eV); this value rules out an ionic diffusion-like process which commonly has an activation energy of 1eV or higher in alumina (Atlas et al., 1962). A similar process was found by Atlas et al. (1962) in the alumina ceramic specimen containing less then 100 ppm impurities and the alumina ceramic specimen containing 670 ppm of Fe ions. They suggested that this phenomenon arises from the intragranular polarisation involving electronic carriers.

Fig. 9.51 shows the frequency dependence of dielectric constant and dielectric loss of ceramic alumina AL23 between 399°C to 704°C. At 399°C the dielectric constant has much smaller frequency dependence than that above this temperature. The strongly dispersive behaviour of the dielectric constant begins to come into the available frequency range at about 459°C (Fig. 9.51(a)). In the dielectric loss plots, a peak, which

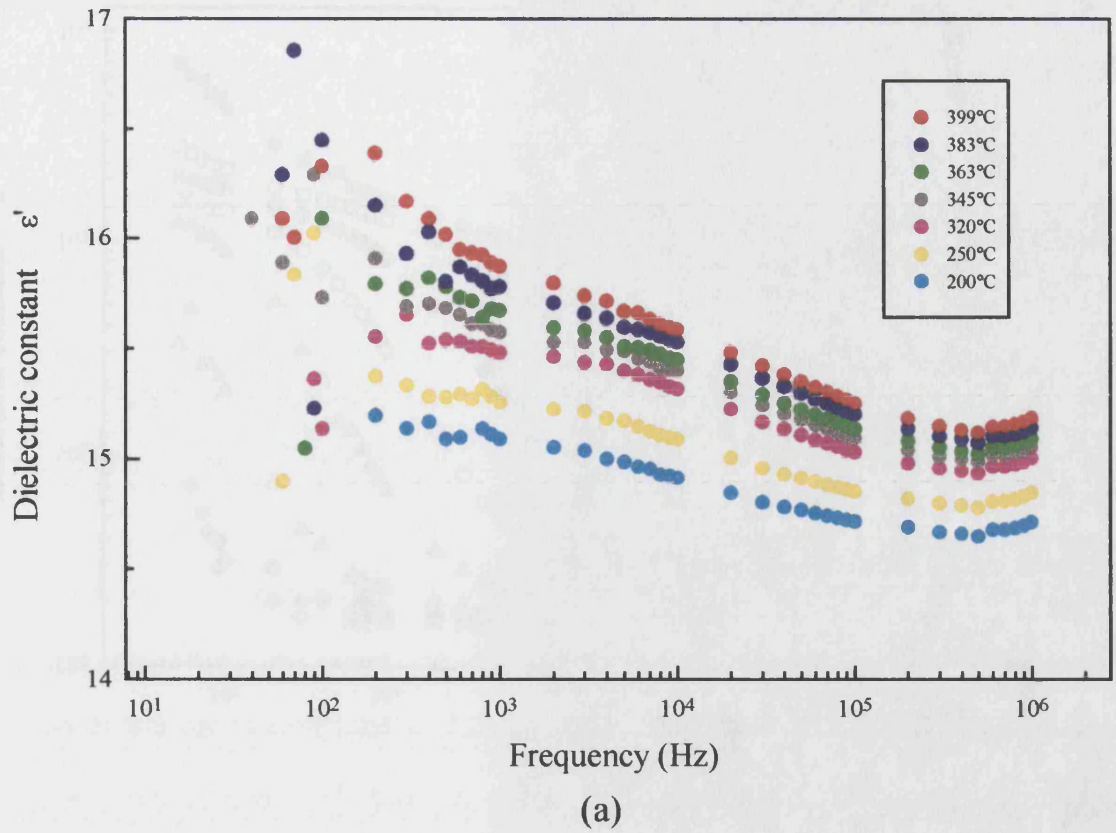

(a)

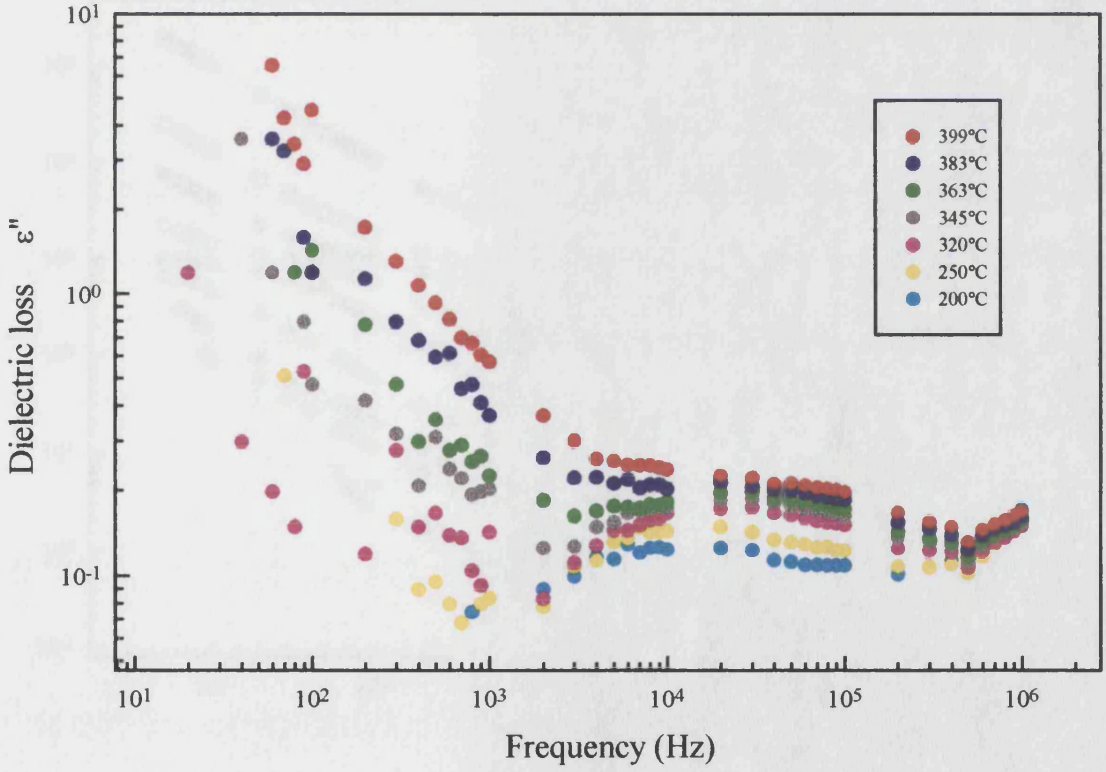

(b)

Fig.9.50 The frequency dependence of (a) dielectric constant and (b) dielectric loss of the ceramic alumina AL23 beween 200°C and 399°C.

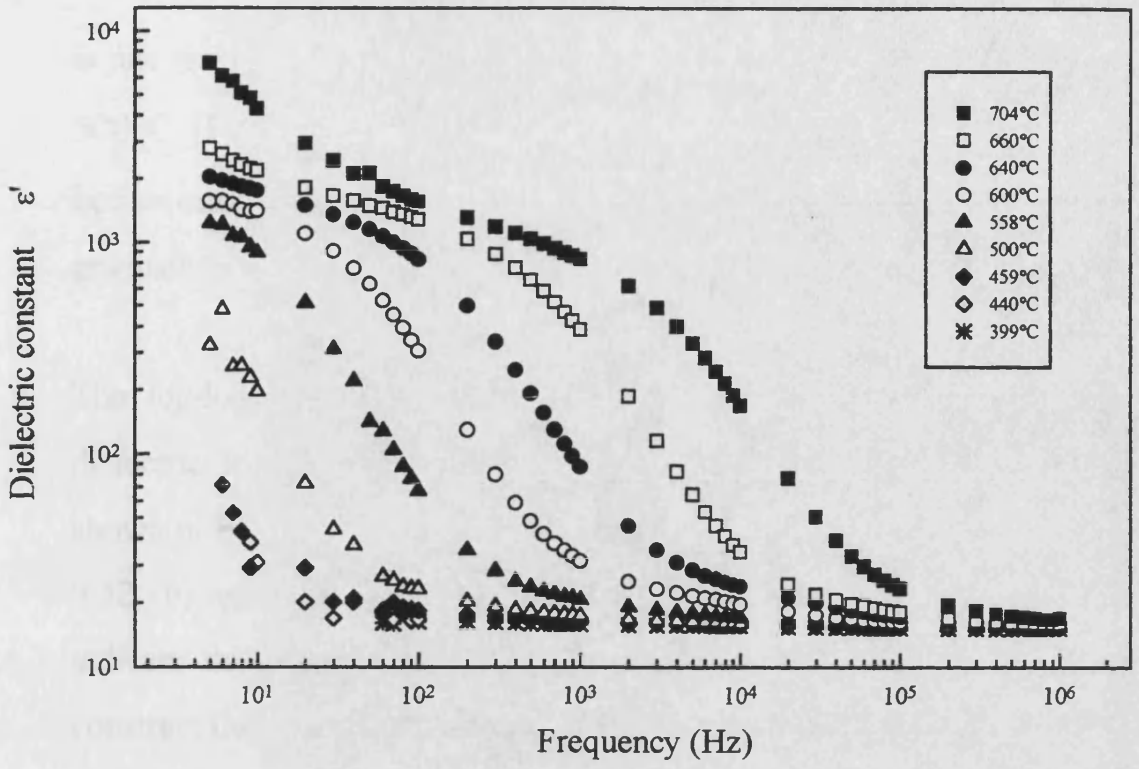

(a)

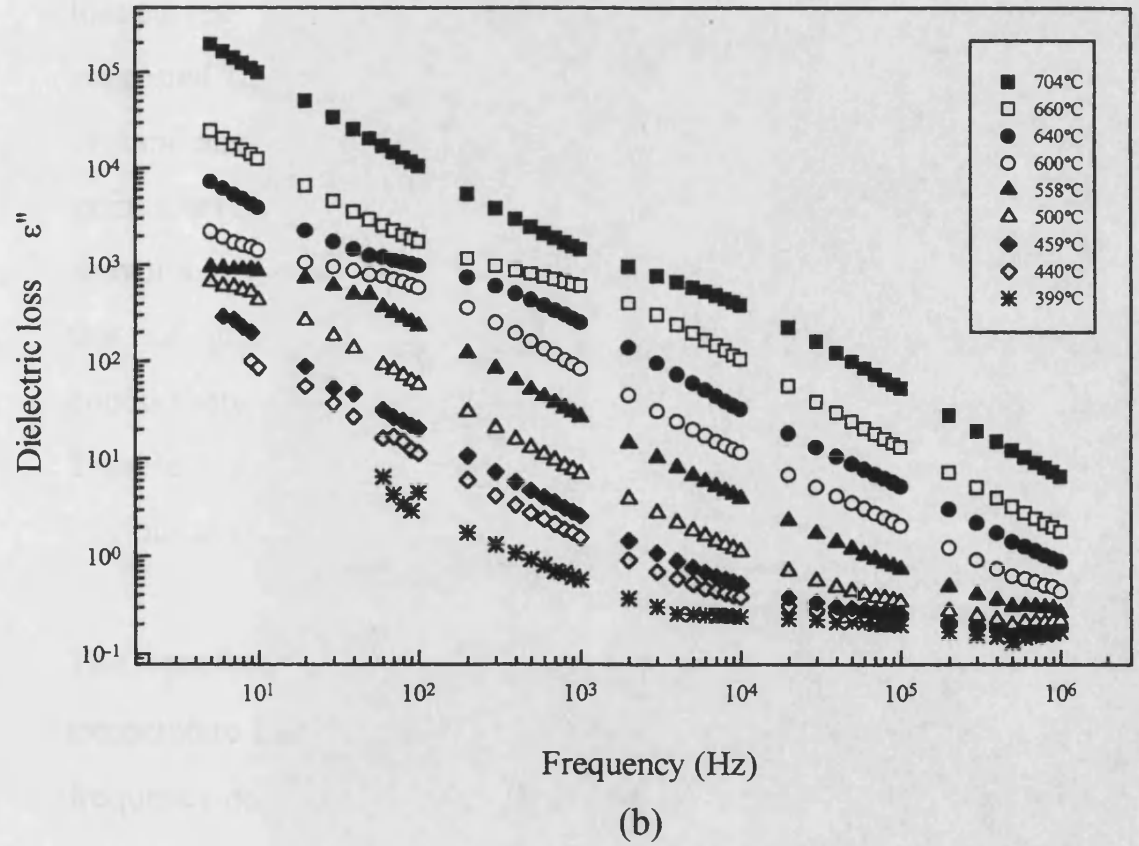

(b)

Fig.9.51 The frequency dependence of (a) dielectric constant and (b) dielectric loss of the ceramic alumina AL23 between 399°C and 704°C.

is just visible, begins to appear in the available frequency range at about 500°C (Fig. 9.51(b)). As the temperature is increased, this dispersion behaviour of dielectric constant and dielectric loss peak moves gradually to a higher frequency, as shown in Fig. 9.51.

The log-log graphs of frequency dependence of dielectric constant and dielectric loss of ceramic alumina AL23 between 399°C and 704°C are shown in Figs. 9.52 (a) and 9.53 (a). The master curves are shown in Figs. 9.52 (b) and 9.53 (b). In these figures A and B are reference points to indicate the shift made of the logarithmic frequency for each curve to construct the master curve. The shift of the curves needed along the X axis to make the master curves is the same for the dielectric constant and dielectric loss curves. For the same reason as that described in section 9.6.1.2 it can be suggested that a Maxwell-Wagner effect (section 3.3.4) is also involved in ceramic alumina AL23. Using the ratio of grain boundary thickness (d) to grain size (D) (table 9.2) and the values of R_b and R_{gb} (table 9.4), it has been shown that the electrical conductivity of the grains is about 750 larger than that of grain boundaries while for ceramic alumina D999 electrical conductivity of the grain is about 3500 larger than that of grain boundaries. Therefore the dielectric loss peaks of ceramic alumina AL23 are not as obvious as those of ceramic alumina D999.

The logarithm of the peak frequency f_p of dielectric loss ε'' against reciprocal temperature between 500°C and 704°C is plotted in Fig. 9.54. Due to the frequency dependency of loss, peaks in ceramic alumina AL23 are not easy to determine; the Fig. 9.54 is plotted using the data of reference points in Fig. 9.53 (b). The almost linear relationship between log (f_p) and the reciprocal temperature (1000/T) gives an average activation energy of 1.9±0.1eV.

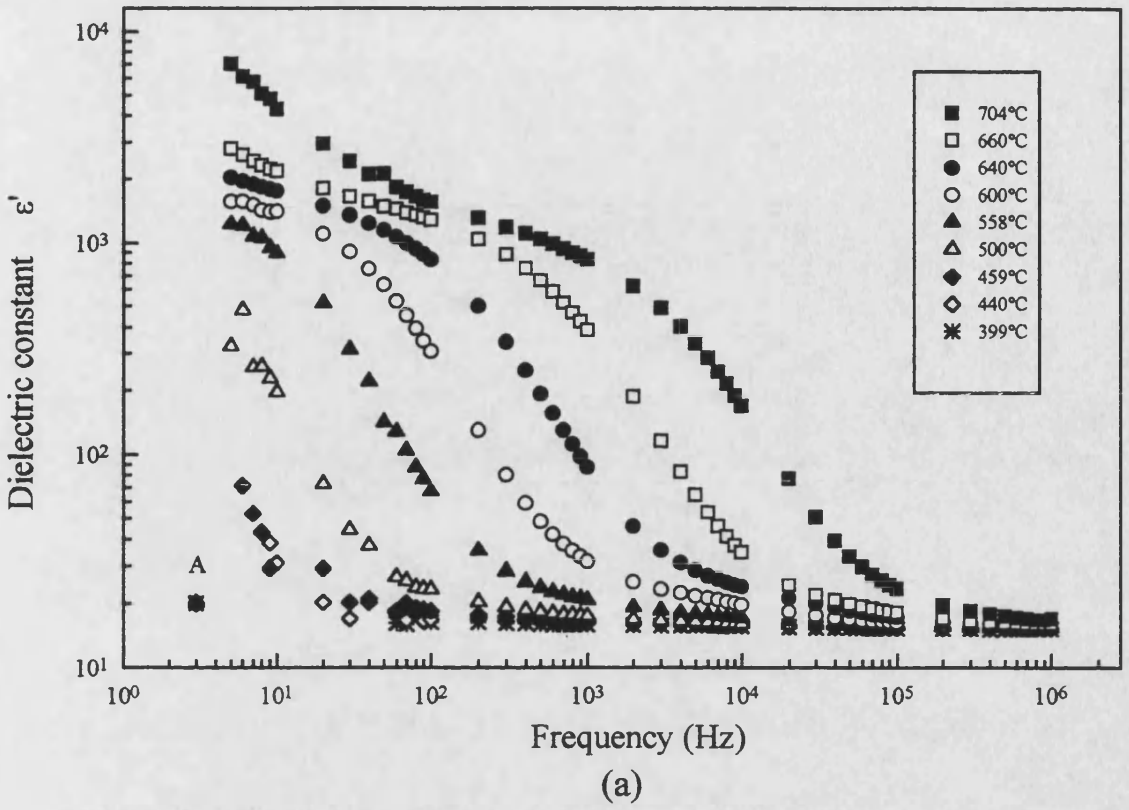

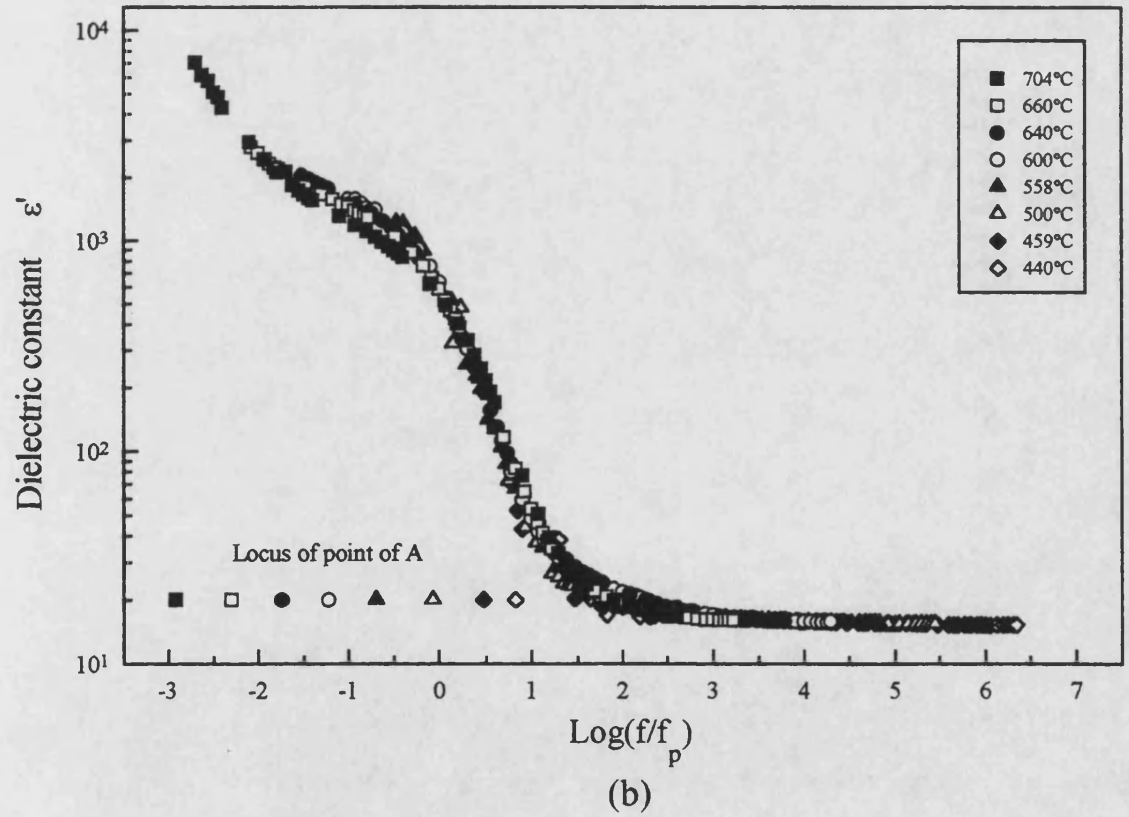

Fig.9.52 (a) The frequency dependence of dielectric constant of the ceramic alumina AL23 between 399°C and 704°C. (b) The master curve of (a).

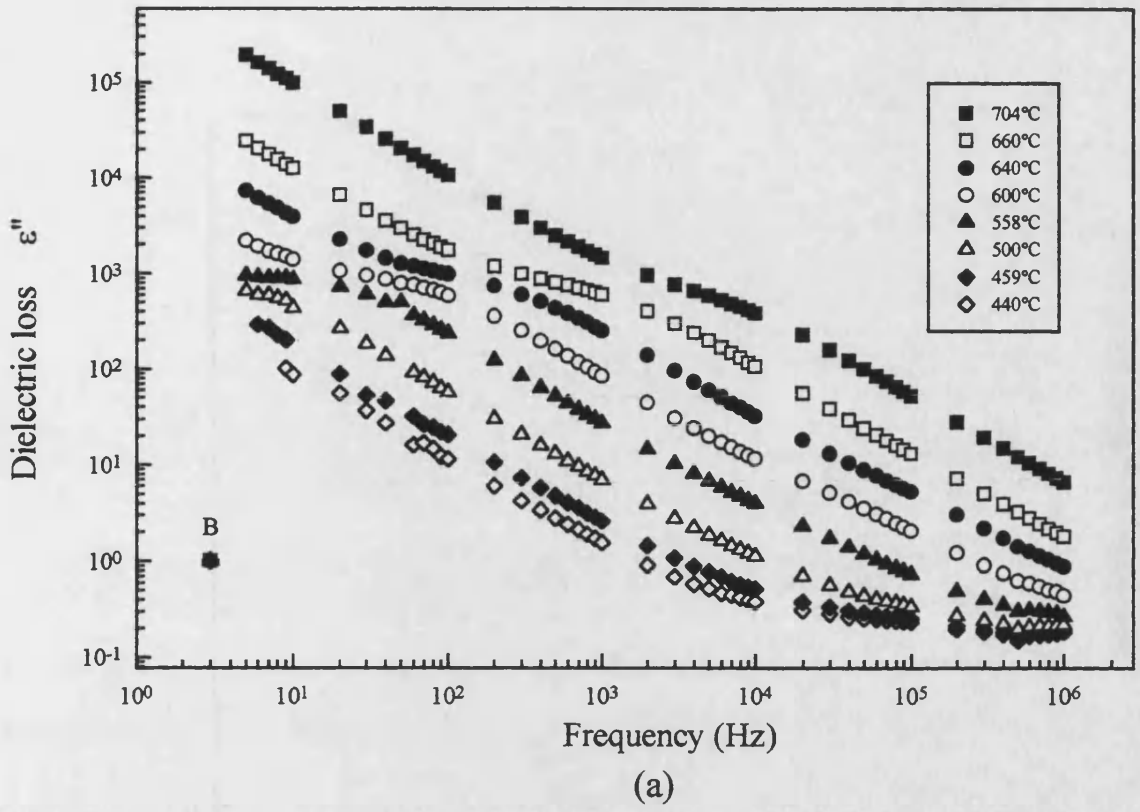

(a)

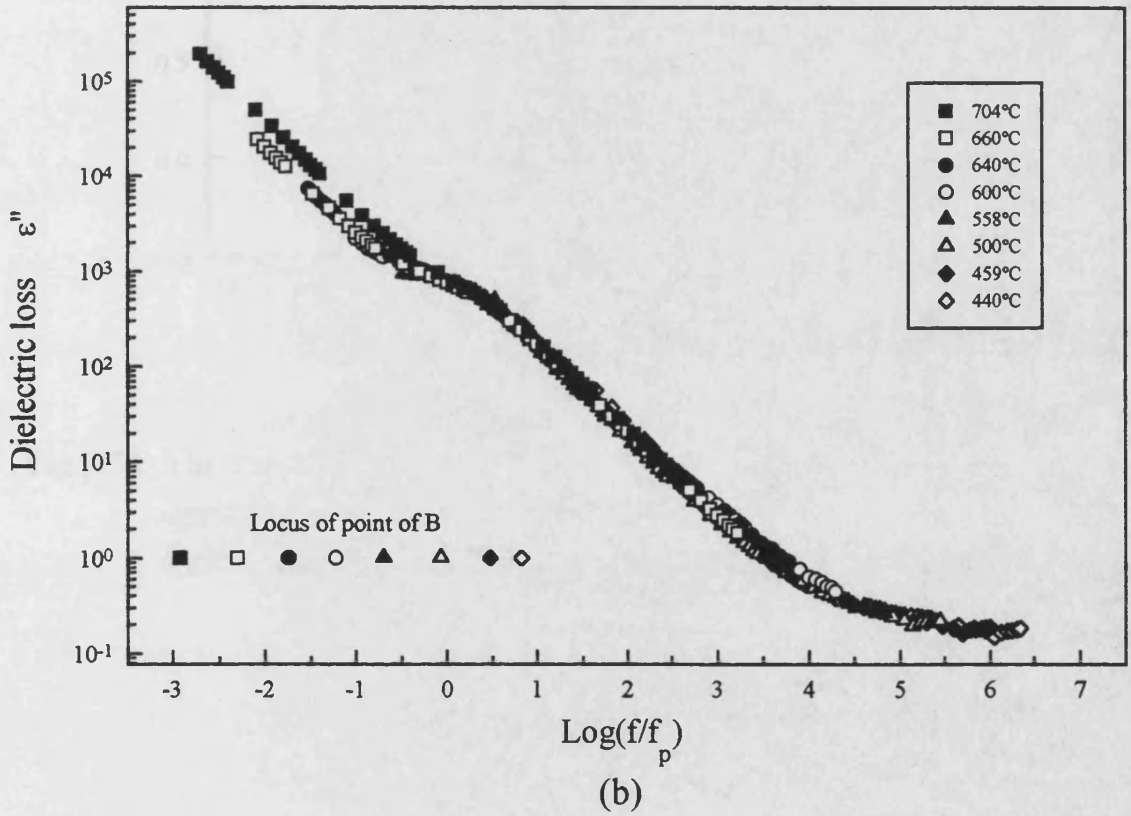

(b)

Fig.9.53 (a) The frequency dependence of dielectric loss of the ceramic alumina AL23 at different temperatures. (b) The master curve of (a).

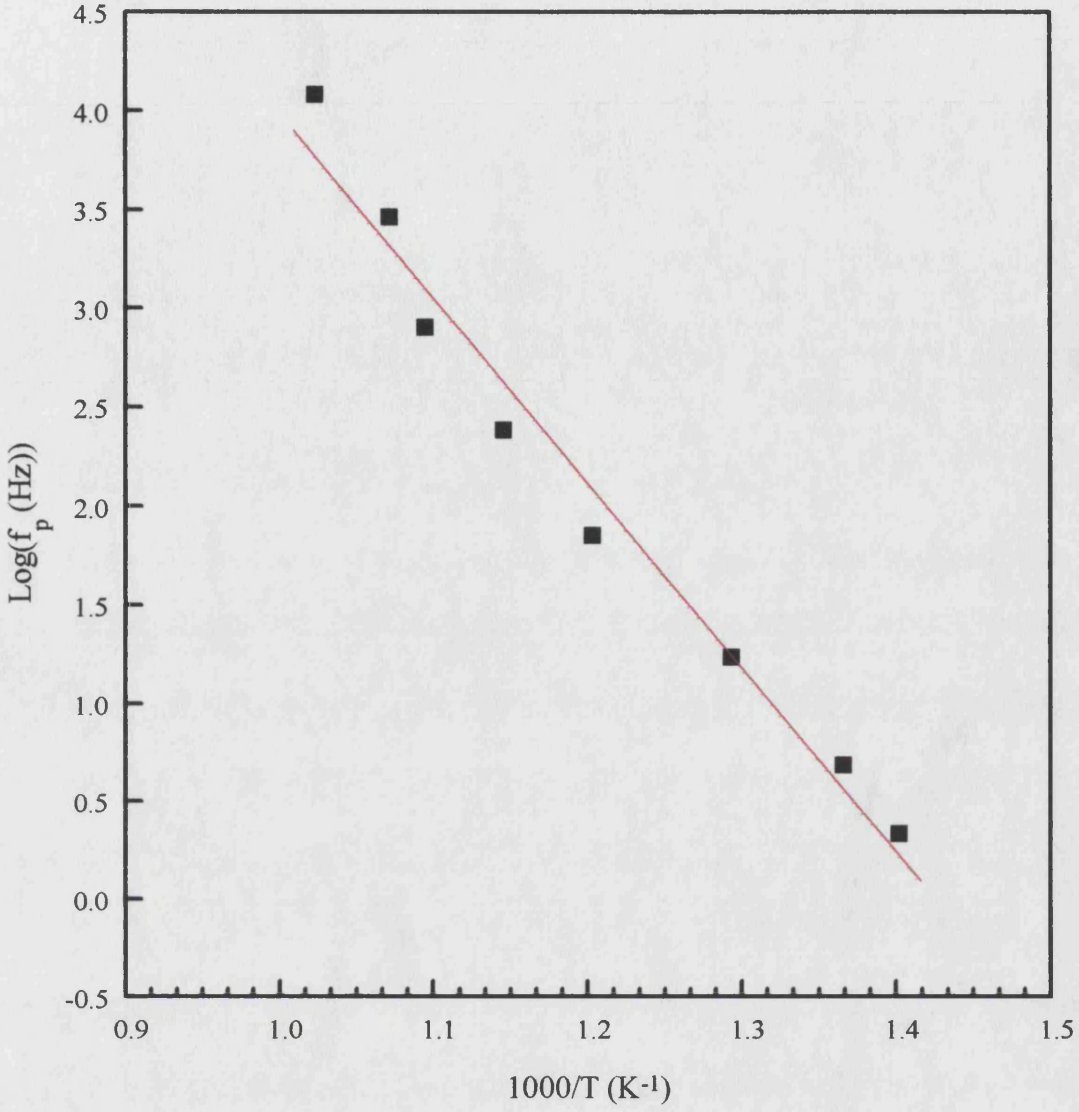

Fig.9.54 The plot of the logarithm of the peak frequency of dielectric loss against reciprocal temperature of the ceramic alumina AL23 between 440°C and 704°C, indicating an average activation energy of 1.9±0.1 eV.

Extrapolating the line in Fig. 9.54 towards lower temperature, it is found that at room temperature (20°C) the relaxation process is very slow having a relaxation frequency (f_p) of about 10^{-18}Hz. This suggests again that a Maxwell-Wagner effect is involved (section 3.3.4).

9.6.2.2 The dielectric constant, dielectric loss in ceramic alumina AL23 below room temperature

Fig. 9.55 shows a plot of the frequency dependence of dielectric constant and dielectric loss of ceramic alumina AL23 between 20K and 320K. It can be seen that in this temperature range two relaxation process are happening. To show the relaxation process in the lower temperature range more clearly, the frequency dependencies of dielectric constant and dielectric loss of ceramic alumina AL23 between 20K and 200K are shown in fig. 9.56. The dielectric loss peaks of this relaxation process are in the shadows of loss peaks of another relaxation process; therefore it is difficult to work out the accurate loss peak frequency and average activation energy of this relaxation process. At 200K the loss peak frequency is about 10^6Hz. The frequency of the loss peak increases with the increasing temperature (Fig. 9.56 (a)). Therefore at room temperature (20°C) the relaxation frequency (f_p) is above 10^6Hz. This suggests that a dipolar relaxation process is involved (section 3.3.3) in the temperature range of 20K and 200K in the frequency range of study.

Graphs of frequency dependence of dielectric constant and dielectric loss of ceramic alumina AL23 between 210K and 320K are shown in Figs. 9.57 (a) and 9.58 (a). The master curves are shown in Figs. 9.57 (b) and 9.58 (b). In these figures A and B are reference points to indicate the shift made of the logarithmic frequency in each curve to construct the master curves.

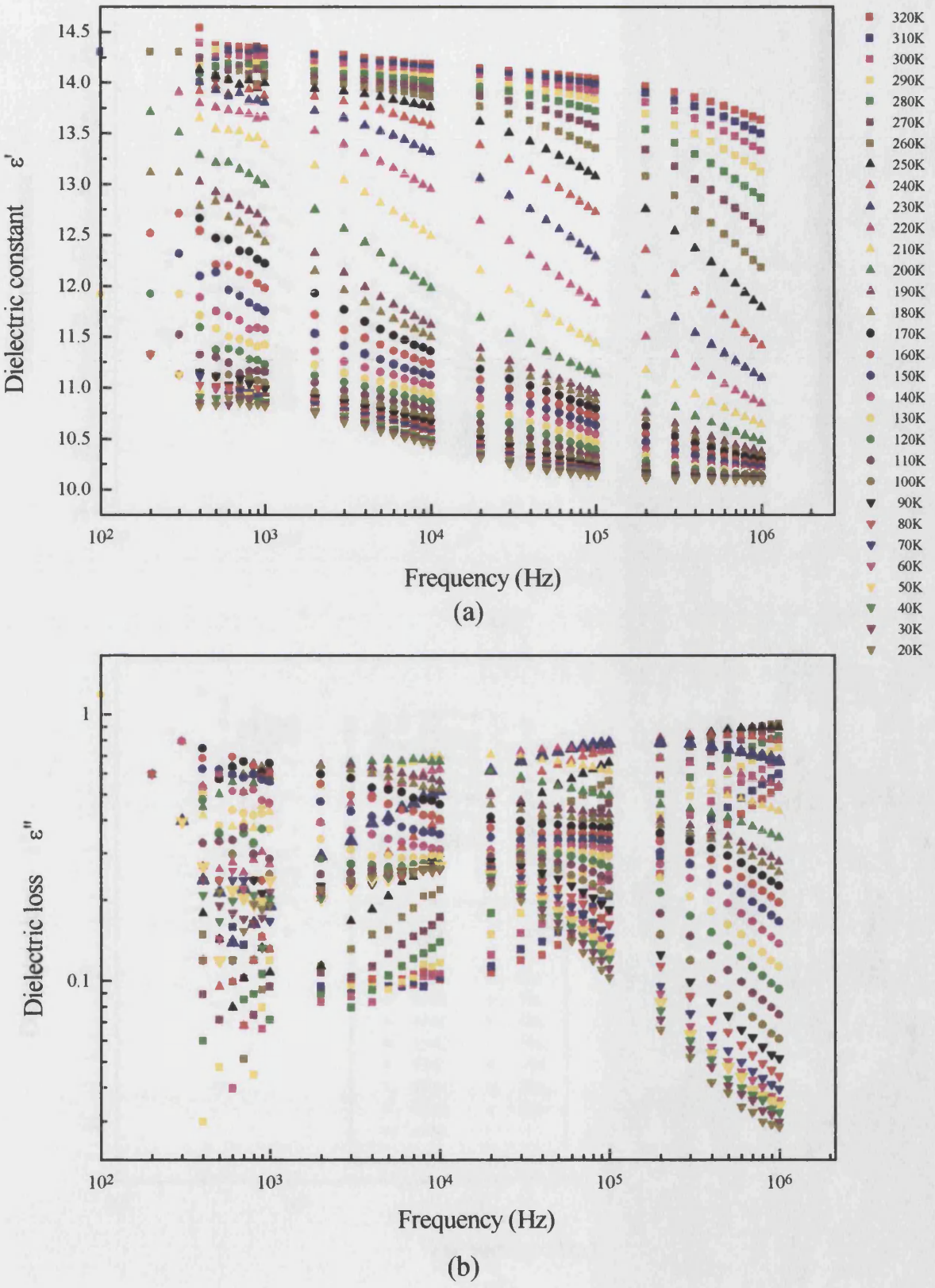

Fig.9.55 The frequency dependence of (a) dielectric constant (b) dielectric loss of the ceramic alumina AL23 between 20K and 320K.

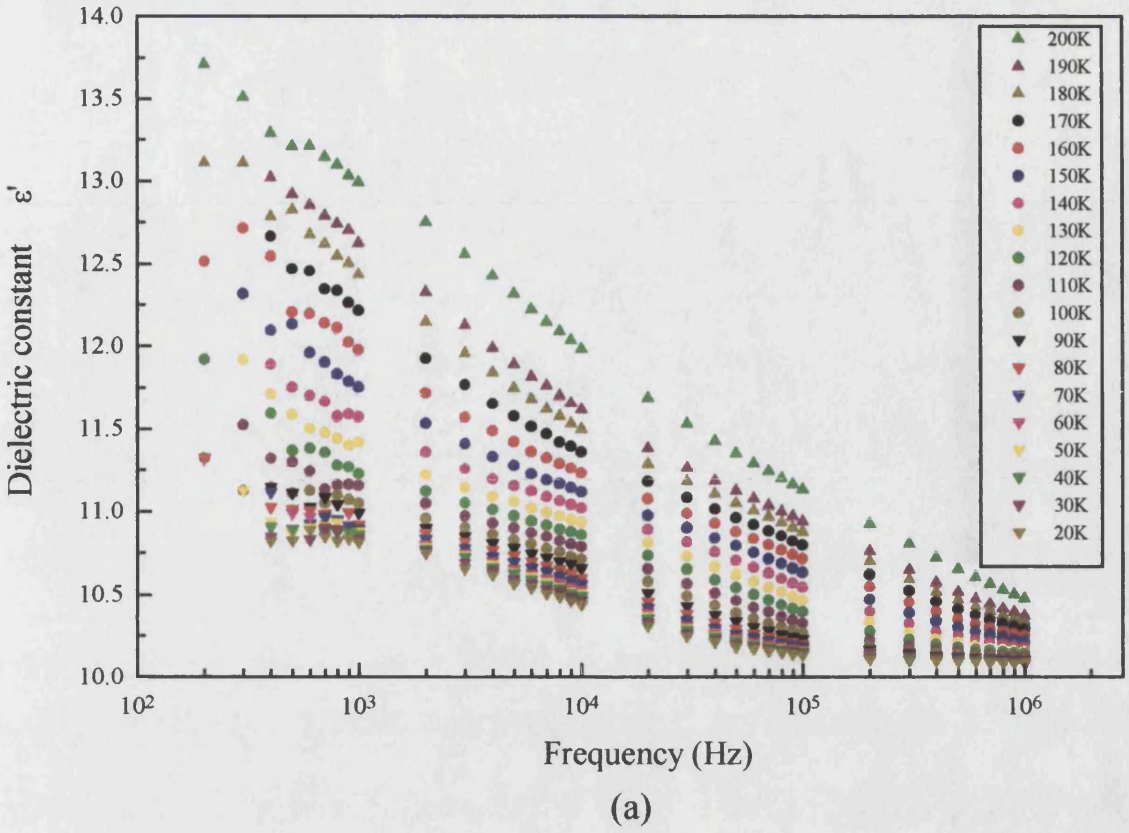

(a)

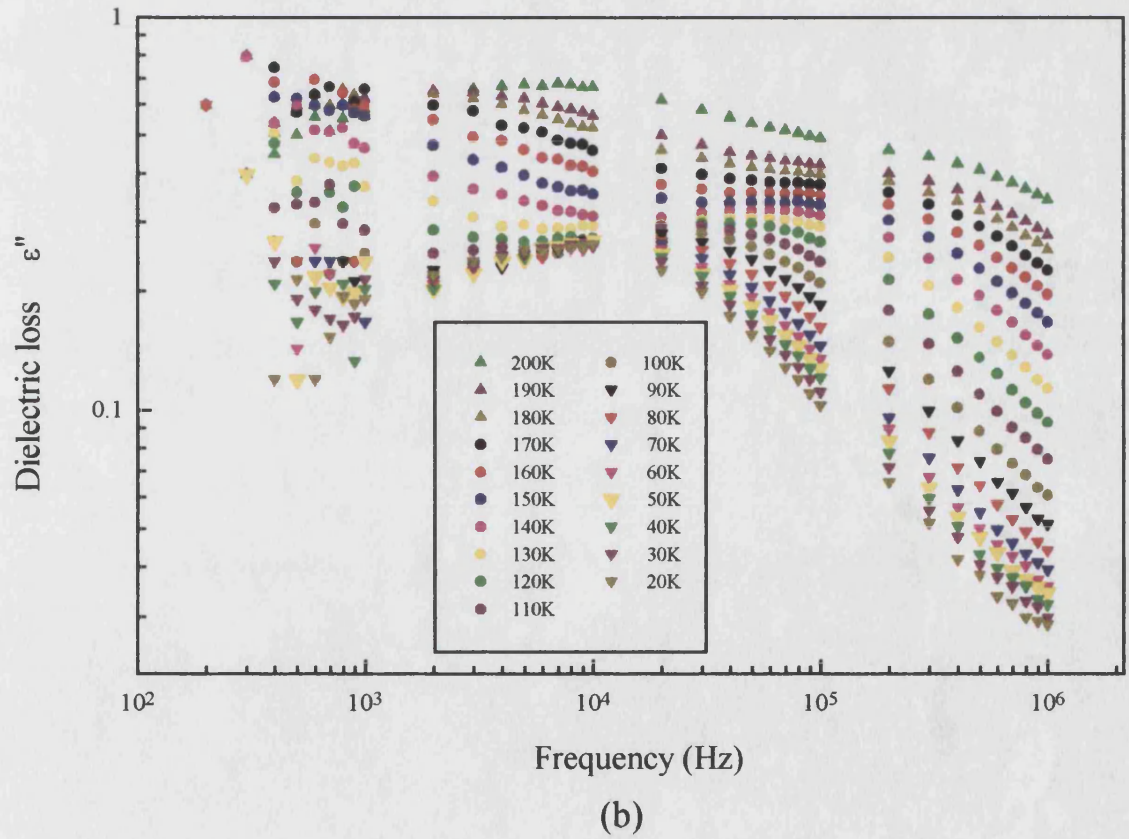

(b)

Fig.9.56 The frequency dependence of (a) dielectric constant (b) dielectric loss of the ceramic alumina AL23 between 20K and 200K.

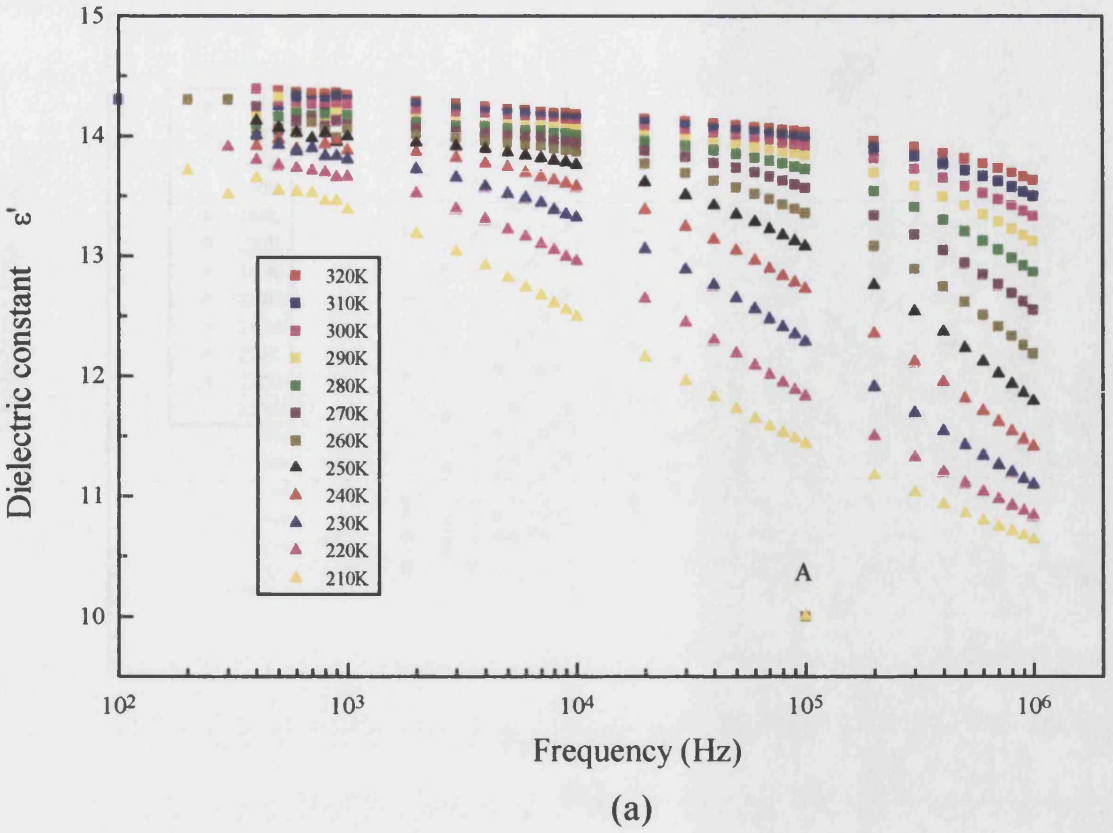

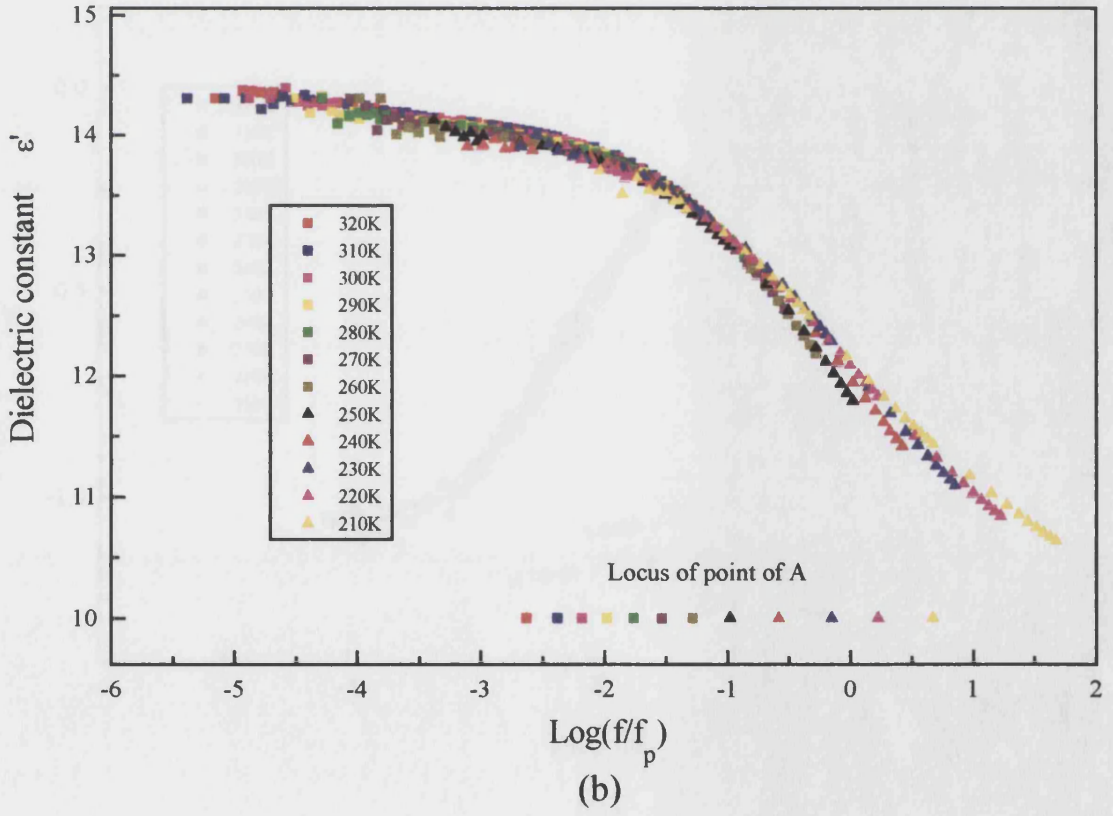

Fig.9.57 (a) The frequency dependence of dielectric constant of the ceramic alumina AL23 between 210K and 320K.
(b) The master curve of (a).

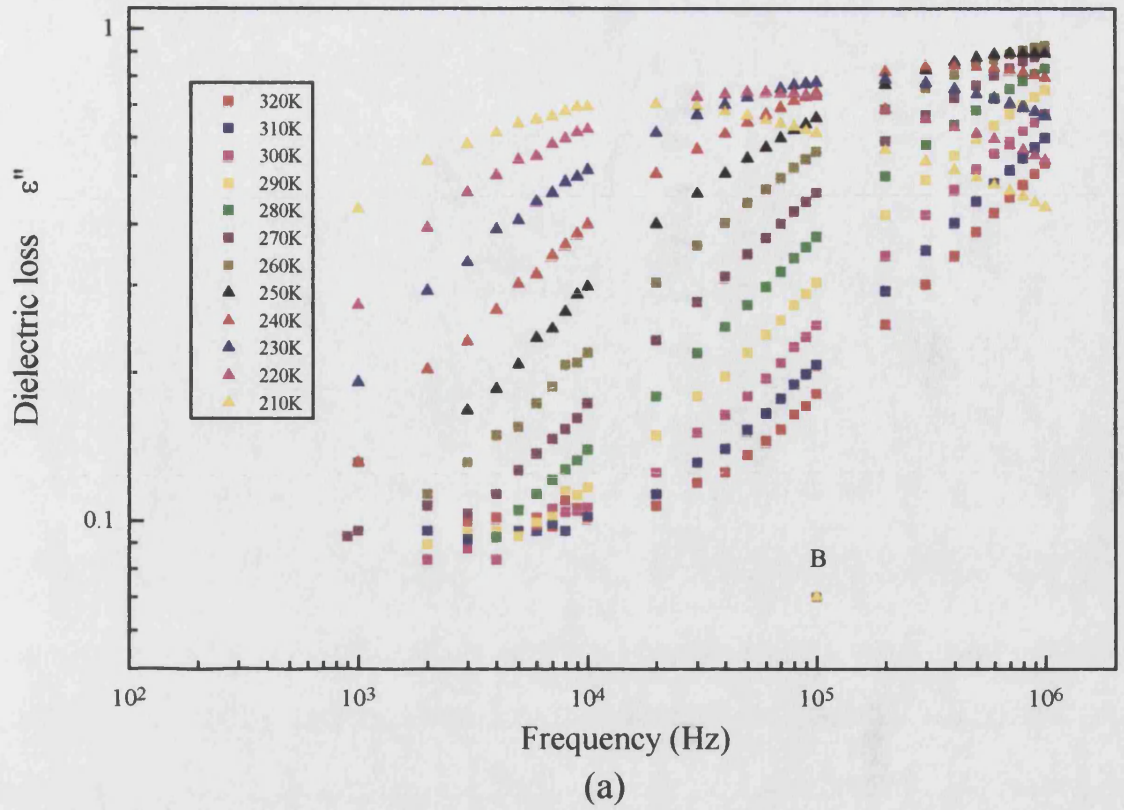

(a)

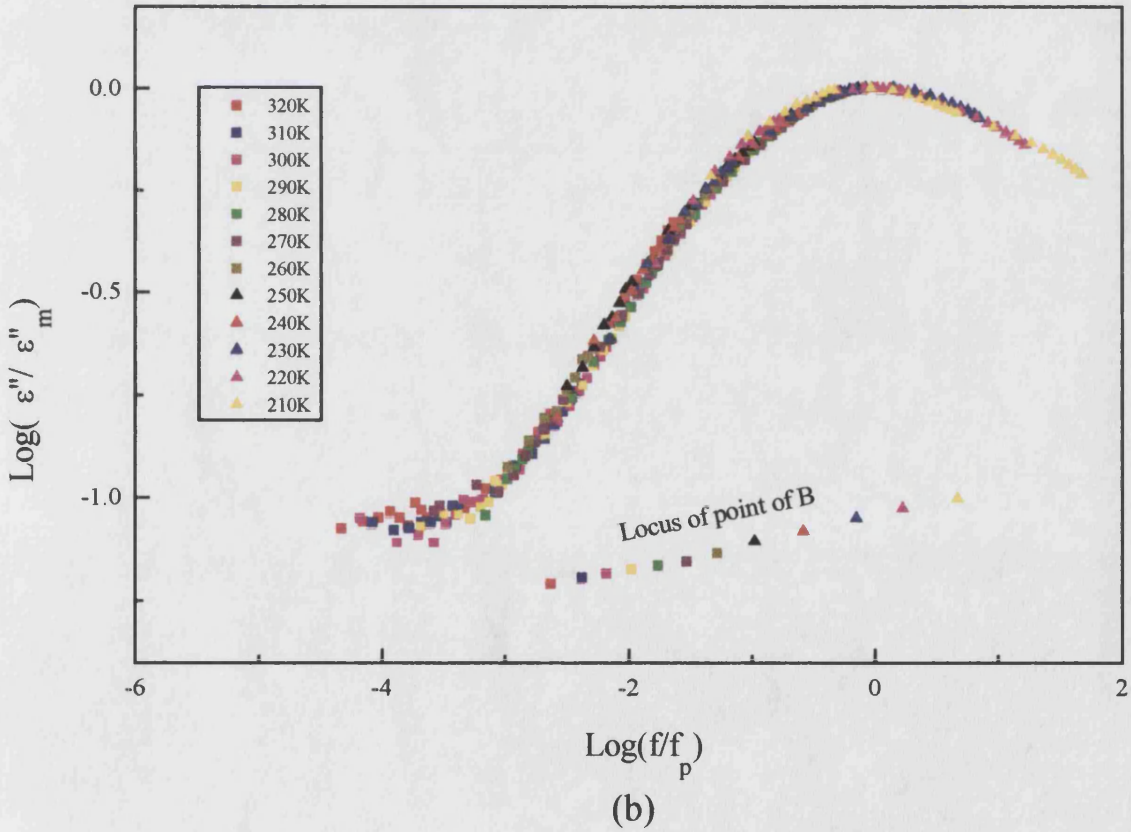

(b)

Fig.9.58 (a) The frequency dependence of dielectric loss of the ceramic alumina AL23 between 210K and 320K.
(b) The master curve of (a).

The shifts needed along the X axis are the same for the dielectric constant and dielectric loss curves. Fig. 9.57(b) and Fig. 9.58(b) are plotted together with the theoretical curves for a Debye relaxation (Fig. 9.59); below the relaxation frequency, the dielectric losses go to minimum at low frequency and the loss peak is broader than that of the theoretical curve for a single Debye relaxation. This suggests that a dipolar relaxation process with a distributed relaxation time is involved (section 3.3.3).

The logarithm of the peak frequency f_p of dielectric loss ε'' of ceramic alumina AL23 against reciprocal temperature (1000/T) between 210K and 320K is plotted in Fig. 9.60. The almost linear relationship between log (f_p) and the reciprocal temperature (1000/T) suggests that the relaxation process is thermally activated and the peak frequency f_p of the dielectric loss ε'' obeys equation 9.9. From the result of the linear fit of the data an average activation energy of 0.4 ±0.01eV is obtained. Extrapolating the line in Fig. 9.60 towards higher temperature, it is found that at room temperature (20°C) the relaxation frequency (f_p) is about 10^7 Hz. This suggests again that a dipolar relaxation process is involved (section 3.3.3).

9.6.3 The dielectric constant and dielectric loss in ceramic aluminas D975 and H880

The dielectric constant and the dielectric loss of material D975 and H880 over the frequency range under study and above room temperature are plotted in Fig .9.61 and Fig. 9.62 respectively. Fig. 9.61 and Fig. 9.62 show an increasing dielectric constant and dielectric loss with temperature at all frequencies and a decreasing dielectric constant and dielectric loss with increasing frequency at all temperatures.

The sign of loss mechanism of a dipole relaxation or interfacial polarisation

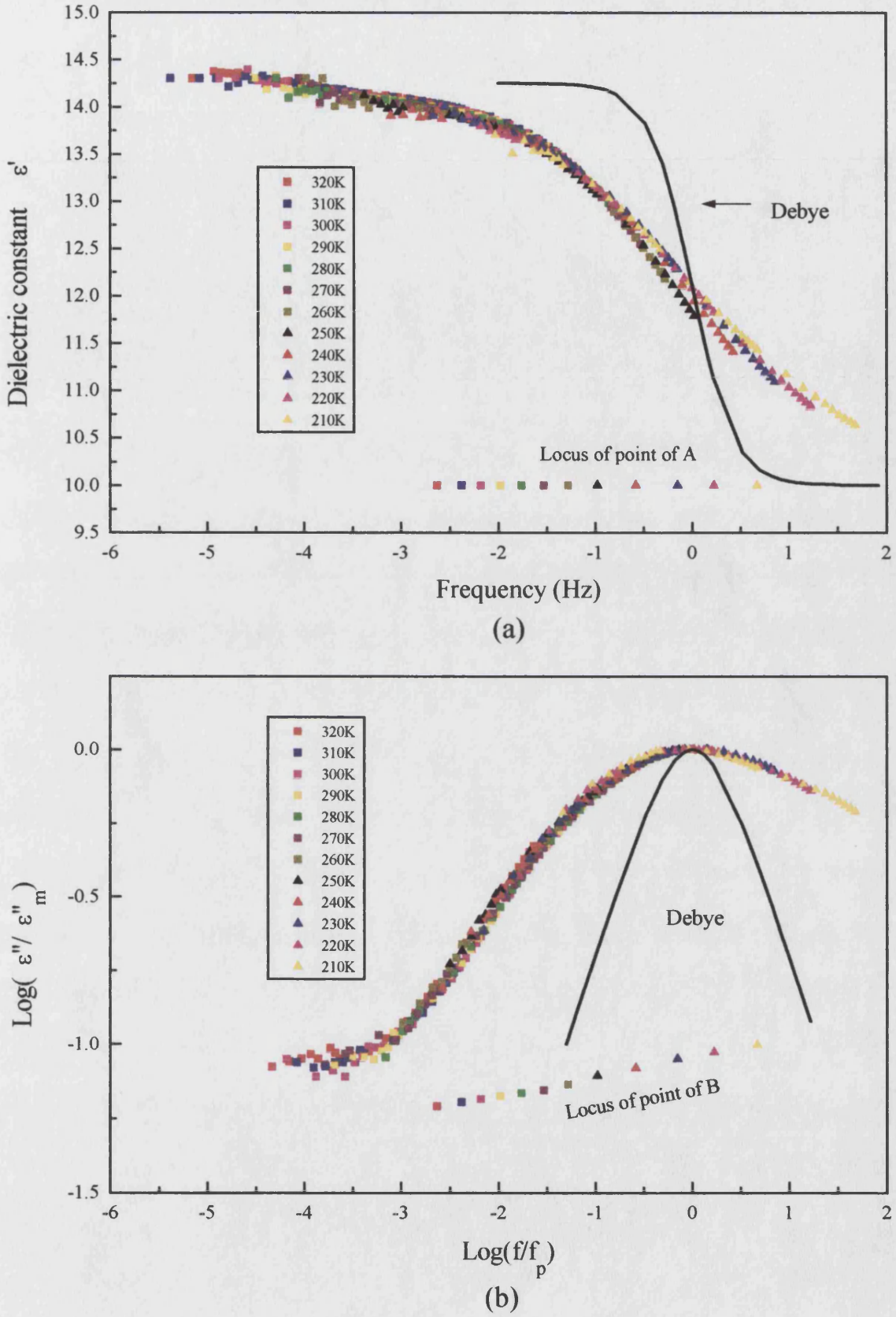

Fig.9.59 The master curve of (a) dielectric constant and (b) dielectric loss of the ceramic alumina AL23 betweem 210K and 320K plotted together with that of a debye system.

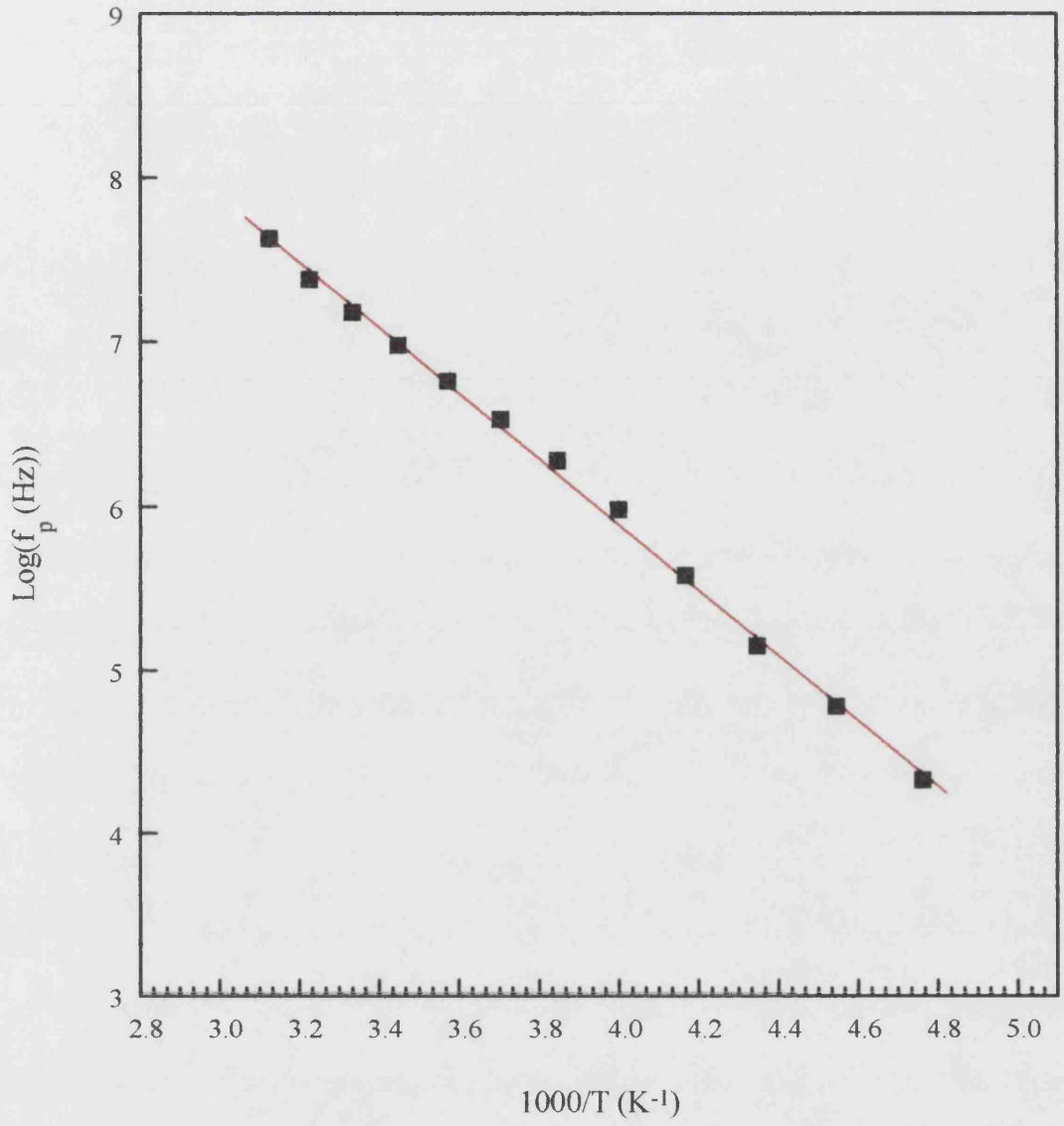

Fig. 9. 60 The plot of the logarithm of the peak frequency dielectric loss against reciprocal temperature of the ceramic alumina AL23 between 210K and 320K, indicating an average activation energy of 0.400±0.006eV.

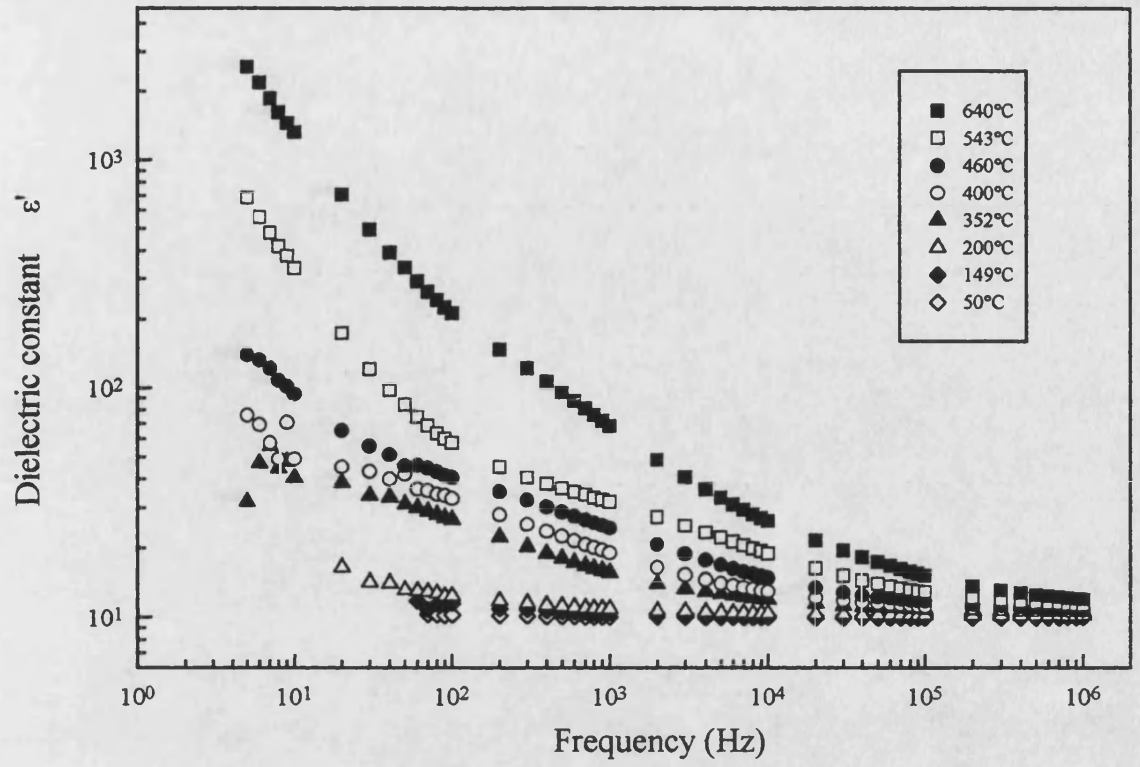

(a)

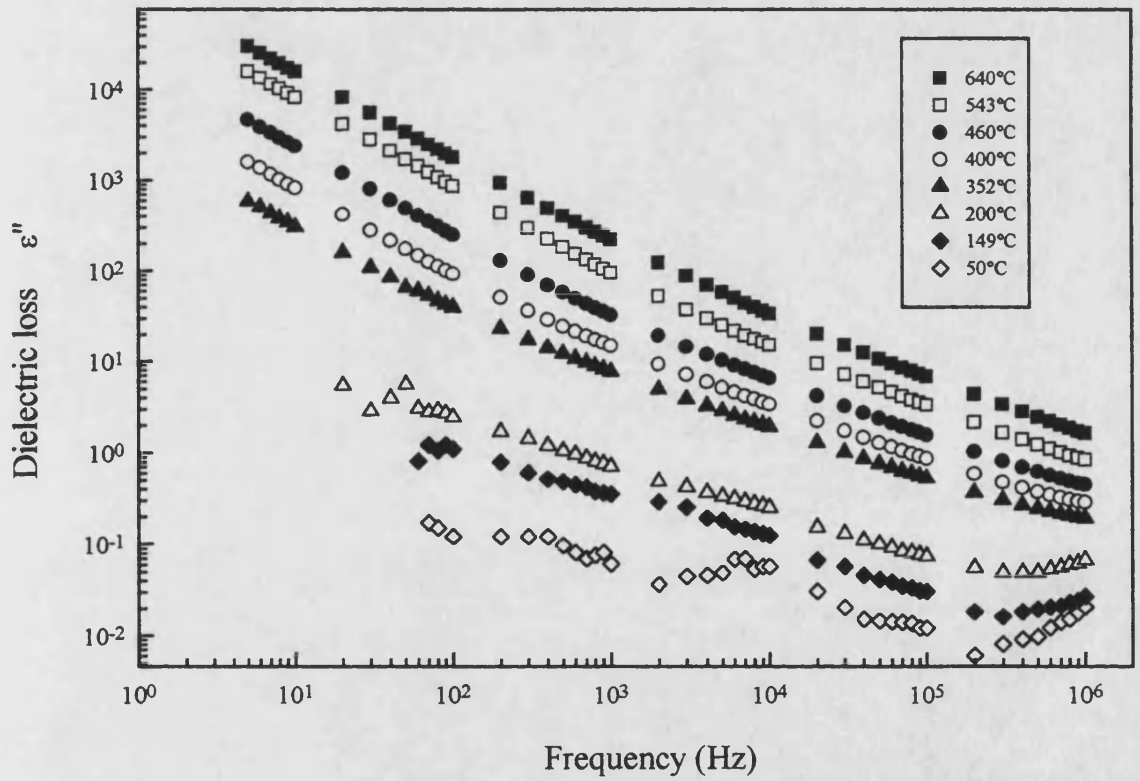

(b)

Fig.9.61 The frequency dependence of (a) dielectric constant and (b) dielectric loss of the ceramic alumina D975 between 50°C and 640°C.

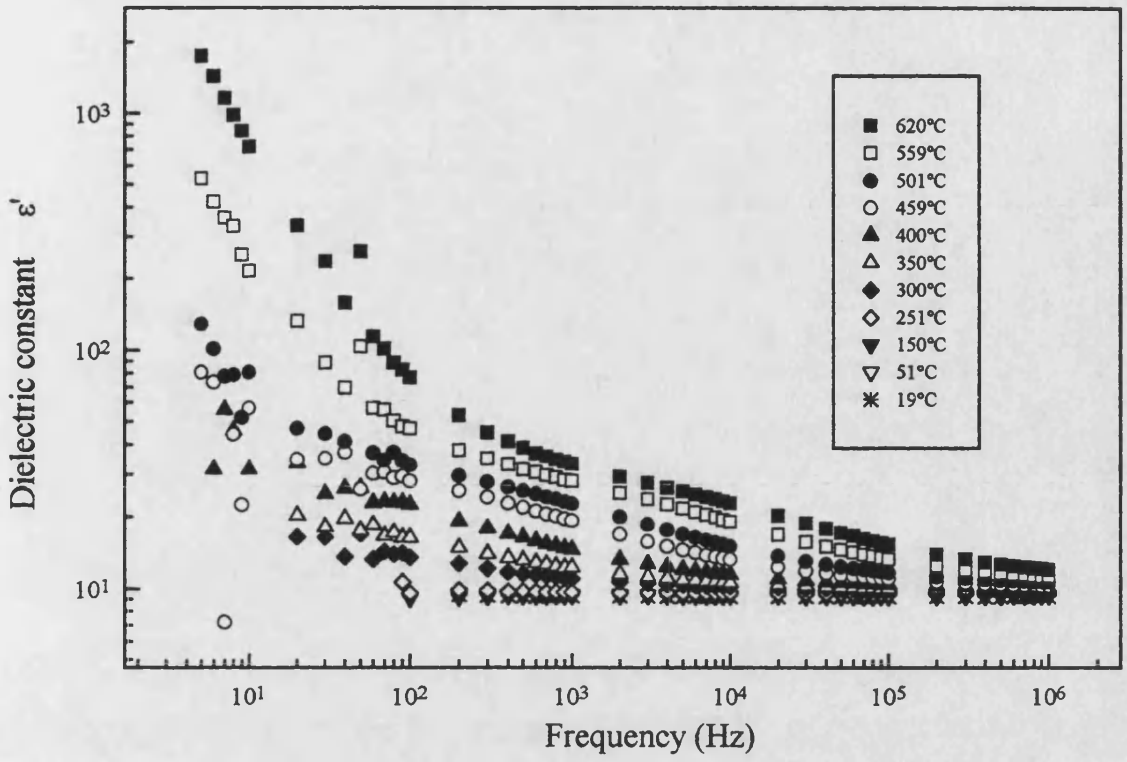

(a)

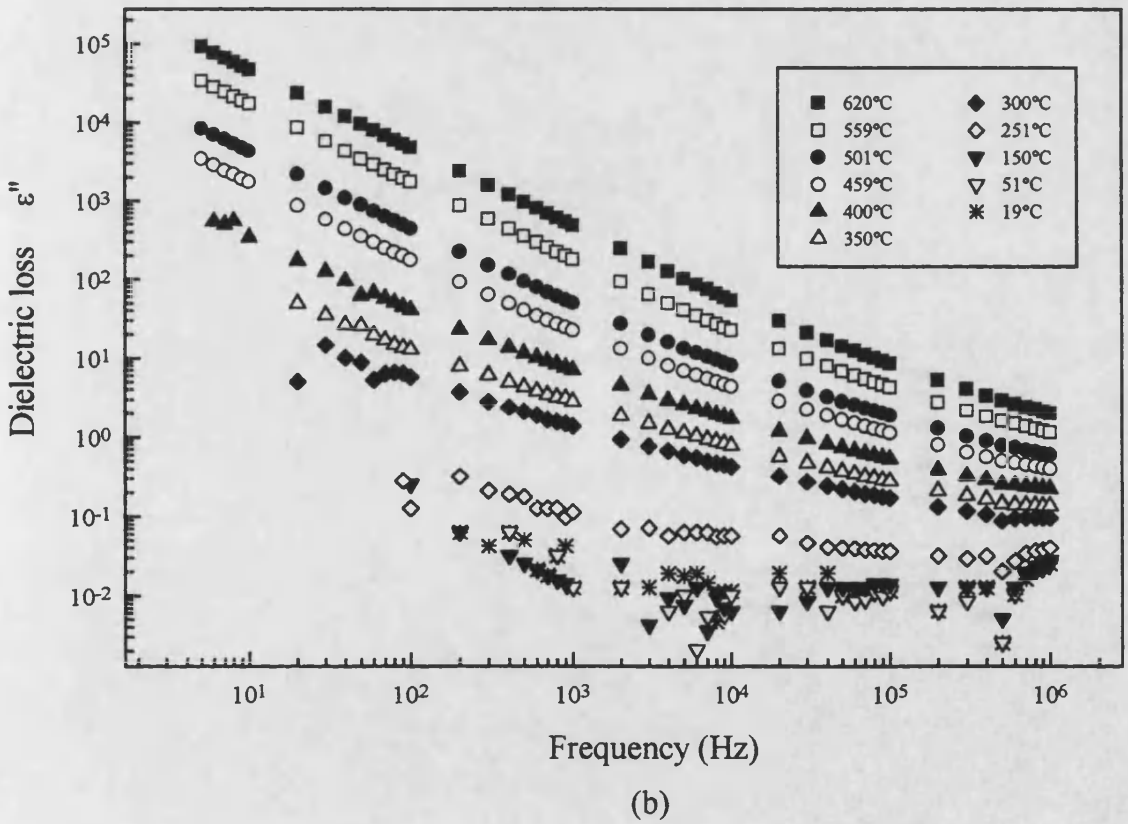

(b)

Fig. 9. 62 (a) The frequency dependence of dielectric constant and (b) dielectric loss of the ceramic alumina H880 between 19°C and 620°C.

of grain boundaries has not been observed from the curves in Figs. 9.61 and 62. From the results shown by the curves we can not tell if there is any dipole relaxation process happened in the grains or not. The complex impedance profiles for both of the sample D975 and H880 show only one semicircle(page 9-23). Therefore conduction along the grain boundaries is domimnant in the sample D975 and H880. This can shadow the dipole relaxation process in grains.

The pronounced dispersion of both dielectric constant ε' and dielectric loss exhibited by Figs. 9.61 and 9.62 above 200°C for H880 and 300°C for D975 strongly suggests the occurrence of interfacial polarisation controlled by electrode barriers.

The graphs of frequency dependence of dielectric constant between 20K and 320K and dielectric loss between 260K and 320K of ceramic alumina D975 are shown in Figs. 9.63(a) and (b). The dielectric loss of ceramic alumina D975 below 280K is small and is beyond the impedance limit of the impedance analyser. No sign of loss mechanism of a dipole rotation or interfacial polarisation of grain boundaries is found in this temperature range. Fig 9.64 shows the temperature dependence of dielectric constant of ceramic alumina D975 at 10^5 Hz and between 20K and 320K. In the temperature range between 200K and 320K the dielectric constant increases linearly with the temperature, indicating a temperature coefficient $(\partial\varepsilon'/\partial T)$ of $(1.19\pm0.02)\times10^{-3}$/K.

The graph of frequency dependence of dielectric constant between 50K and 320K of ceramic alumina H880 is shown in Fig. 9.65. Between 50K and 320K the dielectric loss is low, being out of the measurable range of the impedance analyser. Fig 9.66 shows the temperature dependence of

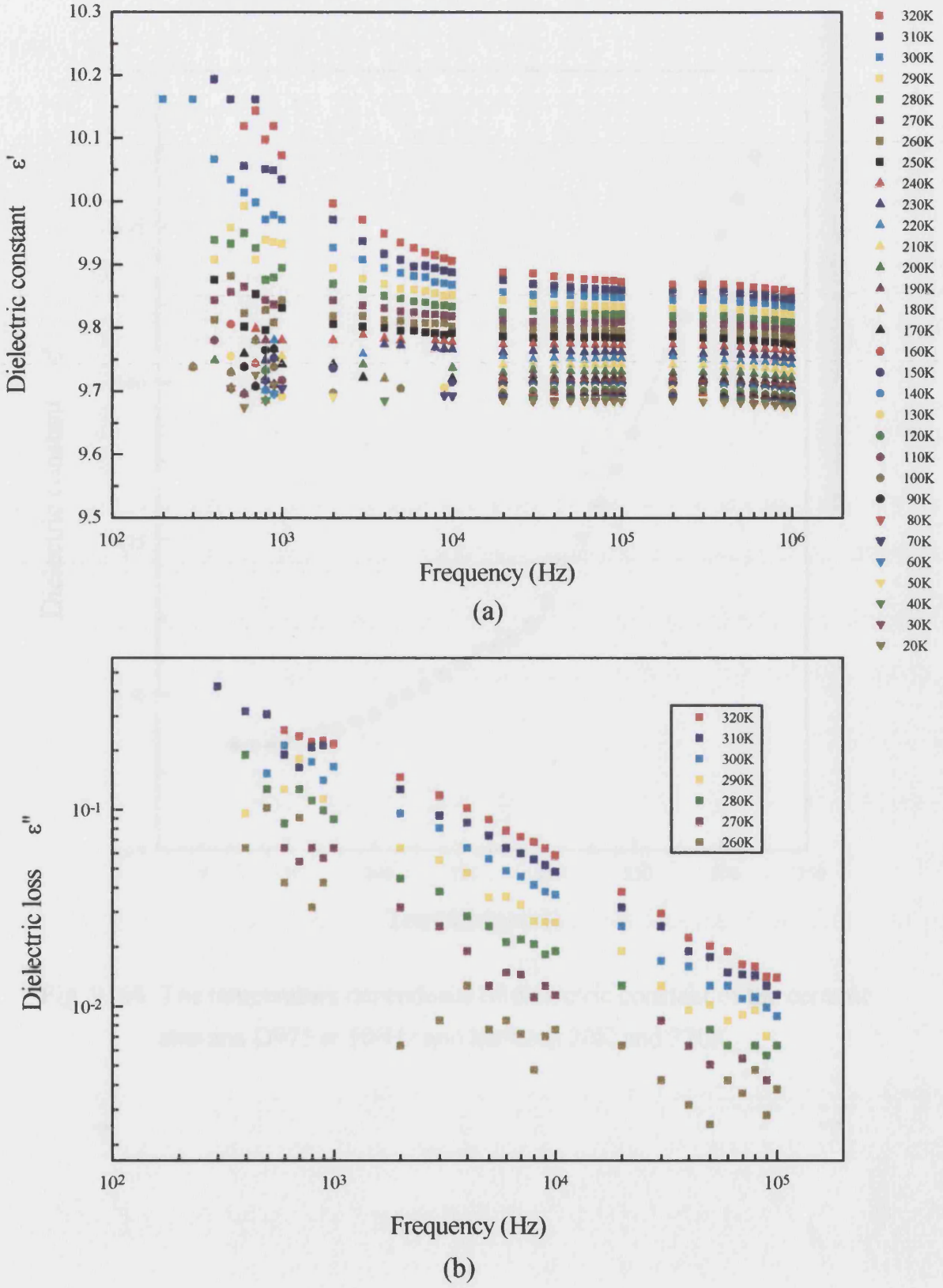

Fig. 9. 63 The frequency dependence of (a) dielectric constant between 20K and 320K and (b) dielectric loss between 260K and 320K of the ceramic alumina D975.

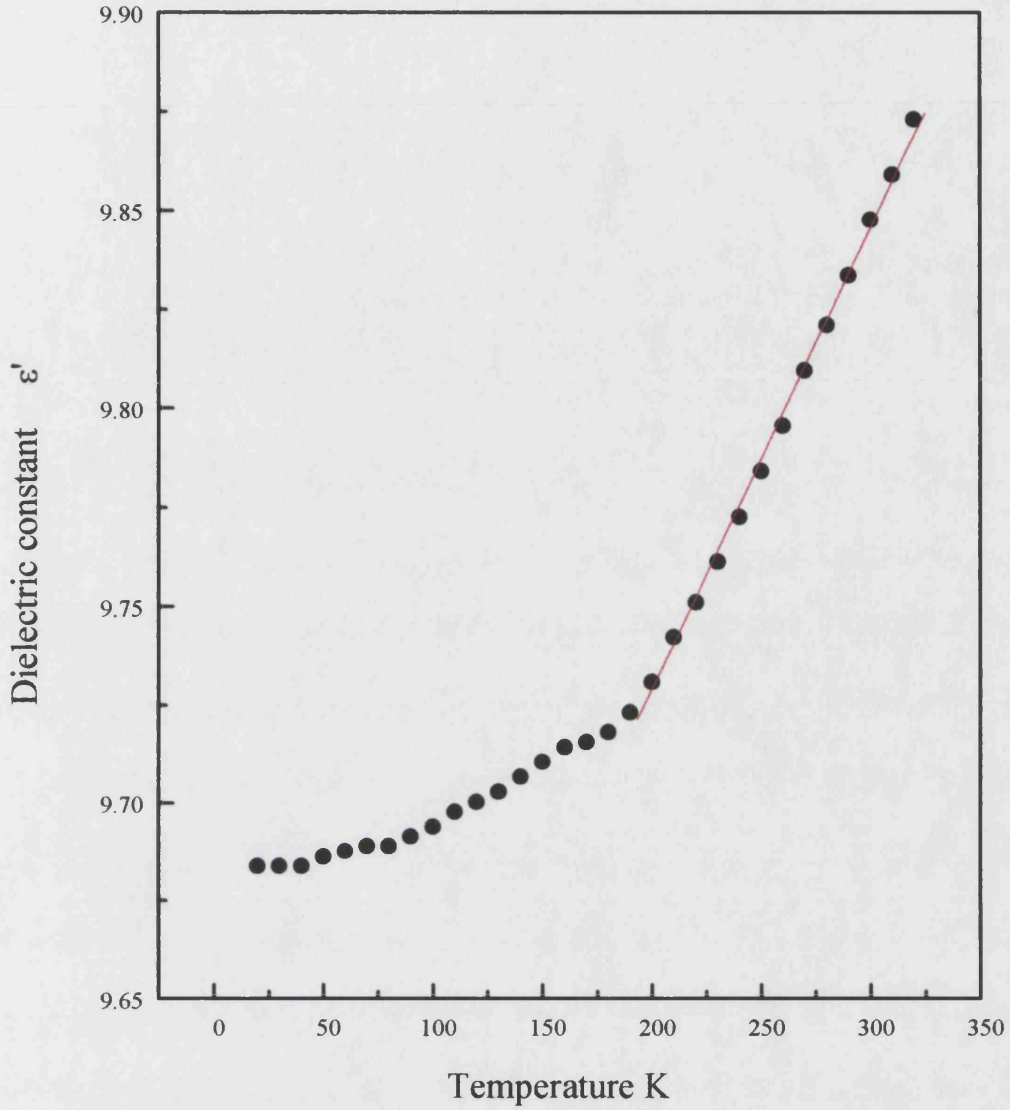

Fig. 9 .64 The temperature dependence of dielectric constant of the ceramic alumina D975 at 10^5Hz and between 20K and 320K.

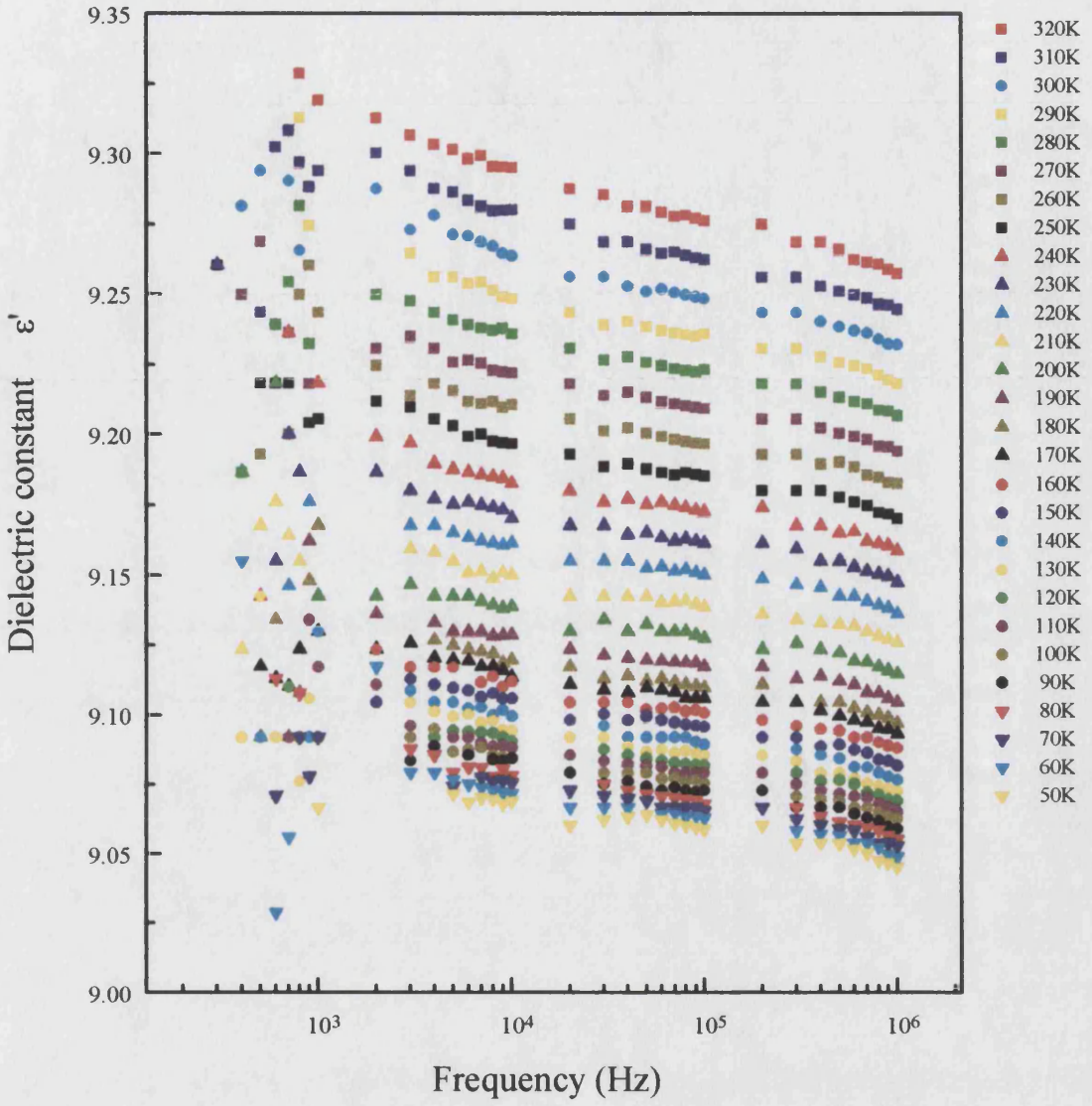

Fig. 9. 65 The frequency dependence of dielectric constant of the ceramic alumina H880 between 50K and 320K.

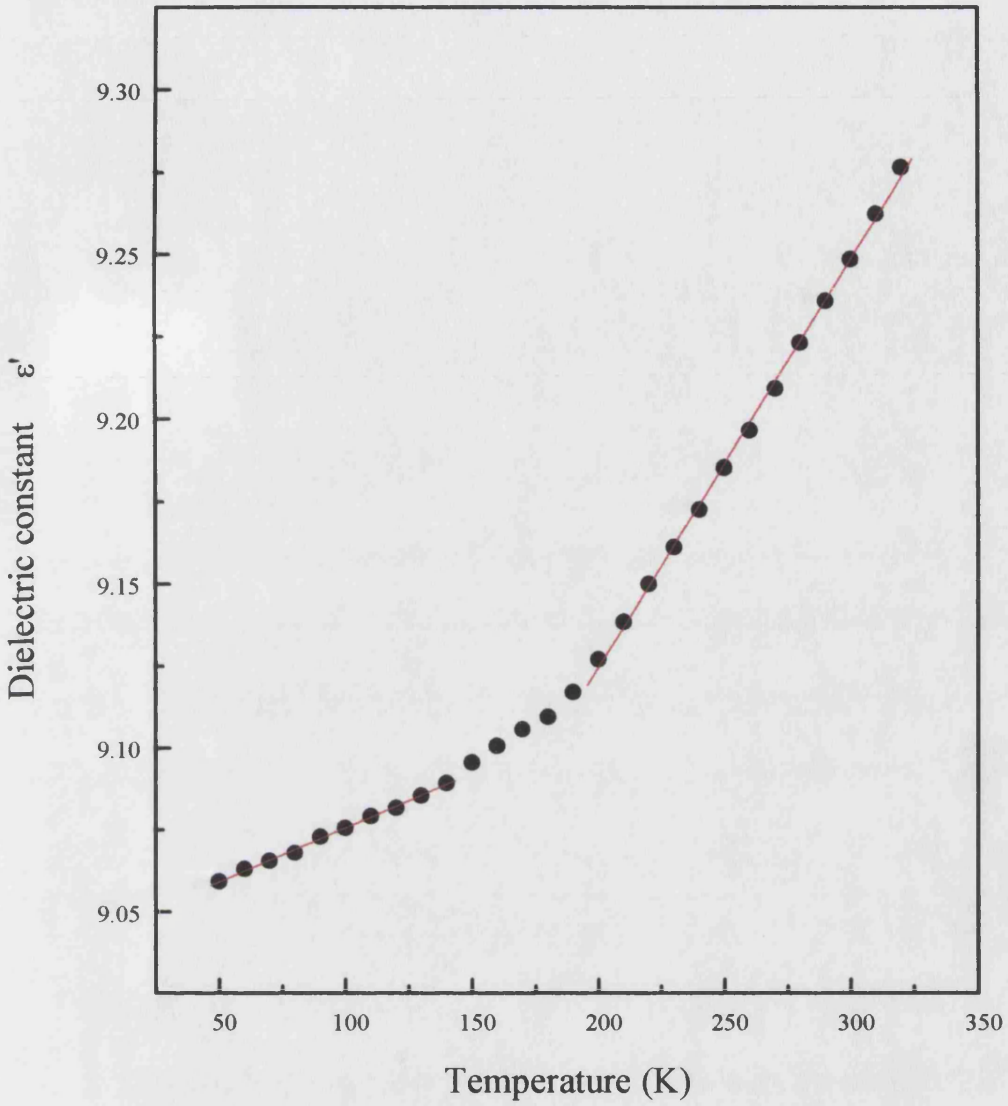

Fig. 9. 66 The temperature dependence of dielectric constant of the ceramic alumina H880 at 10^5Hz and between 50K and 320K.

dielectric constant of ceramic alumina H880 at 10^5 Hz and between 50K and 320K. In the temperature range of 200K and 320K the dielectric constant increases linearly with the temperature, indicating a temperature coefficient ($\partial\varepsilon'/\partial T$) of $(1.24\pm0.02)\times10^{-3}$/K.

9.7 Conclusions

The dielectric properties of different ceramic aluminas can be very different, even for samples of similar nominal purity; therefore nominal purity or grain size are not adequate parameters to describe the behaviour of the dielectric properties of the material. An adequate characterisation of the dielectric properties of the material requires measurement in a very wide frequency and temperature range.

Dipolar relaxation processes were found in ceramic alumina D999 and AL23. The alumina is non-polar and the observed dipolar relaxation processes are due to additives, impurities and defects. With the available information it is not possible to identify the origin of the observed dipolar relaxation processes.

α-alumina is one of the most strongly bonded compounds. Energies of formation of point defects are correspondingly large. The energy of electronic disorder is equally large. The energy of formation of electrons and holes by intrinsic disorder is about 5eV per electron or hole (Kröger, 1984). A mathematical model of electrical conduction in sapphire which describes sapphire as a wide-bandgap semiconductor was developed by Will et al. (1992a). According to this model any activation energy significantly smaller than 4.8eV is due to the extrinsic conduction (Will et al, 1992a). Therefore the electrical resistance of grains (bulk) of ceramic alumina D999

and AL23, which have an activation energy of 1.30±0.01eV and 1.71±0.06eV respectively (table 9.5), is dominated by the impurities.

Chapter 10 General Description of Silicon Carbide

10.1 Crystallography of silicon carbide

The ability of compounds and elements to occur in more than one crystal structure is called polymorphism. Polytypism is a one-dimensional variant of this phenomenon. The so-called polytypes differ by the stacking sequence along one direction (Verma and Krishna, 1966). Silicon carbide is the most widely investigated polytypic substance, having close packed structures.

The only manner in which the close packing of spheres can be done is represented in Fig. 10.1. As show in Fig. 10.1 the "A layer" contains two kinds of triangular voids, one pointed upwards and labelled B, and the other pointed downwards and labelled C. All voids of one kind are related by the same lattice as that of the spheres themselves; so if spheres were to be placed in all the voids of any one kind, they would form another identical hexagonal close packed layer. A three-dimensional close packing would consist of several such layers stacked over each other. Any sequence of the letter A, B, and C, with no two successive letters alike, represents a possible manner of close packing. Each of these modes of close packing is equally economical of space and therefore gives the same density. All SiC polytypes have a binary tetrahedral structure. The Si-C bond is homopolar. Each C atom is surrounded tetrahedrally by four Si atoms, and each Si atom by four C atoms. These tetrahedra are arranged in planes perpendicular to the c-axis. All of the crystal structures may be visualised as being made up of a single basic unit, a layer of tetrahedra which may arbitrarily be chosen as SiC_4 or CSi_4 and consisting of two identical interpenetrating close packed layers, one of Si and other of C,

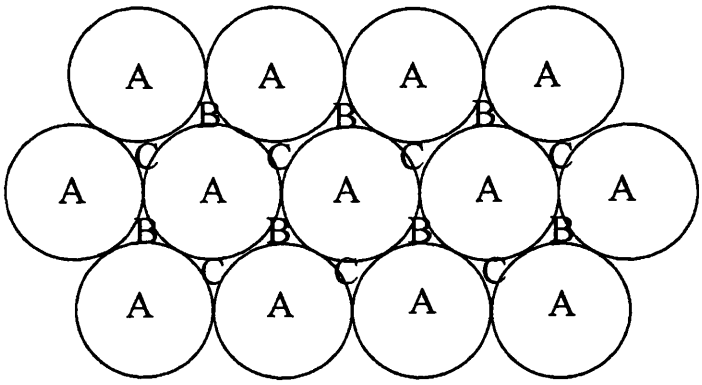

Fig. 10.1 The close parking of spheres. The are three possible positions for a layer- A, B and C. From Verma and Krishna (1966).

with one displaced relative to the other along the c axis by one-fourth of the layer spacing. Therefore the Si and C layers are stacked alternately, each layer occupying half the tetrahedral voids between the close packed layers on either side of it. The structure of different polytypes corresponds to the different stacking sequences. More than 200 silicon carbide polytypes have been determined (Jepps and Page, 1983). One of the crystalline forms is cubic, while the remainder are noncubic. The cubic form has been designated as β silicon carbide and the noncubic form has been designated as α silicon carbide. A common system of nomenclature used to describe crystalline polytypes assigns a number which corresponds to the number of the layers in the unit cell and a letter suffix designating the crystal symmetry; C, cubic; H, hexagonal; R, rhombohedral (Ramdsdell, 1947). The common silicon carbide crystalline polytypes are: 3C, 4H, 6H and 15R (Shaffer, 1969). At atmospheric pressure, 3C β silicon carbide is metastable at all temperatures; it can exist only at temperatures below about 2000°C, transforming irreversibly in to α silicon carbide type 6H at higher temperature (Verma and Krishna, 1966). The polytype 6H is the most common modification of silicon carbide (Verma and Krishna, 1966) and corresponds to a six-layered packing sequence |ABCACB|ABCACB. The structure of polytype 6H is shown in Fig.10.2.

All SiC polytypes have hexagonal unit-cell dimensions:

$$a = b = 3.08\ \text{Å}, \quad c = n \times 2.518\ \text{Å}$$

Where n is the identity period of the stacking sequence in the structure.

10 .2 Properties and usage of silicon carbide

Silicon carbide is one of the most commonly used structural ceramics and semiconductors. The industrial importance of silicon carbide is mainly due to its extreme hardness, good specific strength and Young's modulus as a function of temperature, relatively low weight, corrosion and erosion resistance, very high thermal stability and its semiconducting properties. Only diamond, cubic boron nitride and boron carbide are harder. It is consequently used in the production of abrasives, structural ceramic components, refractory materials and electronics. Like alumina, silicon carbide is very brittle.

Silicon carbide is a two-component system with a homopolar Si-C bond. Its density is 3.217g/cm^3 (Newman 1944) with the composition 70.05 wt% Si and 29.95 wt% C. It is not possible to melt it at atmospheric pressure because it sublimates and dissociates into C and a Si-rich vapour at a temperature appreciably above 2000°C. Therefore silicon carbide has no congruent melting point. Silicon carbide is a high temperature semiconductor whose characteristics depend upon the presence of impurities.

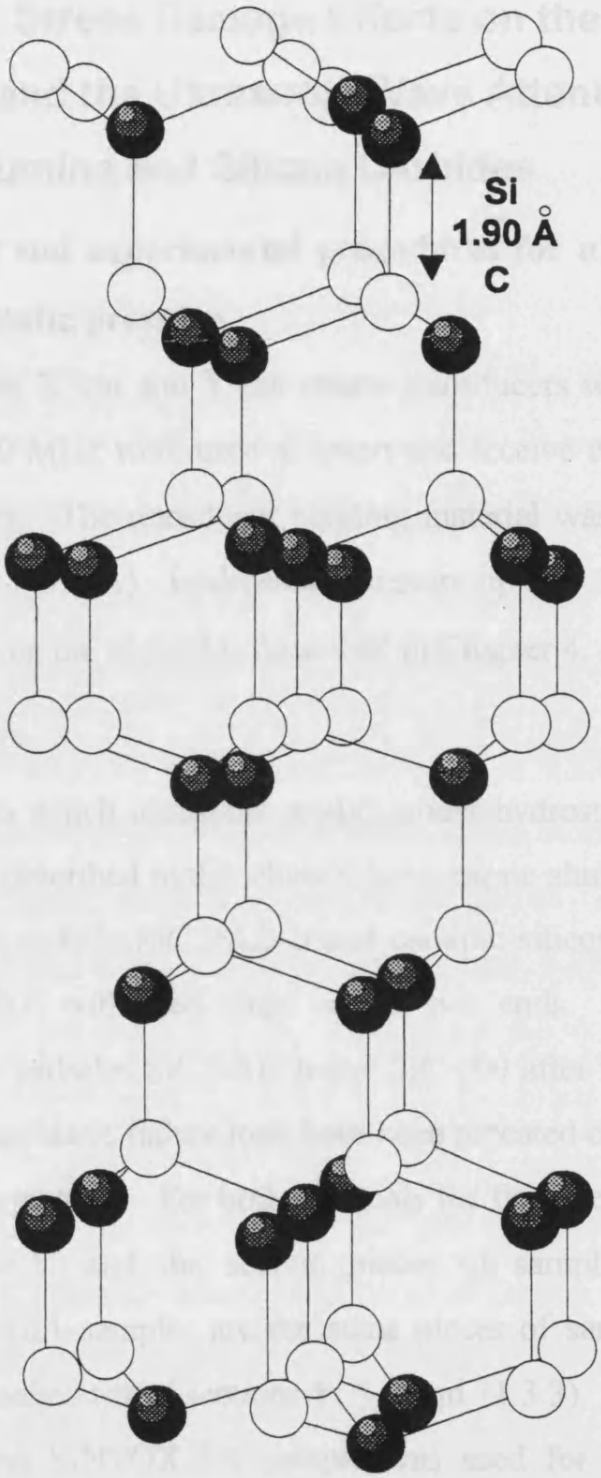

Fig. 10.2 The Structure of α silicon carbide type 6H. Black balls represent C atoms and white balls Si atoms.- from Verma and Krishna (1966)

Chapter 11 Stress Damage Effects on the Elastic Properties and the Ultrasonic Wave Attenuation of Ceramic Alumina and Silicon Carbides

11.1 Samples and experimental procedures for ultrasonic studies under hydrostatic pressure

6mm and 10mm X cut and Y cut quartz transducers with a fundamental frequency of 10 MHz were used to insert and receive ultrasonic pulses in ceramic samples. The transducer bonding material was Dow Resin 276-V9 (Dow-Corp., U.S.A). Hydrostatic pressure up to 0.3 GPa was applied at 30±0.5°C using the apparatus described in Chapter 4.

The samples on which ultrasonic studies under hydrostatic pressure were performed and described in this chapter are ceramic alumina SINTOX FA, ceramic silicon carbide SiC PAD b and ceramic silicon carbide SiC 100 bars from DERA with steel rings on the two ends. Results for both ceramic silicon carbides SiC PAD b and SiC 100 after being loaded up to 70% of the quasi-static failure load have been repeated on the second piece sample of each material. For both materials the first pieces of samples are designated "No.1" and the second pieces of samples are designated "No.2". The No.1 samples are the same pieces of samples as those we used for the baseline tests (sections 11.3.2 and 11.3.3). The same piece of ceramic alumina SINTOX FA sample was used for the measurements before and after the sample being loaded up to 70% of the quasi-static failure load (sections 11.3.1 and 11.4.3). All of the samples are of high purity. The purity and average grain size of the ceramic alumina SINTOX FA are 95% and 8.7μm respectively (data supplied by DERA). The average area equivalent diameters of the grains of the ceramic silicon

carbides SiC PAD b and SiC 100 are 2.49μm and 3.75μm respectively (data supplied by DERA). For sample SiC PAD b the area which is not silicon carbide is 2.02%, including 1% for porosity, and for sample SiC 100 is 2.7% including 1.8% for porosity (data supplied by DERA). The main phase of sample SiC PAD b is SiC 6H with a small amount of a second phase comprising SiC 15R (section 11.2.2). The main phase of sample SiC 100 is SiC 6H with a small amount of a second phase of SiC 4H (data supplied by DERA). The minimum diameter of the ceramic alumina bar is 6.0 mm, while that of the ceramic silicon carbide bars is 4.0 mm. The lengths of the samples before and after being subjected to a stress are listed in table 11.1. Since the samples were sent with two steel rings attached, the densities of ceramic alumina SINTOX FA and ceramic silicon carbide SiC PAD b at room temperature have been taken from measurements made of the dimension and the mass of another four 4×7×12 mm^3 samples, which are made of the same material. The dimensions of 4×7×12 mm^3 samples have been measured using a MICRO 2000 digital micrometer with resolution of 1μm. The mass of the 4×7×12 mm^3 samples has been determined using a SARTORIUS electronic analytical balance with standard deviation of ±0.0001g. The measured densities of the materials are given in table 11.6. The density of the ceramic silicon carbide SiC 100 has been taken as that given by DERA.

Table 11.1 (a) The length of the samples before subjected to a stress at room temperature.

Sample	Length (mm)
SINTOX FA (ceramic alumina)	14.998±0.004
SiC PAD b (ceramic silicon carbide) (No.1)	14.480±0.004
SiC 100 (ceramic silicon carbide) (No.1)	14.478±0.004

Table 11.1 (b) The length of the samples after being loaded to 70% of the quasi-static failure load at room temperature.

Sample	Length (mm)
SINTOX FA (ceramic alumina)	15.001±0.004
SiC PAD b (ceramic silicon carbide) (No.1)	14.479±0.004
SiC 100 (ceramic silicon carbide) (No.1)	14.477±0.004
SiC PAD b (ceramic silicon carbide) (No.2)	14.477±0.004
SiC 100 (ceramic silicon carbide) (No.2)	14.478±0.004

11.2 X-ray diffraction studies of alumina and silicon carbide ceramics in the undamaged state

11.2.1 The results of X-ray diffraction of ceramic alumina SINTOX FA in the undamaged state

The X-ray diffraction spectra of ceramic alumina SINTOX FA taken for different directions from a 4×7×12 mm^3 sample at room temperature are shown in Fig. 11.1. The direction X in the Fig. 11.1 is perpendicular to the 12×4 mm^2 surface, direction Y is perpendicular to the 12×7 mm^2 surface and direction Z is perpendicular to 7×4 mm^2 surface. The X-ray diffraction spectra of ceramic alumina SINTOX FA taken for different directions from a 8×10×10 mm^3 sample at room temperature are shown in Fig. 11.2. The direction Z of the sample is perpendicular to a 10×10 mm^2 surface, directions X and Y are at right angles and each perpendicular to one of the 8×10 mm^2 surfaces. Previously the angles between the c-axis and six planes of α-Al_2O_3 were calculated by Akatsu et al. (1994) as follows: $(10\bar{1}4)$: 76.0°; $(11\bar{2}6)$: 71.6°; $(1.0.\bar{1}.10)$: 84.3°; $(11\bar{2}0)$: 0°;

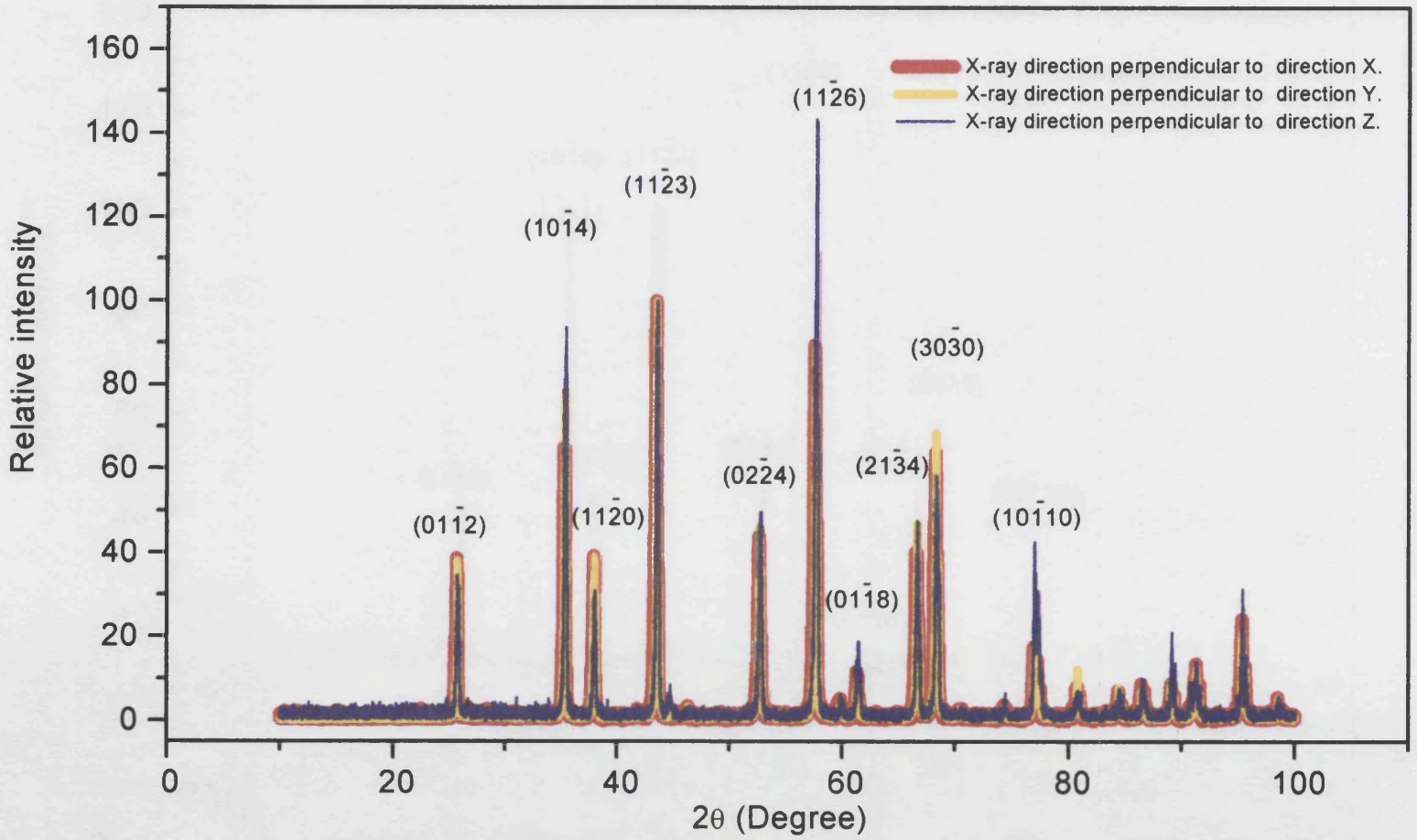

Fig.11.1 The X-ray diffraction spectrum of ceramic alumina SINTOX FA at room temperature.

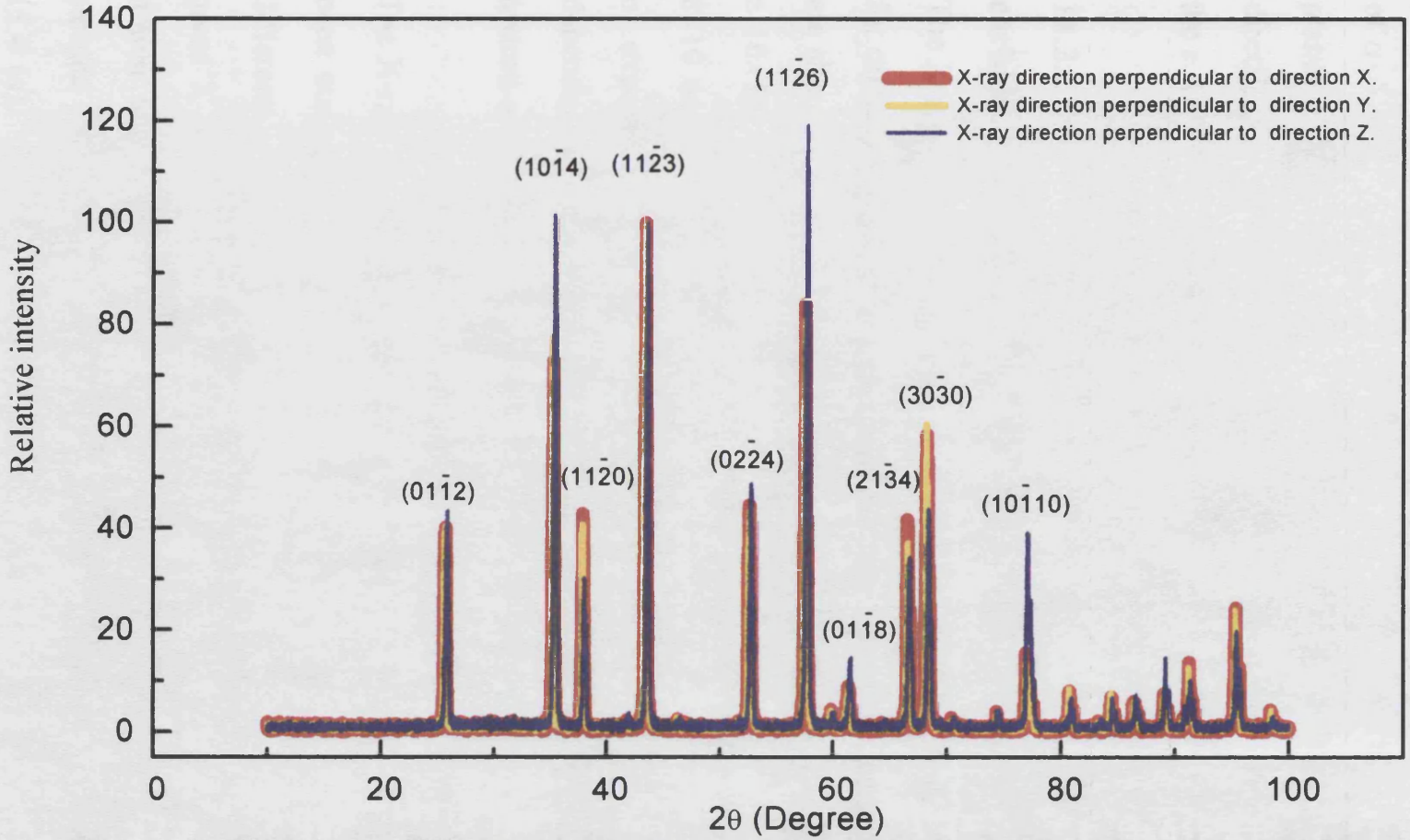

Fig.11.2 The X-ray diffraction spectrum of ceramic alumina SINTOX FA at room temperature.

$(11\bar{2}3)$: 56.3°; $(03\bar{3}0)$: 0°. From the data shown in Fig. 11.1 and 2, it can been seen that planes which make a comparatively large angle to the c-axis of α-Al_2O_3 are preferentially oriented in the Z direction of the sample and planes whose angle to the c-axis is small are preferentially oriented in the direction perpendicular to the Z direction. Therefore, it is concluded that in the c-axis of α-Al_2O_3 grains have preferred orientation in the Z direction.

11.2.2 The results of X-ray diffraction studies of ceramic silicon carbide SiC PAD b in the undamaged state

The X-ray diffraction spectra of ceramic silicon carbide SiC PAD b taken for different directions from a 8×10×10 mm^3 sample at room temperature are shown in Fig. 11.3. The direction 1 in the Fig. 11.3 is perpendicular to a 10×10 mm^2 surface, direction 2 and 3 are perpendicular to one of the 8×10 mm^2 surfaces. From this figure it can be seen that within the limits of experimental error (that is $\sqrt{counts}$) the relative peak height is not dependent on the direction of the incoming X-ray beam. No observable texture of grains has been found in ceramic silicon carbide SiC PAD b.

The X-ray diffraction spectra of ceramic silicon carbide SiC PAD b have been compared with standard X-ray diffraction spectra of all of the 13 different polytypes of silicon carbides in our database. Fig. 11.4(a) gives X-ray diffraction spectra of ceramic silicon carbide SiC PAD b drawn together with the standard X-ray diffraction spectra of silicon carbide 6H and 15R phases. Fig. 11.4 (b) is an enlarged graph of Fig. 11.4 (a). It has been found that the main phase of ceramic silicon carbide SiC PAD b is silicon carbide 6H (Fig. 11.4 (a)). The 15R phase is just detectable (see the black arrow in Fig. 11.4(b)). From the Fig. 11.4(a) it can also be concluded that there is at least one unknown

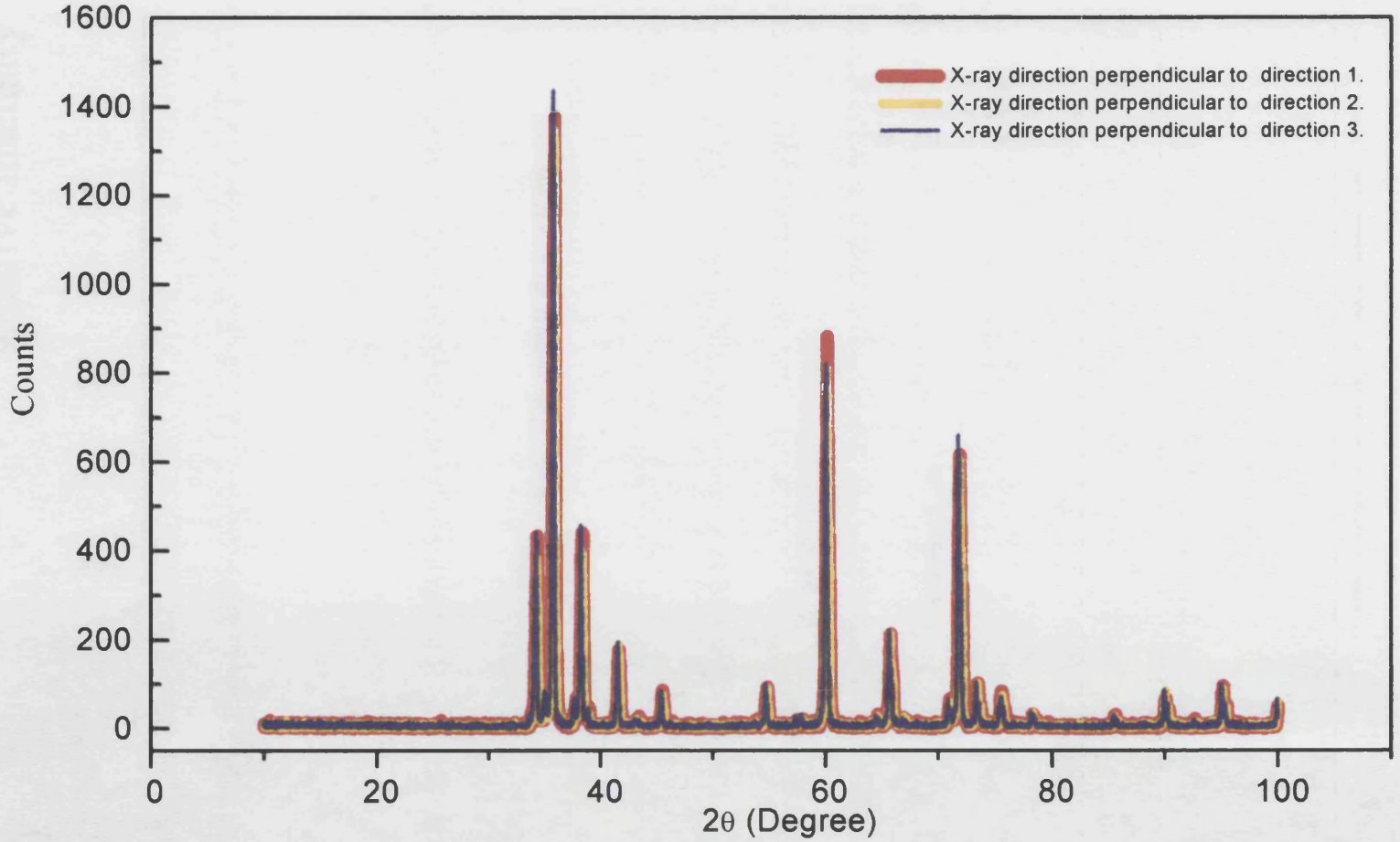

Fig. 11.3 The X-ray diffraction spectrum of ceramic silicon carbide SiC PAD b at room temperature.

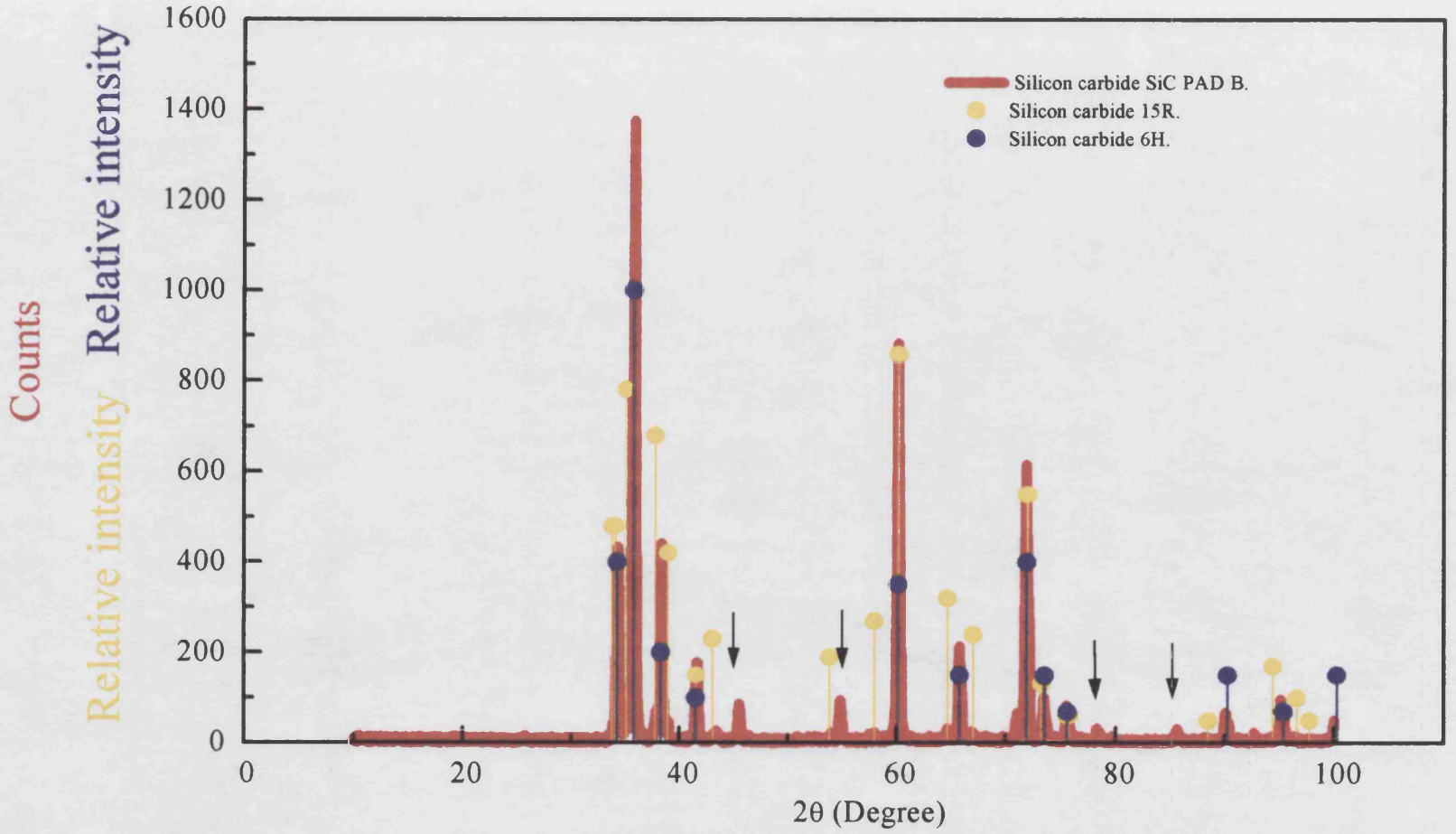

Fig. 11.4(a) The X-ray diffraction spectrum of ceramic silicon carbide SiC PAD b ploted together with the standard diffraction spectrum of silicon carbide 6H and 15R.

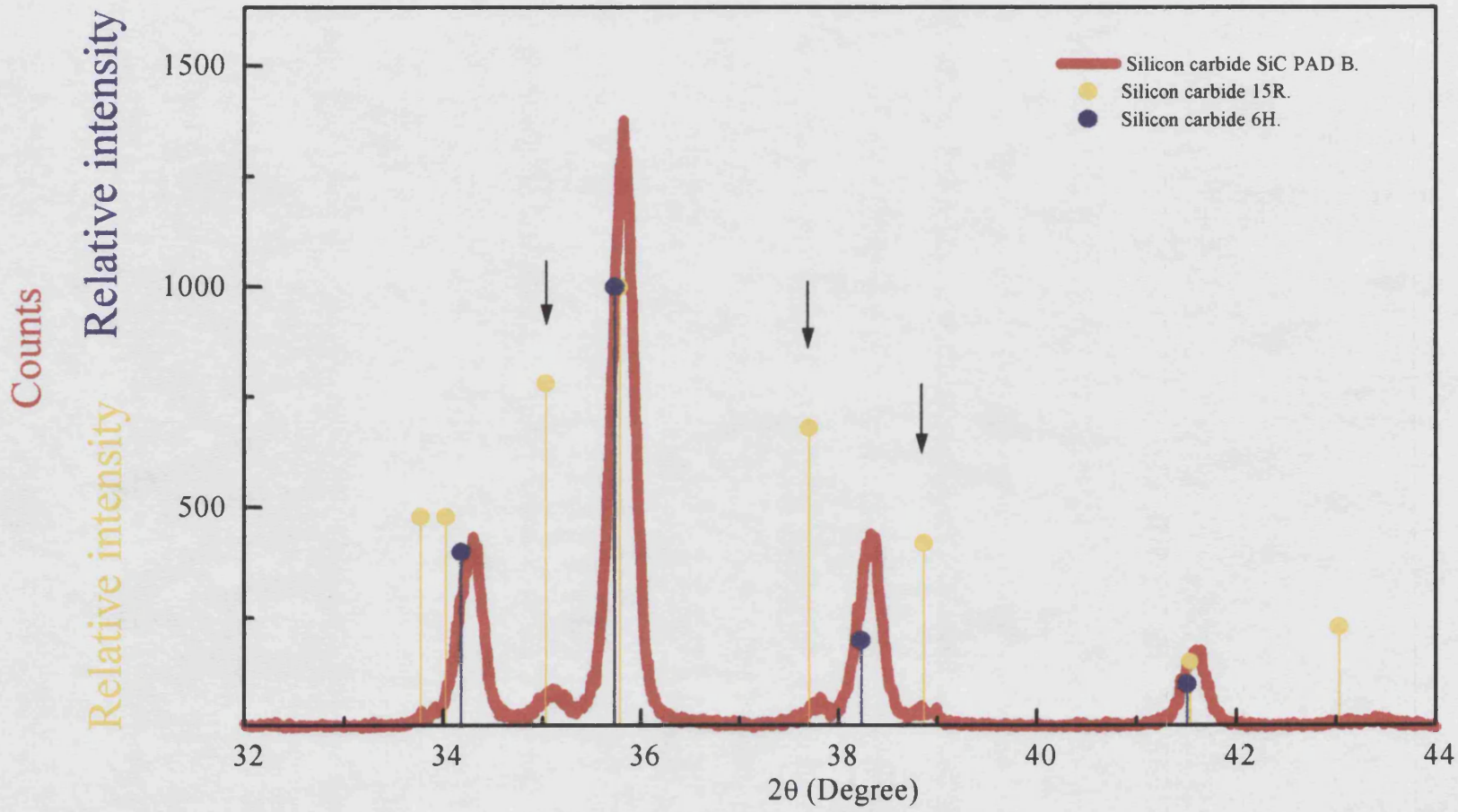

Fig. 11.4 (b) The X-ray diffraction spectrum of ceramic silicon carbide SiC PAD b ploted together with the standard diffraction spectrum of silicon carbide 6H and 15R.

crystalline second phase in ceramic silicon carbide SiC PAD b (see the black arrow in Fig. 11.4(a)). Due to the shortage of information about the additions included in the samples during manufacture, it is difficult to establish what kind of compounds constitute the unknown crystalline phases in ceramic silicon carbide SiC PAD b.

11.3 Hydrostatic pressure dependence of elastic properties and ultrasonic attenuation of ceramic alumina and ceramic silicon carbides in the undamaged state

11.3.1 Hydrostatic pressure dependence of elastic properties and ultrasonic attenuation of ceramic alumina SINTOX FA in the undamaged state

From the results of the X-ray diffraction spectra of ceramic alumina SINTOX FA it has been concluded that the c-axis of α-Al_2O_3 grains has a preferred orientation in the direction Z which is perpendicular to 10×10 mm^2 surface pair of the 8×10×10 mm^3 sample. The velocities of longitudinal and shear mode ultrasonic waves propagated and polarised in different directions, measured on the same sample, are listed in table 11.2. The anisotropy shown by the values of the velocities of ultrasonic waves in the ceramic alumina SINTOX FA is not more than 1.1 %; hence it is feasible to treat the material as isotropic when determining the elastic moduli, the Poisson's ratio, the pressure derivatives of the elastic moduli and the long wavelength acoustic Grüneisen parameters.

Table 11.2 The velocities of longitudinal and shear mode ultrasonic waves propagated and polarised at different directions in ceramic alumina SINTOX FA in the undamaged state at 30±0.5°C. See P7-34 for explanation of the experimental error.

mode	Direction of propagation	Direction of polarisation	Velocity (m/s)
Longitudinal	X	X	9880±3
Longitudinal	Y	Y	9877±3
Longitudinal	Z	Z	9776±3
Shear	X	Y	5838±3
Shear	X	Z	5822±3
Shear	Y	X	5837±3
Shear	Y	Z	5822±3
Shear	Z	X	5814±3
Shear	Z	Y	5813±3

Fig. 11.5 shows the pressure dependence up to 0.3 GPa of the normalised longitudinal natural velocities of ceramic alumina SINTOX FA measured in separate runs at 30±0.5°C and 30 MHz. Fig. 11.6 presents the pressure dependence of the normalised shear natural velocities measured in separate runs at 30MHz and 30±0.5°C. The pressure derivatives of natural velocities of ceramic alumina SINTOX FA measured in separate runs at 30 MHz, at atmospheric pressure and at 30±0.5°C are listed in table 11.3. The ultrasonic attenuation of longitudinal and shear mode waves measured at 30MHz respectively is plotted in Fig. 11.7. The ultrasonic wave velocities and pressure derivatives of natural velocities measured in the separate runs at 30MHz were averaged to give mean values for the corresponding parameters. These averaged values were used for the

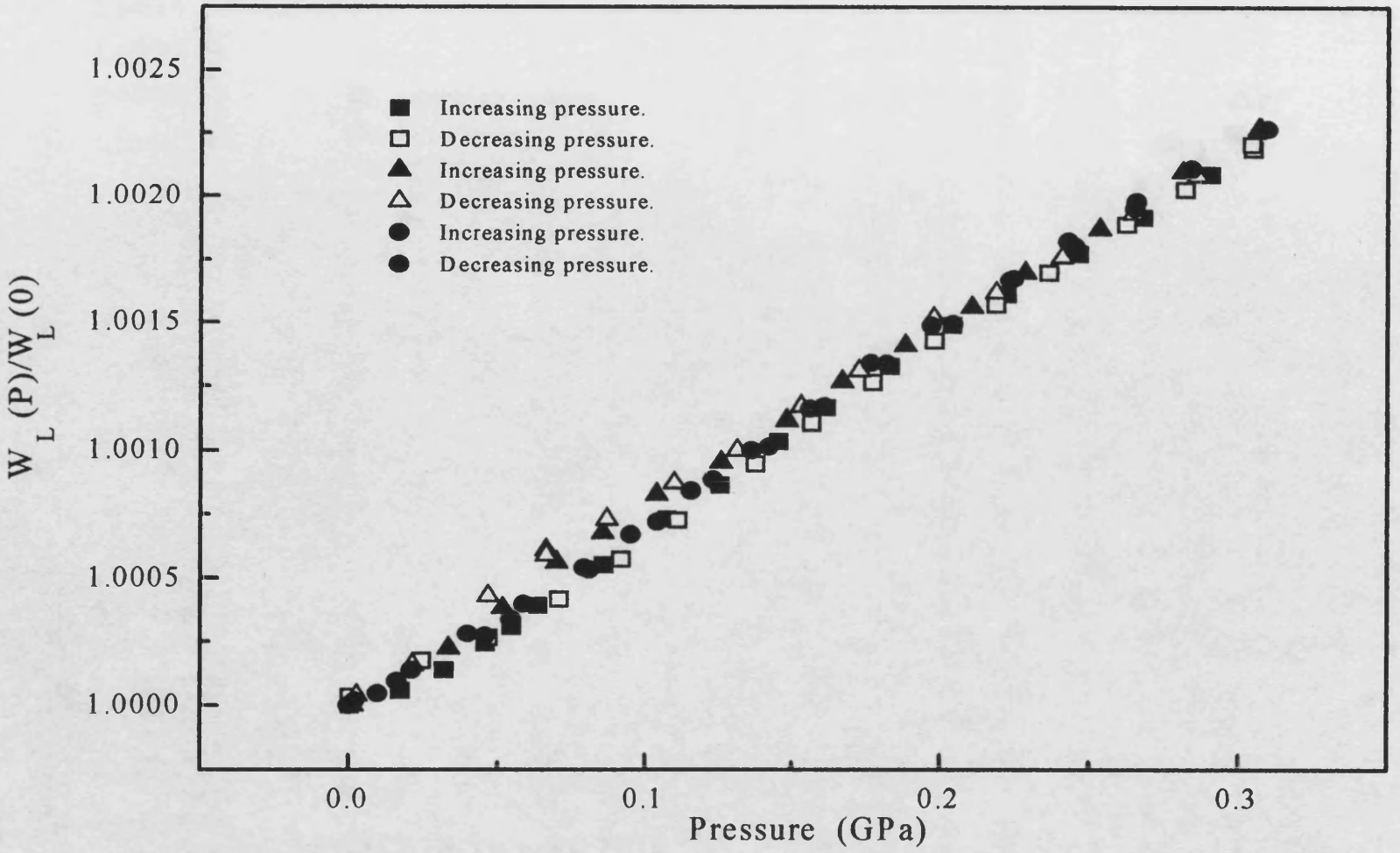

Fig.11.5 The pressure dependence of normalised longitudinal mode natural velocity for the ceramic alumina SINTOX FA at 30 MHz and 30±0.5°C.

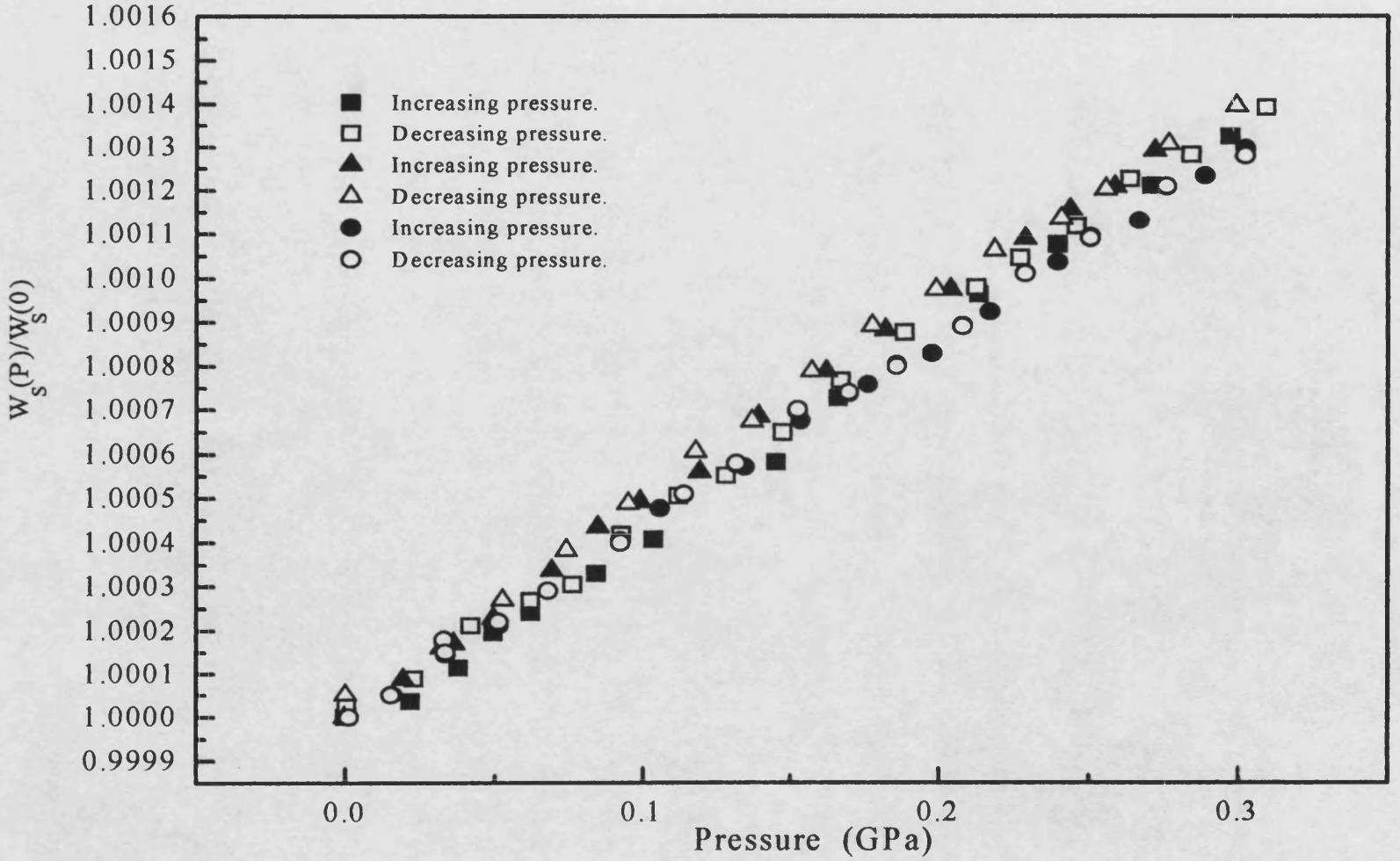

Fig. 11.6 The pressure dependence of normalised shear mode natural velocity of the ceramic alumina SINTOX FA at 30 MHz and 3±0.5 °C.

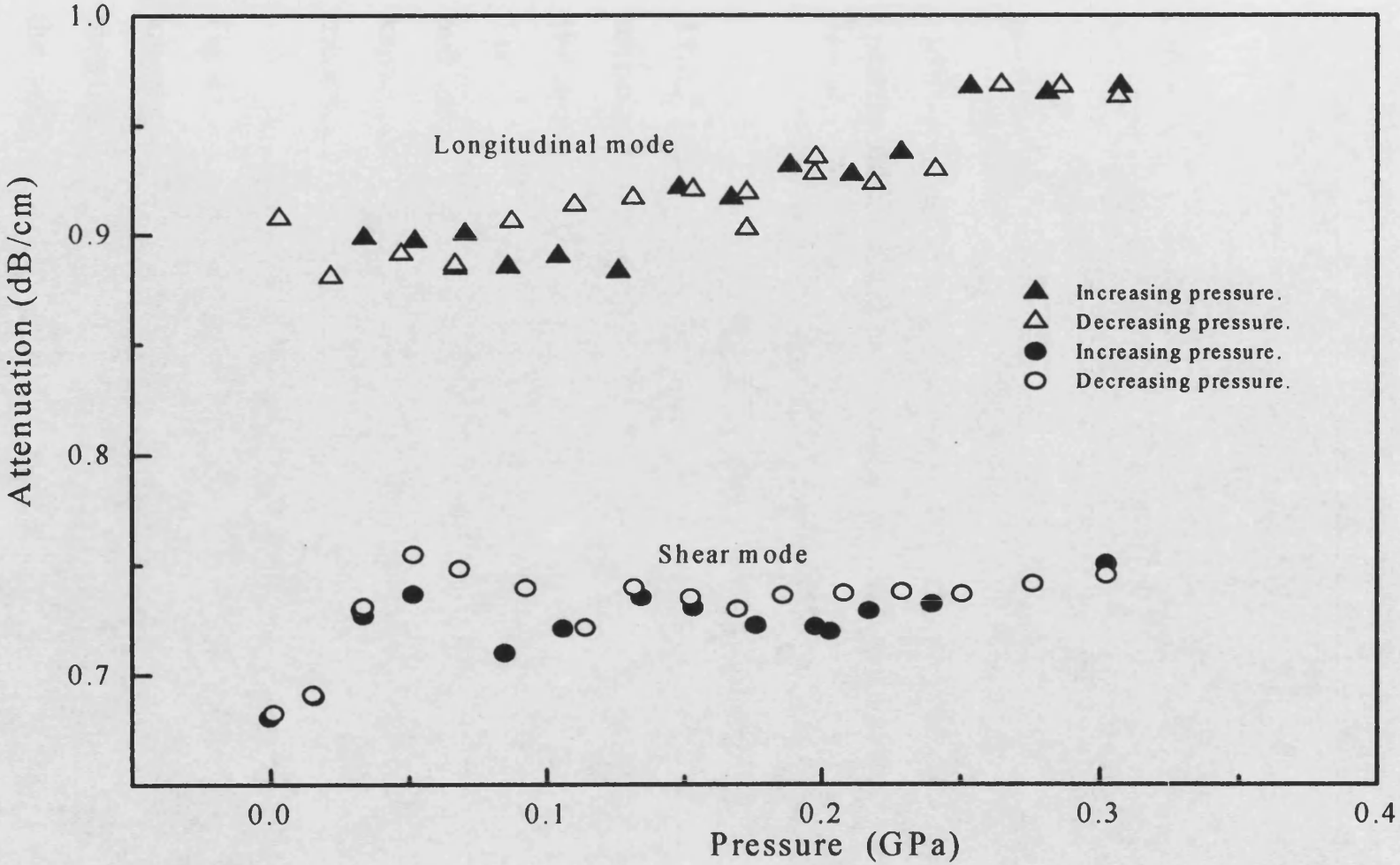

Fig. 11.7 The pressure dependence of attenuation of longitudinal and shear modes ultrasonic wave in the ceramic alumina SINTOX FA at 30MHz and 30±0.5°C.

calculation of the elastic moduli, the Poisson ratio, the pressure derivatives of the elastic moduli and the long wavelength acoustic Grüneisen parameters. The averaged values and calculated results are presented in Table 11.6.

Table.11.3 The pressure derivatives of natural wave velocities for the ceramic alumina SINTOX FA in the undamaged state measured at 30 MHz, atmospheric pressure and 30±0.5°C.

Parameter	1	2	3
$(\partial W_L/\partial P)_{P=0}$ ($ms^{-1}GPa^{-1}$)	72±2	70±2	74±2
$(\partial W_S/\partial P)_{P=0}$ ($ms^{-1}GPa^{-1}$)	27±2	27±2	25±2

11.3.2 Hydrostatic pressure dependence of elastic properties and ultrasonic attenuation of ceramic silicon carbide SiC PAD b in the undamaged state

The 10 MHz longitudinal and shear waves did not give suitable echo trains and the 30 MHz longitudinal waves show large diffraction effects. It is known that these effects were caused by wall reflection. The 50 MHz echo trains were nearly exponential for both longitudinal and shear waves.

Fig. 11.8 shows the pressure dependence up to 0.3 GPa of the normalised longitudinal natural velocities of ceramic silicon carbide SiC PAD b measured in four separate runs at 30±0.5°C and 50 MHz. The four sets of the velocity data are consistent with each other, their dependence on pressure being linear. Fig. 11.9 presents the pressure dependence of the shear natural velocities measured in three separate runs at 47 and 51 MHz and at 30±0.5°C. The pressure derivatives of normalised natural velocities

of ceramic silicon carbide SiC PAD b measured in separate runs at 47, 50, and 51 MHz, at atmospheric pressure and at 30±0.5°C are listed in table 11.4. The ultrasonic attenuations of longitudinal and shear mode waves measured 53 MHz and 47 MHz respectively are plotted in Fig. 11.10. The ultrasonic wave velocities and pressure derivatives of natural velocities measured in the separate runs near 50 MHz were averaged to give mean values for the corresponding parameters. These averaged values were used for the calculation of the elastic moduli, the Poisson ratio, the pressure derivatives of the elastic moduli and the long wavelength acoustic Grüneisen parameters. The averaged values and calculated results are presented in Table 11.6.

Table 11.4 The pressure derivatives of natural velocities for the ceramic silicon carbide SiC PAD b in the undamaged state near 50 MHz at atmospheric pressure and 30±0.5°C.

Parameter	Run 1	Run 2	Run 3	Run 4
$(\partial W_L/\partial P)_{P=0}$ ($ms^{-1}GPa^{-1}$)	56±2	58±2	54±2	54±2
$(\partial W_S/\partial P)_{P=0}$ ($ms^{-1}GPa^{-1}$)	14±2	14±2	15±2	

11.3.3 Hydrostatic pressure dependence of elastic properties and ultrasonic attenuation of ceramic silicon carbide SiC 100 in the undamaged state

The only ceramic silicon carbide SiC 100 sample available from DERA is a bar sample on which is impossible to measure the direction dependence of the ultrasonic wave velocity or the X-ray diffraction spectra. According to DERA this material can be treated as isotropic.

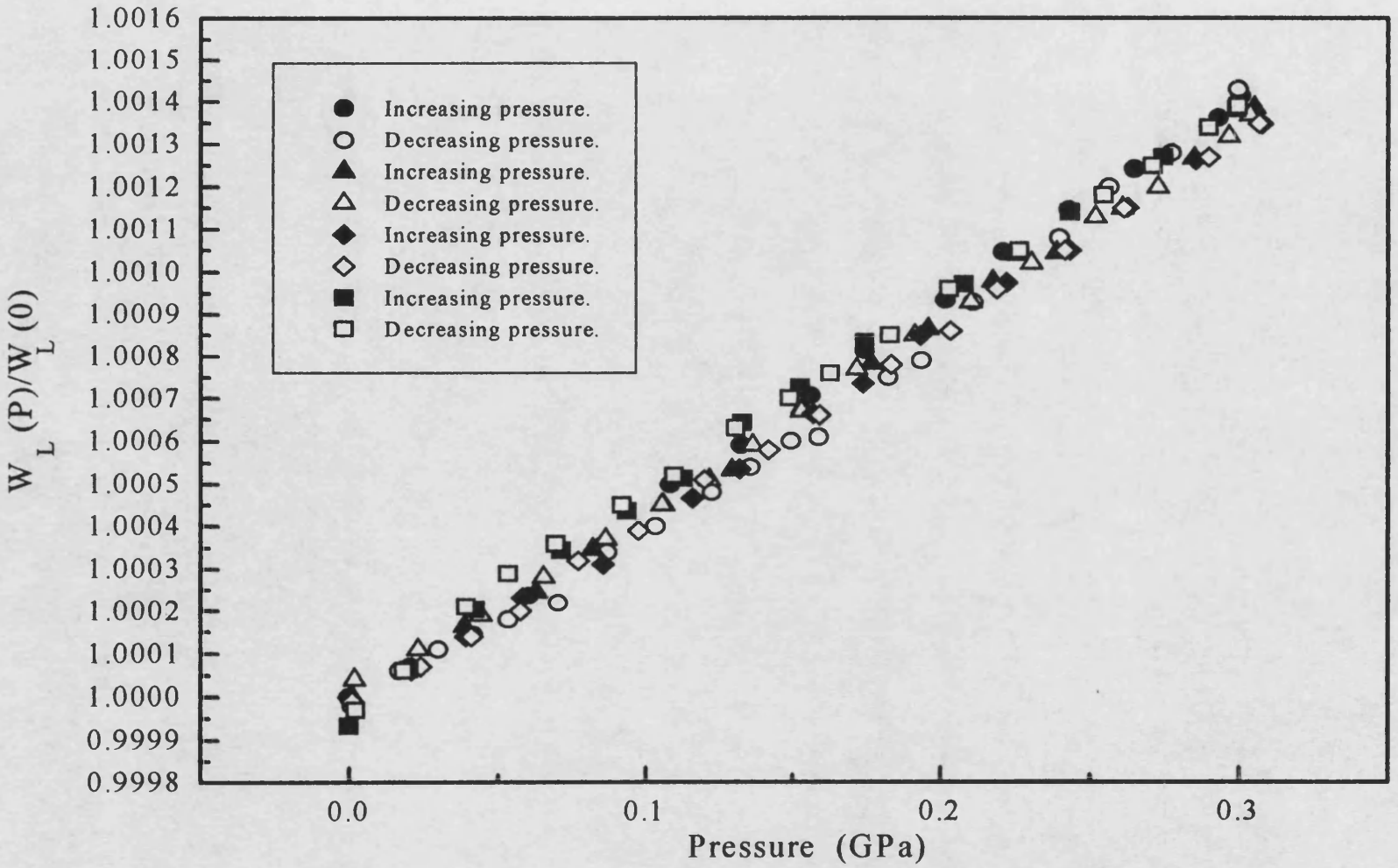

Fig.11.8 The pressure dependence of normalised longitudinal mode natural velocity for the ceramic silicon carbide SiC PAD b at 50 MHz and 30±0.5°C.

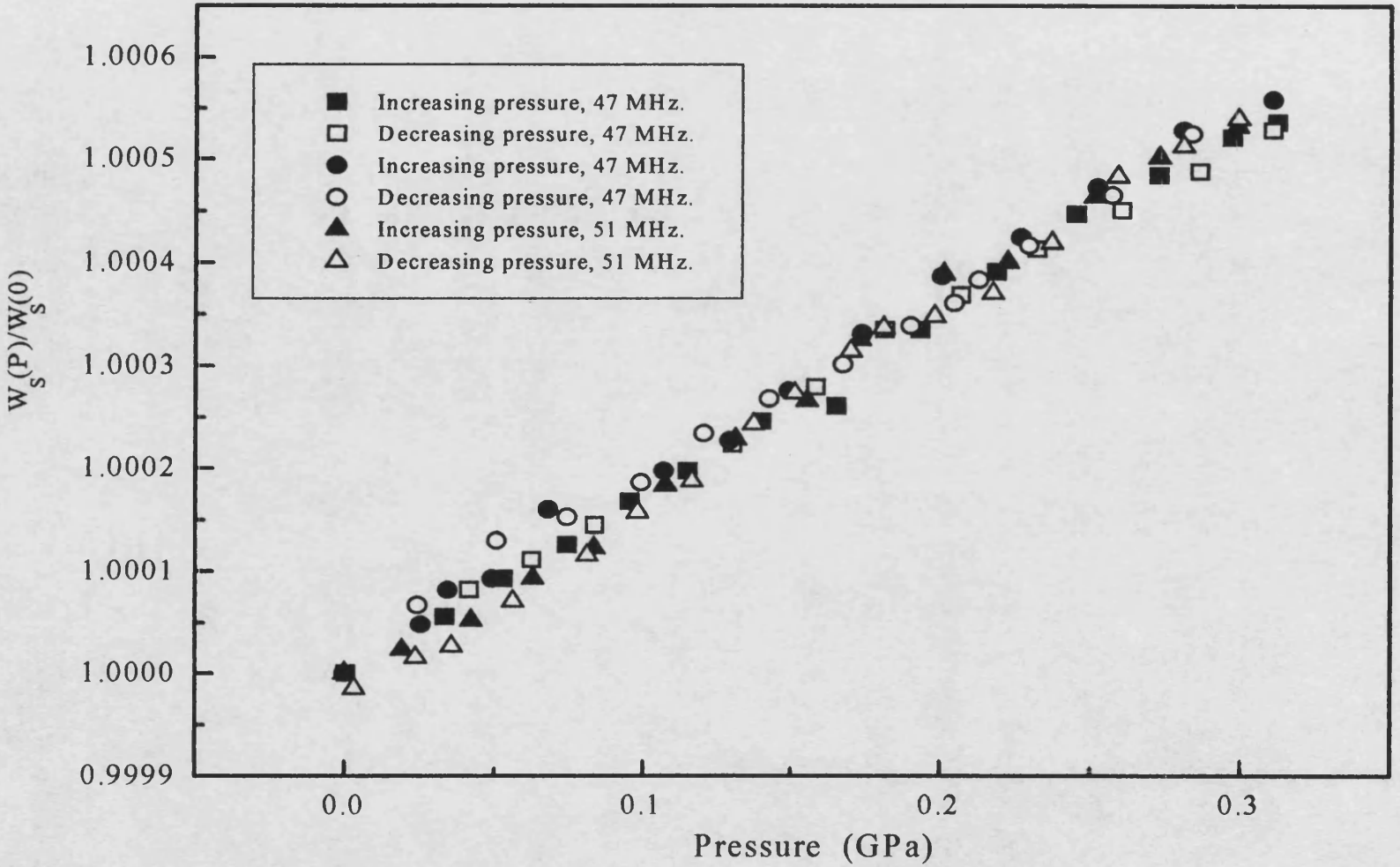

Fig. 11.9 The pressure dependence of normalised shear mode natural velocity of the ceramic silicon carbide SiC PAD b at 47 MHz and 51 MHz and at 3±0.5 °C.

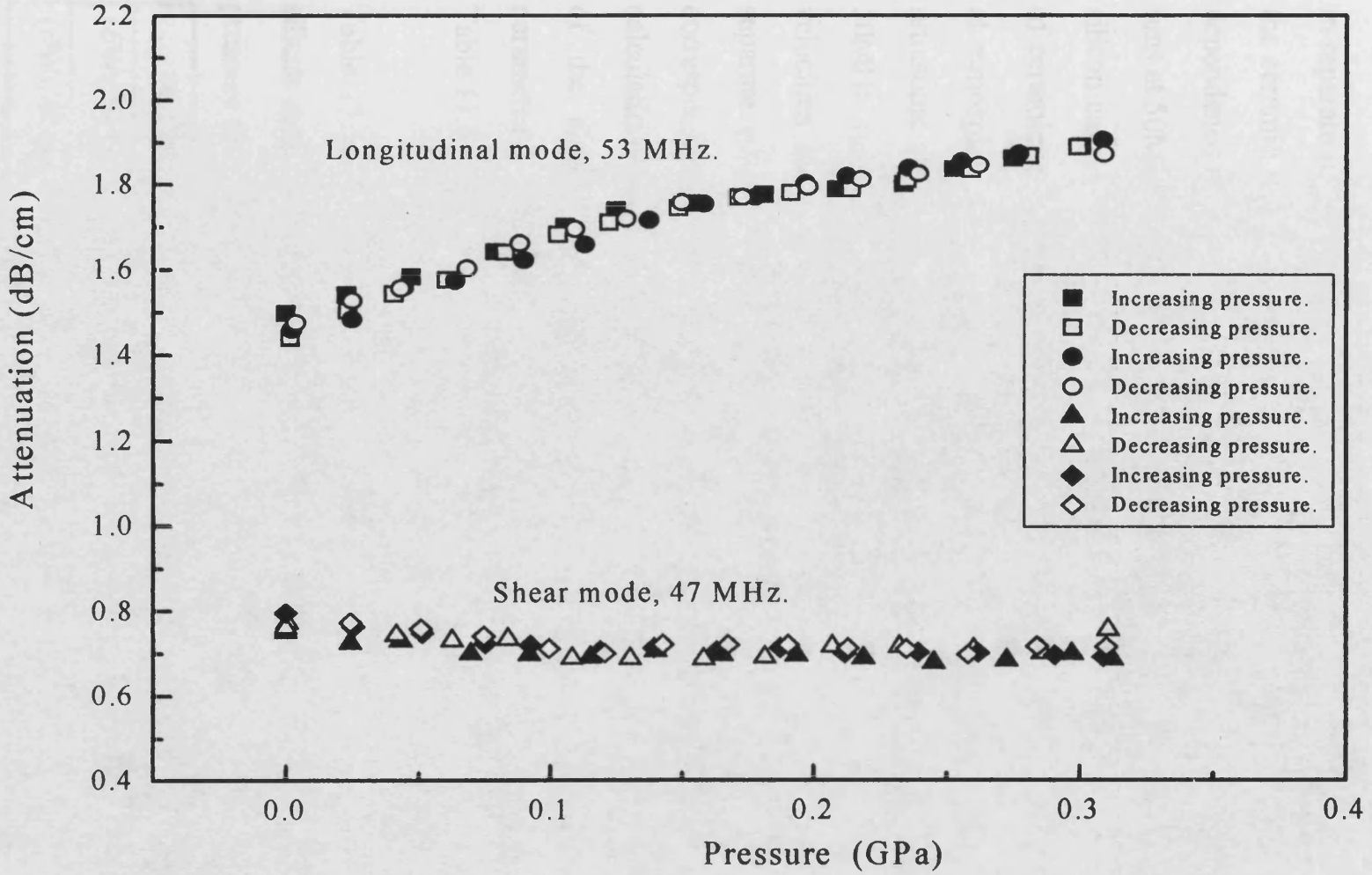

Fig. 11.10 The pressure dependence of attenuation of longitudinal and shear modes ultrasonic wave in the ceramic silicon carbide SiC PAD b at 30±0.5°C.

Fig. 11.11 shows the pressure dependence up to 0.3 GPa of the normalised longitudinal natural velocities of ceramic silicon carbide SiC 100 measured in separate runs at 30±0.5°C and 50 MHz plotted together with the data for the ceramic silicon carbide SiC PAD b. Fig. 11.12 presents the pressure dependence of the normalised shear natural velocities measured in separate runs at 50MHz and 30±0.5°C plotted together with the data for the ceramic silicon carbide SiC PAD b . The pressure derivatives of natural velocities of ceramic silicon carbide SiC 100 measured in separate runs at 50 MHz, at atmospheric pressure and at 30±0.5°C are listed in table 11.5. The ultrasonic attenuations of longitudinal and shear mode waves measured at 50MHz respectively are plotted in Fig. 11.13. The ultrasonic wave velocities and pressure derivatives of natural velocities measured in the separate runs at 50 MHz were averaged to give mean values for the corresponding parameters. These averaged values were used for the calculation of the elastic moduli, the Poisson ratio, the pressure derivatives of the elastic moduli and the long wavelength acoustic Grüneisen parameters. The averaged values and calculated results are presented in Table 11.6.

Table 11.5 The pressure derivatives of natural velocities for the ceramic silicon carbide SiC 100 in the undamaged state at 50 MHz, atmospheric pressure and 30±0.5°C.

Parameter	Run 1	Run 2	Run 3	Run 4
$(\partial W_L/\partial P)_{P=0}$ ($ms^{-1}GPa^{-1}$)	41±2	36±2	39±2	36±2
$(\partial W_S/\partial P)_{P=0}$ ($ms^{-1}GPa^{-1}$)	2±2	1±2	0±2	2±2

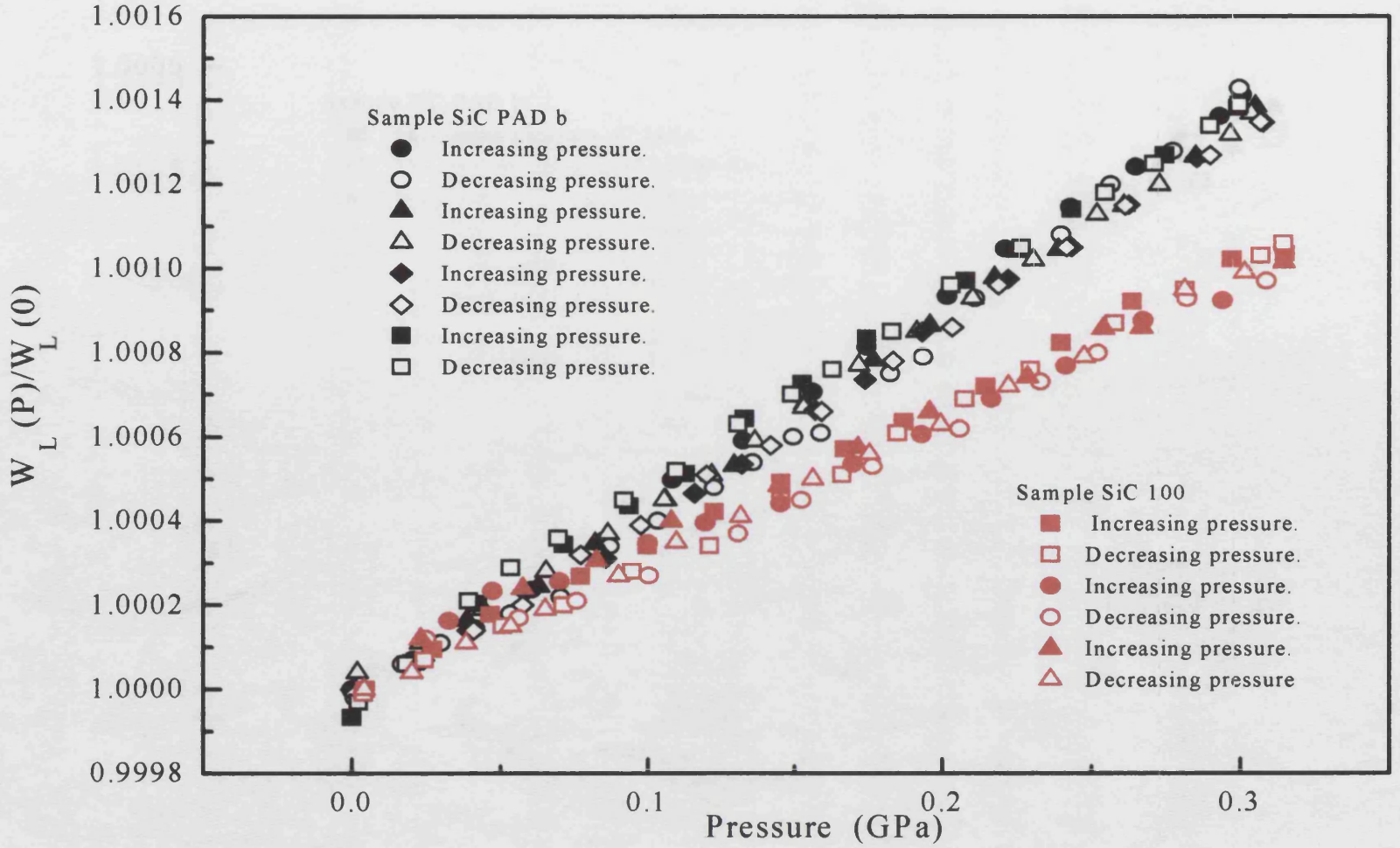

Fig. 11.11 The pressure dependence of normalised longitudinal mode natural velocity for the ceramic silicon carbides SiC 100 and SiC PAD b at 50 MHz and 30±0.5°C.

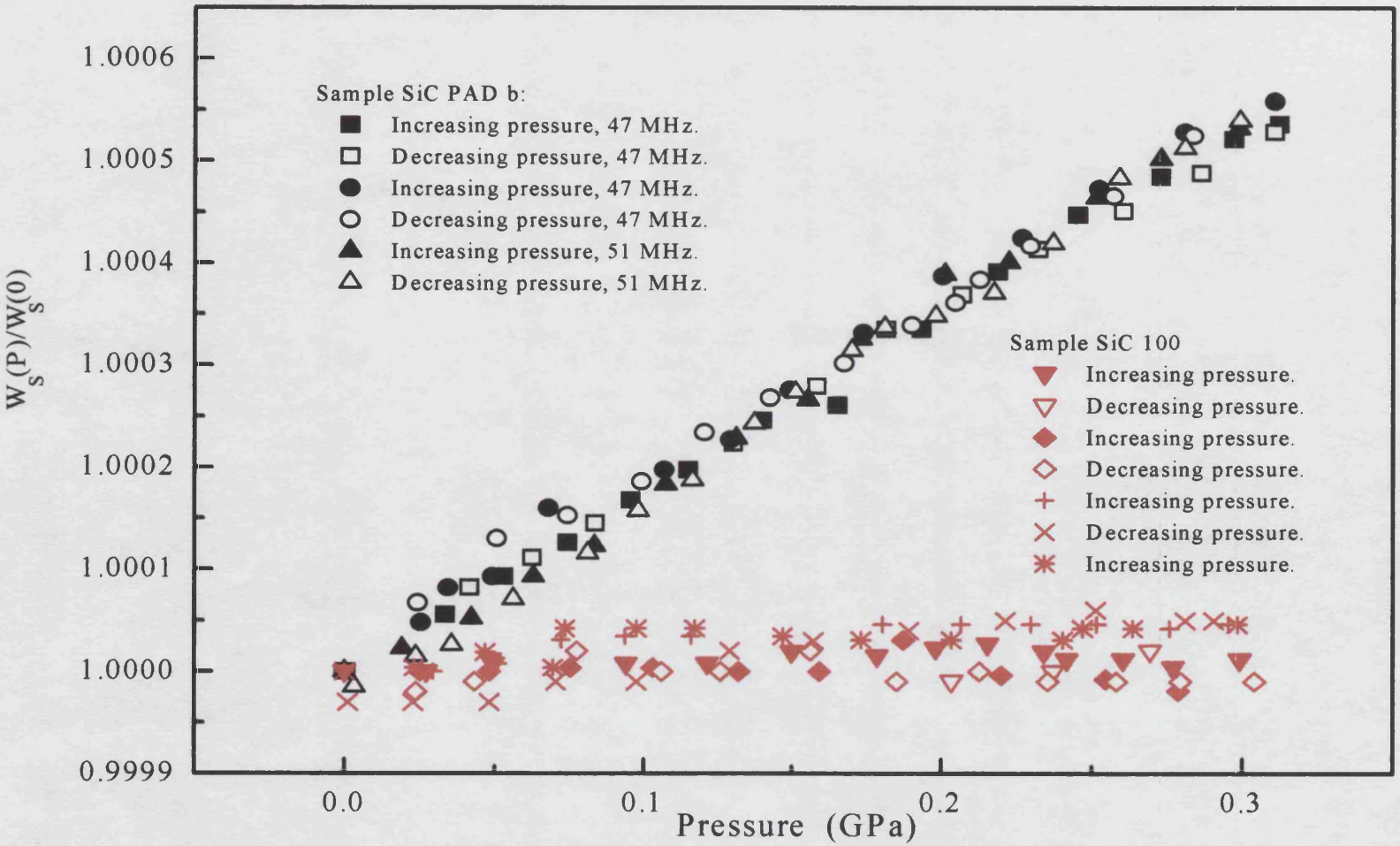

Fig. 11.12 The pressure dependence of normalised shear mode natural velocity at 3±0.5 °C of silicon carbide SiC PAD b at 47 MHz and 51 MHz and the sample SiC 100 at 50 MHz.

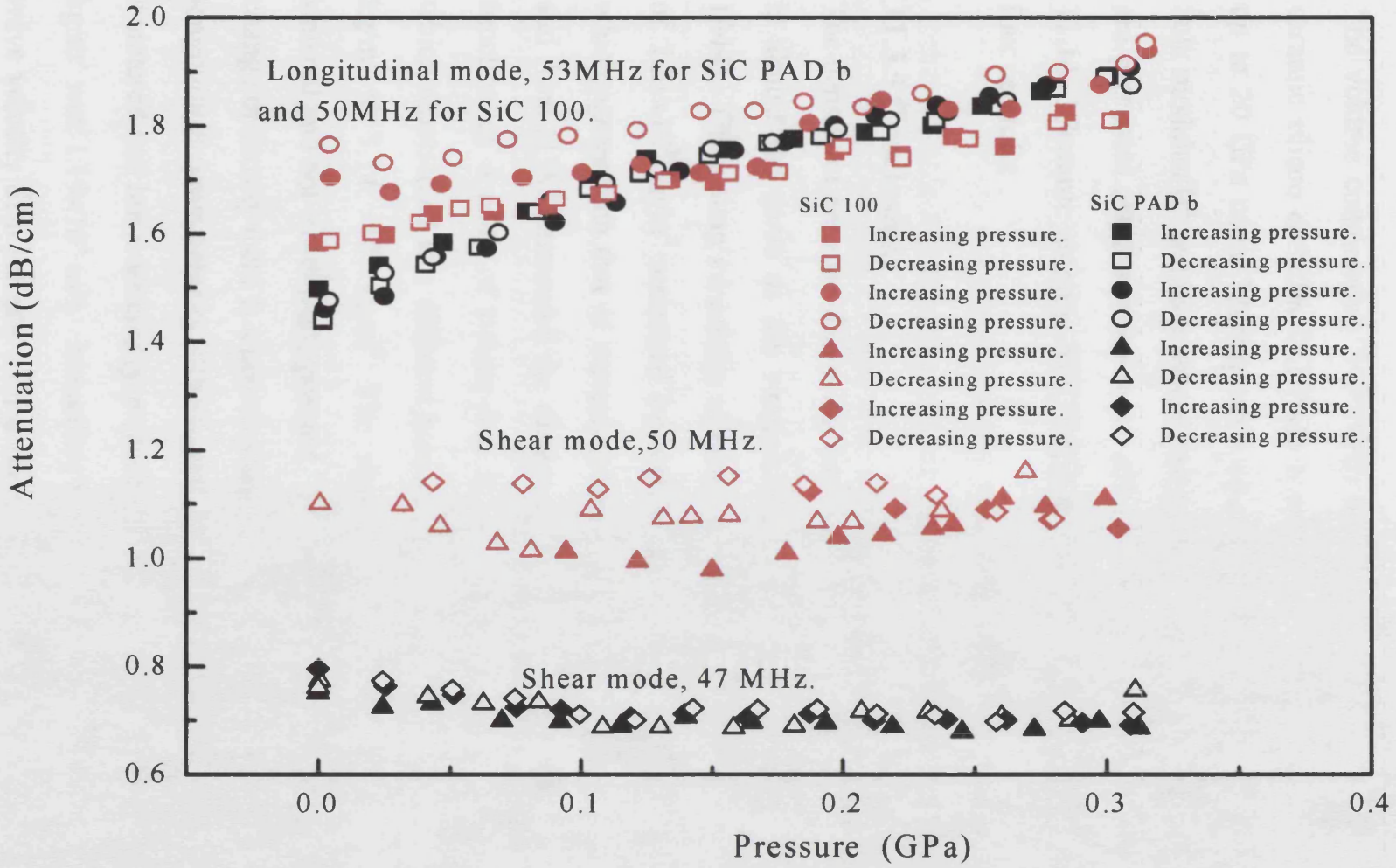

Fig. 11.13 The pressure dependence of attenuation of longitudinal and shear modes ultrasonic wave in the ceramic silicon carbides SiC PAD b and SiC 100 at 30±0.5°C.

11.3.4 Volume compression of ceramic alumina and ceramic silicon carbides in the undamaged state extrapolated to higher pressure

The volume compression V(P)/V(0) of ceramic alumina SINTOX FA, ceramic silicon carbides SiC PAD b and SiC 100 has been extrapolated up to 20 GPa using Murnaghan's equation-of-state (equation 2.32), the bulk modulus B^S and its pressure derivative $(\partial B^S/\partial P)_{P=0}$. The sets of data are presented together with those of the ceramic alumina D999 in Fig. 11.14. Ceramic alumina SINTOX FA is the most compressible of the four ceramics.

11.3.5 Conclusions

The density of ceramic silicon carbide SiC PAD b is 3212±1kg/m^3 which is almost the same as the single-crystal density 3217kg/m^3 (Newman 1944). The Young's modulus of ceramic silicon carbide with the density of 3.21×10^3 kg/m^3 measured by Karmo and Bryzik (1984) is 440GPa which agrees with that of ceramic silicon carbide SiC PAD b. Baaklini and Abel (1988) measured the ultrasonic longitudinal wave velocity as a function of density of twenty-five α ceramic silicon carbide samples, which represented five different batches in the density range of 2.92×10^3 kg/m^3 to 3.14×10^3 kg/m^3. The samples they used were sintered or sintered and hot isostatically pressed. They concluded that for a 1 percent change in density there is a approximately a 1 percent change in ultrasonic longitudinal wave velocity. The longitudinal wave velocity they gave for a sintered and hot isostatically pressed material with density of 3.14×10^3 kg/m^3 was 1.19×10^4 m/s. According to their conclusion, the longitudinal wave velocity of a sample with a density of 3.21×10^3 kg/m^3 should be 1.216×10^4 m/s which agrees with the data of ceramic silicon carbide SiC

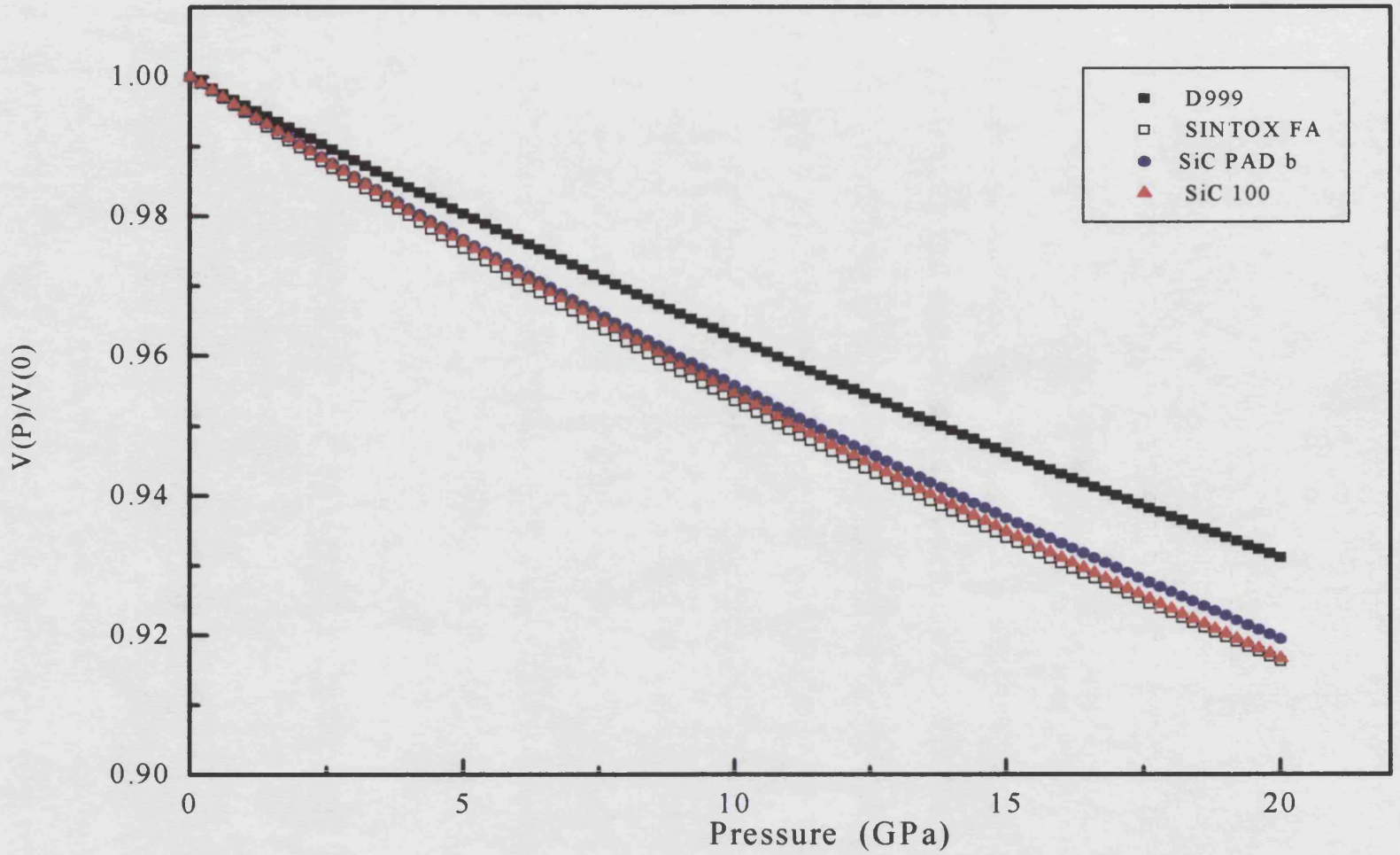

Fig. 11.14 The volume compression of the ceramic aluminas and silicon carbides extrapolated from the bulk modulus B and (dB/dP) measured under moderate pressures and 30±0.5°C.

PAD b within their error range. No shear wave velocity was reported in their paper. The density of ceramic silicon carbide SiC 100 is 1.5% lower than that of ceramic silicon carbide SiC PAD b and the longitudinal wave velocity of ceramic silicon carbide SiC 100 is 1.5% lower than that of ceramic silicon carbide SiC PAD b as well. It can be concluded that the lower longitudinal wave velocity of ceramic silicon carbide SiC 100 is due to its lower density.

In table 11.6 the data measured are listed together with those of ceramic alumina D999. The measured density of the ceramic alumina D999 is 3963±1 kg/m^3, which is comparable with the single-crystal density of α-alumina (3986 kg/m^3). This is a high purity sample (99.4 wt.%). In chapter 8, it was concluded that the data of ceramic alumina D999 reflected the nature of the α-alumina grains in the material, although the data are slightly affected by the purity and density. Ceramic silicon carbide SiC PAD b has nearly the theoretical density and is high purity; its main phase is 6 H α-silicon carbide. Comparing the data for ceramic alumina D999 and ceramic silicon carbide SiC PAD b, it is found that ceramic silicon carbide SiC PAD b has a lower density but higher Young's Modulus. As a structural ceramic, this is an important advantage in building lightweight and strong systems.

From the calculated volume compression V(P)/V(0) shown in Fig. 11.14, it is found that comparing with ceramic alumina D999, ceramic silicon carbide SiC PAD b is easier to compress although both of ceramic alumina D999 have a density comparable with the theoretical density. Both of ceramic alumina D999 and ceramic silicon carbide SiC PAD b are high purity; therefore the differences in the compressibility are mainly due to the difference of the nature of crystals of alumina and silicon carbide. From

Fig. 11.14 it is also found that the ceramic alumina SINTOX FA is easier to compress than the ceramic alumina D999 and that ceramic silicon carbide SIC 100 is easier to compress than the ceramic silicon carbide SiC PAD b. One of the reasons could be the difference in the densities of the materials. The measured density of the high purity ceramic alumina D999 is 3963±1 kg/m^3, which is comparable with the single-crystal density of α-alumina (3986 kg/m^3). The density of ceramic alumina SINTOX FA is 3716±1 kg/m^3 which is 6% lower than that of ceramic alumina D999. The density of ceramic silicon carbide SiC PAD b is 3212±1kg/m^3 which is almost the same as the single-crystal density 3217kg/m^3. The density of SiC is 3163 kg/m^3 (from DERA) which is 1.5% lower than that of ceramic silicon carbide SiC.

Table 11.6 The density, ultrasonic wave velocities V, elastic moduli, pressure derivatives of natural velocities, pressure derivatives of the elastic moduli and the long wavelength acoustic mode Grüneisen parameters γ of the ceramic alumina SINTOX FA and ceramic silicon carbides SiC PAD b and SiC 100 at 30±0.5°C. σ is the Poisson ratio. W is the natural velocity. The data are listed together with those of ceramic alumina D999.

Sample	SINTOX FA	SiC PAD b	SiC 100	D999
ρ (kg/m^3)	3716±1	3212±1	3163[(a)]	3963±1
V_S (m/s)	5806±10	7804±10	7587±10	6399±10
V_L (m/s)	9806±10	12016±10	11830±10	10765±10
C_{11} (GPa)	357±0.7	463.8±0.8	442.7±0.8	459.2±0.9
C_{44} (GPa)	125±0.4	195.6±0.5	182.1±0.5	162±0.5
B^S (GPa)	190±1	203±1	200±1	243±1
E (GPa)	308±2	444±3	419±3	398±3
σ	0.230±0.002	0.135±0.002	0.15±0.002	0.227±0.002
$(\partial W_L/\partial P)_{P=0}$ (ms^{-1}GPa^{-1})	72±2	56±2	38±2	64±2
$(\partial W_S/\partial P)_{P=0}$ (ms^{-1}GPa^{-1})	26±2	14±2	1±2	28±2
$(\partial C_{11}/\partial P)_{P=0}$	5.9±0.2	5.0±0.2	3.6±0.2	6.1±0.1
$(\partial C_{44}/\partial P)_{P=0}$	1.4±0.1	1.0±0.1	0.4±0.1	1.65±0.06
$(\partial B^S/\partial P)_{P=0}$	4.1±0.2	3.7±0.2	3.1±0.2	3.9±0.1
γ_L	1.40±0.04	0.94±0.03	0.64±0.03	1.45±0.03
γ_S	0.86±0.07	0.37±0.05	0.03±0.05	1.07±0.05
γ^{el}	1.04±0.05	0.56±0.04	0.23±0.04	1.20±0.03

(a) Value supplied by DERA

11.4 Hydrostatic pressure dependence of elastic properties and ultrasonic attenuation of ceramic alumina and ceramic silicon carbides after being loaded up to 70% of the quasi-static failure load

11.4.1 Hydrostatic pressure dependence of elastic properties and ultrasonic attenuation of ceramic silicon carbide SiC PAD b after being loaded up to 70% of the quasi-static failure load (45kN)

The silicon carbide SiC PAD b was loaded at a speed of 0.25kN/s up to 45kN on the area with a diameter of 4.0 mm (DERA). Fig. 11.15 shows the pressure dependence up to 0.3 GPa of the normalised longitudinal natural velocities of ceramic silicon carbide SiC PAD b after being subjected to a stress up to 45kN measured on two samples in separate runs at 30±0.5°C and 50 MHz. The velocity data are consistent with each other within the experiment error range, their dependence on pressure being linear. Fig. 11.16 presents the pressure dependence of the normalised shear natural velocities measured in separate runs on two samples at 50 MHz and 30±0.5°C. The pressure derivatives of natural velocities of the ceramic silicon carbide SiC PAD b after being subjected to a stress up to 45kN measured in separate runs at 50 MHz, at atmospheric pressure and at 30±0.5°C are listed in table 11.7. The ultrasonic attenuations of longitudinal and shear mode waves propagated in ceramic silicon carbide SiC PAD b measured near 50 MHz before and after being subjected to a stress up to 45kN are plotted together in Fig. 11.17. In Figs. 11. 16 and 17 the green symbols present the data measured on sample No.1 and the blue symbols present the data measured on sample No.2. From the Figs. 11.15-17 and the table 11.7 it has found that the data measured from two pieces of samples are consistent with each other within the experiment error range.

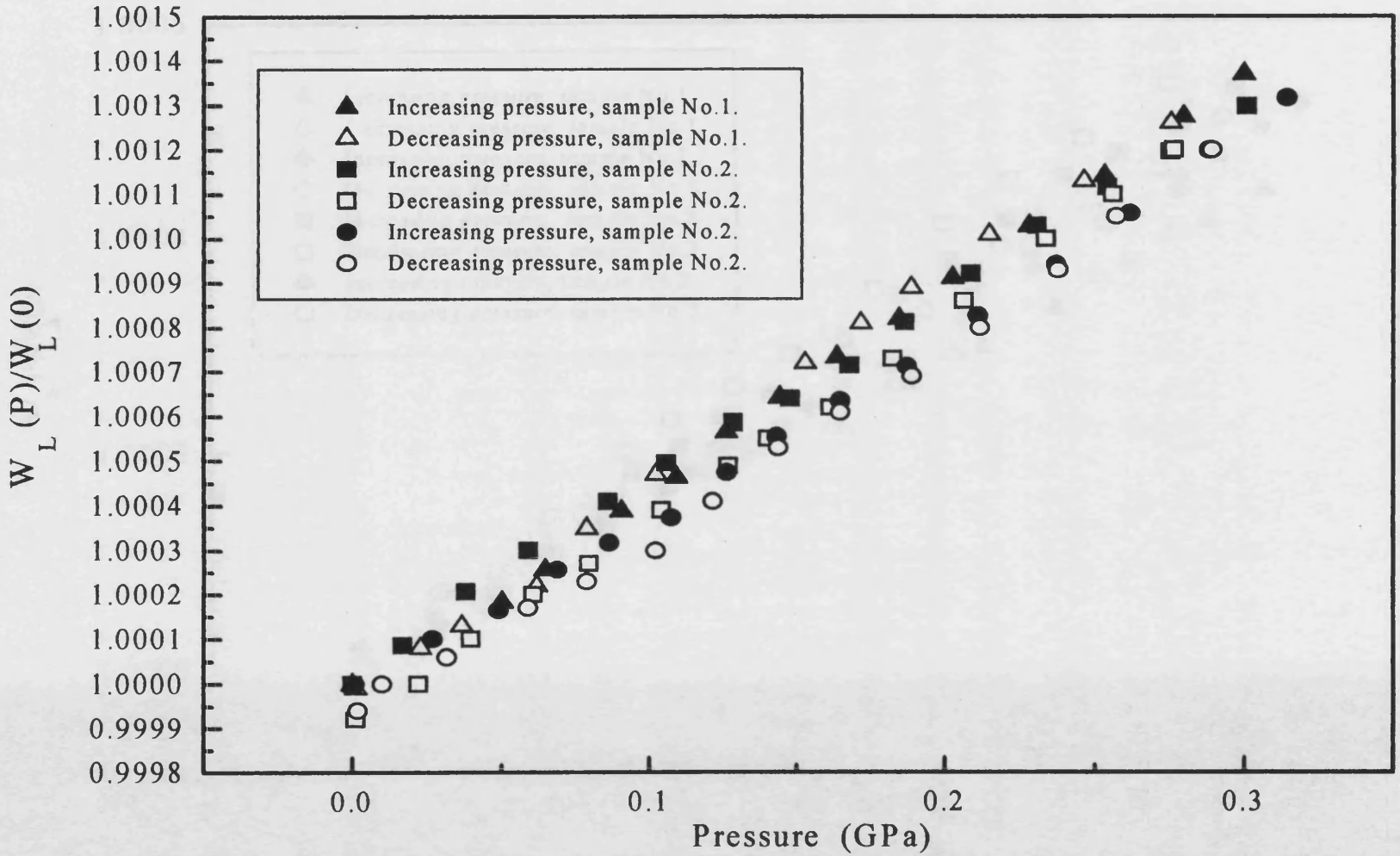

Fig.11.15 The pressure dependence of normalised longitudinal mode natural velocity for the ceramic silicon carbide SiC PAD b at 50 MHz and 30±0.5°C after being subjected to a stress up to 45kN.

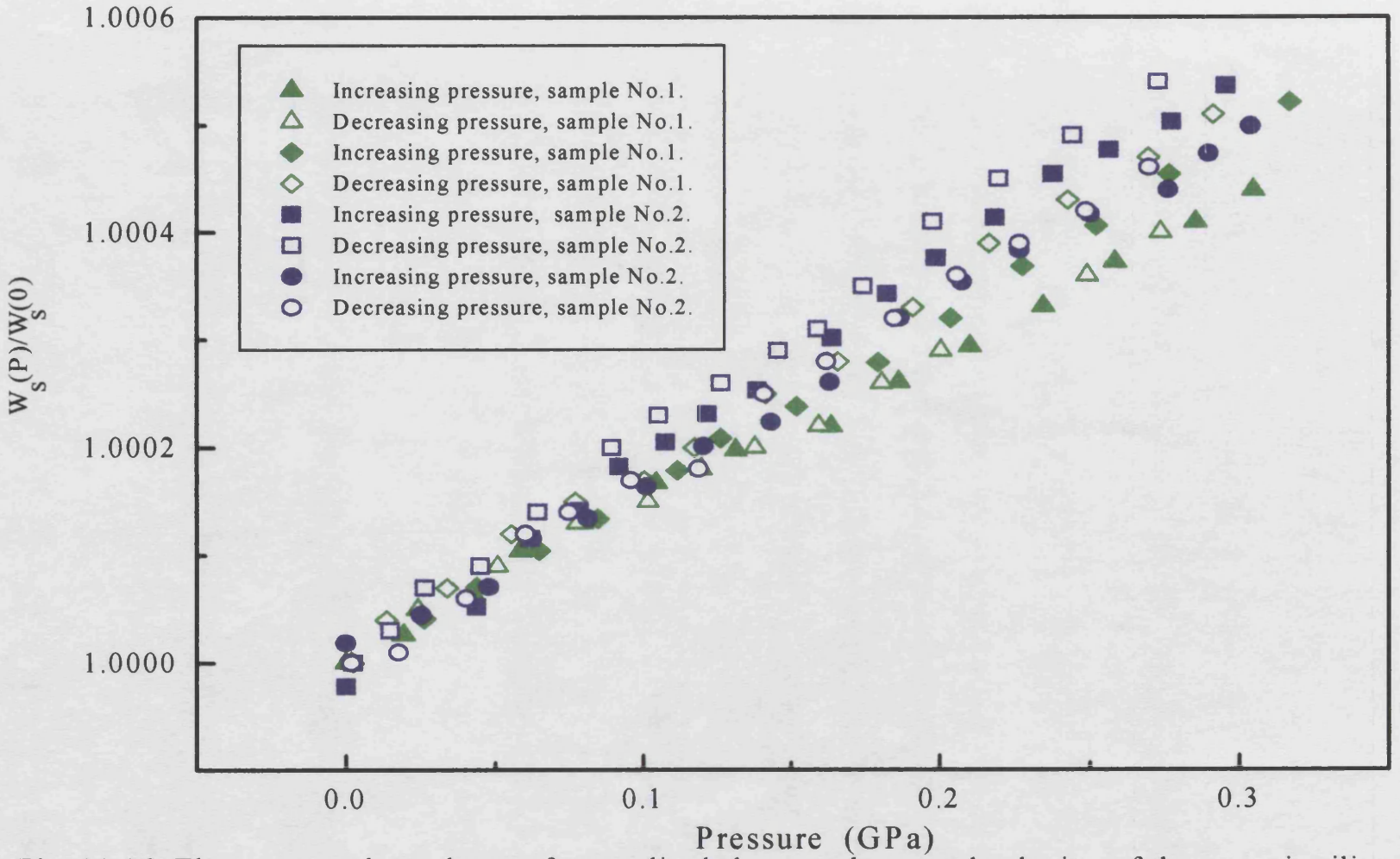

Fig. 11.16 The pressure dependence of normalised shear mode natural velocity of the ceramic silicon carbide SiC PAD b at 50 MHz and 30±0.5 °C after being subjected to a stress up to 45kN.

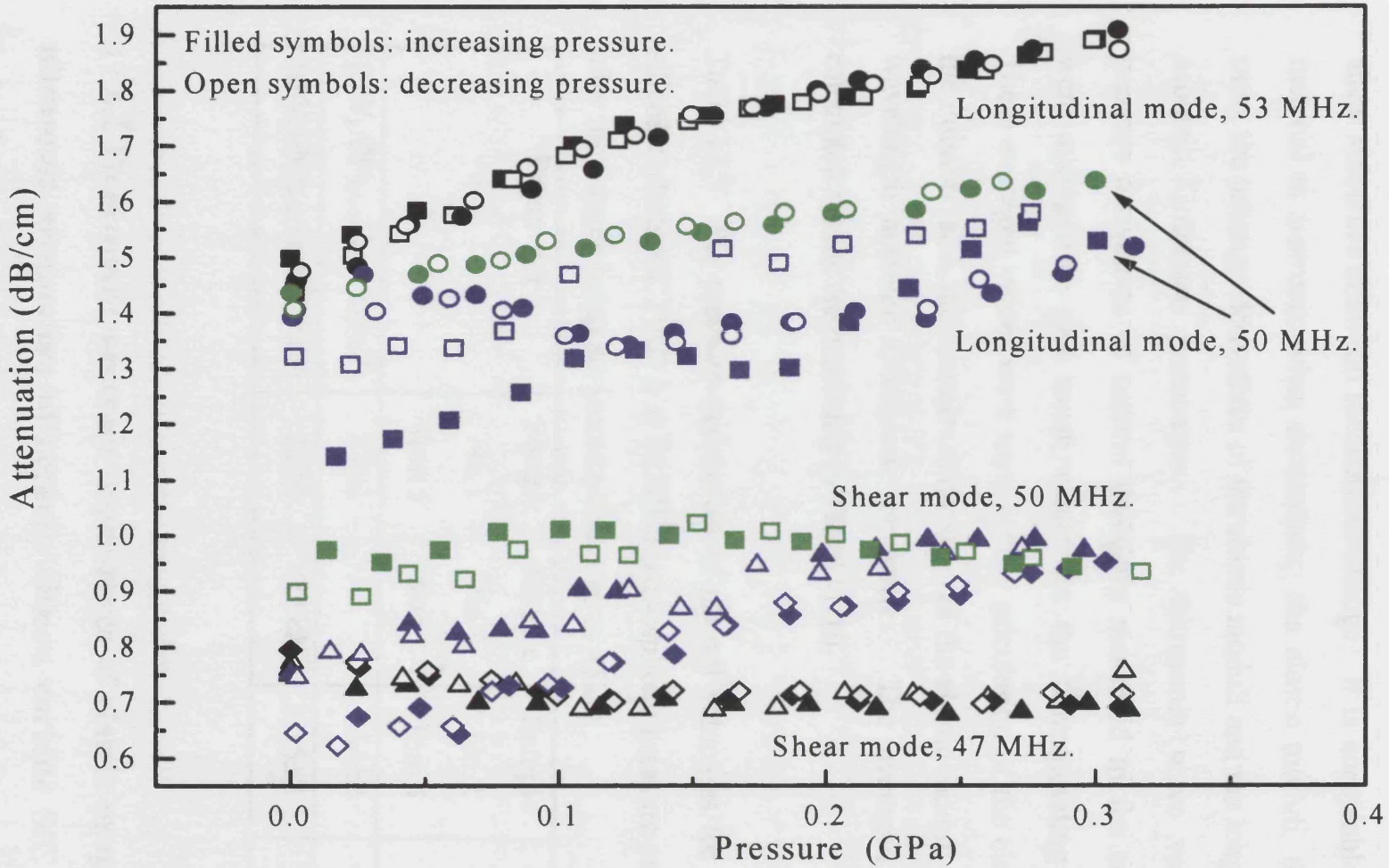

Fig. 11.17 The pressure dependence of attenuation of longitudinal and shear modes ultrasonic wave propagated in the ceramic silicon carbide SiC PAD b at 30±0.5°C before (black symbols) and after (blue and green symbols) being subjected to a stress up to 45kN.

After being subjected to a stress up to 45kN, the longitudinal velocity of sample SiC PAD b increased by 1.7% and the shear velocity showed no significant change; the pressure derivatives of natural longitudinal and shear velocities show no measurable change. It is acceptable to treat the material as isotropic when determining the elastic moduli, the Poisson's ratio, the pressure derivatives of the elastic moduli and the long wavelength acoustic Grüneisen parameters. The ultrasonic wave velocities and pressure derivatives of natural velocities measured in the separate runs were averaged to give mean values for the corresponding parameters. These averaged values were used for the calculation of the elastic moduli, the Poisson ratio, the pressure derivatives of the elastic moduli and the long wavelength acoustic Grüneisen parameters. The averaged values and calculated results are presented in Table 11.10.

Table 11.7 The pressure derivatives of natural velocities for the ceramic silicon carbide SiC PAD b at 50 MHz, atmospheric pressure and 30±0.5°C after the sample being subjected a stress up to 45kN.

Parameter	Sample No.1 Run 1	Sample No.1 Run 2	Sample No.2 Run 1	Sample No.2 Run 2
$(\partial W_L/\partial P)_{P=0}$ ($ms^{-1}GPa^{-1}$)	57±2		54±2	52±2
$(\partial W_S/\partial P)_{P=0}$ ($ms^{-1}GPa^{-1}$)	13±2	11±2	15±2	13±2

11.4.2 Hydrostatic pressure dependence of elastic properties and ultrasonic attenuation of ceramic silicon carbide SiC 100 after being loaded up to 70% of the quasi-static failure load (45kN)

The silicon carbide SiC 100 was loaded at a speed of 0.25kN/s up to 45kN

on the area with a diameter of 4.0 mm (DERA). Fig. 11.18 shows the pressure dependence up to 0.3 GPa of the normalised longitudinal natural velocities of ceramic silicon carbide SiC 100 after being subjected to a stress up to 45kN measured on two samples at 30±0.5°C and 50 MHz plotted together with those of samples SiC 100 and SiC PAD b before being subjected to a stress. Fig. 11.19 presents the pressure dependence of the normalised shear natural velocities measured on two samples in separate runs at 50 MHz and 30±0.5°C plotted together with those of samples SiC 100 and SiC PAD b before being subjected to a stress. The pressure derivatives of natural velocities of ceramic silicon carbide SiC 100 after being subjected to a stress up to 45kN measured on two samples in separate runs at 50 MHz, at atmospheric pressure and at 30±0.5°C are listed in table 11.8. The ultrasonic attenuations of longitudinal and shear mode waves propagated in ceramic silicon carbide SiC 100 before and after being subjected to a stress up to 45kN measured at 50 MHz are plotted together in Fig. 11.20. In Figs. 11. 18-20 the green symbols present the data measured on sample No.1 and the blue symbols present the data measured on sample No.2. From the Figs. 11.18-20 and the table 11.8 it has been found that the data measured from the two samples are consistent with each other within the experiment error range. After being subjected to a stress up to 45kN the longitudinal velocity of sample SiC 100 increased by 0.7%; the shear velocity shows no measurable change; the pressure derivatives of the natural longitudinal and shear velocities changed significantly. The stress load is applied in the uniaxial axis direction of the sample; hence, if the measured parameters have changed after the sample has been subjected to a stress, the material can not be treated as being isotropic. Since the sample is in the shape of a bar, the ultrasonic velocities and the hydrostatic pressure derivatives of the natural velocities can only be

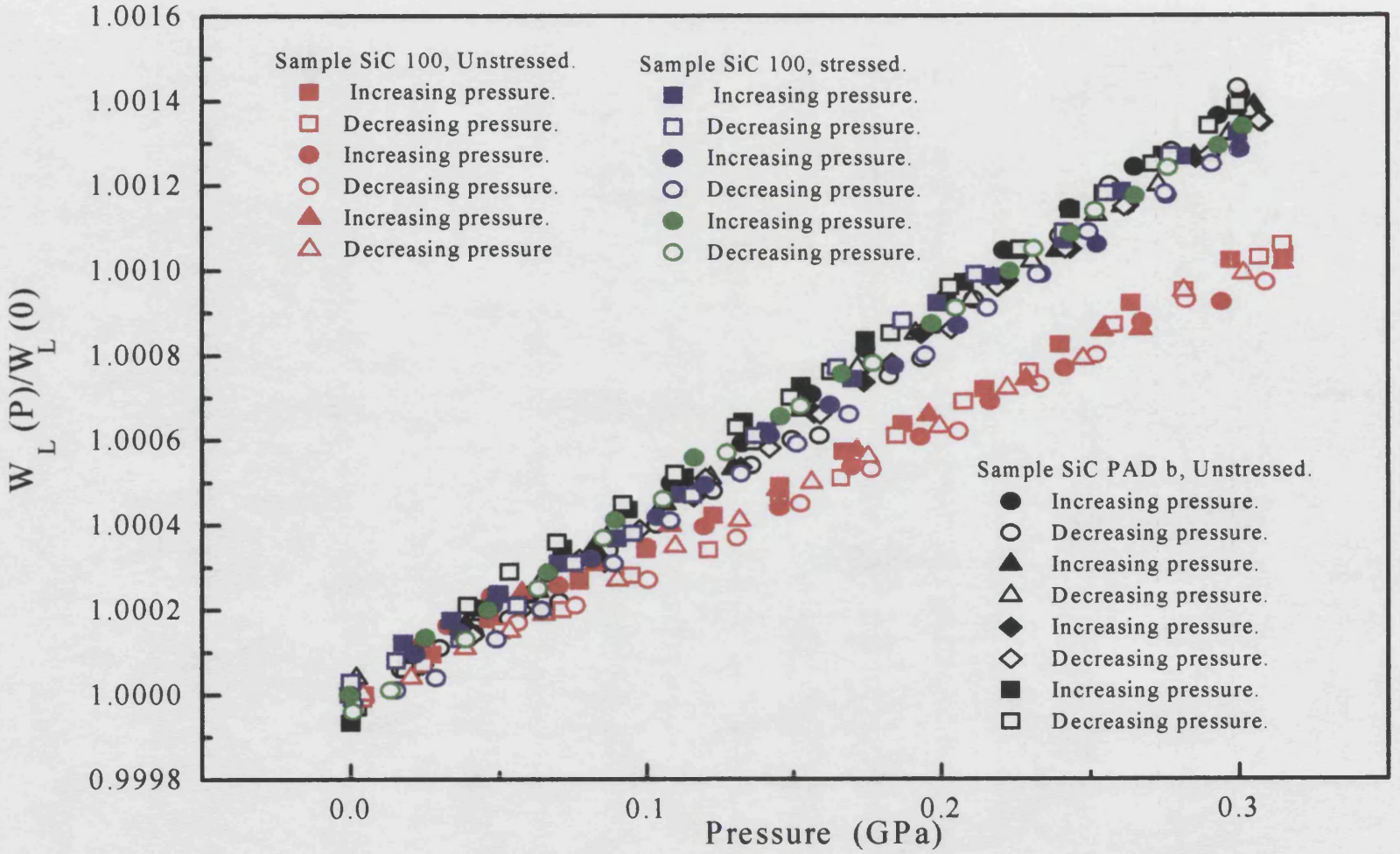

Fig. 11.18 The pressure dependence of normalised longitudinal mode natural velocity for the ceramic silicon carbide SiC 100 at 50 MHz and 30±0.5°C before and after being subject a stress up to 45kN plotted together with those for ceramic silicon carbide SiC PAD b before being stressed.

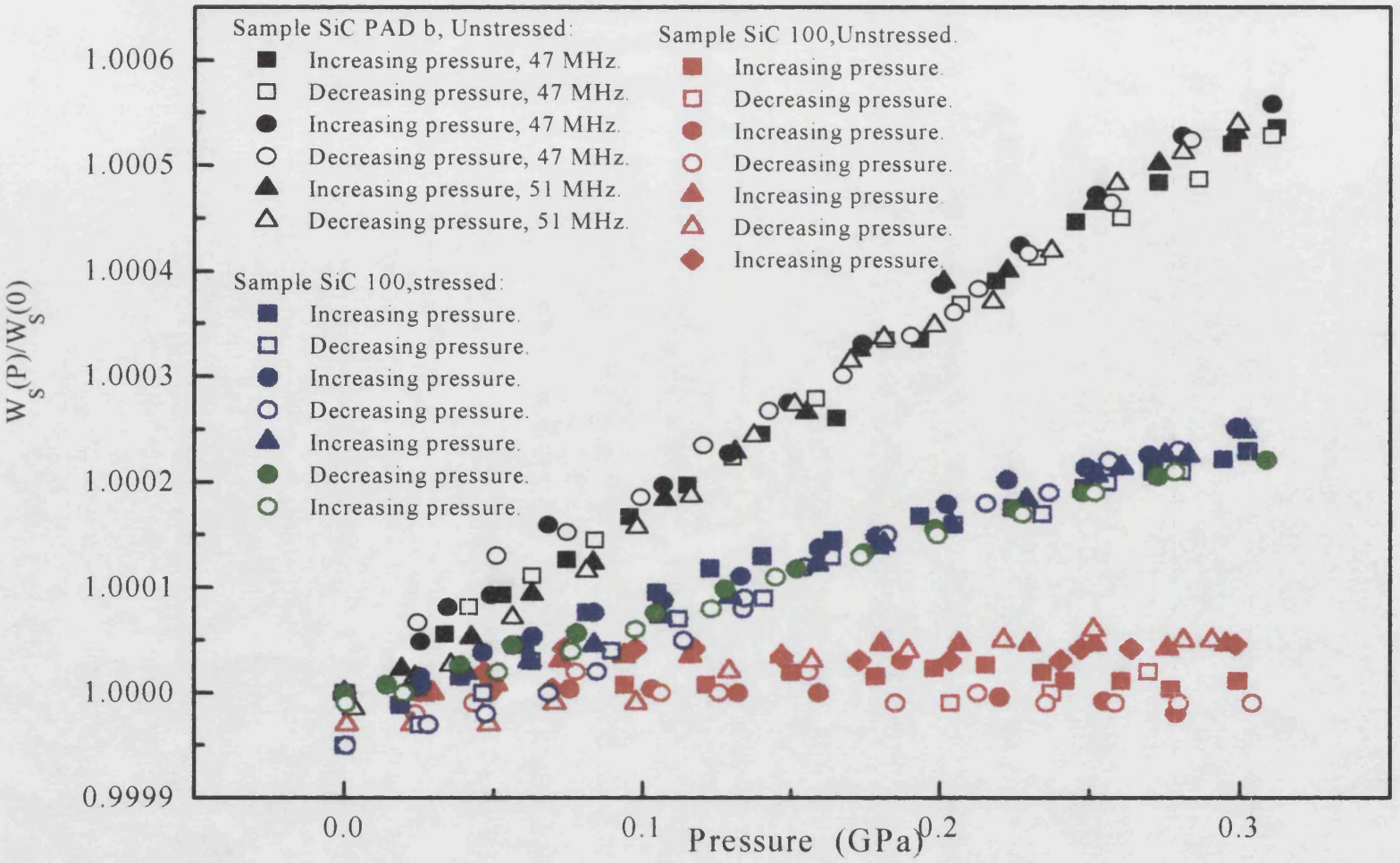

Fig. 11.19 The pressure dependence of normalised shear mode natural velocity for the ceramic silicon carbide SiC 100 at 50 MHz and 30±0.5°C before and after being subject to a stress up to 45kN plotted together with those for ceramic silicon carbide SiC PAD b before being stressed.

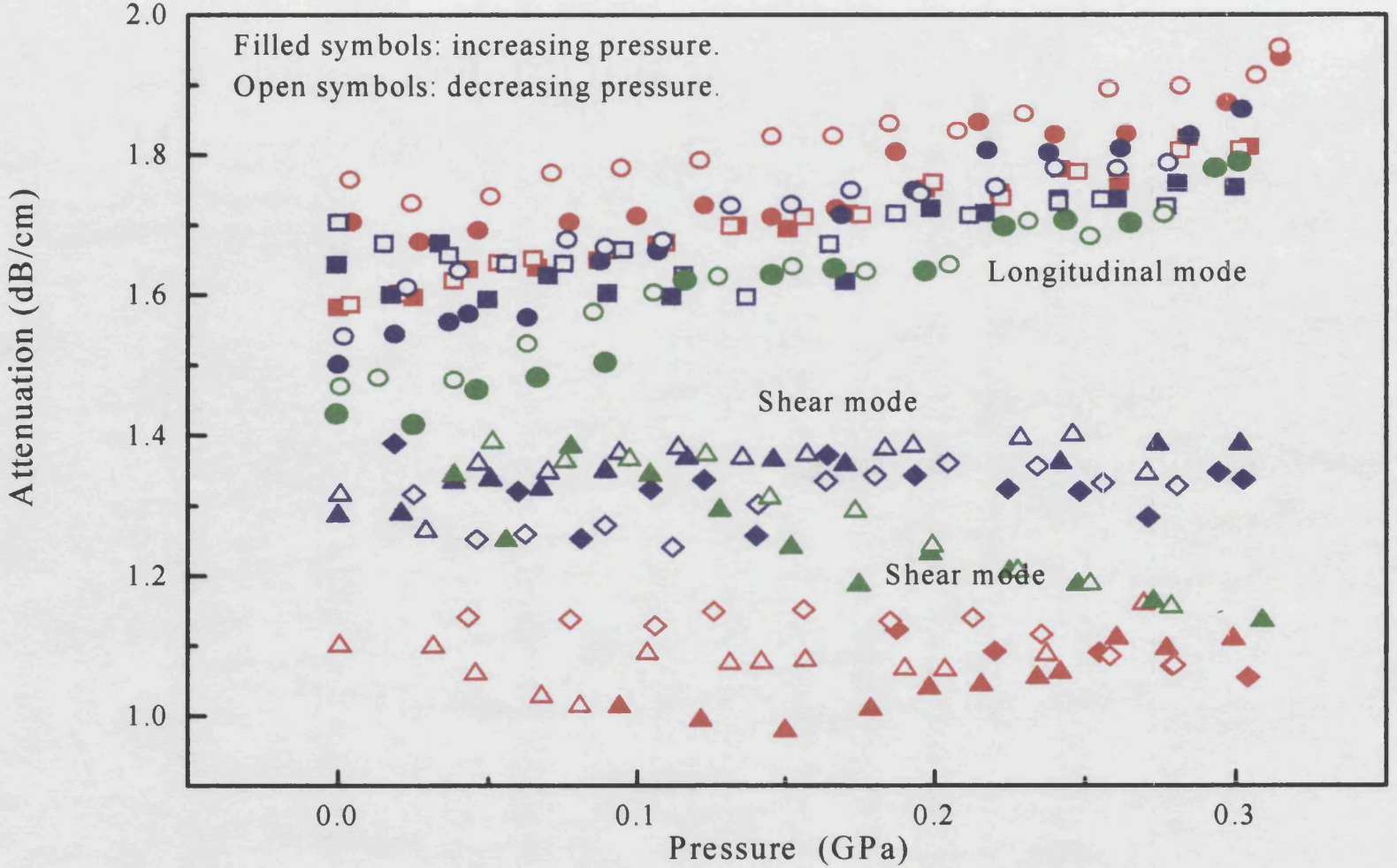

Fig. 11.20 The pressure dependence of attenuation of longitudinal and shear modes ultrasonic wave propagated in the ceramic silicon carbide SiC 100 at 30±0.5°C and 50MHz before (red symbols) and after (blue and green symbols) being subject a stress up to 45kN.

measured in the direction of the uniaxial axis. Therefore, no values of elastic moduli, the Poisson ratio, pressure derivatives of the elastic moduli and the long wavelength acoustic mode Grüneisen parameters γ can be calculated.

Table 11.8 The pressure derivatives of natural velocities for the ceramic silicon carbide SiC 100 at 50 MHz, atmospheric pressure and 30±0.5°C after the sample being subjected a stress up to 45kN.

Parameter	Sample No.1 Run 1	Sample No.2 Run 1	Sample No.2 Run 2	Sample No.2 Run 3
$(\partial W_L/\partial P)_{P=0}$ ($ms^{-1}GPa^{-1}$)	54±2	53±2	54±2	
$(\partial W_S/\partial P)_{P=0}$ ($ms^{-1}GPa^{-1}$)	6±2	7±2	7±2	7±2

11.4.3 Hydrostatic pressure dependence of elastic properties and ultrasonic attenuation of ceramic alumina SINTOX FA after being loaded up to 70% of the quasi-static failure load (65kN)

The ceramic alumina SINTOX FA was loaded at a speed of 0.25kN/s up to 65kN on the area with a diameter of 6.0 mm (the data from DERA). Fig. 11.21 shows the pressure dependence up to 0.3 GPa of the normalised longitudinal natural velocities of ceramic alumina SINTOX FA after being subjected to a stress up to 65kN measured at 30±0.5°C and 28MHz plotted together with those of ceramic alumina SINTOX FA before being subjected to a stress. Fig. 11.22 presents the pressure dependence of the normalised shear natural velocities measured in two separate runs at 30 MHz and 30±0.5°C plotted together with those of ceramic alumina SINTOX FA before being subjected to a stress. The pressure derivatives of natural velocities of ceramic alumina SINTOX FA after being subjected

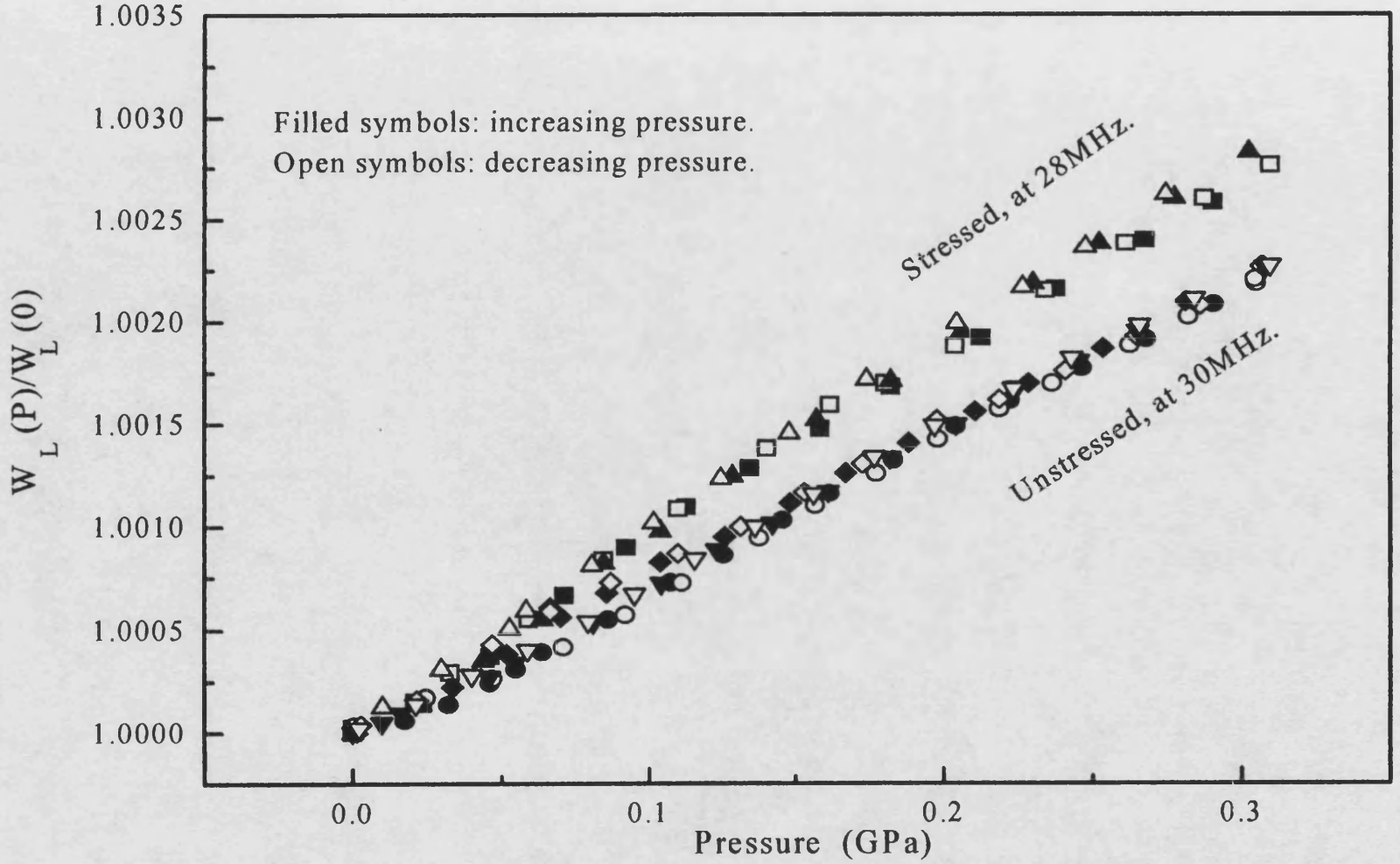

Fig.11.21 The pressure dependence of normalised longitudinal mode natural velocity for the ceramic alumina SINTOX FA at 30±0.5°C before and after being subject a stress up to 65kN.

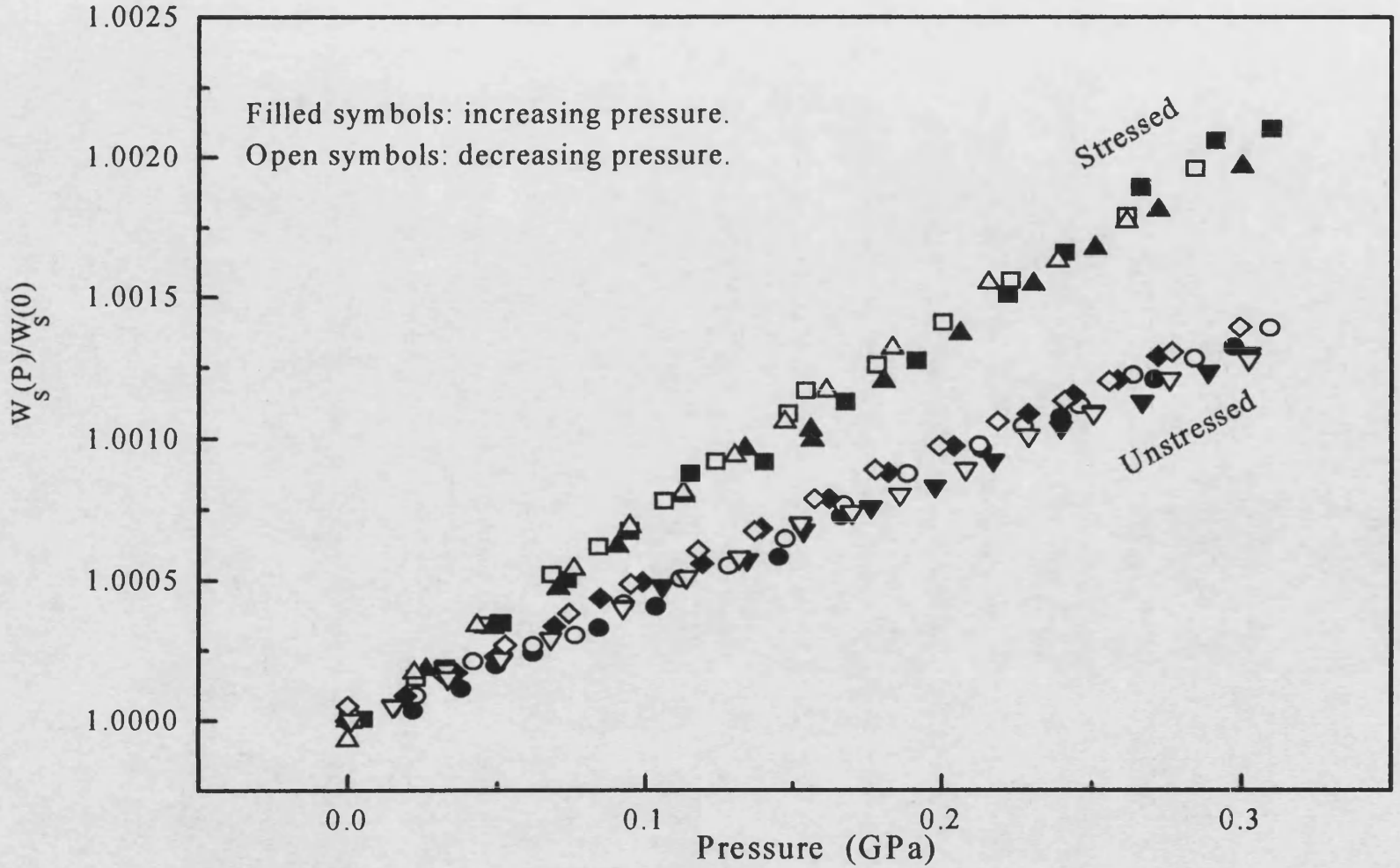

Fig. 11.22 The pressure dependence of normalised shear mode natural velocity of the ceramic alumina SINTOX FA at 30 MHz and 3±0.5 °C before and after being subject a stress up to 65kN.

to a stress up to 65kN measured in separate runs near 30MHz, at atmospheric pressure and at 30±0.5°C are listed in table 11.9. The ultrasonic attenuations of longitudinal and shear mode waves propagated in ceramic alumina SINTOX FA after being subjected to a stress up to 65kN are plotted together with those of ceramic alumina SINTOX FA in unstressed state in Figs. 11.23 and 11.24 respectively.

Due to the same reason as described in section 11.4.2, no values of elastic moduli, the Poisson ratio, pressure derivatives of the elastic moduli and the long wavelength acoustic mode Grüneisen parameters γ can be calculated.

Table 11.9 The pressure derivatives of natural velocities for the ceramic alumina SINTOX FA at atmospheric pressure, 30±0.5°C and near 30MHz and after the sample being subjected a stress up to 65kN.

Parameter	Run 1	Run 2
$(\partial W_L/\partial P)_{P=0}$ ($ms^{-1}GPa^{-1}$)	89±2	93±2
$(\partial W_S/\partial P)_{P=0}$ ($ms^{-1}GPa^{-1}$)	40±2	39±2

11.4.4 Conclusions

From the results shown in Figs.11.23 and 24 has been found that after the sample has been loaded up to 70% of the quasi-static failure load (65kN), the ultrasonic attenuation of ceramic alumina SINTOX FA is about 2.8 times for longitudinal mode wave and 3.8 times for shear mode wave as large as that of the unloaded sample. The results presented in Figs.11.23 and 24 also show that both the longitudinal and shear wave attenuation and the value of its pressure derivative decrease with increasing pressure. The above facts suggest that the quasi-static load process have introduced

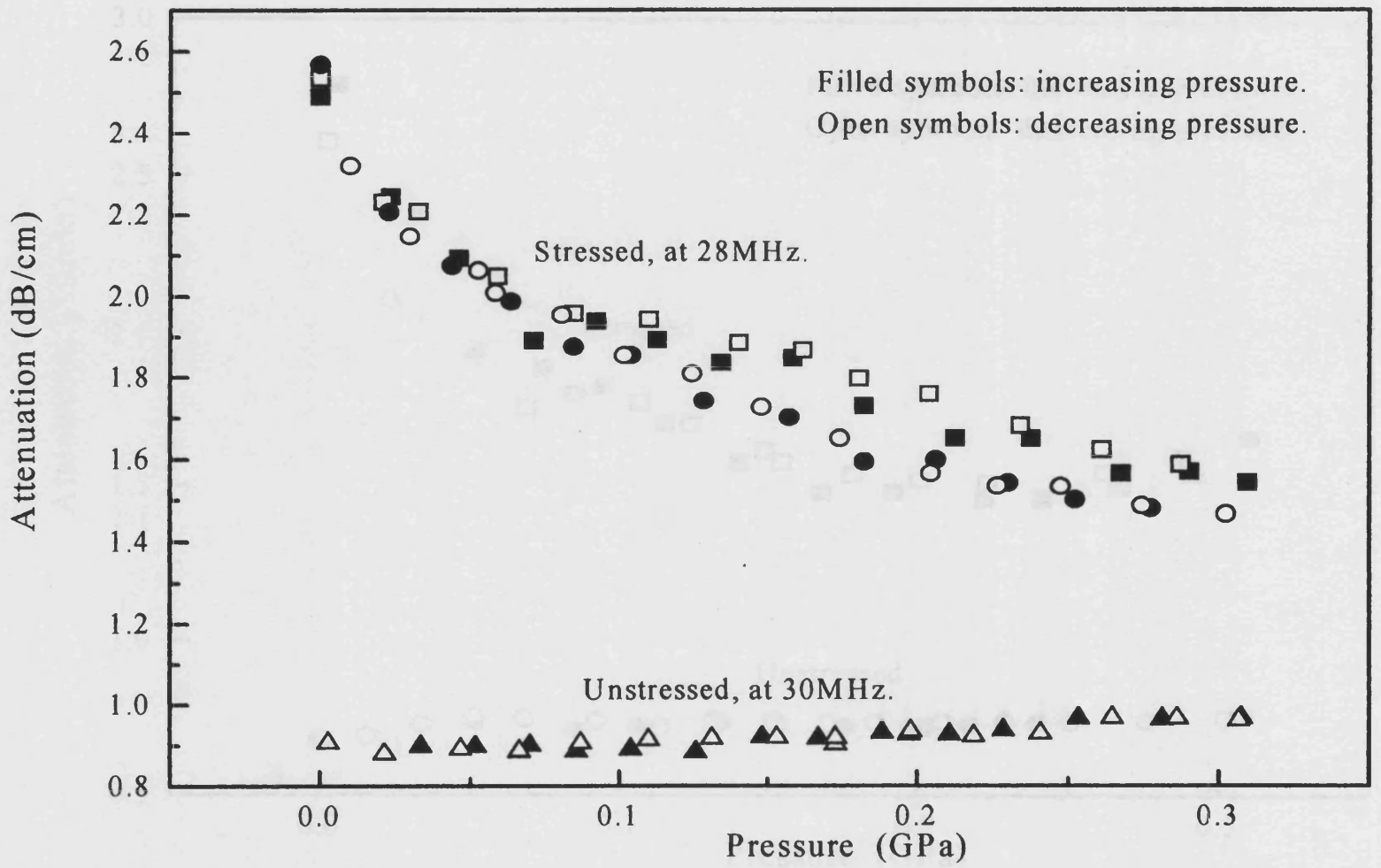

Fig. 11.23 The pressure dependence of attenuation of longitudinal mode ultrasonic wave in the ceramic alumina SINTOX FA at 30±0.5°C before and after being subject a stress up to 65kN.

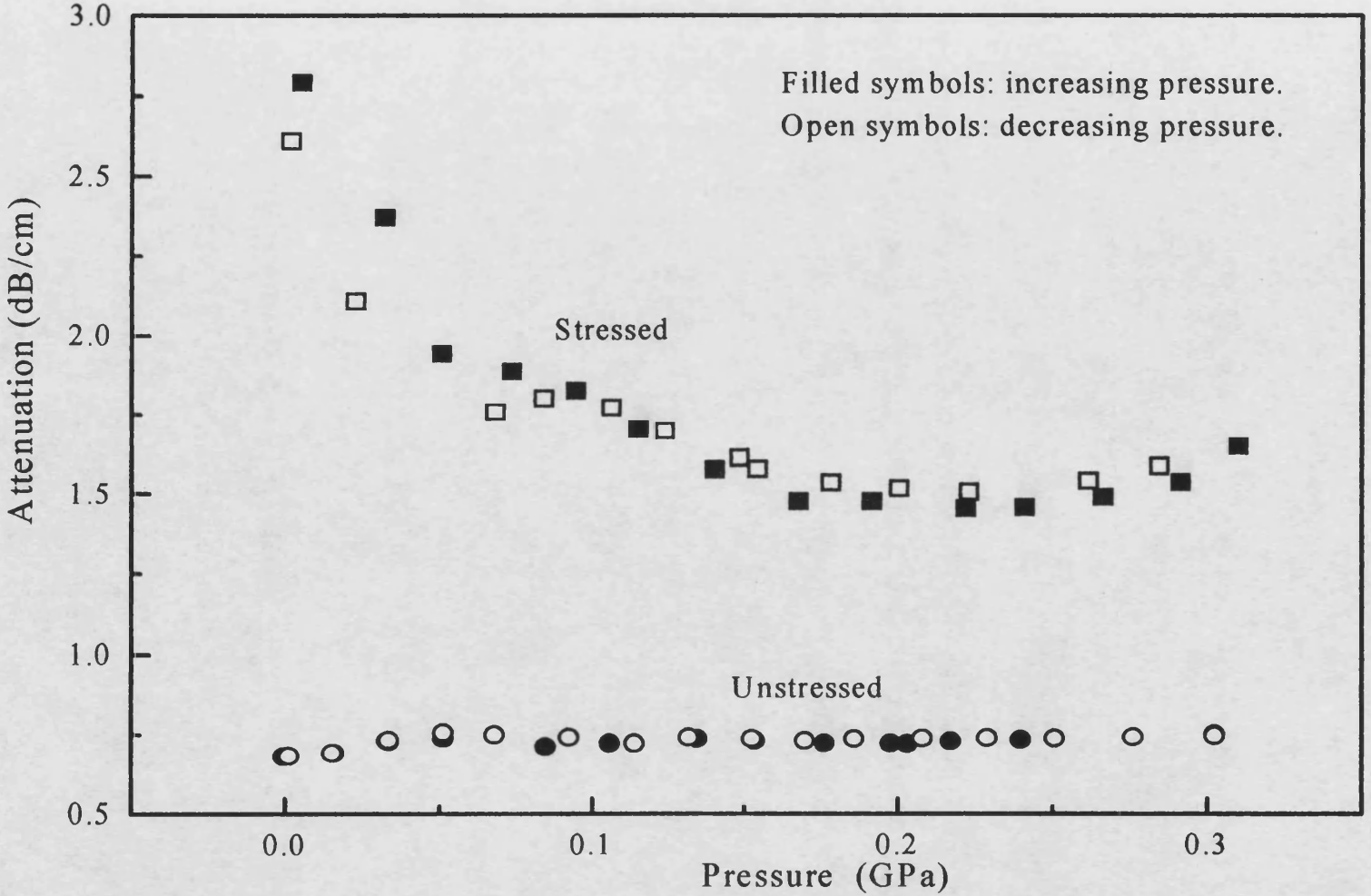

Fig.11.24 The pressure dependence of attenuation of shear modes ultrasonic wave in the ceramic alumina SINTOX FA at 30MHz and 30±0.5°C before and after being subject a stress up to 65kN.

cracks which remain open after quasi-static load have been removed and that the ratio of size (d) of the cracks to the ultrasonic wavelength (λ) is around 0.1, i.e. $d/\lambda \approx 0.1$ (Goebbel et al. 1984). In this case the backscattering amplitude and the d/λ dependence of the backscattering amplitude are large (Goebbel ect. 1984). Therefore decreasing the crack size due to crack closing with increasing pressure causes a large decrease of ultrasonic attenuation especially in the lower pressure range (Figs. 11.23 and 24). The ultrasonic wave frequency used for this sample was 30 MHz with a wavelength of 330 μm for longitudinal mode. It can be concluded that the size of a lot of cracks which were introduced by the quasi-static load is above about 30 μm (0.1λ).

The results presented in Figs.11.17 and 20 show that after being loaded up to 70% of the quasi-static failure load (45kN) no significant increase of the ultrasonic attenuations of ceramic silicon carbides SiC PAD b and SiC 100 has occurred and that the attenuations did not decrease with increase of the pressure markedly. It has been concluded that the quasi-static load process did not introduce a significant number of cracks which did not close after removing the load and have a size (d) comparable with the wave length (λ) used. The ultrasonic wave frequency used on this sample was 50MHz and the wavelength of the shear mode wave is 156μm in sample SiC PAD b and 151μm in sample SiC 100. The conclusion is that there are not a significant number of cracks, which have a size above 15μm (0.1λ), introduced by the sample being loaded up to 70% of the quasi-static failure load (45kN).

After ceramic silicon carbides SiC PAD b and SiC 100 have been loaded up to 70% of the quasi-static failure load (45kN), their ultrasonic

longitudinal mode velocities increased only by 1.6% and 0.7% respectively. These measured longitudinal mode velocity changes are small. The carrier frequency used was 50MHz. It was quite difficult to overlap the echoes. Therefore there is a possibility that the measured longitudinal mode velocity increase could be due to the misoverlap of the echoes. Hence, there is no significant change found in the ultrasonic velocities after the two samples have been loaded.

After ceramic alumina SINTOX FA has been loaded up to 70% of the quasi-static failure load, there is no measurable change found in the ultrasonic velocities.

After ceramic alumina SINTOX FA and ceramic silicon carbide SiC 100 have been loaded up to 70% of the quasi-static failure load, the pressure derivatives of the longitudinal and shear natural velocities are markedly increased. It has been concluded that after being loaded up to 70% of the quasi-static failure load, ceramic alumina SINTOX FA and ceramic silicon carbide SiC 100 are more difficult to compress. The detailed explanation of this phenomenon needs further investigation of changes in the microstructure of the materials, which is outside the scope of this project.

Table 11.10 The density, ultrasonic wave velocities V, elastic moduli, pressure derivatives of natural velocities, pressure derivatives of the elastic moduli and the long wavelength acoustic mode Grüneisen parameters γ of ceramic silicon carbides SiC PAD b and SiC 100 and ceramic alumina SINTOX FA at 30±0.5°C before and after the samples were loaded up to 70% of the quasi-static failure load. σ is the Poisson ratio. W is the natural velocity.

Sample	SiC PAD b (Unstressed)	SiC PAD b No.1 (Stressed)	SiC PAD b No.2 (Stressed)	SiC 100 (Unstressed)
ρ (kg/m^3)	3212±1			3163[(a)]
V_S (m/s)	7804±10	7801±10	7799±10	7587±10
V_L (m/s)	12016±10	12216±10	12215±10	11830±10
C_{11} (GPa)	463.8±0.8		479.3±0.8	442.7±0.8
C_{44} (GPa)	195.6±0.5		195.4±0.5	182.1±0.5
B^S (GPa)	203±1		219±1	200±1
E (GPa)	444±3		452±3	419±3
σ	0.135±0.002		0.156±0.002	0.15±0.002
$(\partial W_L/\partial P)_{P=0}$ (ms^{-1}GPa^{-1})	56±2	57±2	53±2	38±2
$(\partial W_S/\partial P)_{P=0}$ (ms^{-1}GPa^{-1})	14±2	12±2	14±2	1±2
$(\partial C_{11}/\partial P)_{P=0}$	5.0±0.2		4.9±0.2	3.6±0.2
$(\partial C_{44}/\partial P)_{P=0}$	1.0±0.1		1.0±0.1	0.4±0.1
$(\partial B^S/\partial P)_{P=0}$	3.7±0.2		3.6±0.2	3.1±0.2
γ_L	0.94±0.03		0.95±0.03	0.64±0.03
γ_S	0.37±0.05		0.39±0.05	0.03±0.05
γ^{el}	0.56±0.04		0.58±0.04	0.23±0.04

(a) Value supplied by DERA

Sample	SiC 100 No.1 (stressed)	SiC 100 No.2 (stressed)	SINTOX FA (Unstressed)	SINTOX FA (Stressed)
ρ (kg/m^3)			3716±1	
V_S (m/s)	7625±10	7610±10	5806±10	5807±10
V_L (m/s)	11912±10	11964±10	9806±10	9800±10
C_{11} (GPa)			357±0.7	
C_{44} (GPa)			125±0.4	
B^S (GPa)			190±1	
E (GPa)			308±2	
σ			0.230±0.002	
$(\partial W_L/\partial P)_{P=0}$ (ms^{-1}GPa^{-1})	54±2	54±2	72±2	91±2
$(\partial W_S/\partial P)_{P=0}$ (ms^{-1}GPa^{-1})	6±2	7±2	26±2	40±2
$(\partial C_{11}/\partial P)_{P=0}$			5.9±0.2	
$(\partial C_{44}/\partial P)_{P=0}$			1.4±0.1	
$(\partial B^S/\partial P)_{P=0}$			4.1±0.2	
γ_L			1.40±0.04	
γ_S			0.86±0.07	
γ^{el}			1.04±0.05	

Chapter 12 Conclusions

Six ceramic aluminas and two ceramic silicon carbides, made by different manufacturing processes, have been characterised using the X-ray diffraction experiments, scanning electron microscopy, the impedance spectra and the measurements of ultrasonic wave velocities and attenuation and their hydrostatic pressure dependence. The conclusions can be summarised as follows:

1. From the X-ray diffraction experiments it has been found that ceramic aluminas D975 and H880 and SINTOX FA are textured to some extent. The c-axes of α-Al_2O_3 grains are preferentially aligned along a uniaxial axis of ceramic aluminas D975, H880 and SINTOX FA. These materials can be considered to have cylindrical symmetry on a macroscopic scale. It is believed that this uniaxial symmetry axis is induced along the unipressed direction during the fabrication process.

2. By contrast no observable texture of grains has been found in the ceramic aluminas D999 and AL23 and ceramic silicon carbide SIC PAD b from the X-ray diffraction spectra results.

3. From the X-ray diffraction spectra results, it has also been found that sample D975 has at least two crystalline secondary phases. One of them is spinel ($MgAl_2O_4$). The ceramic aluminas AL23, D999 and H880 and SINC53 have at least one crystalline secondary phase.

4. From the X-ray diffraction spectra it has been found that the main phase of ceramic silicon carbide SiC PAD b is silicon carbide 6H and the second phase silicon carbide 15R is just detectable. It is also concluded that there

is at least one unknown crystalline phase in ceramic silicon carbide SiC PAD b.

5. The scanning electron microscopy results show that both the ceramic aluminas D999 and AL23 have equi-axed grains, and the microstructures of the ceramic aluminas D999 and AL23 are isotropic while grains, or some of the grains, of ceramic aluminas D975, H880 and SINC53 are platelet-like with their basal plane preferentially oriented perpendicular to the Z direction.

6. From the measured data of propagation and polarisation directional dependence of longitudinal and shear mode ultrasonic wave velocities in ceramic aluminas D975, H880, AL23, D999, SINC53 and SINTOX FA it has been found that samples D975, H880 SINC53 and SINTOX FA are anisotropic in some degree, while sample D999 and AL23 are isotropic. The velocity principal axes of ceramic aluminas D975, H880, SINC53 and SINTOX FA are normal to the sample surface of the cubic samples. All samples have cylindrical symmetry and have the same uniaxial symmetry as that found from X-ray diffraction spectra results.

7. Along the Z axes of the ceramic aluminas D975, H880, SINC53 and SINTOX FA the longitudinal velocities have smaller values than those in the X and Y directions. These differences could be due to the fact that the total thickness of the grain boundary phase in Z direction is larger than that in the X or Y direction.

8. The hydrostatic pressure dependence of the ultrasonic wave velocities and attenuation in the ceramic alumina samples D999, D975, H880, AL23, SINC53 and SINTOX FA and ceramic silicon carbide samples SiC PAD b

and SiC 100 have been measured at room temperature up to 3.0~0.35 GPa. From the measured data the elastic moduli, the Poisson ratio, the pressure derivatives of the elastic moduli and the long wavelength acoustic Grüneisen parameters have been determined. It has been concluded that the data of the elastic moduli, the Poisson ratio, the pressure derivatives of the elastic moduli and the long wavelength acoustic Grüneisen parameters of ceramic alumina D999 reflect the nature of the α-alumina grains in sample D999.

9. To obtain information about the behaviour of these ceramics up to very high pressure, the volume compression of ceramic alumina samples D999, D975, H880, AL23, SINC53 and SINTOX FA and ceramic silicon carbide samples SiC PAD b and SiC 100 has been extrapolated up to a pressure of 20 GPa using the bulk modulus B^S, its pressure derivative $(\partial B^S/\partial P)_{P=0}$ and Murnaghan's equation-of-state.

10. The microstructure of ceramic aluminas AL23 and D999 has been analysed by using the "brick model", which gives an approximate estimation of 1% and 5% for the ratio of grain boundary thickness to grain size of Ceramic aluminas AL23 and D999 respectively.

11. The activation energies for resistances of bulk and grain boundary of ceramic alumina D999 and AL23 are determined by Arrhenius plots.

12. Between 17°C and 170°C in the frequency range of 10^2 Hz to 10^6 Hz and between 170K and 320K in the frequency range of 10^3 Hz to 10^6 Hz, the dielectric constant of ceramic alumina D999 increases with temperature linearly and has a small frequency dependence. The temperature coefficients of the dielectric constant $(\partial\varepsilon'/\partial T)$ at 10^5 Hz are

$(1.39\pm0.02)\times10^{-3}$/K between 17°C and 170°C and $(1.09\pm0.01)\times10^{-3}$/K between 170K and 320K.

13. A Maxwell-Wagner effect with an average activation energy of 1.30 ±0.01eV has been found in ceramic alumina D999 between 280°C and 520°C and in the frequency range of 5Hz to 10^6Hz.

14. A dipolar relaxation process with a distributed relaxation time and an average activation energy of 0.060±0.002eV has been found in ceramic alumina D999 between 50K and 160K and in the frequency range of 10^3Hz to 10^6Hz.

15. A Maxwell-Wagner effect with an average activation energy of 1.9±0.1eV has been found in ceramic alumina AL23 between 500°C and 704°C and in the frequency range of 5Hz to 10^6Hz.

16. In the temperature range 20K to 320K two dipolar relaxation processes have been found in the ceramic alumina AL23. One of them has a distributed relaxation time; an average activation energy of 0.4 ±0.01eV was found between 210K and 320K in the frequency range of 10^3Hz to 10^6Hz. The second dipolar relaxation process was in the frequency range of 10^3Hz to 10^6Hz between 20K and 200K.

17. In the temperature range of 200K and 320K the dielectric constant of ceramic alumina D975 increases linearly with the temperature with a temperature coefficient $(\partial\varepsilon'/\partial T)$ of $(1.19\pm0.02)\times10^{-3}$/K at 10^5 Hz.

18. In the temperature range of 200K and 320K the dielectric constant of ceramic alumina H880 increases linearly with the temperature with a temperature coefficient ($\partial\varepsilon'/\partial T$) of $(1.24\pm0.02)\times10^{-3}$/K at 10^5 Hz.

19. After ceramic alumina SINTOX FA has been loaded up to 70% of the quasi-static failure load (65kN), cracks have been introduced; the size of many of those cracks is above about 30μm ($\lambda/10$).

20. For the ceramic silicon carbides SiC PAD B and SiC 100, loading by a quasi-static load process up to 70% of the quasi-static failure load (45kN), did not introduce a significant number of cracks which are in a size range above 15μm and which did not close after removing the load.

21. After ceramic alumina SINTOX FA has been loaded up to 70% of the quasi-static failure load, there is no measurable change found in the ultrasonic velocities.

22. After ceramic silicon carbides SiC PAD B and SiC 100 have been loaded up to 70% of the quasi-static failure load, there is no significant change found in the ultrasonic velocities.

23. It has been concluded that after being loaded up to 70% of the quasi-static failure load the ceramic alumina SINTOX FA and ceramic silicon carbide SiC 100 become more difficult to compress.

REFERENCES

Akatsu T., Tanabe Y. and Yasuda E., J. Mater. Res. **9**, 207 (1994).

Anderson J. C., "Dielectrics", (Chapman and Hall LTD, 1964).

Anderson O. L., J. Phys. Chem. Solids **27**, 547 (1966).

Atlas L. M., Nagao H. and Nakamura H. H., J. Am. Ceram. Soc. **45**, 464 (1962).

Baaklini G. Y. and Abel P. B., Materials Evaluation, **46** , 1477 (1988).

Bateman P. C., J. Acoust. Soc. Am., **41** 1011 (1966).

Benson, R. W. & Raelson, V. J., Acoustoelasticity. Product. Engng, **30**, 56 (1959).

Bergmann, R. M. & Shahbender, R. A., J. Appl. Phys., **29**, 1736 (1958).

Born M. and Oppenheimer J., Ann. Phys. **84**, 457 (1927).

Brugger K., Phys, Rev. **137**, A1826 (1965).

Brugger K. and Fritz T. C., Phys. Rev. **157**, 524 (1967).

Brüesch P., "Phonons: Theory and Experiments I: Lattice Dynamics and Methods of Interatomic Forces" (Springer-Verlag, Berlin, 1982).

Cahn R. W, Haasen P, and Kramer E. J., " Material Science and Technlogy Volume 2A: Characterization of Materials Part I", (Weinheim, 1992).

Carisey T., Levin I and Brandon D. G., J. European Ceramic Society, **15**, 283 (1995).

Chang F. "Dielectric and Ultrasonic Studies of Polyethylene Plaques and Cable Insulators", Thesis, Department of Physics, University of Bath, 1996.

Chung [a] D. H. and Simmons G., J. Appl. Phys. **39**, 5316 (1968).

Chung [b] D. H. and Buessem W. R, J. Appl. Phys. **39**, 2777 (1968).

Cullity B. D., "Elements of X-ray Diffraction", (Addison-Wesley Publishing Company, Inc., 1978), P.283.

Debye P., "Polar Molecules", (Chemical Catalogue Company, New York, 1929), P. 94.

Debye P., "Polar Molecules", (Dover, New York, 1945).

Dove M.T., "Introduction to Lattice Dynamics", (Cambridge University Press, Cambridge, 1993)

Dörre E. and Übner H., "Alumina Processing, Properties and Applications" (Springer, Berlin,1984)

Farley J. M, Ph.D. Thesis, Department of Applied physics and Electronics, University of Durham, 1973.

Goebbels K., Hirsekorn S. and Willems H., Ultrasonics Symposium, 841, (1984).

Goebbels K., "Proceedings of the 2nd European Symposium on Engineering Ceramics", edited by F. L. Riley (Elsevier Applied Science, London, 1988).

Harrop P. J., "Dielectrics" (Butterworth and Co (publishes) Ltd, London, 1972).

Hankey R. E. and Schuele D. E., J. Acoust. Soc. Am. **48**, 190 (1969).

James B. J., Phys. Rev. B **45**, 10242 (1992).

Jepps N. W. and Page T. F., Progr. Cryst. Growth Charact. **7**, 259 (1983).

Jonscher A. K., "Dielectric relaxation in solids" (Chelsea Dielectrics Press Ltd, London, 1983)

Karmo R. and Bryzik W., Ceram. Eng. Sci. Proc. 5, 312 (1984).

Kingery, W.D., Bowen, H. K., Uhlmann, D. R., " Introduction to ceramics, 2nd ed. New York, Jone Wiley and Sons (1976).

Kröger F. A., "Electrical Properties of α-Al_2O_3", in "Structure and Properties of MgO and Al2O3 Ceramics", ed. Kingery W. D., **10**, 1, (The American Ceramic Society, Inc. Columbus, Ohio, 1984)

Kittinger E., Ultrasonics **15**, 30 (1977).

Kronberg M.L., Acta Metal., **5**, 507(1957).

Leibfried G. and Ludwig W., Solid State Physics, **12**, 276 (1961)

Mason W. P., "Physical Acoustics and the Properties of Solids" (D. Van Nostrand Company, Inc., Princeton, 1958).

Macdonald J. R., editor, "Impedance Spectroscopy: Emphasizing Solid Materials and Systems" (John Wiley and Sons, New York, 1987).

Maxwell J. C., "Treatise on Electricity and Magnetism", 3rd Edition, (Dover Publication, New York, 1954).

McSkimin H. J. and Andreatch P. Jr., J. Acoust. Soc. Am. **34**, 609 (1962).

Morrell R., "Handbook of Properties of Technical and Engineering Ceramics, Part 2 Data Reviews, Section 1 High-Alumina ceramics" (HMSO Publications Centre, London, 1987).

Murnaghan F. D., Proc. Nat. Acad. Sci. USA **30**, 244 (1944).

Newman W. T., Am. Mineralogist **29**, 249 and 327 (1944).

Nye J. F., "Physical Properties of Crystals, their representation by tensors and matrices " (Clarendon press, Oxford, 1985)

Phillips, D. S., Mitchell, T. E., Heuer, A. H., "Precipitation in the star sapphire III. Chemical effects accompanying precipitation.", Phil. Mag. A, **42**, 417 (1980).

Pollard, H.F., "Sound waves in solids", (Poin Limited, London, 1977)

Powell-Dogan C. A. and Heuer A. H., J. Am. Ceram. Soc. **73**, 3670 (1990).

Ramdsdell L.S., Am. Mineral., **32**, 64 (1947).

Schneider E., Opt. Lasers Eng. **22**, 305 (1995).

Schreiber E. and Anderson O. L., J. Am. Ceram. Soc. **49**, 184 (1966).

Shaffer P. T. B, Acta Crystallographica, **B25**, 477 (1969).

Slater J. C., "Introduction to Chemical Physics" (McGraw-Hill Book Company, Inc., New York, 1939).

Smyth C. P., "Dielectric Behaviour and Structure: Dielectric Constant and Loss, Dope Moment and Molecular Stricture" (McGraw-Hill Book Company, Inc., New York, 1955).

Thurston R. N., Proc. IEEE **53**, 1320 (1965a).

Thurston R.N. and Brugger K., Phys. Rev. **133**, A1604 (1964).

Verma A. R. and Krishna P., "Polymorphism and polytypism in crystals"., (John Wiley and Sons, Inc, New York, 1966).

Wachtman (Jr.) J. B., Scuderi, T. G., Cleek, G. W., J. Amer. Geram. Soc., **45**, 319 (1962).

Wachtman (Jr.) J. B., Tefft W. E., Lam Jr. D. B. and Stichfied R. P., J. Res. Nat. Bur. Stand. **64A** 213 (1960).

Wagner R. J., Ann. D. Physik **40** , 817, (1913).

Wang Q., Saunders G. A., Lambson E. F., Tschaufeser P., Parker S. C., and James B. J., Phys. Rev. B **45**, 10242 (1992).

Will F. G., deLorenzi H. G., and Janora K. H., J. Am.Ceram. Soc. **75**, 295 (1992a).

Will F. G., deLorenzi H. G. H. G., and Janora K. H., J. Am.Ceram. Soc. **75**, 2790, (1992b).

Yogurtcu Y. K., Ph.D. Thesis, University of Bath, 1980.

Appendix A

Computer Programmes

1. Computer Programme: SONIC.BAS

This programme, written in Microsoft QuickBASIC Version 4.5, computes the elastic moduli, the Poisson's ratio, pressure derivatives of the elastic moduli and the long wavelength acoustic mode Grüneisen parameters of the ceramics.

2. Computer Programme: T.BAS

The functions of this acquisition program, written in Microsoft QuickBASIC Version 4.5, are to: (1) measure resistance, (2) measure ultrasonic attenuation, (3) plot ultrasonic overlap frequency, (4) measure ultrasonic attenuation and plot ultrasonic overlap frequency as a function of temperature between 10K and 325K, and (5) set the temperature of the system to a selected temperature by increasing or decreasing temperature in a selected speed in the temperature range of 10K and 325K. The programme controls the temperature controller (Model DRC-91C, LakeShore Cryotronics, Inc.), digital multimeter (Model 5004, Racal-Dana Instruments, Inc.), IEEE current source (Model 9818, Time Electronics LTD.).

3. Computer Programme: ATVLPRE3.BAS

The functions of this acquisition program, written in Microsoft QuickBASIC Version 4.5, are to measure ultrasonic attenuation and to plot ultrasonic overlap frequency and as a function of pressure. The programme controls digital multimeter (Model 5004, Racal-Dana Instruments, Inc.).

4. Computer Programme: ATPRES.BAS

The functions of this acquisition program, written in Microsoft QuickBASIC Version 4.5, are to measure ultrasonic attenuation as a function of pressure. The programme controls digital multimeter (Model 5004, Racal-Dana Instruments, Inc.).

5. Computer Programme: HANDPRES.BAS

The function of this acquisition program, written in Microsoft QuickBASIC Version 4.5, are to plot ultrasonic overlap frequency as a function of pressure.

6. Computer Programmes: LADSET1.BAS, LADSET2.BAS, LADSLECT.BAS, LADMCL.BAS, LADMWM.BAS, LADMWMCL.BAS, LADMCLWM.BAS and LADMHWM.BAS

The functions of this group of programs, written in Microsoft QuickBASIC Version 4.5, are to measure frequency dependence of conductance G and susceptance B in selected frequency range and steps (1) in the selected temperature ranges and steps between 10K and 325K which is controlled by using the temperature controller (Model DRC-91C, LakeShore Cryotronics, Inc.) and (2) at any selected temperature which is controlled manually. The programme controls the temperature controller (Model DRC-91C, LakeShore Cryotronics, Inc.) and LF impedance analyzer (Model 4192A, Hewlett Pachard Ltd). The start programme of this group of programmes is LADSET1.BAS. Other programmes are automatically loaded in.

In all of above programmes the function keys of F_1 and F_{10} have been defined. The function of F_1 key is to save the data and continue to do the measurements. The function of F_{10} key is to save the data and quit.

Before the start any of above programmes start a batch file called "QK.BAT" in the dos environment.

PUBLICATIONS

1. **Hydrostatic Pressure Effects on the a-Axis Resistance of Monocrystalline $Bi_2(Sr,Ca)_{2.8}Cu_2O_{8+y}$**
   H.J. Liu, Q. Wang, G.A. Saunders, D.P. Almond, K. Kitahama and B. Chapman
   Phys. Rev. B **51**, 9167 (1995).

2. **Electrical Resistance under Pressure in Textured $Bi_2Sr_2CaCu_2O_{8+y}$: Enhancement of the Energy Gap and Thermodynamic Fluctuations**
   Q.Wang, G. A. Saunders, H. J. Liu, M. S. Acres, and D. P. Almond.
   Phys. Rev. B **55**, 8529 (1997).

PRESENTATIONS IN CONFERENCES

1. **Elastic Behaviour of Dense Textured $Bi_2Sr_2CaCu_2O_{8+y}$**
   Liu Huijin, J. Li, Chang Fanggao, M Cankurtaran, D.P. Almond, P.J. Ford, G.A. Saunders
   Condensed Matter and Materials Conference - 1992, Institute of Physics, University of Shefield, 15-17 December 1992.

2. **Pressure Dependence of Normal and Superconducting Electrical Properties of $Bi_2(Sr,Ca)_{2.8}Cu_2O_{8+y}$**
   H.J. Liu, Q. Wang, D.P. Almond, G.A. Saunders and B. Chapman.
   High Temperature Superconductors VIII, Birmingham, 19-21 September 1994.

3. **The Anisotropic Elasticity and Nonlinear Acoustic Properties of Dense Textured $Bi_2Sr_2CaCu_2O_{8+y}$**
   Q. Wang, G.A. Saunders, D.P. Almond, P.J. Ford, Chang Fanggao, E.F.Lambson, H.J. Liu, M Cankurtaran, and K.C. Goretta.
   High Temperature Superconductors VIII, Birmingham, 19-21 September 1994.

4. **Comparison of the Hydrostatic Pressure Effect on the Electrical Resistance of Monocrystalline $Bi_2(Sr,Ca)_{2.8}Cu_2O_{8+y}$ with the Predictions of the BCS and RVB Models**
   H.J. Liu, Q. Wang, D.P. Almond, G.A. Saunders and B. Chapman.
   Third HTC Single Crystal Workshop, Birmingham, 26-27 September 1994.

5. **Hydrostatic Pressure Effects on the Electrical Properties of Monocrystalline $Bi_2(Sr,Ca)_{2.8}Cu_2O_{8+y}$**
   H.J. Liu, Q. Wang, D.P. Almond, G.A. Saunders, B.Chapman
   Condensed Matter and Materials Conference - 1994, Institute of Physics, University of Warwick, 19-21 December 1994.